Doctoral theses at NTNU, 2023:41

Sebastian Reymert

Field investigations of crosswinds and vehicle-driver response on bridges

Doctoral thesis

NTNU
Norwegian University of Science and Technology
Thesis for the Degree of Philosophiae Doctor
Faculty of Engineering
Department of Structural Engineering

NTNU
Norwegian University of Science and Technology

Sebastian Reymert

Field investigations of crosswinds and vehicle-driver response on bridges

Thesis for the Degree of Philosophiae Doctor

Trondheim, February 2023

Norwegian University of Science and Technology
Faculty of Engineering
Department of Structural Engineering

NTNU
Norwegian University of
Science and Technology

NTNU
Norwegian University of Science and Technology

Thesis for the Degree of Philosophiae Doctor

Faculty of Engineering
Department of Structural Engineering

ISBN 978-82-326-6227-2 (printed ver.)
ISBN 978-82-326-6117-6 (electronic ver.)
ISSN 1503-8181 (printed ver.)
ISSN 2703-8084 (online ver.)

Doctoral theses at NTNU, 2023:41

Printed by NTNU Grafisk senter

"En god vei er 10 ganger bedre enn en dårlig vei,
men en dårlig vei er 100 ganger bedre en ingen vei"
- Andreas Baalsrud
(Vegdirektør, 1919-45)

"A good road is 10 times better than a bad road,
but a bad road is 100 times better than no road"
- Andreas Baalsrud
(Director General of the NPRA, 1919-45)

Preface

This thesis is submitted in partial fulfilment of the requirements for the degree *Philosophiae Doctor* at the Norwegian University of Science and Technology (NTNU). The work has been carried out at the Department of Structural Engineering, Faculty of Engineering. Professor Anders Rönnquist, Professor Ole Øiseth and Associate Professor Lars Drugge (Department of Engineering Mechanics, KTH Royal Institute of Technology in Stockholm) have supervised the work. The Norwegian Public Roads Administration (NPRA) has funded the work.

Sebastian Reymert

January 24, 2023
Trondheim, Norway

Abstract

There are currently no scientific, evidence-based guidelines for designing wind-related traffic regulations on Norwegian road bridges. The topic of crosswind-exposed vehicles on bridges has been studied theoretically, numerically and in the lab, but not in the field. In this work, a test vehicle is established to take measurements of wind, vehicle and driver response in strong crosswinds. The aim is to identify and characterise gusts that cause drivers to perceive the vehicle as less stable and/or controllable.

Field measurements were taken under strong crosswinds (peak gust speeds between 20 and 32 m/s) on 7 different bridges – of which 4 are suspension bridges, 2 are cantilevered and 1 is cable-stayed – and 2 fixed-base roads in Norway. To the best knowledge, the data set is the first of its kind, with up to 40 repeated crossings at each location, utilising two-point satellite positioning, a 3-component accelerometer and gyroscope, an ultrasonic anemometer and measurements of driver steering input.

Predictable gusts are observed leeward of discrete obstacles to the crosswind such as towers, support piers, substantial structural components under the bridge deck or land at the abutments. It is found that gusts with certain spatial dimensions (1-4 vehicle lengths) and temporal periods (0.36-2 s) induce the most severe adverse handling responses. Stochastic gusts emanating from upstream terrain and the separation of flow over bluff-section bridge girders are found to continually perturb the vehicle-driver system and in some cases to cause front-axle skid events.

In general, it is found that decreasing the driving speed significantly decreases the severity of wind-induced handling motions. On the other hand, if large-scale, coherent vortex shedding is observed in the wake of the towers at a frequency that matches the vehicle's natural roll frequency, then slow driving speeds allow excessive roll motions to develop. This can be a significant comfort issue.

The results allow infrastructure owners to design better mitigation strategies and ensure the safe crossing of vehicles whilst satisfying serviceability and cost requirements. Further research on mitigation strategies is needed, though the modulation of driving speed has been shown to effectively reduce the severity of handling response to wind perturbations.

Acknowledgements

Firstly, I would like to thank my main supervisor, Anders, for giving me the opportunity to move to Trondheim and experience what I have experienced in the last three and a half years as a PhD student. I am grateful to have had Ole as a co-supervisor, who has taken much of the burden after Anders moved into his role as department head. I have been so lucky as to have a third co-supervisor, and a big thank you goes to Lars for always being helpful and quick to respond.

I would like to mention the following colleagues for their direct contributions to this work:

- Anno, who joined me for countless hours on cold and dark Norwegian winter roads in the hunt for strong winds. Your help in the field has been invaluable for this thesis. Your friendship and encouragement in sporting endeavours is also greatly appreciated.
- Øyvind, who was my office mate for the majority of the project and always seems to have the answer. I have borrowed your expertise more times than I can count and sincerely appreciate the time you took to read and give comments on this thesis.
- Gøran, who carried out much of the installation work on the test vehicle and always managed to find a creative solution to practical problems.
- Shaoyao, who jumped on a flight with me to Narvik – which is more than 200 km north of the arctic circle – with less than a couple hours notice only two days into the new year.
- Gunnstein, who took the time to help out with the experiments at Værnes and for giving all round advice on many matters.
- Friederike, Jonas and Anne, who provided translation services free of charge.

A big thank you goes to the people at Avinor (Værnes) who gave us access to an international airport for several hours on two separate occasions. I am grateful to the patient souls of Værnes Fire and Rescue for spending the night supervising us while we burned rubber and drove all over the taxiways and runway. Thank you,

not the least, for your trust. I have had help from multiple people outside of the university:

- Vegard Fossbakken at Trøndelag fylke provided drawings of multiple bridges.
- Per Ove Ravatsås at Norldand fylkeskommune provided drawings of the Helgeland bridge.
- Signe Evjen at SVV Prosjekt Hålogaland helped us with the measurements at the Hålogaland bridge.

The Norwegian Public Roads Administration (*Statens Vegvesen*) has funded this work. I am grateful to Tore Askeland for his continued involvement and interest in the project.

I would like to acknowledge those that have published their code on the MATLAB Central File Exchange and elsewhere for others to use [63–68, 94, 105, 122, 139, 157] and those working at Kartverket who have made Norwegian map data such a rich, accessible and open resource. You have all greatly enhanced this thesis.

All present and past colleagues including Stefano, Gabriel, Bjørn, Aksel, Dario, Marcin, Maria, Tengjiao, Oddbjørn, Haldis and many more have made my day-to-day life as a PhD student at the department thoroughly enjoyable.

Thank you to my family for your support and for providing the upbringing that has brought me to this point in life. I am lucky to have had so many and such varied influences. Thank you mom for showing such strength, particularly in the last year. Thank you dad for dedicating time to reading my thesis and being so interested in and enthusiastic about my work. Last and by far not least, thank you Sara for making my life that much better these last two years. Your contribution to this work is more significant than you might know.

Contents

Chapter 1

Introduction

1.1 Motivation

Bridges in Norway are closed to road traffic when the 3-second mean wind speed exceeds a predetermined value at 90 degrees to the driving direction. Based on the experiences described in this work, this threshold varies from bridge to bridge. Some bridges have been observed to close at 25 m/s while others close only when measurements exceed 32 m/s.

Road users are notified about the closure through automated electronic signs that show the *open/close* status of the roadway as well as the highest wind speed measured somewhere on the bridge in the past x minutes (varies from bridge to bridge). See Figure 1.1 for an example of how one of these electronic signs looks when a bridge is closed. The bridge remains closed for 10 minutes from the last time the threshold was exceeded.

To the best current knowledge, there are no formal, evidence-based guidelines in Norway for deciding what the threshold wind speed should be [21]. Whether a bridge closes at 25 m/s or 32 m/s (or any other speed) is a choice that appears to be made on the basis of experience. The automated closure system is sometimes overridden in order to relieve congestion, or let certain – typically emergency – vehicles across. Sometimes contractors can be found on-site regulating traffic manually as well. The overall system for managing wind-related traffic risks on bridges is therefore still largely dependent on manual evaluations, decisions and interventions.

Important infrastructure

Bridges are important for many communities living along Norway's rugged coastline, particularly for those who live on islands near the mainland. While alternative means of transportation often exist by sea, road connections are typically quicker and more reliable. Ferry services are often affected by weather conditions before

Figure 1.1: The electronic sign at the Tjeldsund bridge showing that the roadway is closed to traffic. (Photo: NTNU/Sebastian Reymert)

bridges are.

Måløy, Rørvik and Sandnessjøen are all examples of towns that only have one fixed road connection to the mainland via the Måløy (cantilevered), Nærøysund (suspension) and Helgeland (cable-stayed) bridges respectively (see Figure 7.1 to see these on a map of Norway). Each of these have been visited during the field sessions in addition to the Hålogaland (suspension), Hardanger (suspension), Tjeldsund (suspension), and Dolmsund (cantilevered) bridges.

For the typical bridge user it is important that bridges are safe to cross when they are open and that they are not closed unnecessarily [80]. From the perspective of a bridge owner – either the Norwegian Public Roads Administration (NPRA) or the local county in the case of Norwegian road bridges – it is important to provide a socio-economic benefit by maximising the ratio of utility to investment. This means maximising the serviceability of bridges for the lowest possible cost.

It is vital to understand how strong winds affect accident risk. The knowledge gained through this work will be increasingly useful going forward as ferry crossings are likely to be replaced by ever longer fixed-link crossings [74] and climate change threatens to make extreme wind a more frequent phenomena than it is today. Winds in Northern Europe that have a 100-year return period today (based on historical data in the period 1976-2005) may have return periods of 83 years by 2011-2040, 76 years by 2041-2070 and 67 years by 2071-2100 according to simulations [151].

1.1.1 Predicting wind-induced accidents

A test vehicle has been used in this work to take measurements of wind, vehicle and driver response under strong winds on various roads and road bridges in Norway. To give an initial idea of which winds (speed and direction) pose a threat to occupant safety, a simplified accident analysis will be presented for the test vehicle. The following is based on the analysis presented in a report by Camara [38].

The assumptions will then be discussed to highlight some of the challenges in making more accurate and/or precise accident predictions. This will motivate the rest of the work presented in this thesis.

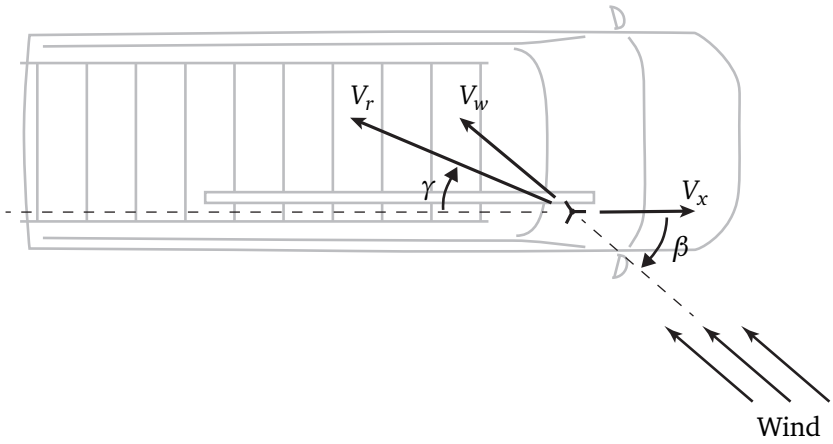

Figure 1.2: The relationship between the wind vector observed by a stationary observer V_w and that measured by the anemometer on the moving vehicle V_r (diagram adapted from [38]).

Background on the method

The idea is to simply calculate the static forces necessary to cause a lateral skid or rollover. The *accident wind speed* necessary to create these forces can be mapped as a function of driving speed and wind direction and can be used with in-situ wind measurements to regulate traffic. The analysis method was proposed by Baker [23] in 1987 and inspired a similar analysis by Camara [38] in 2019, both on the Orwell cantilevered bridge in England.

Camara was in fact commissioned by Highways England to re-evaluate the risk of wind-related accidents on the Orwell Bridge. Changes to the regulations have been enforced following his recommendations and electronic signs have been

placed on the bridge to regulate traffic as a function of wind conditions [8]. He performed two different static analyses – one with only in-plane forces and moments (2D), like the one presented next, and another with full 3D forces and moments. For reference, he also considered the effect of the girder on vehicle aerodynamic loads as well as the excitation of the vehicle by road roughness/undulations and bridge vibrations. This analysis will not be discussed here.

Aerodynamic loads on the vehicle

The aerodynamic loads on a vehicle can be described as a function of air density ρ, incident wind speed V_r, incident wind angle γ (to be defined below), a reference surface area A_f (frontal projection used here) and centre of gravity height h_{cg},

$$\begin{aligned} F_S &= \frac{1}{2}\rho V_r^2 C_S(\gamma) A_f \\ F_L &= \frac{1}{2}\rho V_r^2 C_L(\gamma) A_f \\ F_D &= \frac{1}{2}\rho V_r^2 C_D(\gamma) A_f \\ M_Y &= \frac{1}{2}\rho V_r^2 C_Y(\gamma) A_f h_{cg} \\ M_P &= \frac{1}{2}\rho V_r^2 C_P(\gamma) A_f h_{cg} \\ M_R &= \frac{1}{2}\rho V_r^2 C_R(\gamma) A_f h_{cg}, \end{aligned} \tag{1.1}$$

where S, L, D, Y, P and R denote the side, lift and drag force, yaw, pitch and roll moment respectively [38]. The wind speed V_r and angle of incidence γ in the vehicle's moving reference frame are functions of the vehicle and wind speed vectors as shown in Figure 1.2. The wind vector is defined relative to the road with the incidence angle β. The angle γ is calculated,

$$\gamma = \tan^{-1}\left(\frac{V_w \sin\beta}{V_x + V_w \cos\beta}\right). \tag{1.2}$$

Camara [38] presents his analysis for 5 different vehicle types. For the *large van* type (the test vehicle used in this work is a large van) he references aerodynamic force coefficients from Baker [23]. The aerodynamic coefficients are defined in [23] as a function of the wind incidence angle on the vehicle γ,

$$
\begin{aligned}
C_S &= \sigma_1 \gamma^{0.328} \\
C_L &= \sigma_2[1 + \sin(3\gamma)] \\
C_D &= \sigma_3[1 + 2\sin(3\gamma)] \\
C_Y &= -\sigma_4 \gamma^{1.77} \\
C_P &= \sigma_5 \gamma^{1.32} \\
C_R &= \sigma_6 \gamma^{0.924},
\end{aligned}
\tag{1.3}
$$

where each of σ_i are given in [23]. Substituting these expression into the force equations (1.1) as well as the definition of γ (1.2) gives the aerodynamic forces as a function of the wind speed V_w, incidence angle against the road β and vehicle speed V_x.

The shape of the coefficient curves in [23] are derived from wind tunnel data using a scale model Leyland Atlantean double-deck bus (1958-1986). The curves are then scaled based on wind tunnel data for a variety of different vehicle types at a single incidence angle $\gamma = 30°$. To apply this model to the current case is to make the following assumptions:

1. The aerodynamic coefficient curves for the test vehicle have the same shape as those of a double-deck bus.
2. The curves can be scaled to be appropriate to the geometry of the test vehicle (based on a single point from wind tunnel tests using a similarly shaped van).
3. The wind tunnel tests were performed with the appropriate Reynolds number and turbulence intensity for valid comparison with the real world.

Baker argues that there is a critical Reynolds number above which the coefficients are independent [25]. This Reynold's number was exceeded in the wind tunnel and so the argument is made that the curves are valid for use in assessing real-world environments. This partly addresses point 3. Points 1 and 2 will have to be addressed using engineering judgement.

The shape of the test vehicle is not too dissimilar to the Leyland Atlantean, though aerodynamic force coefficients will likely be higher on the bus. They are both box-like shapes, yet the modern test vehicle has been designed with crosswind response in mind. The concerns can therefore be alleviated by stating that the current approach is at the very least conservative. Nonetheless, the accuracy of the static coefficients can likely be improved significantly.

Accident prediction

The simplest accident model is developed by assuming the vehicle is a 2D rigid body resting on the ground. The free body diagram can be drawn as shown in

Figure 1.3. Two accidents types are possible:

1. *Overturning/rollover:* occurs when the aerodynamic loads cause the windward wheels to lose contact with the ground. For the case drawn in Figure 1.3,
$$F_{z,r} = \frac{mg}{2} - \frac{M_R + F_S h_{cg}}{w_b} = 0. \tag{1.4}$$

2. *Side-slip:* occurs when the aerodynamic loads cause the lateral interaction force between the wheels and the ground to exceed the value available through static friction $F_{y,max}$,
$$F_{y,max} = \mu mg, \tag{1.5}$$

where μ is the friction coefficient describing the friction available between the tyres and the road surface. $F_{z,r}$ and $F_y = F_{y,r} + F_{y,l}$ can be estimated for a range of wind speeds V_w, driving speeds V_x and incidence angles γ. The parameters necessary for the analysis with the current test vehicle are shown in Table 1.1.

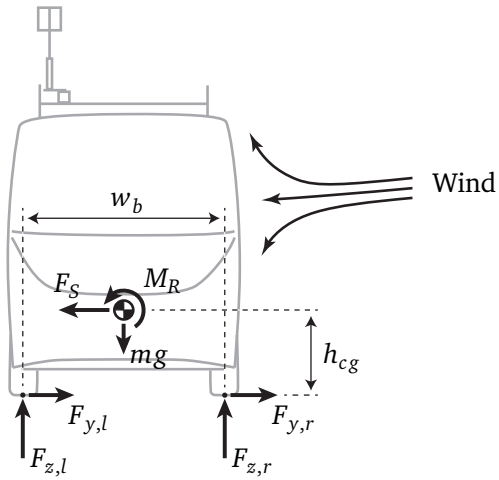

Figure 1.3: A 2D free-body diagram of the vehicle under lateral wind loading (diagram adapted from [38]).

The wind speed required to produce an overturning/rollover accident and the wind speed necessary to produce a side-slip (skid) accident can be calculated for a given wind direction and driving speed. The minimum of these two wind speeds is then defined as the accident wind speed. The accident wind speed can be plotted as a function of driving speed for a selection of wind directions. This is shown in Figure 1.4 for two different coefficients of friction, $\mu = 0.2$ and 0.7.

Table 1.1: Analysis Parameters

ρ	1.225 kg/m^3 **
A_f	4.25 m^2
h_{cg}	0.75 m
m	2,780 kg
w_b	1.79 m

**at 0 m in the International Standard Atmosphere [1].

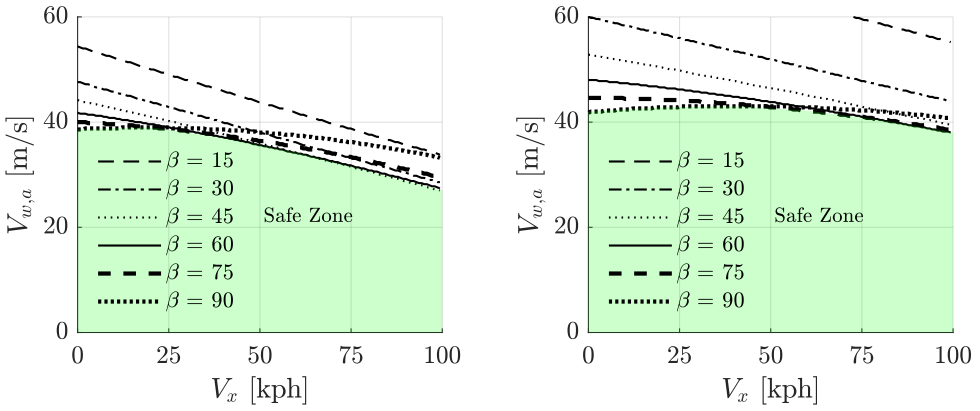

(a) $\mu = 0.2$ (b) $\mu = 0.7$

Figure 1.4: Maps of accident wind speed.

$V_{w,a}$: accident wind speed.
V_x: driving speed.

The lowest value $\mu = 0.2$ comes from the Bosch Automotive Handbook [164] and is the worst case scenario for worn tyres at a driving speed of 90kph on a wet surface. Note that values below 0.1 are possible with non-studded tyres on black ice. The test vehicle is equipped with studded tyres in the winter months. The highest value is the wet condition considered by Camara [38]. The side-slip accident mode is generally the critical one based on this analysis. This explains why the *safe zone* shrinks with μ in Figure 1.4.

The plots in Figure 1.4 are simple to understand and useful in defining speed limits that adapt to wind conditions. However, there are multiple assumptions that could make these plots overly conservative – thereby reducing serviceability unnecessarily – or not conservative enough – thereby failing to reduce the wind-related accident risk to an acceptable level.

Assumptions in the static analysis

The accuracy of the static aerodynamic coefficients has already been discussed. Attaining better estimates could be achieved in a wind tunnel with a scale model of the specific test vehicle. However, there are some more challenging unknowns to tackle. How significant are dynamic effects in relation to static loads? Which dynamics make the biggest difference? Some of the assumptions in the static analysis include:

1. **Steady aerodynamics**

   It is assumed by the application of the static aerodynamic coefficient curves that aerodynamic loads develop quasi-steadily. In reality, loads may be dynamically amplified or attenuated depending on the time period of change in wind speed and/or direction. Changes that are faster than 3 seconds – perhaps poorly captured by the 3-second mean wind speed – may in fact be relevant to vehicle safety. The 3-second mean is used both in Norway and on the Orwell bridge in England to regulate traffic.

2. **A rigid vehicle**

   Vehicles are not rigid structures. There is compliance in the suspension system and chassis that will change the dynamic distribution of vertical and lateral tyre loads. Sources of excitation of the suspension system include the roughness and/or undulations of the road surface and the vehicle-induced and wind-induced motions of the bridge deck.

3. **An unsteered vehicle**

   In the current, real operating environment, vehicles are controlled by human drivers. A driver may be able to avoid wind-induced accidents by applying appropriate steering control. The opposite is certainly possible as well. Drivers

can respond poorly to wind loads and be the primary cause of rollover or side-slip incidents. The static analysis does not consider the handling (lateral) dynamics of the vehicle at all.

4. **Wind homogeneity**

   In order to use the accident curves in Figure 1.4 it is necessary to know what wind speed and direction a vehicle is likely to experience on the bridge. A point measurement of wind speed may not be sufficient to describe the expected wind along the entire span. The assumption in Norway and on the Orwell bridge is that the 3-second mean wind speed measured at one point on the bridge sufficiently characterises the maximum load seen by vehicles across the whole span. Local variations may occur as a result of changes in bridge geometry or local topography.

The biggest contribution of this work will be to describe inhomogeneities in the wind field resulting from structural features of the bridge and local topography (assumption 4). It will be shown that only gusts of a certain frequency (i.e. certain turbulent length scales) are a significant concern to vehicle safety (assumption 1). All analysis is based on field measurements that include a fully featured vehicle (assumption 2) with a driver (assumption 3).

1.2 Recent research

The literature will be systematically reviewed and discussed in Chapter 4 and so only a brief summary of the current state of knowledge will be given here. To support the analysis presented later in this thesis it will be necessary to review some relevant literature at the beginning of some of the other chapters. For example, existing measurements of the Strouhal number in the wake of high aspect ratio cylinders will be reviewed in Chapter 14 to enhance the discussion of the phenomenon observed at the Helgeland bridge. Studies concerned with on-road wind measurements, wind-induced accidents on roads and wind-induced accidents on bridges will be reviewed here.

Vehicle safety on roads

Some of the earliest and best known works on wind-related road accident risk are by Baker [22–29]. In the first of these papers, Baker writes in his conclusion on the static methodology (similar to one used in Section 1.1.1 here),

> "*. . . it must be emphasised that this method has not been checked against reality, and until this is done no great reliance should be placed on the absolute values of accident wind speeds that are predicted.*"

The emphasis in this work will be on observations of wind, vehicle and driver in the real operating environment of road vehicles on public roads in Norway.

On-road field measurements

There are some examples of vehicle-based field measurements of wind that have been undertaken since Baker's first paper:

- Snæbjörnsson et al. [179] performed wind measurements on public roads in Iceland with an ultrasonic anemometer fixed to a vehicle that was equipped with a GNSS antenna. They used the recordings to show that the vector relation shown in Figure 1.2 holds true for their experimental set-up.
- Quinn et al. [162] and Sterling et al. [190] take wind and surface pressure measurements (taps on the surface of the vehicle's body) on a commercial vehicle in a stationary position as well as while driving on a public road in England. In the first work, rolling moment coefficients are estimated using pressure measurements and in the second study the full-scale/field results are compared to CFD and wind tunnel experiments.
- Wordley in [219–221] measured the wind on multiple roads in Australia with different surrounding terrain types. The goal of the experiment was to characterise the frequency content of the wind such that realistic conditions can be re-created in wind tunnel studies.

Other than Snæbjörnsson et al. [179], where wind speeds up to 25-30 m/s appear to have been recorded, the field experiments were performed at relatively low wind speeds ($\sim$ 5 m/s in crosswind during the driven sessions in England [162, 190] and less than 5 m/s in crosswind in the Australian measurements [220]). No study has made use of a substantial measurement system to measure vehicle body acceleration, position, attitude, velocity and driver input.

Vehicle safety analysis on bridges

There is a coupled interaction between all three components of vehicle, bridge and wind:

- ***Vehicle-wind:*** As discussed above, the wind applies forces to vehicles directly. On bridges, vehicles can act like obstacles that change the flow around the structure and in turn the resulting aerodynamic loading on both the bridge and the vehicle.
- ***Bridge-wind:*** Interaction phenomena between bridges and wind include the development of self-excited forces (fluid-structure interaction) like galloping or flutter and more direct response to wind loads like buffeting (in response to turbulence) and vortex-induced vibration.

- ***Vehicle-bridge:*** Vehicles are moving loads that can excite the vibration modes of bridges. The vibration can in turn induce a vibrational response of the vehicle (by the suspension between the wheels/tyres and the body). The dynamics of the two systems can interact and the result could be amplified bridge and/or vehicle response.

The vehicle-bridge-wind system is therefore a complex one. It has been studied from both the perspective of structural health [90, 127, 233, 241] and traffic safety [34, 39, 87, 211, 242]. These cited works are only a small selection of the many works on vehicle-bridge-wind interaction. To probe the existing literature more, please see the published database [165] created for the systematic mapping in Chapter 4.

Mitigation strategies have also be investigated in the literature. The following will be discussed further in Chapter 4, but the most promising wind-induced accident mitigation strategies are:

- Wind barriers to reduce wind loads on vehicles for at least part of the bridge span [41, 46, 92, 114, 131, 223, 224]: these are typically localised near the towers to dampen the sharp changes in wind speed.
- Operational constraints based on in-situ wind measurements [40, 53, 131] like the systems used at the Orwell bridge and on bridges in Norway: constraints may include closure of the bridge or modulation of the driving speed for certain combinations of wind speed and driving direction as suggested in [38].

1.3 Objectives

The overarching aim of this work is to contribute to a better understanding of wind-related accident risks on Norwegian road bridges. This will allow infrastructure owners to design better mitigation strategies that ensure the safe crossing of vehicles whilst satisfying serviceability and cost requirements.

One of the conclusions from the systematic mapping study (Chapter 4) is that models of transient vehicle aerodynamics are a particular area of interest. They are not well developed and are untested in reality. An overall need for more observations of the vehicle-bridge-wind system in reality is identified.

In Chapter 5 it is concluded that vehicle-bridge interaction is unlikely to significantly contribute to vehicle excitations that are relevant to accident risk in Norway. Vehicle-bridge interaction may be a more relevant concern in countries where traffic volumes are larger and bridges have more than one lane in each direction. During the field experiments presented in this work, the test vehicle was mostly on the bridge deck alone.

Given the conclusions of the systematic mapping and the vehicle-bridge interaction studies, it was decided that the core contribution of this thesis would be observations of the wind, vehicle and driver response on bridges. A particular emphasis is placed on understanding the direct load action of wind on the vehicle.

The objectives of the work are to:

1. ***Establish a vehicle-based instrumentation system that can be used to observe wind, vehicle and driver on public road bridges under strong cross-winds***
2. ***Characterise the wind environment on bridges***
    - Is a single-point measurement of wind speed and direction appropriate to characterise the wind-related accident risk posed to vehicle-driver systems?
    - Which features of the wind environment are critical to driver-perceived stability and control?
    - Which features of the structural bridge design affect the presence and severity of safety-critical wind features?
3. ***Describe the vehicle's response to the wind environment under the control of a driver***
    - How can the vehicle-driver's resultant response (the motions of the vehicle resulting from wind perturbations and driver control) be evaluated to describe comfort, stability or controllability?
    - How does the vehicle-driver response change as a function of driving speed?

1.4 Scope

The current experimental study has been limited to:

- bridges and roads in Norway that have been open to normal, public traffic during the period of the measurement campaign,
- cable-stayed, suspension and cantilevered bridges,
- one test vehicle, the VW Crafter L4H3, and
- one test driver, myself.

It is noted that the roads/bridges visited during the field experiments were generally free of traffic. Traffic volumes are low in Norway in comparison to many countries and the experiments were performed under adverse weather conditions

and often during the night. It was typical to see only a handful of other vehicles during the sessions. The only place where there was a notable amount of traffic was at Måløy. Consequently, the effects of traffic will not feature significantly in this work.

Barring the numerical study of vehicle-bridge interaction in Chapter 5, this thesis is purely an observational study of the experimental data collected in the field. The systematic mapping in Chapter 4 along with additional literature reviews at the beginning of some chapters are used to enhance the discussion and draw more significant conclusions. The updating of a single-track vehicle handling model is provided in Appendix A to give background to the description of the handling frequency response functions presented in Chapter 2.

1.5 Organisation of thesis

The core investigation presented in this thesis is shown by the dark arrow in Figure 1.5. It starts with a systematic mapping of the literature on vehicle-bridge-wind systems. The conclusions of the mapping study – combined with a brief investigation of vehicle-bridge interaction – sets the direction for the remaining work. The priority becomes gathering data from the field that describes vehicle-driver response to wind perturbations on bridges.

Chapters 6 and 7 present the instrumentation used in the field and give an overview of the field sessions respectively. Observations of wind features that may be consequential for vehicle safety are made in Chapter 8. The effect of the identified wind features on the vehicle-driver system is described in Chapters 10 through 12. Two particularly interesting wind features are then studied in more detail:

1. ***Tower wakes***: The bridge towers at suspension and cable-stayed bridges form wakes that – upon passing – induce a strong response in the vehicle-driver system. This is found in Chapter 11 to be related to the dimensions of towers and their respective wakes. The characterisation of wakes and aerodynamic loads in the wake of towers is a topic of significant interest in the literature [20, 42, 132, 133, 166, 209, 236]. The mean wind profiles measured in the driving lanes of each of the visited cable-supported bridges are therefore presented and discussed in Chapter 13.
2. ***Vortex shedding***: The phenomenon of large-scale vortex shedding was observed in the wake of the Helgeland bridge towers and is reported in Chapter 14. This is included in this thesis because the oscillatory wind pattern induced a severe roll response of the vehicle. This was a experienced as a comfort issue in the field sessions, but could become a safety issue depending on vehicle type, driving speed and style. The data is also interesting simply as an observation of high Reynold's number vortex shedding (Re of the order of 10^7)

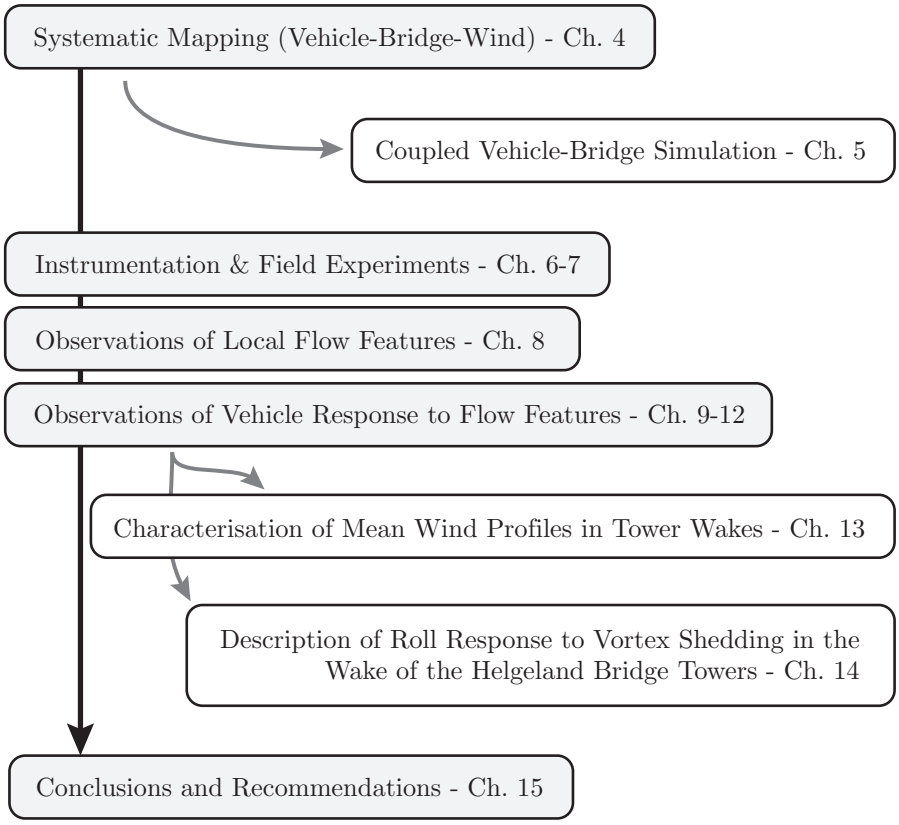

Figure 1.5: An outline of this thesis.

and is compared to the substantial set of literature on simulating the vortex shedding phenomena numerically and in the wind tunnel.

Conclusions and recommendations for infrastructure owners and future research are given in Chapter 15.

1.6 Coordinate systems, symbols

Vehicle coordinate systems

Three coordinate systems are needed to translate information between the GNSS system, the IMU and the virtual space of the single track model (Appendix A). A *global* (earth-fixed, XYZ) reference frame is used to describe the vehicle's translation and orientation relative to the earth and its geographical features. This is the coordinate system used by the GNSS system (see clarification below) and is denoted by E. The *local* S-frame ($x'y'z'$) is fixed to the vehicle's body and is the one used by the IMU.

A third reference is useful to translate GNSS and IMU information for comparison with the single track model. The xyz system shown in Figure 1.6 has its origin on the global XY-plane at the projection of the vehicle's CG. The x-axis points in the longitudinally forward direction of the wheels/suspensions/axles. This system is denoted U.

A common conceptualisation of the vehicle is that it is composed of one or more sprung bodies (all components held by the suspension) and one or more un-sprung bodies (the suspension, axles, wheels and other components not supported by the springs in the suspension). The xyz coordinate system can be thought of as fixed to the un-sprung body, which in the sprung/un-sprung conceptual model remains plane to the global XY-plane.

Geographic coordinate systems

The GNSS system on the test vehicle gives the ellipsoidal latitude, longitude and height coordinates in an earth-centered, earth-fixed (ECEF) coordinate system. For the case of GPS coordinates the ellipsoid is specified by the World Geodetic System WGS 84 standard. This is the system used in this work. A good source for further information about GNSS systems is ESA's navipedia (gssc.esa.int/navipedia).

A *local* earth-fixed, Cartesian coordinate system will be defined at each individual test site. These coordinate systems follow the east-north-up (ENU) convention described in Figure 1.7. A plane parallel to the WGS 84 reference ellipsoid at a given origin (latitude, longitude and height) is defined and the axes X and Y are chosen to be in the east and north directions respectively. The Z-axis is co-linear

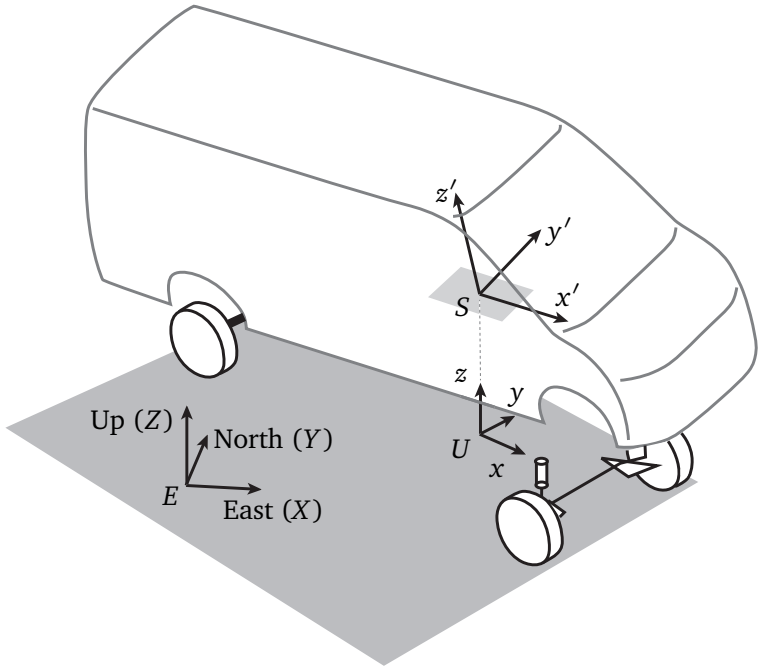

Figure 1.6: Defining coordinate frames fixed to the vehicle.

with the radial axis of the ellipsoid at the origin of the local ENU system. The Cartesian ENU system is a more practical reference frame than the ellipsoidal system and will be used in this thesis.

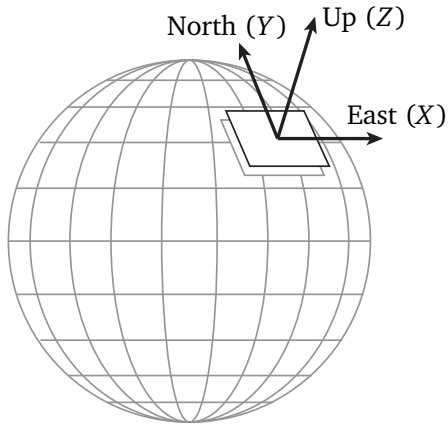

Figure 1.7: The east-north-up (ENU) coordinate system.

An example

An example of a local ENU coordinate system (X-Y) defined at the centre-point between two bridge towers can be seen in Figure 1.8. In this example, the bridge girder runs from the two abutments at end points A and B (assigned arbitrarily). An axis s is then defined from point A to B along the curvilinear path of the road and takes values between 0 and 1 (where 0 is at point A). The axis is denoted T when using metres rather than the normalised value.

The vehicle's S-frame has been sketched (x'-y') and is not necessarily aligned with the bridge. The axes X_b-Y_b are aligned with the bridge axis. The wind's angle of incidence relative to the vehicle's yaw attitude is β. The angle of incidence to the bridge axis is ϕ and the wind's heading in degrees north is denoted Ψ.

Symbols

The symbols used in this thesis are defined under the *Symbols* chapter which is presented after the *References*. Some notes on the use of symbols in this thesis:

- Chapter 5 has been published in the proceedings from the IABMAS conference in 2021. Consequently, the use of symbols has not been changed for

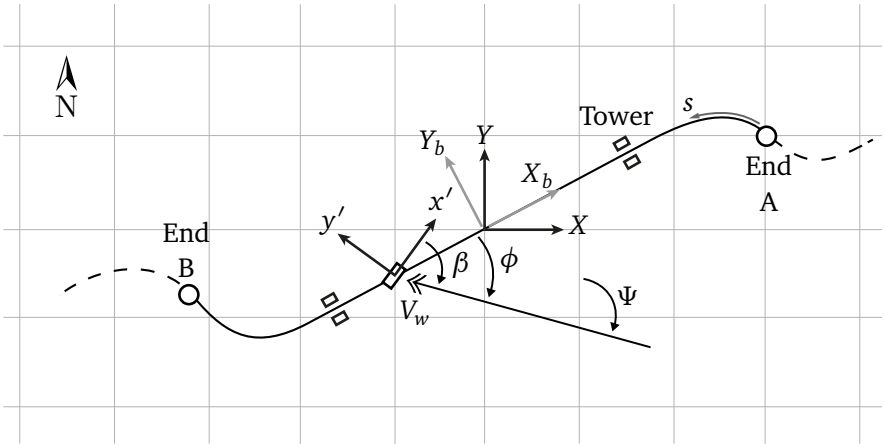

Figure 1.8: A birds-eye view of the bridge, a local ENU system, the vehicle and the wind vector with magnitude V_w.

consistency with the rest of the thesis, nor are symbols from said chapter included in the list at the end. All symbols are sufficiently introduced in the text.

- The definition of aspect ratio AR is different in Chapters 13 and 14 to make better comparisons with the literature in each respective chapter. The abbreviation is clearly defined in each.
- U has been used as both the name of a coordinate system as introduced in this chapter and as a generic characteristic wind speed in the definition of aerodynamic quantities. The appropriate interpretation will be clear from context.

Chapter 2

Background on vehicle-driver crosswind sensitivity

There are three non-trivial factors at play when drivers are confronted with crosswinds on a bridge:

1. The characteristics of the vehicle's handling response to driver input and external perturbations.
2. The characteristics of vehicle aerodynamic loads and their relationship to the characteristic winds seen on bridges.
3. The ability of a human driver to react appropriately to external perturbations.

Each of these topics have been explored in the existing literature and will be tied together in this chapter to provide a background understanding of the crosswind sensitivity of driver-steered road vehicles.

2.1 Vehicle handling characteristics and sensitivity to perturbations

The handling response of a vehicle – as it will be termed and used in this text – refers specifically to the yaw (rotation about z) and lateral (y) motion of the vehicle. The single track model is commonly used to describe the handling dynamics of road vehicles. As shown in Figure 2.1, the tyres on the front and rear axles are each modelled as an equivalent tyre at the front and rear respectively.

The model describes an interaction between the vehicle's lateral motions, the resulting inertial forces, and the lateral forces produced by the tyres F_1 and F_2. The equations of motion are [10, 153]:

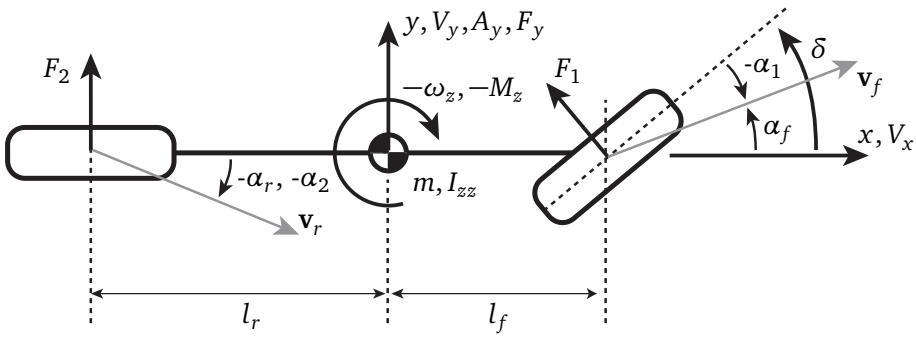

Figure 2.1: A single-track model of vehicle handling dynamics that is described in more detail in Appendix A.

$\alpha_{f/r}$: side-slip angle of front/rear axle.
α_2: side-slip angle of rear tyres (same as α_r for non-steered rear wheels).
α_1: side-slip angle of front tyres.
$\mathbf{v}_{f/r}$: velocity vector at front/rear axle.

$$\begin{bmatrix} \dot{V}_y \\ \dot{\omega}_z \end{bmatrix} = \begin{bmatrix} \frac{-(C_f+C_r)}{mV_x} & \frac{mV_x^2+C_r l_r-C_f l_f}{mV_x} \\ \frac{C_r l_r-C_f l_f}{I_{zz}V_x} & \frac{-(C_r l_r^2+C_f l_f^2)}{I_{zz}V_x} \end{bmatrix} \begin{bmatrix} V_y \\ \omega_z \end{bmatrix} + \begin{bmatrix} \frac{C_f}{m} \\ \frac{C_f l_f}{I_{zz}} \end{bmatrix} \begin{bmatrix} \delta \end{bmatrix}. \tag{2.1}$$

The single track model is described in more detail in Appendix A where a model updating procedure is used to develop an accurate model of the test vehicle's handling dynamics.

Single track dynamics

Pacejka [153] gives a succinct presentation of how the system poles of the single track model change as a function of vehicle and driving parameters. An interesting property to the current study is that an increase in driving speed has the effect of decreasing the damping ζ and undamped natural frequency ω_0 of the system. The damped natural frequency ω_n ($= \omega_0\sqrt{1-\zeta^2}$) remains approximately constant with variations in driving speed.

Abe [10] delves deeper into the vehicle's response to perturbations. He shows that an understeered vehicle develops stabilising transient lateral forces and yaw moments in response to lateral force perturbations acting at the centre of gravity (without driver input). Such a perturbation is commonly introduced by undulations in the road. The undulations cause the vehicle to roll, giving the gravity vec-

tor a horizontal component which looks like an external force acting at the centre of gravity.

On the other hand, the transient forces developed by an oversteered vehicle work to increase the magnitude of the response to perturbing forces. Depending on the driving speed, the vehicle may fall into an unstable spiralling motion. This occurs if the driving speed is above the so-called critical velocity $V_x > V_c$.

The test vehicle used in this work is understeered. Therefore, without driver input, the system works to reduce the handling response to lateral force perturbations acting at the centre of gravity.

Understeer/oversteer

The degree of understeer is a function of the mass distribution of the vehicle and each axle's effective cornering stiffness. The effective cornering stiffness at each axle is in turn a function of tyre characteristics, road surface conditions as well as compliances in the steering and suspension systems. The tyres as well as the steering and suspension systems can introduce a number of non-linear effects. See both of the aforementioned texts for more details on the non-linearities in the vehicle handling system [10, 153].

The degree of understeer can be characterised by the distance from the centre of gravity to the so-called neutral steer point nsp. Figure 2.2 shows an example of single track model of an understeered vehicle where the neutral steer point is behind the centre of gravity and the distance between them is l_{nsp}. By definition, a horizontal load can be applied at the neutral steer point without inducing a yaw motion to the vehicle.

This explains why the understeered vehicle ($l_{nsp} > 0$) is less sensitive to a horizontal perturbation at the centre of gravity. The centre of gravity is ahead of the neutral steer point such that the vehicle rotates with the force and the resulting centripetal force acts in the opposite direction to the perturbing force. During the transient period of motion, the lateral tyre forces are therefore reduced in magnitude by aide of the centripetal force.

An oversteered vehicle rotates into the force such that the resulting centripetal force adds to the perturbing force. This will in turn increase the lateral tyre forces. See Abe [10] for a full description of the transient development of forces in this situation. The distance l_{nsp} is related to the static margin [10] and the understeer gradient [153].

Aerodynamic perturbations

The point at which a resultant aerodynamic load acts on the body is called the centre of pressure – sometimes called the aerodynamic centre. This point can move depending on the flow conditions – primarily the wind's incidence angle γ [134].

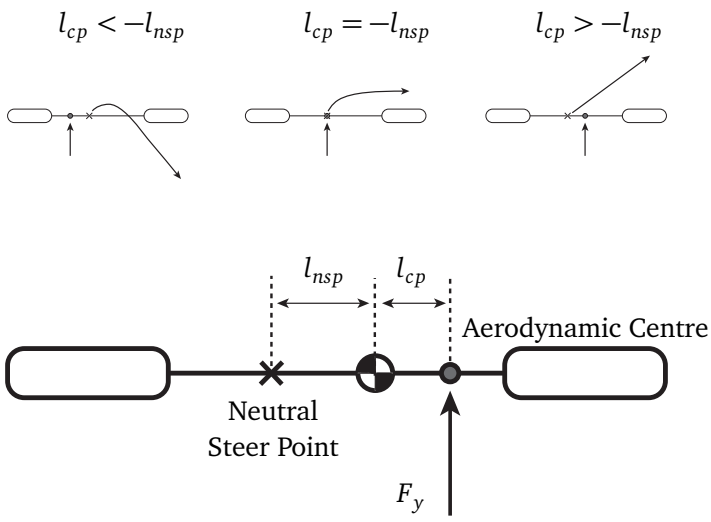

Figure 2.2: The neutral steer point, centre of pressure and centre of gravity and their effect on the transient response to a hat-shaped crosswind gust (based on sketches in Table 4.1 of [10]).

An aerodynamic perturbation will therefore act much in the same way as a perturbation acting at the centre of gravity if the aerodynamic centre is ahead of the neutral steer point as shown in Figure 2.2. Without driver input, the vehicle will respond such that the response is dampened.

As clarified by the graphical formulation in [134], a steering input in a traditionally front-steered vehicle is equivalent to applying a *perturbing* – or more appropriately a *controlling* – force at the front axle (ahead of the neutral steer point). The vehicle's response to steering input therefore gives an indication as to it's response to wind perturbations if the neutral steer point, centre of gravity and aerodynamic centre are arranged as shown in Figure 2.2.

The three sketches at the top of Figure 2.2 show how the vehicle is expected to react to a hat-shaped crosswind gust for different combinations of l_{nsp} and l_{cp} according to [10]. If the aerodynamic centre trails the neutral steer point then the vehicle turns into the crosswind gust. If the two points are coincident, then the vehicle simply gets translated to the side. Lastly, if the aerodynamic centre is ahead of the neutral steer point, then the vehicle is translated and turns with the gust.

Alexandridis et al. [18], Favre et al. [79], MacAdam et al. [135] all conclude that the crosswind sensitivity of a given vehicle is determined by the placement of the neutral steer point, centre of gravity and aerodynamic centre. Favre et al. [79] show through a coupled *vehicle dynamics-CFD* analysis that the lateral deviation

due to a crosswind gust is minimised by moving the aerodynamic centre towards the centre of gravity, but still ahead of the centre of gravity and the neutral steer point. The neutral steer point should then be moved forward, but should remain behind the aerodynamic centre. Keep in mind that the neutral steer point should remain behind the centre of gravity to maintain an understeer characteristic that dampens out handling response to road undulations (as explained previously).

Frequency response function

As shown by Pacejka [153], the frequency response function of the lateral acceleration A_y and yaw rate ω_z to steering input δ can be plotted to reveal the sensitivity of the vehicle handling model to different frequencies. The response functions for the current test vehicle (the parameters have been updated using a procedure presented in Appendix A) are shown in Figure 2.3 and have been plotted using the state-space formulation of the single track vehicle given in Pacejka [153].

The gain on the yaw rate starts to fall at around 0.5 Hz and is reduced significantly (to about 0.3 /s at all driving speeds) at 10 Hz. This is less than 10% of the static gain for the 80 kph case (∼3.47 /s). The lateral acceleration gain has a minimum at the higher driving speeds at $f \approx 1.3$ Hz and above this frequency it appears that the driving speed has little impact on the frequency response. The driving speed has a clear significance at the lower frequencies, with large variations in the zero-frequency gain. Additionally, at the highest driving speed a peak appears in the yaw rate gain near the handling natural frequency that is not equally evident at the lower driving speeds.

The gain for an non-steered vehicle loaded by an aerodynamic load F_{ay} at the aerodynamic centre is plotted on the last two sets of axes in Figure 2.3. The solid lines show the gain when the aerodynamic centre is located at $1/3l_b$ – one third the vehicle body length (see Figure 6.3 for the definition of l_b) – from the front (a rule of thumb used in [134]). In this case $l_{cp} = -0.35$ m and is between the centre of gravity and the neutral steer point. This makes the lateral acceleration gain different to the steering case in that there is no longer a minimum at ~ 1.3 Hz. Instead the curve looks more similar to the yaw rate gain. Placing the aerodynamic centre ahead of the centre of gravity ($l_{cp} = 0.35$ m) reproduces a response function very similar to the steering case (with a dip and a minimum near $f = 1.3$ Hz).

In summary:

- The vehicle's response to lateral input forces is dependent on the location at which the force is applied as well as the neutral steer point and centre of gravity.
- An understeered vehicle will by the nature of its cornering characteristics and weight distribution dampen the handling response to undulations in the road and work to reduce the tyre lateral forces.

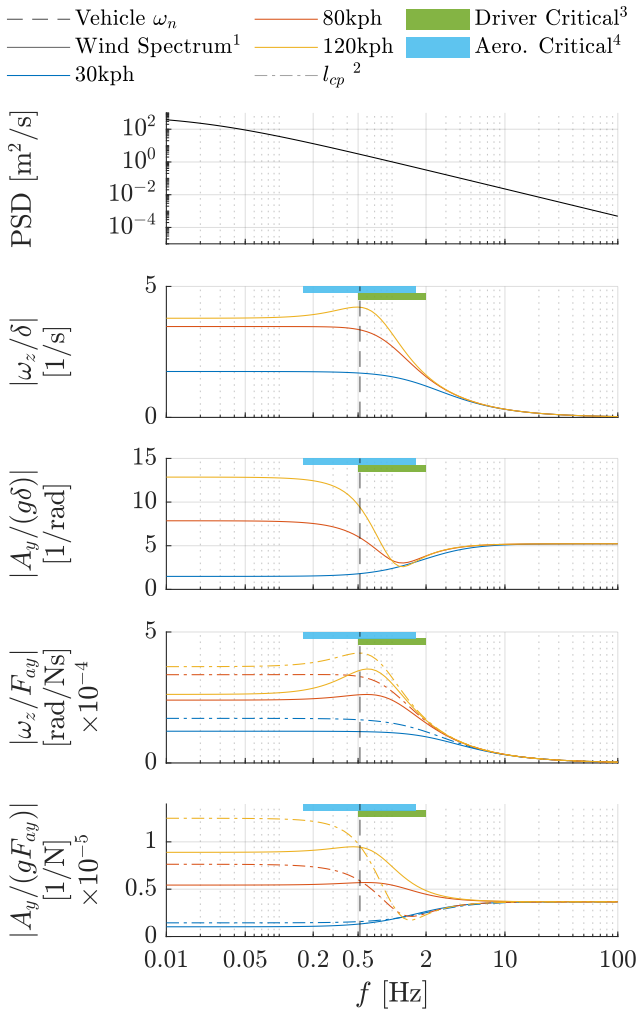

Figure 2.3: The wind spectrum and transfer function for the steered and wind-perturbed single track model.

[1]Wind spectrum according to N400 5.6.5 [7] at 60 m above terrain category 0, $v_{b,0} = 30$ (Alstahaug, Nordland, where the Helgeland bridge is located).
[2]$l_{cp} = -0.35$ m for the solid lines and 0.35m for the dotted and dashed lines.
[3]0.5-2 Hz range according to [170, 205].
[4]Reduced frequency k_f range 0.05 to 0.5 translated to f at 80 kph, $l_b = 6.8$ m.

- An equivalent damping mechanism will result for lateral aerodynamic loads if the aerodynamic centre is forward of the neutral steer point.
- The steering/handling characteristics of the vehicle (linked to the driver's ability to control the vehicle) and the wind sensitivity are therefore closely linked.
- According to the frequency response function of the single-track model, the vehicle's handling response is most sensitive to input forces below 10 Hz.
- The vehicle's handling response is approximately equally sensitive to (equal gain) static loads as to non-static loads up to about 0.2 Hz.
- The driving speed increases the lateral acceleration and yaw rate gains across the frequency domain, yet has most effect below about 1.3 Hz (particularly for the lateral acceleration).
- The shape of the frequency response function is similar for steering inputs and aerodynamic forces (as long as the aerodynamic force acts fore of the neutral steer point).
- Having the aerodynamic centre between the centre of gravity and the neutral steer point increases the sensitivity (gain) to loads in the range $\sim$ 1-5 Hz.

It should be kept in mind that the aerodynamic centre and neutral steer point can move during a transient manoeuvre [10, 79] and that non-linearities can be introduced to the handling system through the tyres (the friction forces can reach a saturation point) as well as the steering and suspensions mechanisms. The description of the system given above is therefore only approximate and most accurate in steady-state situations.

This section has described the vehicle's handling characteristics. Next, it is useful to understand how the wind environment can be described and how wind characteristics relate to the aerodynamic loads developed on the vehicle body.

2.2 Wind characteristics & vehicle aerodynamics

The topic of vehicles driving through crosswinds has been tackled before:

- using a theoretical framework [22–24, 28, 208, 234],
- using a wind tunnel [25, 59–61, 99, 167, 222],
- using a computational framework (often CFD) [70, 95, 98, 125, 133, 137, 168, 199, 200, 217, 232],
- using a full-scale vehicle on a test track in natural winds [32],
- using a full-scale vehicle on a test track in artificial winds/gusts [69, 83, 84, 109, 124, 135],

- or using a full-scale vehicle driven on public roadways in natural winds [107, 123, 162, 179].

Sims-Williams [178] has written a useful review paper on the characteristics of the crosswind environment and resulting aerodynamic loads of on-road vehicles. The results most pertinent to this work:

- "*The on-road spectral energy begins to roll off at a few Hz*" ([178], p.179)
- Length scales of 2-20 vehicle lengths are important to consider because the spectral energy is typically high at these frequencies, the vehicle response is not quasi-steady, the aerodynamic loads are unsteady (aerodynamic admittance may exceed unity) and suspension natural frequencies for vehicles typically lie in this range.

To illustrate the roll-off in the wind spectrum (atmospheric turbulence), a typical design spectrum from the Norwegian bridge design normal (N400:2022 [7], which in turn references NS-EN 1991-1-4:2005+NA:2009 [2]) has been plotted on the first set of axes in Figure 2.3. This differs from the diagrams shown by Sims-Williams [178] based on Wordley [219] where the roll-off for measured on-road spectra starts at approximately 10^0 as opposed to 10^{-2} or below as shown in Figure 2.3. Wordley's measured spectrum suggests there is more energy in region near 10^0 likely due to turbulence induced by road-side obstacles. As stated by Sims-Williams [178]:

> "*On-road turbulence may stem from vehicle velocity changes, natural wind turbulence and traversing through a steady spatial wind distribution produced by road side-obstacles. For road vehicles this last term is of greatest significance.*"

As will be demonstrated in Chapter 8, in the case of bridges it is not only road-side obstacles like the towers that affect the wind distribution, but also topography and structural bridge features under the bridge deck.

Critical scales

The rule-of-thumb that defines 2-20 vehicle lengths as a critical length scale range can also be presented using reduced frequencies. As determined by Theissen [196], the unsteady magnification of the aerodynamic yaw moment on a passenger vehicle is predominantly a function of what he terms the Strouhal number. To avoid confusion with the traditional use of the Strouhal number to describe the normalised frequency of oscillatory flows (as it is used in Chapter 14), the same mathematical definition is used here, but the reduced frequency terminology instead. In this

work, k_f is the reduced frequency and is mathematically the same as Theissen's Strouhal number,

$$k_f = \frac{f D}{U}, \tag{2.2}$$

where f is the frequency at which a gust is experienced by the vehicle, D is a characteristic length (the length of the vehicle body is used in this text l_b, whereas the wheel base is used by Theissen) and U is a characteristic velocity (the driving speed is used in this text V_x). Using this definition, the reduced frequency can be simply described as the ratio of the time taken to travel the length of the vehicle $\Delta t_{l_b} = V_x/l_b$ to the time taken to pass through a gust of spatial dimension D_{gust}, $\Delta t_G = V_x/D_{\text{gust}}$:

$$k_f = \frac{\Delta t_{l_b}}{\Delta t_G}, \tag{2.3}$$

or similarly in terms of spatial dimensions,

$$k_f = \frac{l_b}{D_{\text{gust}}}. \tag{2.4}$$

This makes the spatial dimension of the wakes and pressure fields of road-side obstacles (towers, support piers etc.) particularly interesting.

Note that in some texts [178] the reduced frequency is defined using the angular frequency:

$$k_f = \frac{\omega D}{U} = \frac{2\pi f D}{U}, \tag{2.5}$$

and in other texts [154] the reduced frequency is defined as exactly half of Equation 2.5.

Translating the 2-20 vehicle length range to a reduced frequency range is simply done by taking the reciprocal as shown by Equation 2.4. This gives a critical range of $0.05 < k_f < 0.5$, which corresponds well with Theissen's results which show an amplification of the unsteady yaw moment in the range $0.05 < k_f < 0.45$. This 2-20 vehicle length range has been plotted as a coloured patch – labelled *Aero. Critical* (blue) – in Figure 2.3. The reduced frequency has been translated to the frequency axis (in Hz) using the test vehicle length $l_b \approx 6.8$ m and a driving speed $V_x = 80$ kph.

As illustrated in Figure 2.3, the highest gains in vehicle handling response to aerodynamic loads ($|A_y/F_y|$ and $|\omega_z/F_y|$) may be found within this aerodynamically critical range. The lateral acceleration to driver input gain $|A_y/(g\delta)|$ also has a minimum in this range, indicating that the driver may have to provide high energy inputs to stabilise the vehicle. The vehicle may therefore be experienced as less stable and/or controllable in response to gusts.

2.3 Driver response to perturbations

Schaible, in his PhD thesis [170], concludes that there are four distinct frequency ranges for drivers of road vehicles in response to crosswinds. As reported by Theissen [196]:

1. The driver compensates fully for *static* aerodynamic loads (much in the same way they compensate for the drainage slope of road decks).
2. At frequencies in the range 0 to 0.5 Hz, the driver is generally able to compensate for wind-induced handling motions.
3. At frequencies in the range 0.5 to 2 Hz, the driver is unable to compensate for wind-induced handling motions. On the contrary, the driver often amplifies the wind-induced motions up to a certain frequency within this range. The amplification is highest at frequencies close to the typical handling eigenfrequency of the vehicle at around 1 Hz.
4. The driver does not affect the vehicle response for wind-induced perturbations above 2 Hz.

These conclusions are based on measurement data collected on two full-scale vehicles (BMW E36, now known as the 3-series and E38, now known as the 7-series) in artificial gusts with three separate drivers. The artificial gusts were generated using fans.

Schaible's analysis involved estimating the transfer function gains for the yaw rate response both with and without driver input. The understanding of a driver's frequency-dependent ability to compensate for wind perturbations is based on a comparison of the two transfer functions (steered and non-steered). There were variations in the results between drivers and vehicle types, though what is summarised above is part of the final conclusion to the thesis.

Figure 2.4 is a recreation of one of Schaible's transfer function plots comparing the transfer function of a steered vehicle to a non-steered vehicle. The transfer function is between the time-derivative of the yaw rate $\dot{\omega}_z$ and the product γV_r^2, where γ is the wind vector's incidence angle in the vehicle's reference frame (recall Figure 1.3) and V_r the magnitude. The aerodynamic moment is expected to scale with the square of the wind speed (a basic aerodynamic result, see *aerodynamic coefficients* in [19]) and the incidence angle at small values ($\gamma < 40°$, see for example Fig. 4, the side force coefficient as a function of wind incidence in Baker [22]).

The *steered* gain in Figure 2.4 is lower than the *non-steered* gain below about 0.5 Hz. This indicates that the driver is successfully compensating for the perturbations in handling response. Then there is a range between 0.5 and approximately 1.75 Hz where the *steered* gain is larger, indicating that the driver is worsening the handling response. Beyond this, the driver either has no input to the system or does not have an impact on the resulting handling response.

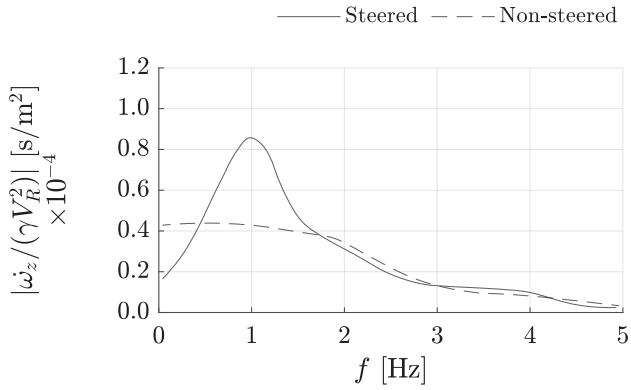

Figure 2.4: A comparison of the transfer functions of one steered and one non-steered vehicle, here re-drawn from Figure 70 in [170] with data from the BMW E38, a driving speed of 150kph, and under the control of driver b (as defined in [170]).

It was noted by Schaible in the final conclusion that drivers who do not attempt to correct for perturbations above approximately 0.4 Hz contribute to a better overall handling response in comparison to those drivers who do attempt to compensate for higher frequency perturbations.

Similarly, MacAdam et al. [135], who also conducted full-scale experiments with fan-generated artificial gusts, observed that drivers could be placed into two categories. Those who tried to continuously compensate for the wind-induced perturbations and those who gave minimal input to the system. The latter group was the most successful in minimising handling response.

Wagner and Wiedemann [205] present a very similar plot to Schaible's transfer function plots in their Figure 4. In this case, the *steered* and *non-steered* lines cross at almost precisely 0.5 and 2 Hz. This range has been plotted in Figure 2.3 as a coloured patch (green) labelled *Driver Critical*.

2.4 Summary: the wind-vehicle-driver system

Figure 2.3 illustrates the wind's energy distribution (atmospheric turbulence) in the frequency domain as well as the vehicle's transfer function superimposed with the frequency ranges that have been identified as critical for unsteady (and possibly amplified) aerodynamic loads as well as adverse driver response. From this stems the hypothesis that the frequency range 0.5-2 Hz will be particularly critical due to the overlap – in much of this domain – of the driver critical range with the critical aerodynamic range. The vehicle's handling eigenfrequency lies at the bottom of

this range and the frequency response gains are high both to driver input as well as aerodynamic perturbations. Another important observation from the figure is that increasing the driving speed makes the vehicle more sensitive to aerodynamic perturbations in this critical range.

Chapter 3

Background on quantifying and qualifying vehicle-driver response

In the last chapter, some theory was presented on the sensitivity of vehicles to crosswinds. In this chapter, the aim is to find useful methods of describing the response that has been measured in the field. Ratings of controllability, stability or comfort have not been taken during the field experiments. Consequently, the quantitative data collected will be labelled and compared with reference values that have been found in the literature. The methods, measurement quantities and reference values presented in the literature will be reviewed here for later reference in Chapters 9 to 12.

3.1 Possible measures of vehicle response

Many authors concerned with the safety of vehicles on crosswind-exposed bridges use the same accident criteria. Baker [22] proposed a set of theoretical accident types and associated criteria in 1986 for use with computational and analytical analyses. For each accident type, an accident is said to have occurred if:

1. *one wheel vertical reaction falls to zero* (termed an overturning accident),
2. *the lateral deflection exceeds 0.5 m* (termed a side-slip accident), or
3. *the angular deflection exceeds 0.2 rad* (termed a rotation accident where *rotation* refers to yaw rotation).

within 0.5 s of a crosswind perturbation (without driver interaction). These criteria are used to map out a set of acceptable wind and driving speeds in which wind-induced accidents are avoided. The argument is made that the 0.5 seconds provides a safety margin to the real case of a steered vehicle where the driver will begin

stabilising steering motions within 0.2-0.4 s (Baker quotes these as typical reaction times).

Baker's paper has been cited 127 times as of 11/08/2022 according to Semantic Scholar and his criteria have been used directly to predict the occurrence of wind- and/or bridge vibration-induced accidents in multiple texts [36, 47, 87]. Similar and/or modified accident criteria have been used, for example, by [53, 113, 230] and several similar accident criteria have been proposed by for example Rocchi et al. [166] and Chen et al. [46]. These last two works do not set criteria for the rotation (yaw) accident type. More complex models than the 2D static analysis presented in Chapter 1 are typically used. Compliance in the suspension system, excitation by road undulations, and vehicle-bridge interaction are often considered.

Instead of trying to predict accidents, some researchers have simply evaluated driver and passenger comfort on wind-exposed bridges [39, 238, 242]. Comfort criteria are established in standards like ISO2631-1 [3], ISO2631-4 [4] or EN12299:2009 [6].

From a regulatory perspective the question is how to distinguish between an acceptable response and an unacceptable response. Baker's criteria are attractive because they are logical and easy to apply to theoretical and numerical examples. These criteria are difficult to evaluate using the current data because:

- The test vehicle is driver-steered. It is difficult to define and/or identify a period of 0.5 s where the driver does not apply a steering input.
- The vertical tyre forces are not estimated by the instrumentation. This could likely be developed – for example using a Kalman filter – but there is currently no way to evaluate how close any one of the tyres is to lifting off from the road surface.
- The GNSS data was not always found to be reliable (particularly around towers or tunnel entrances/exits) and nor was the bridge motion measured simultaneously with the vehicle's. This makes the side-slip criterion difficult to evaluate as an accurate estimate of the vehicle's position relative to the lane is difficult to obtain.
- No significant rotations close to the accident criterion on rotation were observed in the field. This could simply mean that this accident mode was not the critical one for the vehicle in the field. Regardless, the criterion is not found to be useful useful in describing the relative safety of the vehicle response using the current data.

The approach used here is to quantify the response of the vehicle and make comparisons to qualitative descriptors developed in the literature. Three candidate response measures have been chosen:

- the lateral acceleration A_y,

- the yaw rate ω_z, and
- the roll rate ω_x.

The first two describe the handling response of the vehicle (and are related to Baker's side-slip and rotation accident types) and the roll rate is related to the rollover (overturning) accident type. Each measurement quantity is therefore an obvious candidate for use in defining an un-/acceptable vehicle response. Useful reference values of all three measures can be found in the literature.

Lateral acceleration A_y

The lateral acceleration of a vehicle in a turning manoeuvre is often approximated as a scaling of the side friction coefficient μ by $A_y = \mu g$ (using a point mass model) [5, 120, 195]. There is a limit to how much friction is available for any given combination of tyre, road surface and condition and so roads are designed using values of μ that give a margin for safety.

The design values of μ should account for the aforementioned variations as well as temporary increases in required friction from special manoeuvres such as braking and lane changes. Sometimes there are environmental and practical concerns as well. Nonetheless, the design value of μ will be substantially lower than absolute physical limitations on friction. At 80 kph on rural roads, [5] recommend a design value of 0.14 (1.37 m/s^2) and [120] a value of 0.13 (1.26 m/s^2, based on eq. 10.4b in [5]). These values have been reproduced in a summary table – Table 3.1.

Eboli et al. [77] use the recommended values of μ as a function of driving speed from [120] to classify driver behaviour directly as safe or unsafe.

Lateral accelerations also appear in multiple standards on the human experience of vibrations [3, 4] and comfort on railways [6]. In the latter text, quantities of continuous comfort, comfort during discrete events and in transition curves are defined, all of which depend – at least in part – on the lateral acceleration.

Brandt et al. [32] performed experiments on a test track at high speeds (140-185 kph) with crosswind gusts of amplitude up to ~ 10 m/s. Multiple drivers were instructed to drive the same car along a straight path and to press a trigger button when they experienced *prominent high speed stability issues*. A statistical analysis revealed that the drivers collectively related large changes in lateral acceleration ΔA_y and yaw rate $\Delta\omega_z$ to handling instability, but not translations or rotations in any of the other directions (including the roll rate). An argument is made that a change in lateral acceleration ΔA_y (within a 2.9-second sliding window, the term *amplitude-of-change* will be used in this work) above 0.58 m/s^2 is a reasonably good predictor of a subjective trigger event. This amplitude-of-change value is reproduced in Table 3.1.

Xu et al. [225] performed a series of measurements on a variety of vehicles, each with a different driver and on various types of roads in China with the aim to

Table 3.1: An overview of reference response values from the literature

Measure	Ref.	Description	Value	Units
A_y	[5]	Design friction coefficient	1.37	m/s^2
A_y	[120]	Design friction coefficient	1.26	m/s^2
A_y	[225]	90^{th} percentile, 4-lane highway (80-100kph)	1.92	m/s^2
A_y	[135]	4/10 uncontrollable in cross-wind guantlet (peak)	1.35	m/s^2
A_y	[135]	8/10 uncontrollable in cross-wind guantlet (peak)	2.74	m/s^2
A_y	[164]	Small-signal range	$0-0.5$	m/s^2
A_y	[164]	Linear range	$0.5-4$	m/s^2
A_y	[164]	Transition range	$4-6$	m/s^2
A_y	[164]	Limit range	>6	m/s^2
ΔA_y	[32]	Subjective instability (2.9s)	0.58	m/s^2
$\dot{A}_y$	[5]	Clothoid/spiral design value	0.3-0.9	m/s^3
$\dot{A}_y$	[73]	Clothoid/spiral design value (at 80kph)	0.51	m/s^3
ω_z	[135]	4/10 uncontrollable in cross-wind guantlet (peak)	2.89	deg/s
ω_z	[135]	8/10 uncontrollable in cross-wind guantlet (peak)	11.04	deg/s
$\Delta\omega_z$	[32]	Subjective instability (2.7s)	0.84	deg/s
ω_x	[106]	At point of vehicle rollover	250-350	deg/s
$\lvert\omega_x\rvert_{1s}$	[6]	When $P_{CT}=1$	3.68	deg/s

[1] Data set includes only peak values for identified fixed radius sections on the road.
[2] Measured at headrest, the 0-10 scale can be interpreted as 0:*no wind effect* and 10:*uncontrollable* due to crosswind effect.
[3] Approximate value at which test drivers pushed trigger button to indicate feeling of instability.
[4] Using equation (16) under *7 Comfort on Curve Transitions* in [6] assuming pure roll motion, this value gives the 1 s RMS value of roll rate needed to give a P_{CT} that equals one, indicating that 1% of passengers would feel discomfort.
Note: a fuller descriptions of the values are given in the text where reference to the table is made.

quantify typical values of lateral acceleration on roads. The 90$^{\text{th}}$ percentile values of lateral acceleration varied by the type of highway, with:

- $A_y^{90^{\text{th}}} = 1.26$ m/s^2 on 6-lane highways,
- $A_y^{90^{\text{th}}} = 1.92$ m/s^2 on 4-lane highways, and
- $A_y^{90^{\text{th}}} = 3.72$ m/s^2 on 2-lane highways.

It should be noted that the term *highway* might be vague. The 2-lane highways, as they are designated in the text, had speed limits between 20 and 60 kph and elevation grades up to 9%. They have no median separator and 4/6 of the roads traverse mountain ridges. These would not be termed highways in Norway. Nonetheless, the results give typical 90$^{\text{th}}$ percentile values of lateral acceleration that can be used as references against the results given here. The value for 4-lane highways with speed limits between 80 and 100kph are the most relevant for comparisons with the current data and are reproduced in Table 3.1.

MacAdam et al. [135] gathered subjective measures of controllability from multiple drivers steering a vehicle through artificial gusts. One gust was formed by a series of 8 fans in parallel blowing in the same direction (forming a *pulse* gust) and another by fans that were placed in a pattern on both sides of a test track creating an alternating wind field (*gauntlet*) pushing the vehicle from side to side.

Various vehicle configurations were compared, where the worst configuration was deemed to have a controllability score of 8, where 1 corresponds to *no wind effect* and 10 to *uncontrollable*. The configuration with the worst controllability score of 8 presented with an RMS lateral acceleration of 1.37 m/s^2 (peak $\sim$ 2.74). The most controllable configuration had an average score of 4 and an associated RMS of 0.67 m/s^2 (peak $\sim$ 1.35). Note that the acceleration measured at the headrest was approximately 1.6 times that at the centre of gravity. These values are considered relevant for comparison and are reproduced in Table 3.1.

The Bosch Automotive Handbook [164] says the following about "*ranges of lateral acceleration*":

- 0-0.5 m/s^2 is the small-signal range. "*The phenomenon to be considered in this range is the straight-running behaviour, caused by crosswind and irregularities in the road, such as ruts*." [164]
- 0.5-4 m/s^2 is the linear range where the linear single track model is appropriate.
- 4-6 m/s^2 is the transition range (where some vehicles may still behave linearly, whilst others may behave non-linearly).
- >6 m/s^2 is the limit range and is only reached in *extreme situations*.

These are useful reference ranges and are given in Table 3.1.

Lateral jerk $\dot{A}_y$

The time derivative of A_y gives the lateral jerk in m/s^3. Lateral jerk is used in the design of transition curves (spirals or clothoids). Similarly to the side friction factor, design values take into account variations in vehicle/road parameters, driver behaviour and practical considerations. Recommended values of 0.3-0.9 m/s^3 are quoted in [5] whereas a value of 1.2 m/s^3 is recommended to minimise the length of the spiral. Dumont and Tille [73] recommend 0.51 m/s^3 for a driving speed of 80 kph. These values are summarised in Table 3.1. Note that Brandt et al. [32]'s value of 0.58 m/s^2 for ΔA_y is equivalent to a minimum jerk of 0.20 m/s^3 within the 2.9 second window.

Yaw rate ω_z

Jones and Wilson [106] use the yaw attitude and yaw rate to describe the conditions necessary for the on-road rollover of vehicles. Brandt et al. [32], as stated above, found a statistical link between driver-observed instability events and changes in yaw rate. Similarly to the lateral acceleration, they found that a change in yaw rate $\Delta\omega_z$ within a 2.7-second sliding window above 0.84 deg/s was a good predictor of subjective triggers indicating instability events (also in Table 3.1).

MacAdam et al. [135] found that subjective ratings of controllability could be predicted very well by a linear function of the RMS of yaw rate.

> "*The high degree of correlation between subjective ratings and the measured yaw rate responses is surprisingly strong, suggesting that nearly all of the variation in subjective ratings can be accounted for by the RMS levels of the yaw rate alone.*"

This would suggest that the yaw rate is a key input to the human driver's internal model of vehicle physics. The head-rest acceleration was also found to be a good predictor of perceived controllability followed by the lateral acceleration. The controllability score of 8 (as a reminder, 10 is uncontrollable) was associated with an RMS yaw rate of 5.5 deg/s and a peak value of 11.0 deg/s. This value, along with the peak yaw rate for the most controllable configuration (with a score of 4) is given in Table 3.1.

Roll rate ω_x

The roll rate features in the standards on human perception of motion [3, 4] and is specifically considered for comfort evaluations on transition curves on railways [6]. Meanwhile, MacAdam et al. [135] found that "*increased roll motion due to decreased suspension roll stiffness was associated with lower driver subjective evaluations of vehicle crosswind sensitivity*".

Contrary to the above, Brandt et al. [32] did not find a statistical link between subjective evaluations of stability events and the roll response of the vehicle. It could be that drivers had such a good internal model of the vehicle physics that roll response was filtered out from the handling response of the vehicle. Otherwise it could be that the roll responses measured were so small that they did not lead to a feeling of instability. The maximum roll velocity change $\Delta\omega_x$ within a 3-second window was 3.6 deg/s in their statistics. In this work, values in excess of 10 deg/s in a 2-second sliding window have been observed.

Typical and/or comfort/controllability limit values of roll rate are difficult to find in the literature. Nonetheless, presented in Table 3.1 are the values given by Jones and Wilson [106] for the roll rates typically seen at the point of rollover for a road vehicle. This is an extreme value from which a very wide safety margin is expected.

Another reference value is given at the bottom of Table 3.1 using the comfort index for curve transitions on railways given in [6]. The value of P_{CT} is to be interpreted as the percentage of train passengers who are predicted to find the motion of the train carriage uncomfortable during a curve transition. The value is dependent on 1 s RMS values of lateral acceleration and jerk as well as roll rate. The value given in the table is the roll rate necessary to give a P_{CT} value of 1 assuming no other motions (zero lateral acceleration or jerk) and seated passengers. This should give an idea of the lower threshold for an uncomfortable roll rate for seated passengers.

Summary: reference values

Table 3.1 provides an overview of the reference values found in the literature. In general, there is a reasonable agreement between sources. For example, the 90$^{\text{th}}$ percentile of peak lateral accelerations on fixed radius curves recorded on 80-100 kph roads in China is 1.92 m/s^2, which is about 40% higher than the design friction coefficient set out in AASHTO's Green Book [5] for highways in the United States. This is a reasonable separation given the simplifications in the point-mass model (relating friction coefficient to lateral acceleration) as well as variations in the behaviour of drivers from the design case (particularly on dry roads).

3.2 A note on response to road undulations

The undulations of the road induce a repeatable handling and roll response. The vehicle's lateral acceleration, yaw rate and roll rate signals follow a similar curve for each repeated recording. This was noticed while processing the data presented in some of the later chapters, but is presented here because it presents an opportunity to quantify wind-induced loading separately from road-induced response.

Figure 3.1 shows five repetitions of the test vehicle driving on one segment of a mountain pass (80 kph speed limit, as close to 0 m/s wind as was observed during the field sessions). It is particularly the roll response of the vehicle that shows little variation between repetitions and appears to be completely explained by road undulations. The yaw rate, on the other hand, appears to be more independent of road undulations and the lateral acceleration lies somewhere in between the yaw rate and roll rate in terms of the degree of road-induced response.

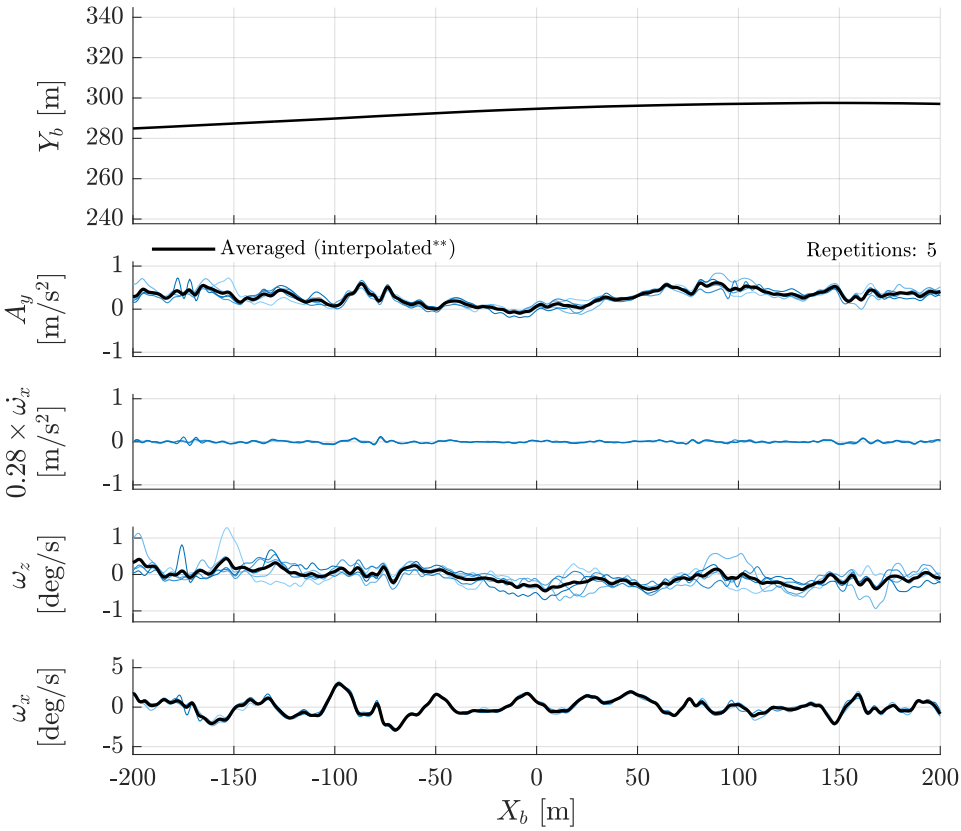

Figure 3.1: An example of the lateral, yaw and roll response of the test vehicle during the field session at Dovre 1 (the field experiments will be introduced in Chapter 7). ©Kartverket (road shape)

**Signals have been re-sampled onto one discretisation of the X_b domain and then averaged at each step
Note: all signals have been low-pass filtered with a Butterworth filter with a cut-off frequency of 5 Hz.

The lateral acceleration signal is affected both by the roll rate and the roll attitude of the vehicle. The IMU is slightly above the roll axis of the vehicle (∼0.28

m above) such that part of the measured lateral acceleration is simply the result of roll rotation. The resulting lateral acceleration at the IMU due to the roll rate has been estimated and is plotted in Figure 3.1. This component is insignificant.

The roll attitude will rotate the IMU such that a component of the gravity vector is captured on the y-axis. This component may be more significant, but is difficult to estimate with the current instrumentation. This is likely the reason for the higher repeatability of the lateral acceleration compared to the yaw rate.

The repeatability of the roll response is useful because any variations from the mean curve can be interpreted as being caused by external perturbations other than road undulations. On the road, the main source of external perturbations other than road undulations is wind loads.

3.3 Summary

The lateral acceleration, yaw rate and roll rate have been selected as measurement quantities to describe various aspects of road vehicle safety observed in the field. Some useful reference values from the literature:

- Typical lateral accelerations under normal driving conditions are expected to be below 4 m/s^2 (linear range) and below 0.5 m/s^2 (linear range) under straight-line driving in response to road undulations and wind [164].
- Brandt et al. [32] has shown that subjective wind-induced instability events can be identified by finding amplitude-of-change values above 0.58 m/s^2 and 0.84 deg/s for lateral acceleration A_y (2.9 s sliding window) and yaw rate ω_z (2.7 s sliding window) respectively.
- In response to a crosswind gauntlet, MacAdam et al. [135] has found peak lateral acceleration and yaw rate values that describe a 4/10 uncontrollable vehicle configuration ($A_y = 1.35$ m/s^2 and $\omega_z = 2.89$ deg/s) and an 8/10 uncontrollable vehicle configuration ($A_y = 2.74$ m/s^2 and $\omega_z = 11.04$ deg/s). Zero on the scale refers to *no wind effect* while 10 is *uncontrollable*.
- Under pure roll, a seated passenger on a train will start feeling uncomfortable once the roll rate exceeds 3.7 deg/s [6].
- The roll rate in response to road undulations is a very repeatable signal such that any variance from the expected signal could indicate the presence of additional external perturbations like wind gusts.

Chapter 4

Systematic metadata analysis of wind-exposed long-span bridges for road vehicle safety assessments

Sebastian Reymert, Anders Rönnquist and Ole Øiseth
J. Bridge Eng., 2022, 27(2): 04021104

Abstract

Long-span bridges are part of a vital road infrastructure for communities living in the coastal regions of Norway. New projects considering advanced bridge concepts will contribute to solidifying this dependency. These are locations that are increasingly exposed to extreme weather and authorities have concerns about vehicle safety. The traffic safety problem can have implications for new designs as well as the management and possible retrofitting of existing bridges. This work provides insights into the maturity of computational models and simulation procedures, the readiness of technological concepts to mitigate accident risk as well as gaps in the relevant research domain. This is achieved by a systematic literature search, mapping and metadata analysis. It is found that the major area for development in current models is the ability to credibly predict the vehicle's operating wind environment on bridges and the resulting aerodynamic loads on the vehicle. Another identified gap is the critical lack of real-world observations and experience. Little evidence of knowledge transfer from domains outside of civil engineering is found despite this being a complex multi-disciplinary problem. The technological readiness of solutions explored in current research is found to be low, with no evidence of any going beyond the proof-of-concept stage.

4.1 Introduction

4.1.1 Motivation

Long-span road bridges are often in locations where they are regularly exposed to strong, dynamic winds. This can increase the likelihood of accidents by creating unfavorable driving conditions. Namely by exposing vehicles to stronger aerodynamic loads than they might experience elsewhere on the road as well as the wind-induced motion of the deck. In addition, the bridge itself may be at increased risk of failure as a result of the combined intermittent loading by both wind and moving vehicle loads.

This work is part of a larger infrastructure project looking to improve the E39 coastal highway in Norway. It involves the construction of multiple long-span bridges (fjords up to 5,000 m wide) to replace some of the current ferry services. Crossings are typically in mountainous and/or coastal terrain (fjords) where high-speed wind events occur with increasing regularity. There are concerns from the Norwegian Public Roads Administration (NPRA) and the public with regards to the safety of road vehicles while crossing new and existing bridges. This is particularly a concern for the proposed long-span crossings. The feasibility of new technology to assess and mitigate the risks posed to vehicle safety needs investigation. This may be a considered in the design of the new bridges or used to develop/apply technological solutions that ensure uninterrupted access to critical transportation lines after construction.

There are a number of studies that have been published on this topic. These vary from the purely theoretical to experiments in the field and have a wide range of focuses. However, there is currently no published work that provides a high-level metadata analysis of the type of research being undertaken, possible solutions to the safety problem and where future efforts are best directed. This work achieves this by building an unbiased and representative database of current studies and uses this to provide a critical analysis of the maturity of models and technological readiness of the solutions explored by researchers.

A well-defined, systematic approach is used to find the relevant literature. Key methods and findings are extracted and entered into a metadata database. In addition to this, works are categorised across three different facets describing the research. This leads to the creation of a map that efficiently conveys what type of research has been performed, with which focus and to what extent. This map is analysed to give insights into the development progress of modelling and simulation strategies and technological concepts to mitigate road vehicle accidents. Critically, it reveals where the biggest gaps in knowledge and understanding lie and what should be in focus going forward. A formal framework for the development of numerical models [172] and the ISO standard for technological readiness [103] are used as tools to assess the maturity of models and the readiness of technology

concepts.

Systematic mappings and systematic reviews are commonplace in some areas of research. For example, the journal *Environmental Evidence* provides specific guidelines and submission protocols for these types of research article [161]. They have also been introduced in software engineering, such as the systematic mapping study by Petersen et al. [159]. A search revealed little evidence of any such articles or practice in the fields of engineering relevant to the current topic. This is is a complex, multi-faceted problem that benefits from the insights resulting from the analysis of a systematic map.

4.1.2 Background

Systematic mappings and systematic reviews are not commonly used in the fields of civil, structural, vehicle or wind engineering and will therefore be introduced in some more detail.

Traditional review articles are rooted in a pre-digital era. The number of articles on a given topic were fewer and it was significantly more difficult and/or cumbersome to access them. They typically give an historical background and thorough explanation of theories and methodologies. The content is often a result of the author's years of expertise on the topic. The list of relevant literature they provide is also valuable to many readers. These are still relevant today as exemplified by Chen and Chen [52] and Cai et al. [37]. Both articles provide an extensive review of the research methods used to study the vehicle-bridge-wind system with descriptions of critical technical details.

A systematic review differs from this by making use of formalised objectives and a structured approach to the search. The results of the review are also presented in a structured, often tabulated format. The benefits are best summarised by Petersen et al. [159]; 'a well-defined methodology reduces bias, a wider range of situations and contexts can allow more general conclusions, and use of statistical meta-analysis can detect more than individual studies in isolation'. Note that the quoted summary is itself based on a reading of the work by Kitchenham and Charters [115].

Petersen et al. [159] also provide a clear definition of the systematic mapping; 'a systematic mapping study provides a structure of the type of research reports and results that have been published by categorizing them and often gives a visual summary, the map, of its results'. A systematic map will be utilised here for original research on the topic of vehicle-bridge-wind systems. A high-level, unbiased analysis gives valuable results for the future development of safe and serviceable bridge infrastructure. The technical details of the methods and findings in the literature are left for the interested reader in the individual texts. The full list can be found in the associated database [165].

4.1.3 Objectives

The objective of the present work is to systematically search for, map, and analyse the metadata of current research concerning the interaction of dynamic winds, long-span bridges and road vehicles. The underlying goal is to be able to critically assess the vehicle safety problem in the context of strong winds on bridges. In this vein, it is interesting to get a high-level understanding of:

- The focus of current research
- The maturity of modelling approaches
- The application readiness of technological solutions
- Where future efforts are best directed

4.2 Research methods

4.2.1 Search phrasing

The efficient database search method used here follows that presented by Labonnote et al. [119], based on the work of Petersen et al. [159]. The search phrase is composed using Table 4.1. A search phrase is formed by placing boolean *or* operators between terms in each of the columns and *and* operators between each respective column. The tabular format makes it easier for the researcher to clearly define the scope of study. An overview of the databases that were searched and the results that were found can be seen in Table 4.2.

The search phrase was developed through multiple iterations to give the most complete and precise list of relevant literature as possible. At first, a rather broad search phrase was used to gauge the quantity of results available. Additional constraints were added (and removed) progressively until the results appeared to be satisfactorily complete and precise. Nonetheless, the search is unlikely to provide complete coverage of the literature of interest. Even if this was the case, it will be seen that not all texts can be sourced. The current work is primarily an analysis of the metadata. The results and conclusions are unlikely to be strongly influenced by a small number of articles. The aim of the search is not to provide a complete list of relevant literature, but rather a representative list that is as complete as possible. The high quantity of results from each given database shown in Table 4.2 suggests that the list considered here is indeed representative.

4.2.2 Screening

A reduced list of only relevant literature is established by two screening processes. The basis for removal in the first step is one of the following:

Table 4.1: Structuring the search phrase.

How?	What?	Specification	Not
"numerical analysis"	"bridge"	"long span"	"short span"
model	AND	"long-span"	"short-span"
modelling	"vehicle"	floating	rail
modeling	AND	"cable stayed"	train
experiment	"wind"	"cable-stayed"	
field		suspension	
"wind tunnel"		long	
parameter		"floating tunnel"	
"case study"			
coupled			
interaction			
analysis			
vbi			
safety			

Table 4.2: Summary of search results.

Database	Search Results
Scopus	255
Engineering Village	223
Web of Science	122
Science Direct	105
NTNU/Oria	48

- not in the English language
- clearly irrelevant based on the article title or journal/conference title
- is a duplicate

The second phase involves reading the abstracts. Entries are removed if they do not align with or make significant contributions towards the objectives. Note that 4 texts that were deemed of interest to this mapping could not be sourced using available resources. This concerns [78, 89, 144, 194]. Further filtering inevitably occurs as the mapping process proceeds. An overview of the search and screening process can be seen in Figure 4.1.

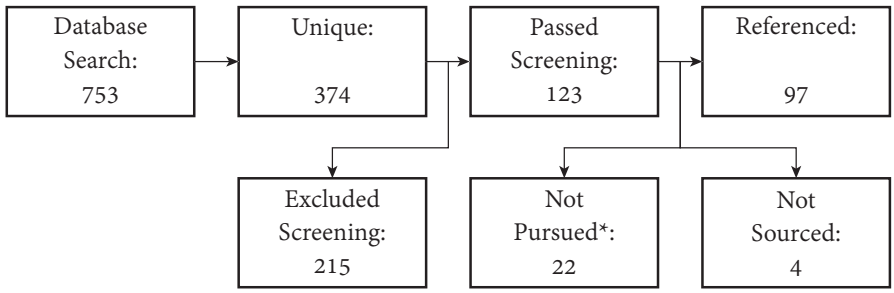

Figure 4.1: Overview of search and screening process. *Conference articles not immediately available were not pursued further

4.2.3 Choosing a mapping scheme

Petersen et al. [159] managed to establish a clear and insightful map by categorising across three facets. The same number is chosen here and allows for a similar visualisation.

The major challenge in the mapping process is the choice of the three facets and the categories within. These must be chosen to best serve the objectives. In addition, the map cannot be too intricate as to confuse the reader, yet must still provide enough resolution to allow for fruitful discussion of the presented research methods and outcomes.

One of the primary goals is to evaluate the technological readiness of possible solutions to ensuring the safe crossing of vehicles on wind-exposed bridges. The choice of facets and categories should reflect this. Since the majority of research is centred around the numerical modelling of physical systems, it is decided to refer to a formal description of the model development cycle to aide in making said choices. This description is given under *The Model Development Cycle* below.

The process was therefore a lengthy and iterative process that involved reading each full article at least once as well as the abstracts and conclusions multiple times. An initial categorisation was established through a process of digital bookmarking and keyword searches. The details of the modelling and experimental methods were extracted and tabulated per category. This database has been published as a digital database [165] and will be used to enhance the analysis below. Multiple cycles of categorisation across different facets were performed before the presented facets and categories were chosen.

4.2.4 The model development cycle

A good reference for describing the model development process is the report *Terminology for model credibility* from the Society for Modelling and Simulation [172].

Therein lies a diagram describing the model development cycle. It has been re-created for the discussion here and can be seen in Figure 4.2.

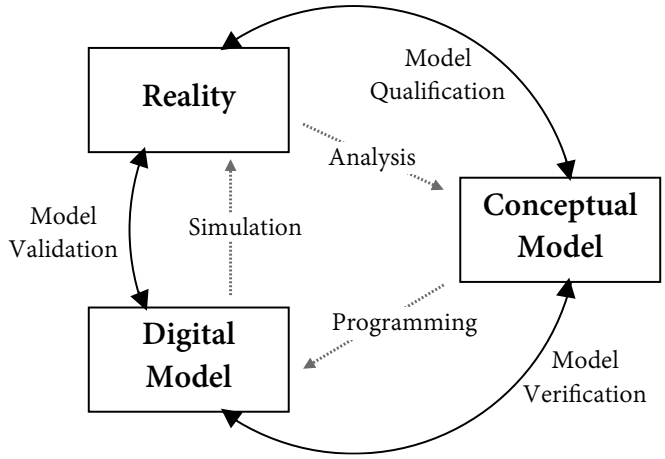

Figure 4.2: The model development cycle. [172]

In short, the cycle is an iterative process composed of three parts that can each be described by outcome and activity. The process typically begins with observations of *reality* that are used to form a conceptual model. The outcome is a qualified model and the activity required to achieve this is analysis of the observations. The conceptual model is then interpreted and programmed into a digital model. The digital model needs to be an accurate representation of the conceptual model. When this is achieved, the model can be considered a verified one. Finally, a simulation procedure is performed to find a solution. Ensuring that this solution is an accurate representation of reality is the process of model validation. This is typically established only for a *domain of applicability*. Following validation, the model can then be used to perform simulations that give valuable input for solving engineering problems. For example, a model could be used to predict the wind and vehicle speed combination at which traffic accidents are most likely to occur on a bridge.

The model development activities presented by research articles can loosely be categorised into the following list. This list is a subset of the categories describing the *research type* facet of the research to be presented below. The relationships between these category definitions and the stages in the model development cycle are described here in order to aide in the discussion to follow.

- *Observational* research involves making observations of physical phenomena - preferably from *reality* but also from the lab or well-established numerical simulation packages (i.e. computational fluid dynamics) - and analysing the data to suggest or provide the basis for mathematical conceptual models.

This is the very beginning of the model development cycle or takes place when existing models need to be re-assessed.

- *Evaluation* research involves all considerations in the digital implementation of a conceptual model. The main activities are programming and/or an evaluation of the programmatic implementation. This can be viewed as the next step along the development cycle from observational research. This suggests that there is enough confidence in the conceptual model to warrant an attempt at further development.
- *Simulation* research involves the use of the model to make predictions of reality and often also an analysis of the results of the simulations. This is the last step of the development cycle and should - if credible - result in a valid model ready for application within a given domain.

The relationship between the categories used below and the model development cycle should give an indication as to the maturity of the models. This will be utilised in the discussion below. Note that this is an indication of model maturity only. Any technology based on these models may still be far from application readiness.

4.3 Mapping scheme

The facets chosen for this mapping are described below. The corresponding categories are described in Tables 4.3, 4.4 and 4.5.

Focus Area: Which physical element of the vehicle-bridge-wind system is in focus? This is sometimes clearly established in the abstract. However, it was often found that a look back over the content of the text and especially the conclusions showed a slight shift from what was indicated in the abstract. Consequently, the conclusion generally had more clout over categorisation of this facet.

Research Type: How can the stage of research or technological development be described? The categories and their definitions are formulated from a modelling perspective. The categories will therefore be applicable to many engineering research problems, yet are likely to differ from those relevant in other scientific fields.

Key Research Tool: What is the enabling research technique that lead to the significant outcomes? The multi-disciplinary nature of the current problem encourages, or even necessitates, the use of multiple engineering research tools. It can sometimes be difficult to choose one key technique from any given contribution. Again, the information presented in the conclusions is relied on more heavily than, for example, the abstract. In cases of significant uncertainty, the novelty of

the tools in the context of the rest of the relevant literature is considered.

Evaluation vs. simulation research

On the research type facet, there is a fine line between the categories of evaluation and simulation research which can make the task of categorisation difficult. In order to reduce bias and simplify this procedure, a rule was established. To be classified under the simulation category, it must be possible to establish that some sort of performance indicator has been used to evaluate the response of the physical system - not the behaviour or performance of the modelling method or simulation procedure. The best method by which to determine this is to look at the figures and tables presented in the text in the context of the conclusion. For example, Zhou and Chen [238] evaluate driver comfort by generating estimates of overall vibration total value (OVTV), a weighted sum of root-mean-square values of acceleration at a point on the vehicle body. Plots of OVTV as a function of various parameters can be found in the body of text and are in focus in the conclusion.

The map

The result of the mapping process is visualised using the bubble plot shown in Figure 4.4. Note that 100% of entries in the relevant literature are represented on each set of axes. Percentages have not been provided given that the total number of entries in the relevant literature lies so close to 100 (97).

Table 4.3: Focus area facet.

Complete System	The work focuses on an approach that describes the vehicle-bridge-wind system as a whole.
Bridge Response	The structural response of the bridge features heavily in the outcomes of the work.
Vehicle Aero.	The aerodynamic forces acting on the vehicle feature heavily in the outcomes of the work.
Vehicle Response	The structural-mechanical response of the vehicle features heavily in the outcomes of the work.
Bridge Aero.	The aerodynamic forces acting on the bridge feature heavily in the outcomes of the work.

4.4 Author and audience perspectives

The relevant literature is made up of 88 journal articles and 9 other contributions. Those belonging to the former have been mapped into categories. The categories

Table 4.4: Research type facet.

Evaluation	The work is evaluative of the implementation of a modelling methodology.
Simulation	The work is evaluative of the solution or results of a pre-supposed modelling methodology. The results are treated as an analog of the physical system and analysis of the behaviour of the system is given.
Observational	Key outcomes of the work are observations of physical phenomena. This might be in the lab, in the field or using established numerical tools such as commerial computational fluid dynamics packages.
Experience	The personal experience of the author or authors is presented and discussed.
Review	The work presents a review of existing literature.
Solution Proposal	A solution to an engineering problem is proposed.

Table 4.5: Key research tool facet.

Numerical Model	A numerical model is a representation of a mathematical model of a physical system.
Wind Tunnel	The collection of data or observation of phenomena in a wind tunnel facility.
CFD	Computational Fluid Dynamics. Researchers here often use a numerical tool as an analog of wind tunnel tests.
Empirical Model	An analytical model or numerical implementation thereof derived from observation and experiment.
Various	It is not possible to choose a unique key research tool for the text, for example in experience or review articles.
Field Data	The defining feature of the work is the use of field data. This might be used in a model or a processing technique for better observation of the physical system is presented.

are chosen to best reflect the content of each journal as a whole based on the description given on their homepage. The results are visualised in Figure 4.3.

An overwhelming majority of articles come from journals associated with the field of civil engineering (76%), followed by vibrations (7%) and transportation (3%). The weight of civil engineering journals is perhaps unsurprising. However, a rather significant 24% of articles come from a variety of other areas. This is an indication that the search and filtering process has been appropriately unbiased. It is notable that areas more closely associated with vehicle engineering are absent such as vehicle dynamics, aerodynamics or control. In fact, no category containing the word 'vehicle' is present at all.

This indicates that those participating in research on the current topic are likely to have a greater interest and/or competence in the bridge's response rather than the vehicle's. Meanwhile, it will be demonstrated below that there is a perceived need for a new vehicle-wind interaction model in the bridge environment. There may be significant advantage gained by seeking new perspectives and knowledge transfer. This from actors in vehicle engineering research and development or maybe even from aerodynamicists working in other arenas.

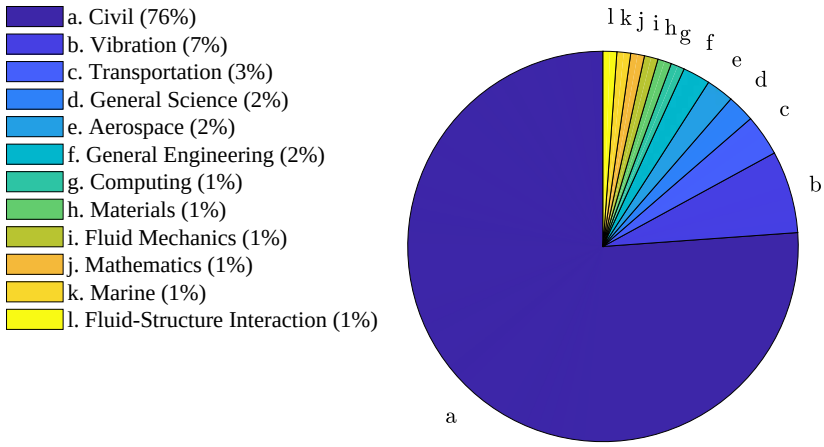

Figure 4.3: An overview of journal categories.

4.5 Discussion

4.5.1 Numerical modelling

The map (Figure 4.4) shows that the majority of research in this area is of a computational nature. 62/97 texts are categorised as simulation or evaluation, in which

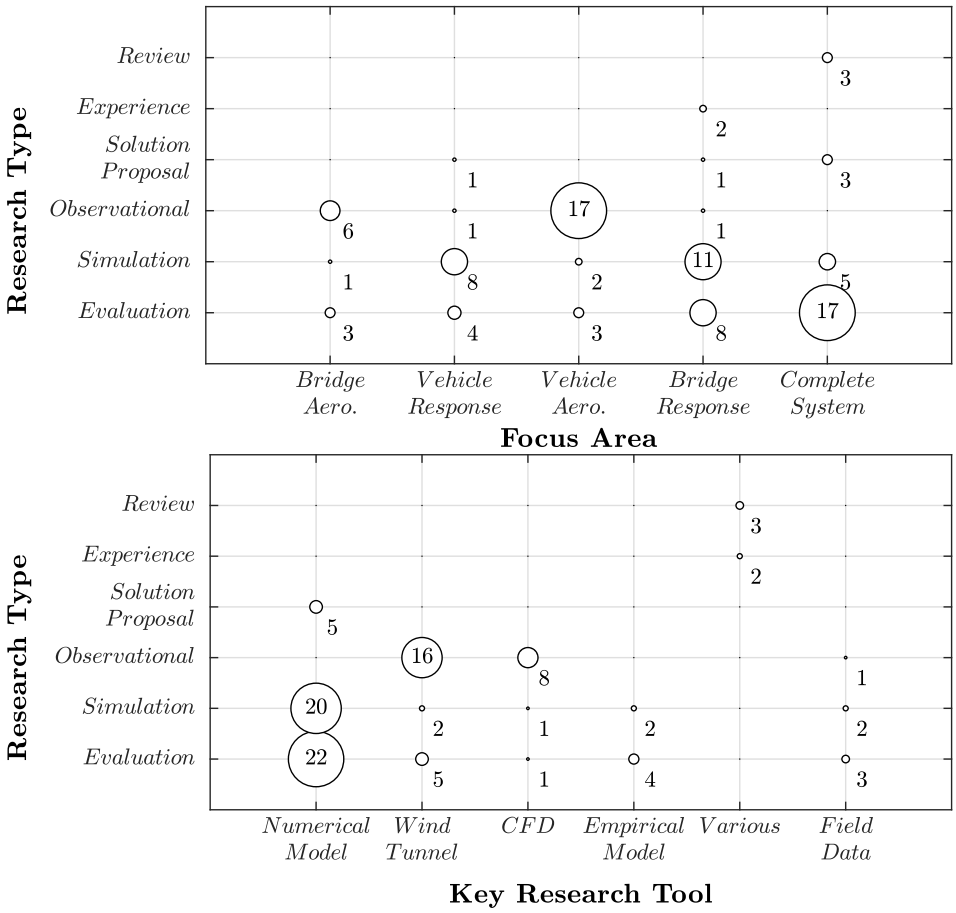

Figure 4.4: A map of the relevant literature.

the bulk of analysis relates to the methods or results of simulations. At least 45/97 texts present a description of how models of the vehicle, bridge and wind systems are coupled together. This includes only the articles where the details of said interactive model are explicitly described. There are therefore a substantial number of examples of how the full, interactive vehicle-bridge-wind system can be modelled and simulated. This is unlikely to be a limiting factor for the development of road-bridge safety technology.

4.5.2 Review and experience articles

Approximately 5% of the relevant literature is of the review or experience article type. All review articles found are specific to the vehicle-bridge-wind system rather than any of the subsystems therein. This suggests the search and screening process was sufficiently precise. The fact that there are three review articles points to significant research interest in this area over substantial time. This conclusion is supported by the quantity of references articles (97).

Only 2 experience articles present themselves on the map. There are multiple possible explanations for this. The first one might be that this type of article is not valued as highly as other types of research. Interestingly, these two articles are each published in journals that appear only once in the relevant literature; [30] in *Structure and Infrastructure Engineering* and [216] in *Marine Structures*.

Another possible explanation is that this distribution of the type of research article published reflects the maturity of the research field. Assuming that experience articles are valued in the current research community (contrary to the above, or at least partly so), the lack of experience articles might suggest there is a lack of experience. Such articles typically share an individual or group's *lessons-learned* of solving practical engineering problems. This is typically with reference to a specific project. Consequently, it would seem that few have practical experience considering the combined vehicle-bridge-wind system in reality. This may not be surprising given the likely high cost of practical investigations involving vehicles and bridge infrastructure. Nonetheless, the apparent low level of practical experience will make considerations of vehicle safety on the bridge particularly difficult for practitioners and administrators in the near term.

4.5.3 Solution proposals

On the surface, the low number of solution proposals (5/97) points to a low level of technological readiness. Of the 5 articles, all are primarily backed by numerical models. There are no solution proposals based on data from the field or laboratory. An overview of the types of solution proposed and the number of articles that propose them:

- Vehicle-based vibration suppression devices to control bridge motions, 4 articles
- Operational constraints based on wind speed/direction and vehicle driving speeds, 2 articles

Even if these solutions are proposed on the back of credible models, their technological readiness is unlikely to be high. Nor are the solutions necessarily going to lead to improved vehicle safety. For example, the studies that propose vehicle-based vibration suppression devices [35, 49–51] demonstrate the virtues of this solution in a numerical simulation. Suppression of bridge vibration may have multiple benefits, but not necessarily for the safety of traffic on the bridge. This has not been proved. As evidenced by the fact that all solution proposals are based on numerical models, this has yet to be demonstrated in the field, or even in the lab. Consequently, the technology readiness level (TRL) according to [103] is at most 2/9, where the 'formulation of the technology concept and/or application has been established'.

Other concepts

There are additional concepts for solving the traffic safety problem on long-span bridges that do not reveal themselves on the map. The reason for this will be discussed further below. Nonetheless, this is where the searchable metadata in the aforementioned database becomes useful [165].

Wind barrier

One concept is the use of a wind barrier on the bridge deck to shield vehicles from oncoming wind. They are typically proposed in the vicinity of bridge towers to reduce the impact of sudden changes in wind magnitude and direction. 5 articles that present results pertaining to the use of a wind barrier as a shield for vehicles can be found by filtering the *Keywords* column with the search phrase 'barrier'. The reason these have not been categorised as solution proposals is because the focus is on understanding the vehicle aerodynamics/response (4 articles) and the complete system response (1 articles). The articles are deemed to make a more significant contribution to those areas and are not explicitly focused on the development of the wind barrier as a solution. 3/5 articles are observational and 4/5 make key use of the wind tunnel. Given this information, the TRL level is ostensibly 3 or lower, *experimental proof-of-concept*.

In-situ operational constraints

Another concept is to map out the combinations of driving speeds and wind con-

ditions (speed and direction) that are unsafe for a given vehicle or set of vehicles. This information can then be used to establish in-situ speed limits or other limitations on bridge traffic based on measured wind conditions. To investigate, the search phrase 'driving speed' is used in the *Keywords* column. The search returns 14 articles of which 8 also have the keywords 'accident' and 'wind speed'. This demonstrates interest in this concept beyond the explicit solution proposals described above. All 8 entries are based on numerical models. Again, this limits the possible TRL to 2.

4.5.4 Vehicle aerodynamics

The distribution of entries along the vehicle aerodynamics axis in Figure 4.4 suggests a strong interest in the development of new *conceptual models*. This is clearly evidenced by the majority of studies being categorised as observational. This shows at the very least, that there is a perceived need for new prediction models for wind-induced loads on vehicles in the bridge environment.

The first set of axes in Figure 4.4 shows that there are 17 articles at the *Vehicle Aerodynamics-Observational* intersection. These papers make up 7 of 8 entries at the *CFD-Observational* intersection on the second set of axes. Similarly, they make up 10/16 entries at *Wind Tunnel-Observational*. Therefore, all observations in the *Vehicle Aerodynamics* category are made in the wind tunnel or using CFD. Also, vehicle aerodynamics dominates the observational research category. This is clear evidence that current actors are looking for a better understanding of the vehicle's aerodynamics in the bridge environment.

There are five studies that have moved down the *Vehicle Aerodynamics* axis from observational into simulation and evaluation type research. This indicates that some researchers have progressed said observations into digital models and simulations. An overview of specific interests:

- Local vehicle aerodynamic load variations near bridge towers, 3 articles
- Vehicle aerodynamic load variations resulting from wind interaction with bridge decks and/or barriers, 3 articles

4.5.5 Field data

Whilst the categorisation process was strict for the categories across all three facets, a looser definition of *key research tool* was used for the field data category. The definition was loosened in order to highlight any references to reality rather than mathematical models. Figure 4.4 shows that 6 studies have been placed in this category. However, the focus in all studies bar one is in fact a simulation methodology. Field data is rather used to enhance or make simulations statistically significant. An investigation reveals:

- Kim et al. [113] and Wang et al. [212] present and utilise historical weather data
- Wang et al. [214] present and utilise driving speed statistics
- Zhou and Sun [239] present and utilise statistics on traffic, wind and wave characteristics
- Wang et al. [211] present a hybrid simulation methodology using measured bridge response

The remaining text is unique in that the focus is on the collection and analysis of measurements made on a bridge [55]. There does not appear to be any observations of vehicle response in the real, fully coupled wind-excited system. Similarly, the wind effects relevant to vehicle aerodynamics that have been studied thoroughly using CFD and the wind tunnel (effects of the tower, bridge girder and barriers) do not seem to have been studied in the field. These have been identified as a key area of interest above and so observations from reality will have a significant impact on future technological development. Data can be used for the development of new conceptual models, confirmation of observations from numerical studies and the calibration/validation of models.

4.6 Conclusions

A systematic search and filtering process has been used to compile a precise and representative list of literature relevant to the vehicle-bridge-wind system. Metadata about the methods and findings of each article can be found in an external, searchable database [165]. The data has been mapped across multiple categories describing three different facets of the research and has been presented here. The map is used to lead an investigation into the level of understanding of the system and the technological development of concepts that can help reduce the accident risk for vehicles crossing long-span bridges. The database is used as a tool for additional analysis along with a formal description of the model development cycle [172] and technological readiness levels [103]. Some key insights from the analysis:

- A 76% majority of journal articles are published in civil engineering journals. There are no contributions from journals that fall into any category containing the word ‘vehicle’. This presents a prime opportunity for knowledge transfer. This is particularly true of research related to the vehicle’s aerodynamic characteristics, as will be seen below.

- The numerical modelling of the fully coupled vehicle-bridge-wind system has been thoroughly studied and features in at least 45/97 entries in the relevant literature. The development of such numerical models is unlikely to be the limiting factor for technological development.
- The following technological concepts to reduce accident risk on long-span bridges have been explored by researchers:
  - In-situ operational constraints (speed limit or other restrictions to bridge traffic) based on measurements of wind conditions
  - Wind barriers to shield vehicles from winds
  - Vehicle-based devices for suppression of bridge vibration
- The technology readiness level [103] for these concepts do not appear to be higher than level 3. That is to say there is some evidence of an *experimental proof-of-concept* for some proposals. No concept has been proven to be effective in reducing accident risk in a real operating environment.
- The majority (17/22) of *observational* research concerns the vehicle's aerodynamic loads in the wind environment on the bridge. This type of research activity is associated with the very early stages of model development. The vehicle's aerodynamic loads in the wind environment on the bridge is ostensibly the least understood part of the vehicle-bridge-wind system amongst current actors.
- Based on the focus of observational research, the important aspects of the vehicle's operating environment to be understood includes the effects of the following:
  - Bridge girder
  - Bridge towers
  - Wind barriers
- There is little (2/97 articles) published work describing experience of considering the vehicle-bridge-wind system in engineering practice. The apparent void in experience is likely to seriously hinder the technological development of safety solutions for vehicles on wind-exposed bridges.
- Another gap that is similarly detrimental to technological development is the lack of data gathered in the field (mentioned in only 6/97 texts). Field data is crucial to the evaluation of existing and synthesis of new conceptual models as well as the validation of simulation results.

In summary, the development of technology that reduces the risk of vehicle accidents on wind-exposed long-span bridges is likely to be most limited by a lack of

understanding of the vehicle's operating environment on the bridge. Future studies should focus on this and should do so in the real operating environment rather than the lab or using numerical simulation.

Chapter 5

Coupled vehicle-bridge-driver modelling of exposed long-span fjord crossings: an initial study

Sebastian Reymert, Anders Rönnquist, Ole Øiseth, Øyvind W. Petersen and Lars Drugge
Bridge Maintenance, Safety, Management, Life-Cycle Sustainability and Innovations, Proceedings of the Tenth International Conference on Bridge Maintenance, Safety and Management (IABMAS 2020), Sapporo, Japan, 11-15 April, 2021, 3406-3414

Abstract

Bridges built over wide fjord crossings (2,000 to 5,500 m) will serve as critical structures for Norway's new E39 coastal highway. An important capability for the Norwegian Public Roads Administration is the evaluation of the level of accident risk for motor vehicles on cable-stayed and floating bridges during high velocity wind events. This work develops a simple computational model to evaluate the importance of bridge- vehicle interaction in the vehicle-bridge-driver system in the presence of winds. The present results suggest that the vehicle-bridge interaction forces may be small in magnitude relative to aerodynamic forces on the structure and the vehicle. Future analyses may be simplified by obtaining the response of the bridge and using it as an input to an isolated vehicle dynamics model. The limitations of the model are discussed along with the challenges of achieving more accurate safety analyses. The need for data from field tests is motivated and the parameters for a planned experimental study using a large van on an existing long-span bridge are presented.

5.1 Introduction

The new E39 coastal highway route aims to replace current ferry crossings with bridges and tunnels in order to reduce the travel time between Kristiansand and Trondheim. This will involve the construction of multiple long-span fjord crossings which may be exposed to strong wind conditions. The Norwegian Public Roads Administration (NPRA) aims to keep these road crossings operational to the same extent as today's ferries. There is a need to understand the impact of wind forces on the safety and comfort of road users.

This work presents an initial analysis of the interaction between vehicles and bridges in the presence of high velocity winds. The potential to simplify established interaction models when applied to long span fjord crossings in Norway is highlighted. In particular, it is noted that vehicle-induced bridge vibrations play a minor role in the system and that the vehicle handling dynamics can likely be uncoupled from the lateral bridge dynamics. Data collected from the Hardanger bridge suggests wind-induced vibrations may be even more significant (in comparison to vehicle loads) than the current model suggests. A brief discussion of further modelling challenges and considerations is presented to motivate future numerical and experimental work. This will involve collecting vehicle response measurements as a large van crosses an instrumented cable-stayed bridge.

5.2 Vehicle-bridge interaction

The interaction between vehicle and bridge is studied using a modal analysis of the bridge and simplified vertical and lateral models of the vehicle.

5.2.1 Bridge modelling

The equations of motion of the bridge are integrated in time using modal coordinates. The modal mass, damping and stiffness matrices are extracted from an FE model of the Hardanger bridge. Details of this model and its calibration using field data can be found in Petersen et al. [160]. The mode shapes $X_i(x)$ are approximated by a modal analysis in Abaqus providing a lateral and vertical displacement y and z and torsional rotation θ at discrete span-wise locations x_j, $j = \{1, 2, ..., 325\}$. The FEM nodes at the centerline of the bridge deck are used. Approximations of the continuous mode shapes are given by linear interpolation. The first 143 modes (ignoring cable modes) are included in the vertical bridge analyses, frequencies from 0.05 to 3.98 Hz. The first 15 modes are drawn in Fenerci and Øiseth [81].

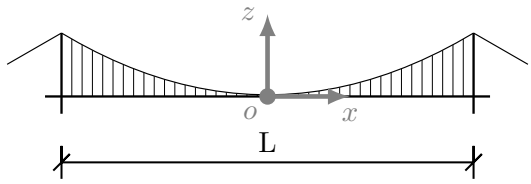

Figure 5.1: Sketch of the Hardanger bridge.

5.2.2 Wind loading

Realisations of the wind field are generated by Monte Carlo simulations using the spectral densities given in Øiseth et al. [148] and a time step $\Delta t = 0.048$ s. Linearised buffeting theory is used for calculating the wind buffeting loads on the bridge deck due to turbulence. The self-excited forces are taken into account by quasi-steady theory (i.e. constant aeroelastic damping and stiffness matrices are added to the structural system). This mainly increases the effective damping ratio of the modes. The process is repeated four times considering the wind speeds $U =$ 5, 10, 15, 20m/s.

The turbulence intensity in directions y and z, see Figure 5.1, are chosen to match on-site measurements and are $I_{u_y} = 0.15$ and $I_{u_z} = 0.075$ respectively.

5.2.3 Vertical motion

The interaction equations used are a slight variation of the method presented by Cheung et al. [54]. The vehicle is modelled as an unsprung mass m_1 and sprung mass m_2 connected by a spring-damper pair as shown in Figure 5.2.

The degrees of freedom of the coupled system are each of the generalised modal coordinates q_i and the displacement z_2 of the sprung mass m_2. Note that assumed vibration modes presented in Cheung et al. [54] are not used here, but are replaced by approximations from the FEM. The unsprung mass m_1 is assumed to move with the bridge (ie. the vehicle's tyres remain in contact with the bridge at all times such that z_1 equals the displacement of the bridge at the vehicle's location).

Some of the equations from Cheung et al. [54] will be presented here for the purposes of developing the lateral interaction equations in Section 5.2.4. See the referenced paper for a full derivation. The force the vehicle imparts on the bridge is,

$$f_c(t) = (m_1 + m_2)g + m_1 \frac{d^2 z_1(t)}{dt^2} + m_2 \frac{d^2 z_2(t)}{dt^2}, \tag{5.1}$$

where f_c can be written in terms of the generalised bridge displacements to give generalised interaction forces,

$$Q_i^*(t) = -f_c(t) X_i(x)|_{x=x_v}. \tag{5.2}$$

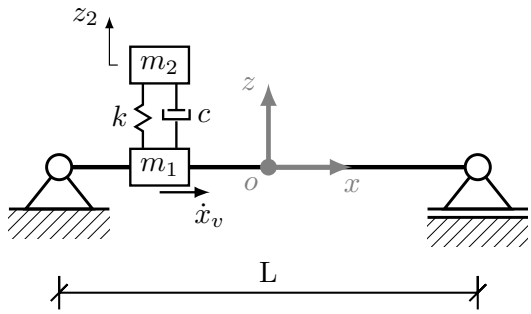

Figure 5.2: Unsprung and sprung mass on bridge beam model.

After some manipulation, the equations of motion of the vehicle and bridge can be made to form a matrix system, where the subscript sv is used to denote the fully coupled vertical interaction system,

$$\mathbf{M}_{sv}\begin{Bmatrix}\ddot{\vec{q}}\\ \ddot{z}_2\end{Bmatrix}+\mathbf{C}_{sv}\begin{Bmatrix}\dot{\vec{q}}\\ \dot{z}_2\end{Bmatrix}+\mathbf{K}_{sv}\begin{Bmatrix}\vec{q}\\ z_2\end{Bmatrix}=\left\{p^*\right\}. \tag{5.3}$$

The loading term p^* is given by,

$$p_i^*(t)=-(m_1+m_2)gX_i(x_v(t)) \tag{5.4}$$

The system above is converted to an appropriate state-space system and solved using a 4$^{\text{th}}$-order Runge-Kutta integration scheme. The implementation has been validated against the results presented in Cheung et al. [54]. Note that the matrices in (5.3) are a function of the location of the vehicle x_v and so the system is time-variant.

Vehicle moving load

The vehicle has the properties described in Table 5.1, chosen as convenient numbers based on values given in Xu [226]. The undamped natural frequency is ω_v = 3.00 Hz and the damping ratio, $\zeta_v = 0.35$. The excitation due to the moving spring-mass-damper is characterised by its velocity using the parameter α, defined in Cheung et al. [54] as,

$$\alpha=\dot{x}_v\pi/\omega_{b,1}L, \tag{5.5}$$

where $\omega_{b,1}$ is the first natural frequency of the bridge and L its length. For this problem $\alpha = 0.17$, possibly suggesting that dynamic amplification due to the moving load will be limited (see Figure 3 in Cheung et al. [54], noting that a direct comparison is difficult as some dimensionless parameters are difficult to calculate for the Hardanger bridge).

The vehicle begins its motion at x = -4,000 m, reaches the bridge at approximately x = -650 m and continues beyond the bridge to 1,000 m. In Section 5.2.3

Table 5.1: Vehicle parameters.

Parameter	Value	Unit
m_1	3,000	kg
m_2	4,500	kg
I_z	100,000	kgm^2
k	1,600	kNm^{-1}
c	60	kNsm^{-1}
$\dot{x}_v$	22.22	ms^{-1}
g	9.81	ms^{-2}
l_1	3.00	m
l_2	5.00	m

it will be seen that this leaves approximately 150 seconds for the motion of the bridge to develop in the presence of wind loading. The vertical displacement at midspan for this time period can be seen in Figure 5.3 labelled 'spring-mass-damper' or 'SMD'.

The quasi-static curve shows the static solution at each time step of the SMD solution, while the 'moving point load' is the result of a transient dynamic simulation of a constant point load moving at the same velocity as the spring-mass-damper. The bridge deflects a maximum of ≈ 30 mm with some minor dynamics associated with excitation of some of the lower bridge modes. The effects of vehicle dynamics do not seem to be significant given the indistinguishable difference between curves (a) and (c) in Figure 5.3.

Vehicle* & *wind loads

Generalised aerodynamic loads on the bridge are simulated only for the first 50 modes, frequencies from 0.05 to 0.84 Hz. It is assumed that wind-induced bridge excitation at higher frequencies is negligible.

Curve (d) in Figure 5.3 is the result of a simulation of the spring-mass-damper system travelling over a bridge that is excited by wind loading with a mean velocity $U = 5$m/s as described in §5.2.2. It is clear that both the vehicle as well as the wind have an impact on the response of the bridge.

In Figure 5.4 a higher mean wind velocity is considered, $U = 20$m/s. In this case, the vehicle's contibution to the bridge response is much less significant in comparison to that of the wind. Visually in Figure 5.4, there is only a very minor deviation of curve (c) from (b). It might be concluded that at such high wind speeds, the effects of the vehicle on bridge response can be neglected. Alternatively, the quasi-static effect of the vehicle could perhaps be superimposed on the response

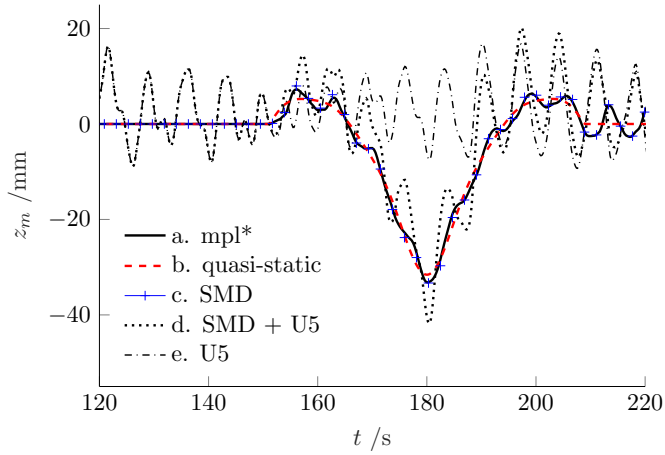

Figure 5.3: Vertical response of the bridge at mid-span due to a moving heavy duty vehicle. *moving point load

of the bridge to wind loading.

Figure 5.5 allows for a light visual comparison between the generated wind vibrations used here and a twice-integrated acceleration signal measured at the midspan of the Hardanger bridge (sensor H5E in Figure 4 in Fenerci and Øiseth [81]). The data plotted is a short sample from January 29, 2016 between 14:00 and 14:30, where a mean wind speed of 19.77 m/s was recorded at the same spanwise location using anemometer A6. A high-pass filter with a passband frequency of 0.03 Hz was applied before each consecutive trapezoidal integration.

The two curves are visually similar in nature, noting that an offset has resulted from the integration. It is also noted that the standard deviation of the measured signal is 165 mm versus 90 mm for the simulation. This further highlights the relatively low impact a vehicle has on the bridge response in the presence of strong winds. Further analysis and comparisons with measurement data will be included in future work.

Interaction force

Tyre forces will be critical to any vehicle safety analysis and so models should predict these accurately. Note that the wind-vehicle interaction has not been considered in the following analysis.

Equation 5.1 can be used to calculate the interaction force $f_c(t)$ given the solution to (5.3). The mean, standard deviation and peak deviation (from the mean) of the interaction force for the time period the vehicle spends on the bridge can be seen in Table 5.2. Note that this is the mean value for 100 realisations.

It will be important in future studies to consider the impact a $\approx 5\%$ change in

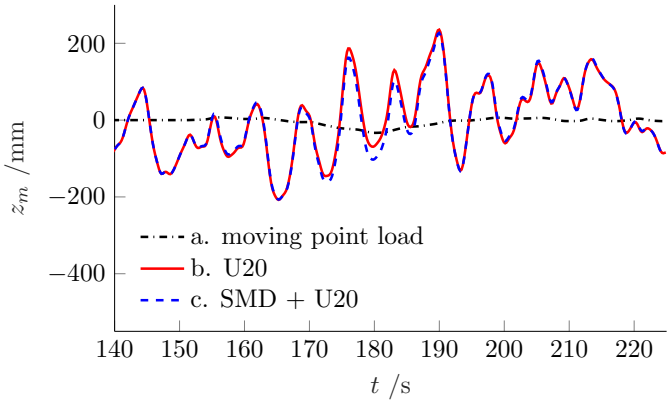

Figure 5.4: Vertical response of the bridge at mid-span due to a moving heavy duty vehicle and high velocity wind.

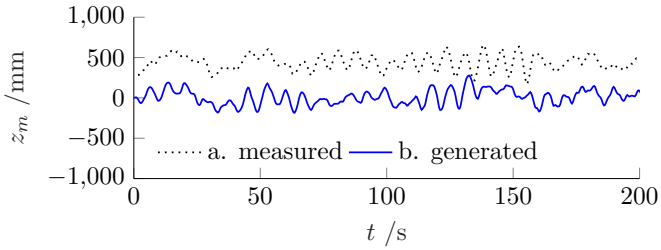

Figure 5.5: Generated vs. measured vertical response at midpoint of bridge.

Table 5.2: Statistical properties of interaction forces.

Simulation	Mean	Std.	Peak Dev.
	kN	%	%
SMD, U5	73.58	0.04	0.46
SMD, U10	73.58	0.15	1.25
SMD, U15	73.58	0.32	2.89
SMD, U20	73.58	0.56	4.55

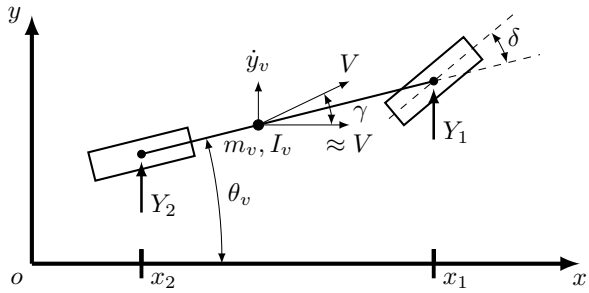

Figure 5.6: A diagram of the single track model, degrees of freedom y_v, θ_v and input δ.

overall vertical contact force may have on the stability of the vehicle. Note that the above analysis considers only the interaction between the vehicle body as a whole and the bridge. Pitching and rolling motions in the vehicle may lead to higher variations in the contact force between each individual tyre and the road. It is unlikely that the bridge will induce significant pitching and/or rolling motion in the vehicle given the large scale and long period of its vertical and torsional mode shapes (see Table 2 and Figure 14 in Fenerci and Øiseth [81]). Road roughness or irregularity may lead to more significant excitation.

5.2.4 Lateral motion

Modelling lateral vehicle-bridge interaction requires a vehicle model that accurately captures handling dynamics. One well-established model is the single-track or bicycle model. More about this model and how it differs from higher fidelity approximations can be seen in Abe [10] and Pacejka [153]. The equations of motion can be developed by considering the diagram in Figure 5.6.

The model has two degrees of freedom; lateral displacement y_v and rotation

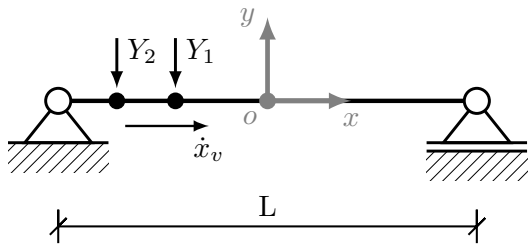

Figure 5.7: A diagram of the bridge under front and rear axle loads.

about the centre of mass θ_v. The lateral tyre forces are summed for the front and rear axles and are Y_1 and Y_2 respectively. These forces will interact with the lateral forces on the bridge. The equations of motion for the vehicle in a ground-fixed reference frame are derived in Abe [10],

$$m_v \ddot{y}_v = F_y, \quad F_y = 2Y_1 + 2Y_1, \tag{5.6}$$

$$I_v \ddot{\theta}_v = F_\theta, \quad F_\theta = 2l_1 Y_1 - 2l_2 Y_2. \tag{5.7}$$

The lengths l_1 and l_2 describe the distance from the centre of mass to the front and rear axles respectively.

The equations of motion for coupled lateral dynamics are derived as follows using transformations to generalised coordinates. The displacement of the bridge can be written,

$$y_b(x,t) = \vec{X}^T(x)\vec{q}, \tag{5.8}$$

taking $\vec{X}$ to be a column vector of the y-displacement of the mode shapes. It should be noted that the total derivative of y_b with respect to time at the location of the vehicle x_v is,

$$\left.\frac{dy_b}{dt}\right|_{x=x_v} = \vec{X}(x_v)^T\dot{\vec{q}} + \dot{x}_v\vec{X}'(x_v)^T\vec{q}, \tag{5.9}$$

with $'$ denoting differentiation with respect to x.

Interaction forces

Assuming a linear tyre model where the lateral tyre forces are a function of the sideslip angle β, the axle forces can be written,

$$Y_1 = -K_1\beta_1, \tag{5.10}$$

$$Y_2 = -K_2\beta_2, \tag{5.11}$$

where the sideslip angles are given by,

$$\beta_1(t) = \frac{1}{\dot{x}_v}(\dot{y}_v - \dot{y}_b(x_1)) + \frac{l_1}{\dot{x}_v}\dot{\theta}_v - \theta_v - \delta, \tag{5.12}$$

$$\beta_2(t) = \frac{1}{\dot{x}_v}(\dot{y}_v - \dot{y}_b(x_2)) - \frac{l_2}{\dot{x}_v}\dot{\theta}_v - \theta_v. \tag{5.13}$$

Note that the bridge lateral velocity at the position of each axle $\dot{y}_b(x_1)$ and $\dot{y}_b(x_2)$ have simply been subtracted from the vehicle's lateral velocity to give the vehicle sideslip relative to the road surface on the bridge. This is thought to correctly model the interaction between a vehicle and a laterally moving driving surface. This assumption has not been validated experimentally and it is highly desirable to do so.

All terms in (5.12) and (5.13) are functions of time. Substituting (5.9) into (5.12) and (5.13) and subsequently into (5.10) and (5.11) gives,

$$F_y = 2\left(a_1\dot{y}_v + \vec{b}_1\dot{\vec{q}} + \vec{b}_2\vec{q} + a_2\dot{\theta} + a_3\theta + a_4\delta\right), \tag{5.14}$$

$$F_\theta = 2\left(a_5\dot{y}_v + \vec{b}_3\dot{\vec{q}} + \vec{b}_4\vec{q} + a_6\dot{\theta} + a_7\theta + a_8\delta\right). \tag{5.15}$$

The new variables introduced here are given in Appendix B.

Generalised interaction forces

Equation 5.2 can be used to evaluate the interaction forces on the bridge, summing the force from the front and rear axles,

$$\vec{Q}^* = \vec{Q}^*_{Y_1} + \vec{Q}^*_{Y_2}, \tag{5.16}$$

$$\vec{Q}^* = \vec{c}_1\dot{y}_v + \mathbf{D}_1\dot{\vec{q}} + \mathbf{D}_2\vec{q} + \vec{c}_2\dot{\theta} + \vec{c}_3\theta + \vec{c}_4\delta(t). \tag{5.17}$$

The new variables introduced here are given in Appendix B.

Assembly of equations

Equation 5.3 can be re-written for the coupled lateral dynamics sl,

$$\mathbf{M}_{sl}\begin{Bmatrix}\ddot{\vec{q}}\\ \ddot{y}_v\\ \ddot{\theta}_v\end{Bmatrix} + \mathbf{C}_{sl}\begin{Bmatrix}\dot{\vec{q}}\\ \dot{y}_v\\ \dot{\theta}_v\end{Bmatrix} + \mathbf{K}_{sl}\begin{Bmatrix}\vec{q}\\ y_v\\ \theta_v\end{Bmatrix} = \mathbf{F}_{sl}, \tag{5.18}$$

where,

$$\mathbf{F}_{sl} = \begin{Bmatrix}\vec{c}_4\\ 2a_4\\ 2a_8\end{Bmatrix}\delta(t). \tag{5.19}$$

The matrices in this equation are,

$$\mathbf{M}_{sl} = \begin{bmatrix}\mathbf{M} & 0 & 0\\ 0 & m_v & 0\\ 0 & 0 & I_v\end{bmatrix}, \tag{5.20}$$

$$\mathbf{C}_{sl} = \begin{bmatrix} \mathbf{C} - \mathbf{D}_1 & -\vec{c}_1 & -\vec{c}_2 \\ -2\vec{b}_1 & -2a_1 & -2a_2 \\ -2\vec{b}_3 & -2a_5 & -2a_6 \end{bmatrix}, \tag{5.21}$$

$$\mathbf{K}_{sl} = \begin{bmatrix} \mathbf{K} - \mathbf{D}_2 & 0 & -\vec{c}_3 \\ -2\vec{b}_2 & 0 & -2a_3 \\ -2\vec{b}_4 & 0 & -2a_7 \end{bmatrix}. \tag{5.22}$$

Note that **M**, **C** and **K** are the modal mass, damping and stiffness matrices for the bridge under wind loads (ie. **C** and **K** are aeroelastic). The bridge coupled with the vehicle handling dynamics can now be analysed by solving (5.18) in the time domain. Again, the system is re-formulated as a state-space system and solved using a 4$^{\text{th}}$-order Runge-Kutta method.

Cornering stiffness

The cornering stiffness at each axle is estimated as proportional to the vertical load as described in §1.2.1 of Pacejka [153]. A constant of 20 is chosen here in an attempt to over-estimate the interaction between the vehicle and the bridge. The cornering stiffnesses are $K_1 = 460$ and $K_2 = 275$kN/rad for the front and rear axles respectively.

Analysis

Only the first 50 modes (including cable modes) are used in lateral analyses, frequencies from 0.05 to 0.84 Hz.

The coupled model is compared to a decoupled equivalent in Figure 5.8. In this latter model, the bridge's response to wind loads is obtained in the absence of the vehicle and used as the input to a separate single-track analysis. The coupled approach produces curves (b) (sampled here at a low sample rate and plotted using circle markers for ease of interpretation), while the separated analysis leads to (a). The maximum difference between curves (a) and (b) for the bridge is found to be less than 0.25 mm, whereas this value is 5 mm for the vehicle response. Note that the vehicle and bridge displacements (y_b and y_v) are nearly identical due to the overestimation of cornering stiffness.

It is clear from this that the lateral interaction forces (ie. the lateral tyre forces) do not develop to sufficiently large magnitudes to influence the response of the bridge. Note that aerodynamic loads on the vehicle itself have not been considered.

Considering the results of this analysis, it is concluded by the authors that the lateral dynamics of the bridge and vehicle systems can be decoupled without significant loss of accuracy.

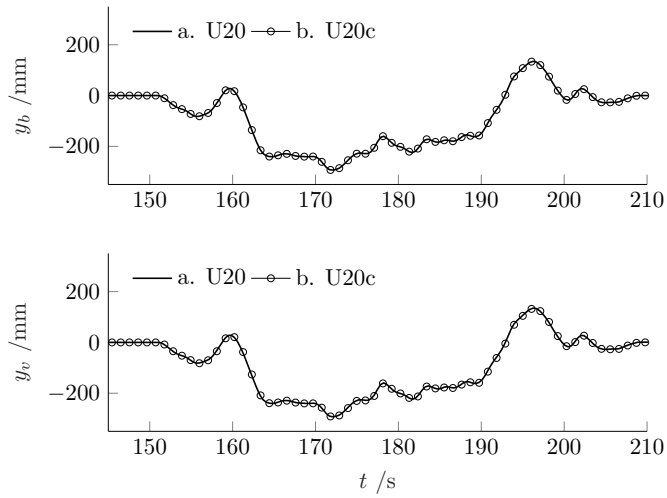

Figure 5.8: Lateral displacement response of bridge y_b and vehicle y_v.

5.2.5 Torsional motion

A set of 100 simulations of the torsional motion of the bridge under U20 wind conditions presents a standard deviation of 0.16° at the middle of the bridge. This magnitude of rotation is unlikely to lead to significant rolling motions in vehicles travelling on the bridge. However, one of the lanes of traffic is approximately 4 m from the geometric centre of the bridge. The vertical displacement experienced by a vehicle in this lane has a standard deviation $\approx 4 \times 0.16(\pi/180) \times 10^3 = 11.2$mm. This value is about 10% of that seen in the vertical modes.

Due to the relatively low magnitude of these vertical displacements, they have not been considered in these analyses. They may be considered in future studies.

5.2.6 Conclusions on vehicle-bridge interactions

It is concluded in Camara et al. [39] that vehicle-induced bridge vibrations play a minor role in the wind-excited bridge-vehicle system. The bridge is more strongly affected by direct wind action. Similarly, 'the vehicles are mostly influenced by the wind and by the pavement irregularities.' The results of this initial study align well with the first conclusion. The latter conclusion on road irregularity is an opportunity for further development and can readily be introduced in the current implementation.

5.3 Model limitations

The analysis presented above is simple and computationally efficient, yet has many limitations. Its use in the evaluation of accident risk must be considered in the context of experimental data. A follow up from this initial study will include results from a full-scale experiment as described in §5.4.

It should also be noted that some non-stationary events have occured since the start of the monitoring programme of the Hardanger bridge in 2013. The gusts of wind and resulting displacement of the bridge can be significantly larger than shown here in a simulated stationary process.

5.3.1 Accident modes

The literature presents a variety of accident criteria, though they are often variations of those proposed by Baker [22]. The criteria are stated as thresholds on the vertical tyre reaction force, vehicle lateral deviations from path and absolute yaw deviation. Exceeding these thresholds will lead to what is described as overturn, sideslip and rotation accidents, respectively. The criteria proposed by Baker are applied in Xu [226] and Wang and Xu [207], whereas some variation on them can be found in Chen and Chen [48], Cheung and Chan [53], Zhou and Chen [237] and Rocchi et al. [166]. Briefly, it is clear from these studies that the response of the vehicle to aerodynamic loads will be a critical consideration for any accident analysis.

5.3.2 Vehicle aerodynamics

Various simple aerodynamic theories have been applied to the case of a vehicle driving on a bridge, and particularly to the case of entering a sharp-edged gust, for example when emerging from behind a bridge tower. A quasi-static approach is used in Guo and Xu [87]. It is pointed out that the prediction of the yaw moment coefficient corresponds poorly with experimental results. Attempts to correct this include the development of a lateral force distribution method that takes into account the fact that the front of the vehicle enters the gust first, see Charuvisit et al. [42]. This causes a high initial yawing moment that changes as the vehicle passes through the gust.

There are multiple examples of wind-tunnel experiments in the literature, such as Chen et al. [46] or Dorigatti et al. [71]. The immediate focus going forward from this work will be a full-scale experiment more similar to Snæbjörnsson et al. [179]. Wind tunnel and CFD studies of a bridge section with a model vehicle are under consideration as well.

5.3.3 Vehicle model

Both pitch and roll dynamics will have an effect on tyre traction and may be an important consideration. Many coupled analysis studies use a system of masses, springs and dampers such as that used in Xu [226] (for example Cai and Chen [34] or Wang et al. [211]). The parameters (ie. the lumped mass, equivalent stiffness and damping) of these models may be difficult to evaluate and validate experimentally.

On the other hand, Lundahl et al. [130] shows how variations of the single-track and double-track models (including various combinations of pitch and roll with lateral and longitudinal load transfer) can be used to describe vehicle motion during optimal maneouvres. These models may be more appropriate to experimental comparison and/or validation. The state variables are simply the translational and rotational motion of the vehicle body and the parameters required can more easily be obtained from the measurement of said states during test maneouvres.

5.3.4 Tyre model

A vehicle's lateral dynamics can generally be considered linear when lateral accelerations are below 4 m/s^2 according to Reif [164] (pg. 958). The highest lateral acceleration of the bridge for the 100 simulations considered here is ≈ 0.18 m/s^2.

For the current analysis where only the bridge is excited by the wind it is therefore appropriate to use a linear tyre model. Future work that considers the aerodynamic forces on the vehicle may benefit from a non-linear tyre model such as Pacejka's magic formula or the Fiala model, see Pacejka [153] for more details.

5.3.5 Driver model

Baker proposed a driver model in Baker [24] in which the steering angle δ is given as a proportional gain on the vehicle's lateral displacement y_v and velocity $\dot{y}_v$. He also proposed that the driver has a reaction time (input signal delay) of 0.25 s.

This type of controller can be extended to include integral and derivative action as well, capturing the ability of a human to predict the path of a vehicle and correct for course deviations. This type of driver model is presented in Abe [10] where it is also identified that a human has the ability to learn or 'get a feel for' the handling characteristics of the vehicle they are controlling. A PID controller model would change depending on factors affecting the driver's capabilities. This might include, but is not limited to, previous driving experience, familiarity with a specific vehicle or state of mind.

It will be important to statistically characterise driver model parameters for the domain of human drivers under consideration. In this case, this is all people who

are legally allowed to operate vehicles on Norwegian public roads and the various environmental and physiological conditions they may face.

This area of research would benefit from a statistically significant dataset describing the behaviour of drivers in the conditions of interest. This makes the prospect of large scale monitoring of bridge traffic desirable.

5.4 Description of experiment

The following is planned for early 2020 to characterise the response of vehicles to wind and bridge vibrations. A large van will be driven across the Hardanger bridge in the presence of strong winds. The test vehicle has the approximate length, width and height,

$$l = 6.8\text{m}, \quad w = 2.0\text{m}, \quad h = 2.6\text{m}, \tag{5.23}$$

chosen to provide high aerodynamic force and moment coefficients. The vehicle is instrumented with a real-time kinematic (RTK) positioning system that makes use of a base-station GPS receiver fixed on the ground and two mobile GPS receiver fixed to the vehicle. An accelerometer/gyroscope will also measure its rigid body dynamics while additional sensors will be aqcuired to measure steering input from the driver and the wind velocity at the vehicle's location. The Hardanger bridge is also instrumented with accelerometers and GPS receivers as well as an array of anemometers. Consequently, the following signals will be available for system characterisation and model validation.

- 3x translational accelerations of vehicle body
- 3x rotational velocities of vehicle body
- 2x RTK corrected positions on vehicle
- 1x steering input
- 2x wind velocity (longitudinal/lateral)
- 16x3 translational accelerations along the bridge span
- 4x3 translational accelerations in the bridge towers
- 8x3 wind velocities along the bridge span

See Fenerci and Øiseth [81] for further details around the instrumentation of the bridge.

5.5 Conclusions

The current results suggest that the problem of vehicle response to turbulent wind and sharp-edged gusts (those experienced from passing traffic or bridge towers)

may be studied in isolation from the bridge model. The vehicle has little impact on the lateral vibrations of the bridge and so the bridge vibrations can simply be used as an input to a vehicle dynamics model. Sideslip and yaw accidents may be equally well predicted without consideration of coupled vehicle-bridge interaction. Similarly, a brief analysis of the torsional motion of the bridge shows that the angles that might be experienced by a vehicle on the bridge are very small. An overturn accident may also be equally well predicted without consideration of coupled vehicle-bridge interaction, or indeed the vibrations of the bridge at all. More insight into accident inducing phenomena may result from focussing future modelling studies on the interaction of the vehicle with direct aerodynamic forces and the human driver. These conclusions are to be re-considered in the context of field data from planned full-scale experiments.

Chapter 6

Experimental equipment

The conclusions of the previous two chapters set the path for the rest of the thesis. There is a need to gather data and experiences from the field. The analysis will focus on the vehicle-driver system's response to wind loads. The largest responses – in handling, roll and driver steering input – are sought to make the analysis as insightful and relevant as possible. The choice of test vehicle and measurement equipment reflects this. Firstly, the vehicle is a sizeable body that generates large aerodynamic forces and moments. Secondly, the instruments are functional in the relevant operating environment. The strongest winds are found near the coast in the winter months. Heavy snow and rain is to be expected.

This chapter will begin with a design specification for the instrumentation followed by a description of the equipment, key technical specifications, and a review of the installation of the equipment.

6.1 Design specification

The vehicle must:

- have a large projected front and side area,
- be legally operable using a European class B license, and
- be practical to manoeuvre and park.

The sensory and logging equipment should ensure that the vehicle-driver response is observable. A most complete and readily usable system is sought to reduce the amount of time spent getting the system operational. The measurement system must:

- be easy to install and operate,
- allow for the real-time (manual) monitoring of data,

- be stand-alone and able to operate on a 12V vehicle power supply,
- be able to measure the position, velocity and acceleration at one point on the vehicle,
- take up to 4 additional inputs from external sensors (wind and steering),
- not cause the vehicle to become impractical or illegal to drive on public Norwegian roads, and
- be operable in heavy wind, snow and rain.

Note that the final selection of equipment is also subject to financial constraints as well as procurement laws and regulations.

Figure 6.1: The test vehicle shown with instruments in the field. (Photo: NTNU/Sebastian Reymert)

6.2 Equipment

Given the design specification, a Volkswagen Crafter 35 (L4H3 body) was acquired to serve as the test vehicle. It was equipped with a Racelogic VBOX 3i (hereafter VBOX) logger configured for use with 2 accompanying GNSS antennae, 1 IMU and 1 GNSS base station. GNSS information is sent from the base station to the VBOX via radio link to make corrections using an RTK algorithm.

The VBOX can sample 4 analogue signals from third-party sensors at the same rate as the information from the Racelogic (principal) devices. In the most recent configuration, one voltage signal comes from a potential divider (the SM1-25

string-pot by Measurement Specialities Inc.) that is calibrated to measure the steering angle of the front tyres. The other 3 signals come from an ultrasonic anemometer (WindMaster Pro by Gill Instruments Ltd.) providing a 3-component wind velocity vector.

The test vehicle with the full system installed can be seen on site during a field trip in Figure 6.1. A pictorial diagram of the wired connections between devices in the VBOX system can be seen in Figure 6.2.

6.3 Technical data

6.3.1 Vehicle

The key geometric and inertial parameters for the vehicle are presented here. Some of these will be used for analysis in later chapters. Other parameters are simply presented for reference. Values are given in Table 6.1 and parameter definitions in Figure 6.3. The width, height and length of the body, w_b, h_b and l_b along with the wheelbase l_{wb} are taken from a VW Crafter datasheet [204]. The other values are derived as follows, where the header numbering follows the superscripts/notes in Table 6.1.

Table 6.1: Key geometric parameters of the vehicle.

Parameter	Value	Unit
l_b	6.836[1]	m
l_{wb}	4.490[1]	m
l_f	1.86[2]	m
l_r	2.63[2]	m
w_b	2.040[1]	m
h_b	2.590[1]	m
h_{cg}	0.75[3]	m
w_t	1.79[4]	m
A_s	13.4[5]	m^2
A_f	4.4[5]	m^2
m	2,780[2]	kg
I_{zz}	14.0[6]	kNm^2
I_{xx}	1.5[6]	kNm^2

[1] Datasheet [204] [2] Weighbridge
[3] Load cell [4] CAD [5] Trace
[6] Estimated

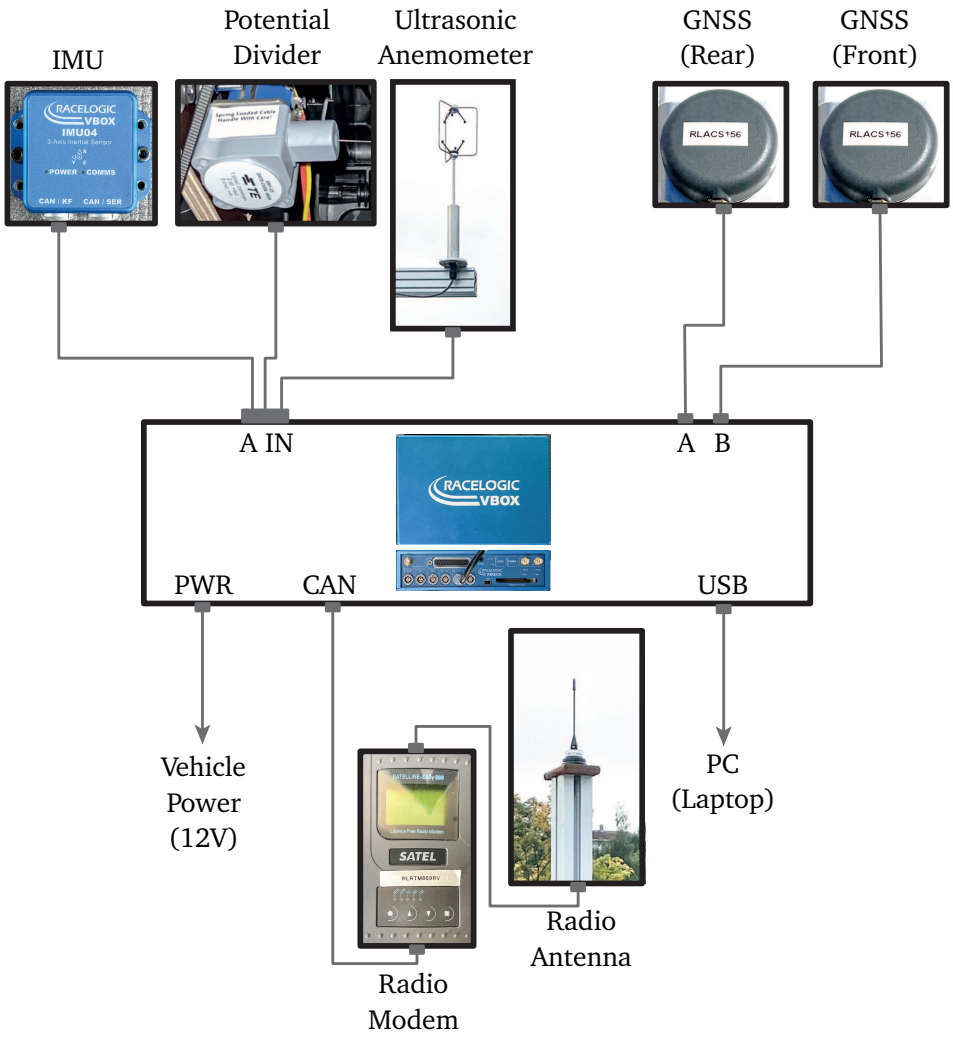

Figure 6.2: A diagram of the sensors connected to the VBOX 3i data logging system. VBOX notation is used to label the ports. (Photo: NTNU/Sebastian Reymert)

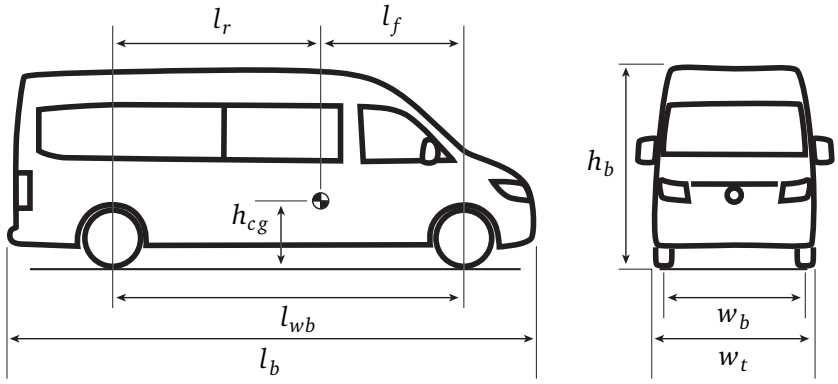

Figure 6.3: Definition of key geometric parameters of the test vehicle.

2. CG by weighbridge

One of the NPRA's weighbridges (the one at Trondheim Trafikkstasjon) was used to measure the load on each of the axles. The weight at the front is denoted m_f and the weight at the rear m_r. Summing the two gives m, the total weight of the vehicle. The longitudinal position of the CG is calculated,

$$l_f = \frac{l_{wb} m_r}{m}, \qquad l_r = l_{wb} - l_f. \tag{6.1}$$

3. CG by load cells

A set of wireless load cells were used to measure the change in load on the rear wheels at non-zero body pitch. The Intercomp SW777RFX Professional scale system was used and the rear wheels were lifted using the end of an hydraulic vehicle lift. When lifted at the rear, the load on the rear axle reduces and is denoted m'_r. Deriving by use of a balance of moments, the height of the CG above the axles of the vehicle h'_{cg} can be estimated using m'_r and the pitch angle of the vehicle θ_y,

$$h'_{cg} = \frac{l_{wb}}{m \tan \theta_y} \left(m_r - m'_r \right). \tag{6.2}$$

The height of the CG above the ground is then h'_{cg} plus the axle height above the ground. The vehicle was lifted to make two different pitch angles such that the estimate of CG height is based on two data points. For a picture of the load cell and the vehicle on the hydraulic lift see Appendix C.

4. Dimensions by CAD

The track width w_t is measured as the distance between the mid-plane of two tyres on opposite sides of the vehicle. The value presented in Table 6.1 was measured using a CAD model that contains the key features and dimensions of the vehicle.

The CAD model of the vehicle was created for the purposes of building a multi-body model of the vehicle and has been useful as a reference for other analyses as well. It derives from simplifications of 3-dimensional scans of the undercarriage as well as measurements using a measuring tape and laser. For more details of the scans and the CAD model see Appendix D.

5. Areas by trace

The outer boundaries of the front and side projection views given in the technical datasheet [204] were traced in Fusion 360 (CAD package). A sketching tool was used to calculate the areas of these outlines.

6. Estimates of moments of inertia

An estimate of the yaw moment of inertia I_{zz} is given by data from the weighbridge. Using the parallel axis theorem,

$$I_{zz} = m_f l_f^2 + m_r l_r^2. \tag{6.3}$$

The assumption is that in yaw, the vehicle has the same moment of inertia as two masses, each sized according to the respective axle load, centered above each axle.

The roll moment can be estimated using an empirical model. The model used here is based on data collected about a series of vehicles available in the United States up to November 1998 [93]. The test vehicle was introduced in 2017 by a European manufacturer and may therefore deviate from the patterns found in the data presented in the referenced work. Nonetheless, the empirical model will be used as a starting point for lack of a better and equally simple method.

In Figure 7 of [93], the roll moment of inertia I_{xx} of various types of vehicles, including vans, are plotted as a function of mass. The moments are normalised by I_{xx}^* defined in Equation 6.4 below. The plots show no distinct relationship between vehicle mass and the roll moment. Typical vans have I_{xx} in the region 0.65-0.75$\times I_{xx}^*$. A rounded number within this range is estimated for the test vehicle and given in Table 6.1.

$$I_{xx}^* = m\left(\frac{w_t}{2}\right)^2. \tag{6.4}$$

6.3.2 Instrumentation

The technical details of the VBOX measurement system and sensors will be presented here. As with the geometric and inertial parameters given above, the accuracy, precision and level of noise for any given signal will be characterised further in any chapter where said characteristics are a relevant concern.

The VBOX data logger receives and processes information from 4 principal devices at a rate of 100 Hz: the 2 GNSS antennae, the IMU and the radio modem (with information from the base station). These signals are used by the VBOX to describe the position, orientation, translation and rotation velocity as well as acceleration of the vehicle. According to the manufacturer, when the system is operating optimally, the accuracy and precision of measurements should be those given in Table 6.2. The noise characteristics of the IMU are given in Table 6.3.

Table 6.2: An overview of the advertised [163] accuracy and precision of the principal VBOX signals derived from GNSS.

Signal	Precision	Accuracy	Unit
Velocity	0.01	0.1	kph
Absolute Position (Horizontal)	1.8	5	mm
Absolute Position (Vertical)	1.8	10	mm
Heading	0.01	0.1	deg
Slip Angle		<0.04[1]	deg
Pitch/Roll Angle		<0.028	deg

[1] Assuming an antenna separation larger than 2.5 m

Table 6.3: An overview of the advertised characteristics of the IMU.

Signal	Noise Density	Bias Stability	Units
Angular Rate (X,Y,Z)	0.015	0.0035	$deg/s/\sqrt{Hz}$ & deg/s
Acceleration (X,Y,Z)	150	40	$\mu g/\sqrt{Hz}$ & μg

An important feature of the system is that data can be logged in one of two ways: by saving data transferred by serial connection to a PC or directly to a compact flash (CF) storage card inserted into the VBOX. Logging by the latter method can be triggered manually or automatically. In the automatic mode, triggering can be configured to occur when a threshold value of velocity is exceeded. This can be very convenient, unless measurements are desired in a location where no velocity can be estimated due to a lack of satellite visibility. This was the case during some of the field sessions. Manual logging requires access to the VBOX which is located

in the load space of the test vehicle.

Logging on the PC is done manually and gives the user the convenience of arranging data into logical sets while performing experiment runs. The PC can be located in the cab with the driver and passenger during the field sessions.

One weakness of the logging functionality of the VBOX is that not all signals are available via the serial connection. The missing signals are primarily the raw GNSS data. This data is manipulated internally in the box and only the results of the manipulations are sent via serial. The raw signals remain in the VBOX and can only be logged on the CF. This can be problematic when data saved on the PC and recorded on the CF are not concurrent, which is almost always the case given there is no option to trigger the two logging mechanisms simultaneously.

The analogue signals are sampled at 100 Hz with a 24-bit resolution across a ±50 V range. This is equivalent to a 6.0×10^{-6} V resolution. The ultrasonic anemometer and potential divider (string-pot) provide voltage signals to the VBOX to measure the wind vector and steering angle respectively.

Ultrasonic anemometer

The ultrasonic anemometer's precision and accuracy in measuring the wind vector is given in Table 6.4. It is primarily a digital device outputting the wind velocity vector at a 32 Hz rate. The specific anemometer used in this work has the analogue output option.

The wind velocity can be output in a variety of formats along with additional information (such as status flags) on up to 4 voltage signals. In the final configuration used here the polar wind direction (from 0 to 360°), the wind speed in the horizontal plane (up to 50 m/s) and the wind speed in the vertical direction (up to 50 m/s) were chosen as output signals. These are translated to a voltage from 0 to 5V and are re-sampled at 100 Hz by the VBOX. The signal is digitised by the VBOX with a resolution of 6.0×10^{-6} m/s and 4.3×10^{-4}° for the velocities and direction respectively. This is more than enough to resolve the full precision of the original signals (ref. Table 6.4).

Table 6.4: An overview of the advertised characteristics of the WindMaster Pro.

Signal	Precision	Accuracy	Unit
Wind speed	0.01	<1.5% RMS[1]	m/s
Direction	0.1	2[1]	deg

[1] at 12 m/s wind speed

Potential divider

The string-pot is a potential divider that outputs an analogue voltage signal proportional to the travel of a draw-wire or string. The resolution of this signal is theoretically infinite. The string is drawn out to a drum that is fixed to a span of the steering column next to the accelerator and brake pedals (see Figure 6.4). The resolution of the digitised steering angle signal is therefore a function of said drum's radius. The angle measured at the steering column has a resolution of $8.7 \times 10^{-5\circ}$. Given the ratio between the steering wheel angle and the wheel-on-ground steering angle, this is equivalent to an approximate $5.8 \times 10^{-6\circ}$ resolution in the steering angle δ at the ground.

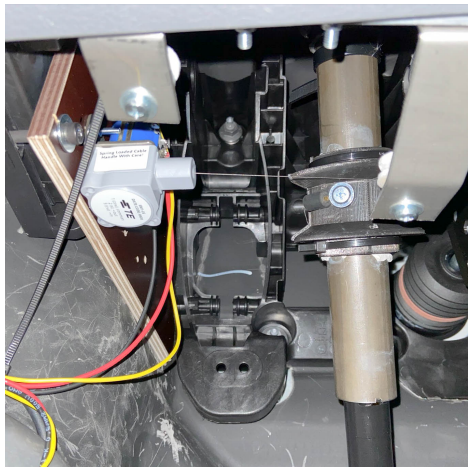

Figure 6.4: The installation of the string-pot. The draw-wire is wrapped around a drum that is attached to the steering column. (Photo: NTNU/Sebastian Reymert)

6.4 Installation

The installation of the instrumentation in the test vehicle is described diagrammatically in Figure 6.5. The vectors shown in this figure describe the location of some of the instruments relative to the IMU. This is used as the reference point for practical reasons. The IMU is located on the floor in the load space of the vehicle and is easily accessible. There is also no movement of this device in relation to the body, whereas the CG can change location depending on how the vehicle is loaded. The vectors for the final instrument configuration can be found in Table 6.5.

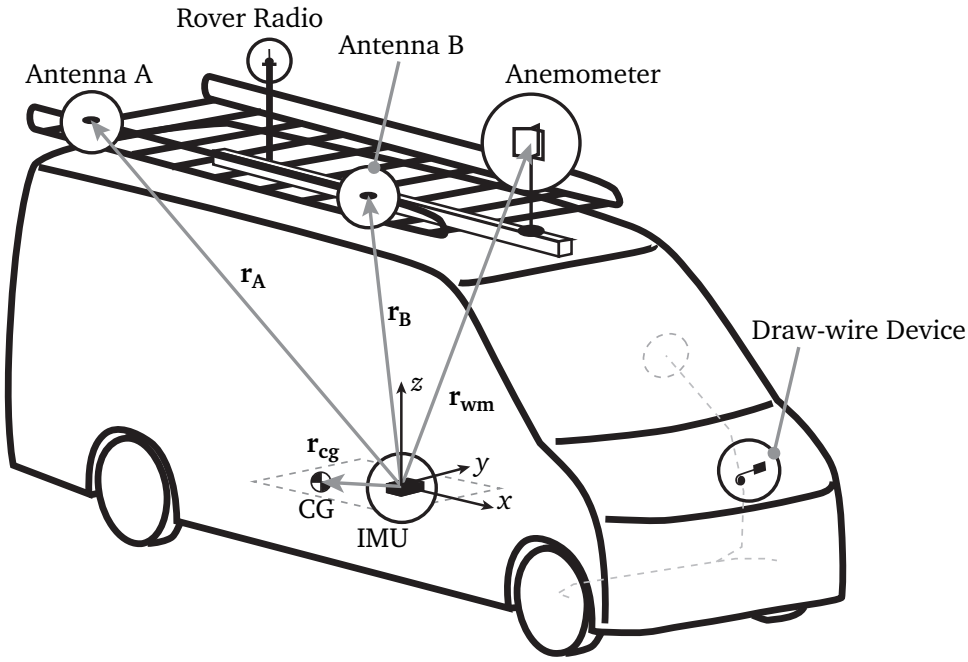

Figure 6.5: The installation location of the sensors in the VBOX instrumentation system.

Table 6.5: The position vectors for the instrument measurement locations. The unit is m.

	$\mathbf{r_{CG}}$ [1]	$\mathbf{r_A}$	$\mathbf{r_B}$	$\mathbf{r_{WM}}$
x	0.00	-3.25	-0.33	1.32
y	0.00	-0.75	-0.60	-0.75
z	0.09	2.16	2.14	2.76

[1] For the vehicle without the roof rack and tools cabinet installed.

GNSS antennae

As indicated in the diagram in Figure 6.5 and shown in the image in Figure 6.1, the primary devices in the VBOX system are mounted on a roof rack. The GNSS antennae are magnetically mounted on plates that are clamped to one of the side-railings of the roof rack. This is shown in Figure 6.6a where the cable is strapped to the clamp using a wire-tie to avoid damaging the antenna should the magnetic mounting fail under disturbance from vibrations.

The antennae are placed in a fore/aft configuration as far apart as possible. The distance is limited by the size of the roof rack as well as cable length. The spacing achieved is 2.92 m. This should ensure maximum slip/heading angle accuracy according to the VBOX datasheet [163].

(a) Detail of GNSS receiver mounting

(b) Detail of radio antenna mounting

Figure 6.6: The GNSS and radio antenna installations. (Photo: NTNU/Sebastian Reymert)

IMU

The IMU is mounted directly to the floor in the load space. This can be seen in Figure 6.7. The connection between the floor and the chassis is stiff and should not affect measurements in the lower frequency range (<10 Hz).

Strut

The anemometer and radio antenna are mounted to an aluminium strut with a 120x120 mm cross-section (manufactured and delivered by Rollco AB). The strut

(a) Direct floor-mount using bolts

(b) Placement on the floor of the load space

Figure 6.7: The IMU's installation in the vehicle. (Photo: NTNU/Sebastian Reymert)

is clamped at three locations onto the crossbars of the roof rack and cantilevered above the windscreen. The length of the strut was limited for practical reasons related to the delivery of the strut. The length of cantilever was limited to reduce the magnitude of vibrations at the mounting point of the anemometer.

Ultrasonic anemometer

The anemometer is mounted to the strut via a 10 mm steel plate. The anemometer was placed as far ahead of the roof rack as possible given the limitations due to vibrations explained above. The aim was to avoid as much as possible the effect of the vehicle's body on the measured wind at the anemometer location.

Radio antenna

The radio antenna is placed as high up as possible to maximise visibility to the base station antenna. This is achieved by placing the antenna on top of a vertically attached strut as can be seen in Figure 6.6b. The position of this strut is centered between the two GNSS antennae to minimise the effect of any possible interactions/disturbance between the GNSS and radio signals.

Potential divider/string-pot

The string-pot is mounted on a custom mounting plate below the steering console as shown in Figure 6.4. The draw-wire is then threaded directly onto a drum that is clamped onto the steering column. Any rotation of the drum is captured as linear travel of the wire in/out of the string-pot.

Base station

The base station can be seen in Figure 6.8 where it is pictured in operation in the field. The base station needs to have good line-of-sight for both the GNSS receiver as well as the radio. The GNSS needs a clear view of the sky while the radio needs a clear view to the receiver antenna on the vehicle. In this work, the measurements are being taken on a bridge and so there needs to be a clear view from the base station location to the radio antenna on the vehicle when it is on the travelling the full span of the bridge.

The picture in Figure 6.8 shows an ideal location. The base station has been placed high in altitude. The GNSS has a good view of the sky without trees or highlands nearby. There is also a clear, uninterrupted view of the entire bridge from the radio antenna.

Figure 6.8: The base station in operation over Måløy with the bridge in the background. The GNSS receiver antenna is mounted on the tripod (left) and the radio modem and antenna on top of a telescopic mast (right). (Photo: NTNU/Sebastian Reymert)

6.4.1 Summary

For reference, the vehicle, data acquisition and sensor system are specified in summary Table 6.6.

Table 6.6: A summary and specification of the experimental equipment.

Description	Specification
Vehicle	CRA 35 KAS L4H3 177 4M/AUT
Summer tyres	Continental ContiVanContact 200 235/60 R 17C 117/115 R
Winter tyres	Pirelli Winter Chrono 235/65 R 16C 115/113 R M+S (Studded)
Data logger	VBOX 3iSL 100Hz RTK v5 (RLVB3ISLR-V5)
Base station	VBOX DGNSS Base Station RTK
Base station radio module	VBOX Base Station Radio Module - Medium range 869.4125MHz (Satel) - EU (RLRTM869BS)
Vehicle radio module	VBOX Radio Module - Medium range 869.4125MHz (Satel) - EU (RLRTM869RV)
IMU	VBOX Inertial Measurement (RLVBIMU04-V2)
Ultrasonic anemometer	WindMaster Pro 32Hz 0-65m/s 4 off 14 Bit Analogue Outputs
String-pot/potential divider	SM1-25

Chapter 7

Field experiments

A series of data sets have been collected that describe the motion of the vehicle, the response of the driver, and the wind field along various sections of road – both fixed-base and elevated on a bridge girder – at coastal and mountainous locations in Norway. See Figure 7.1 for a labelled map of the experiment locations. In 8 out of the 11 data sets the vehicle was driven across a bridge. Included are four suspension bridges, two cantilevered bridges and one cable-stayed bridge. A sketch of all the included bridges as well as a small map showing the bridge and roads in relation to the terrain can be seen in Figure 7.2.

This chapter provides an overview of the data sets and motivates the choices made in the planning and collection of data in the field. Some of the challenges faced during the field sessions are discussed at the end.

7.1 Experimental objectives

The objectives of the field experiments are:

- to measure the vehicle-driver response on bridges and ground-fixed roads in strong crosswinds as near to critical for vehicle safety as possible,
- to characterise extreme wind conditions in various terrains and on various bridges in Norway, and
- to investigate the effect of driving speed as a mitigating factor for wind-induced road accidents.

7.2 Approach

The time and location of the field sessions were primarily determined by opportunity. Visits were made to locations where strong crosswinds were forecast that

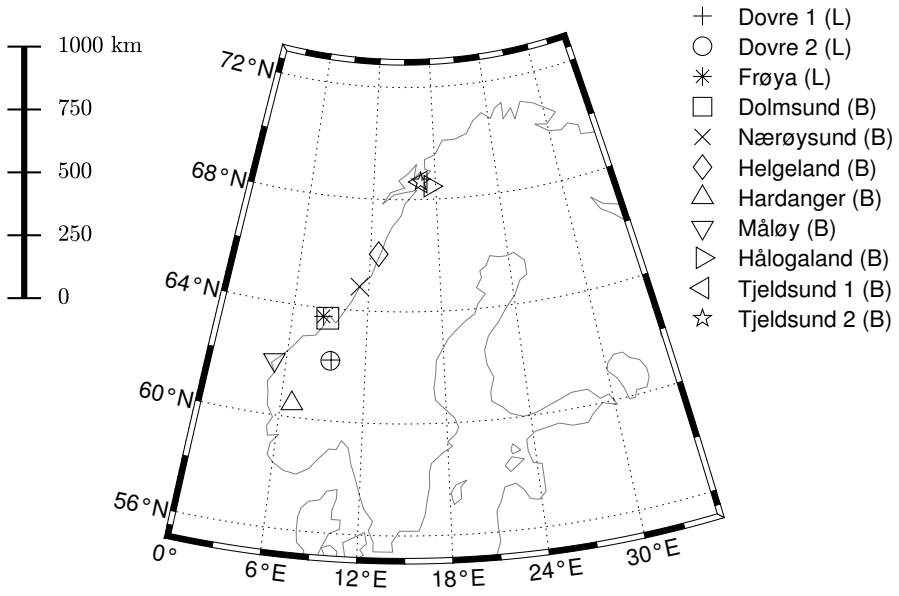

Figure 7.1: A map of Norway in UTM projection showing the locations of the field experiments. Created using `m_map` package [157].

L: Land-fixed road
B: Bridge

could be reached in time to perform experiments. At the same time, the NPRA has expressed an interest in – or concern for – the consequences of the motion of the longest bridge spans on traffic comfort and safety. Data from the longest bridges can provide insights for the development of even longer spans.

The Hardanger and Hålogaland bridges, with the longest main spans in Norway, were therefore prioritised. In addition to their relevance for future bridge projects, there are monitoring systems installed on these bridges that can provide measurements of bridge motion and wind at various points along the span. Unfortunately, neither of the two monitoring systems were fully operational during the field visits made with the test vehicle.

The Måløy bridge was visited after a discussion with the NPRA where it was stated that the bridge is often closed as a result of strong winds. The wind-related closure of this bridge appears to be a controversial topic amongst the residents of the Vågsøy island [80] which is connected to the mainland via the Måløy bridge.

The remaining bridges, Helgeland and Nærøysund, were chosen without any other motivation than the opportunity to collect data in strong winds. Cable-stayed and suspension bridges were prioritised due to the potential for higher amplitude and lower frequency bridge vibration than on cantilevered bridges. Cable-supported bridge also feature towers that are known to be a source of wind-related vehicle instability (as demonstrated in Chapter 4).

The sessions on ground-fixed roads were performed simply to have a comparison to data on the bridges. The locations at Dovre and Frøya are convenient to access by road from Trondheim and presented with strong winds. The results from Frøya were found to be less relevant than the other results and will therefore be mentioned only briefly in the rest of the thesis. The results from Frøya are not presented alongside the other results and have been collected in Appendix F.

The Dolmsund bridge was chanced upon in transit between Trondheim and Frøya and proved to be an interesting case. While crossing the bridge the evening before the experiments, the tyres on the front axle momentarily lost traction in response to a gust – a front axle skid event. These events were observed at other locations as well and will be discussed further in Chapters 11, 10 and 12. Consequently, measurement sessions were performed on the bridge the following day.

Figures 7.1 and 7.2 show the location of all test sites visited and drawings of the bridges respectively.

7.3 Design of experiments

The field sessions were performed ad hoc and were typically initiated by the weather warning system *Varsom* provided by the Norwegian Water Resources and Energy Directorate (NVE). By subscribing to yellow, orange and red wind warnings for the entire country and using the Meteorological Institute's wind forecast (*yr.no*) it

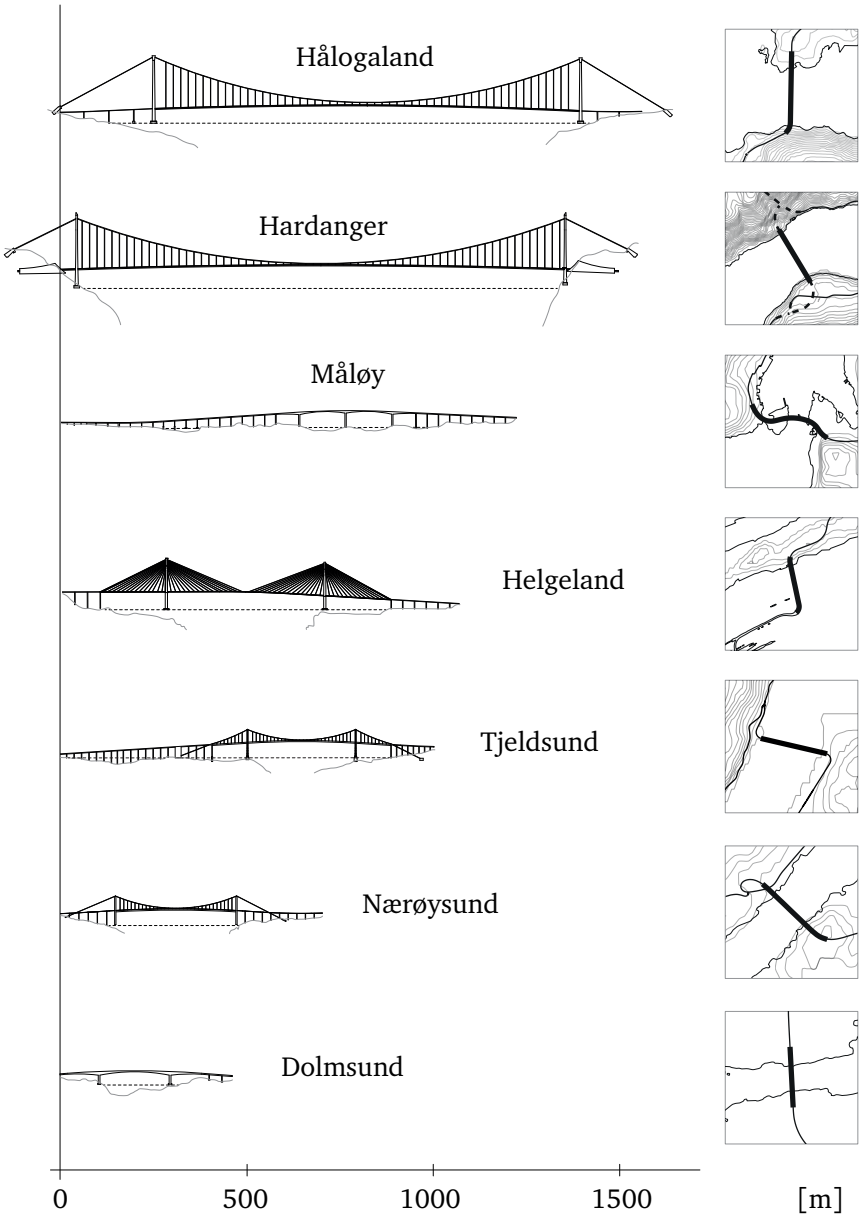

Figure 7.2: A sketch of the bridges at each test location [185–189, 202, 203] along with a contour and road map (© Kartverket) showing the bridges in the terrain. Contours are given per 20 m of elevation. The portion of road that is elevated from the ground (i.e. on the bridge) is highlighted with a thick black line.

was possible to get notifications and identify appropriate roads, bridges and wind conditions.

The notifications were typically given 12-48 hours in advance of the weather event of interest. Given that some of the locations were up to 12 hours away by road, this left little time for preparation. Consequently, the test vehicle had to be ready for dispatch at all times.

The experiments were timed as much as possible to coincide with the strongest winds. Generally, it was possible to reach the location in time for this. However, the Helgeland bridge, for example, was closed for traffic upon arrival. The field session was executed some hours after the peak of the storm when the bridge had been re-opened for traffic. All experiments were subject to weather- and regulation-related constraints on the road of interest and in transit to the field location.

Driving speed

As stated in Section 7.1, the objectives for the experiments are to characterise the wind field/profile along the selected segments of road/bridge as well as to measure the vehicle-driver response along said segments.

It was reasoned that the profile should be measured with a sufficient spatial resolution which is a function of the sampling frequency of the anemometer and the driving speed of the vehicle. Meanwhile, the vehicle-driver response should be measured at a driving speed that is representative of typical road users. Unfortunately, these two aims cannot always be achieved simultaneously.

For the majority of the included road sections, the speed limit was 80 kph at the time of experiment. The only exception is the Måløy bridge where the speed limit was 60 kph (and 50 kph at time of experiment due to road works). It is common to see speed limits of 60, 70 and 80 kph on Norwegian roads, where 80 kph is the general rule for main roads outside of built-up areas. Therefore, where the speed limit permits, the speed of 80 kph was considered the most relevant case for the evaluation of vehicle-driver response.

At 80 kph, the spatial resolution of the along-road wind profile sampled at 32 Hz is 0.7 m. Assuming perfect performance of the anemometer, then this would likely satisfy the need to characterise wind profiles related to the terrain surrounding the bridge (larger scales). However, for the purposes of characterising the wind gust profile seen at the towers, a finer resolution is desired (smaller scales).

At higher driving speeds (70 or 80 kph) it was found that an anti-spike algorithm in the anemometer would occasionally activate. The wind measurements collected by the VBOX have been seen to hold a constant value following the identification of *unrealistic* values by the anti-spike algorithm [206]. Examples of this will be shown later in this thesis (for example in Chapters 8, 11 and 13).

In order to measure the wind profile near the towers with a higher resolution

and to avoid problems with the anti-spike algorithm, a set of passes at 30 kph was considered a second priority (following the 80 kph case) at the bridges with towers. At this driving speed the wind profile can be described with a resolution of 0.26 m along the road axis.

In the interest of demonstrating the effect of driving speed on vehicle-driver response it was decided to perform passes at 60 and 70 kph as well where possible. These are not only typical speed limits seen on Norwegian roads, but may also be representative of the driving speed bridge users choose for themselves when they have been warned of high wind speeds.

Cases of drivers choosing to lower their driving speed on wind exposed bridges were observed during the field sessions. All bridges discussed here have electronic signs at either end that display a warning message at high wind speeds along with a wind speed reading from an anemometer placed on the bridge deck as explained in Chapter 1.

Repetitions

Across the different field sessions it was observed that the periods of strongest wind speeds were generally well predicted by the Meteorological Institute and that these periods could be as short as 1-2 hours, but generally lasted longer than 3 hours. As a rule of thumb, gust speed forecasts of at least 23-24 m/s lasting for a minimum of 2-3 hours were considered a condition to make field sessions worthwhile.

All efforts were made to time the passes such that they coincided with the strongest winds and the experiments were designed to make best use of the this time period. Sets of 5 repetitions in each direction were judged to balance the need for statistically significant data with the time limitations of the wind events. This generally allowed for the collection of 10 passes at each of the 4 driving speeds.

The non-stationarity of the wind, the length of the section of road or bridge and the availability of roundabouts and/or side roads for u-turns all played a role as well. Not all of this information is known beforehand and so the execution of passes and the order of execution was sometimes decided on site. The maximisation of vehicle response at 80 kph was the first priority. Second was the characterisation of the wind profile at 30 kph.

The progression of the experiments may in cases have been influenced by the needs of the driver and/or the research assistant in the passenger seat. The sessions, including set up, often lasted 4 hours or more and sometimes took place late at night or in the early hours after a day of travelling. All passes at each location were performed by the same male driver, myself, aged 25-26 during the experiments.

Table 7.1 gives an overview of the passes made at each of the test locations. The final two columns describe the instrument configuration on the test vehicle.

Table 7.1: An overview of the field locations and test repetitions.

Description	Target Speed[1]	Direction[2]	Repetitions[3]	CF[4]	RTK[5]
Dovre 1	80	E/W	5/5	•	•
Sum			*10*		
Dovre 2	80	E/W	5/5	•	•
Sum			*10*		
Frøya	80	E/W	5/5		•
Sum			*10*		
Dolmsund Bridge	70	N/S	5/5		•
	80	N/S	1/1		•
	50	N/S	1/1		•
Sum			*14*		
Nærøysund Bridge	80	E/W	5/5	•	
	30	E/W	5/5	•	
	60	E/W	5/5	•	
	70	E/W	5/5	•	
	70	E/W	3/3	•	
Sum			*46*		
Helgeland Bridge	70	N/S	5/5	•	
	80	N/S	5/5	•	
	60	N/S	5/6	•	
	30	N/S	5/5	•	
Sum			*41*		
Hardanger Bridge	30	N/S	5/5	•	
	80	N/S	5/5	•	
	80	N/S	5/5	•	
Sum			*30*		
Måløy Bridge	50	E/W	12/12	•	•
Sum			*24*		
Hålogaland Bridge	30	N/S	5/5	•	•
	60	N/S	5/5	•	•
	80	N/S	5/5	•	•
Sum			30		

continues on next page ...

continuation					...
Tjeldsund Bridge 1	30	E/W	5/5	•	•
Sum			10		
Tjeldsund Bridge 2	70	E/W	5/5	•	•
Sum			10		

[1] This is typically the speed input to the cruise control. In certain situations it was necessary to manually adjust the speed to comply with traffic regulations and/or situations on the road.
[2] E - East, W - West, N - North, S - South, determined by quadrant along the bridge's straight-section axis.
[3] Repetitions are given per direction, separated by a forward slash to correspond with the direction.
[4] CF - Compact Flash, indicates that the flash card was installed and functional during the runs.
[5] RTK - Real Time Kinematic, indicates that the base station was installed, functional and in range such that GNSS information on the vehicle could be corrected by the VBOX RTK algorithm.

Table 7.2 summarises the date, time and duration of the field sessions.

Instrument configurations

Table 7.1 shows that there are inconsistencies in the configuration of the instrumentation across the different field sessions. It was endeavoured to have a fully functioning VBOX system with the compact flash (CF) installed as well as the base station in operation.

The compact flash was not installed during the trip to Frøya (which includes the Dolmsund bridge) due to procedural error. This means that some of the raw GNSS data that cannot be transferred via serial to the PC does not exist for this data set. The base station was damaged during installation at the Nærøysund site and was not operational again until after the test at Helgeland had taken place.

At Hardanger, the wind event was short and the drive from Trondheim long. Consequently, collecting measurements in the strongest wind was prioritised over spending time on the installation of the base station. Regardless of time constraints, the installation at Hardanger is a very challenging task due to the steep fjord walls. As will be seen, the GNSS antennae mounted on the vehicle struggled to maintain satellite lock around the towers and entrance to the tunnels at either end of the bridge. It is unlikely that the operation of the base station would have improved this.

Table 7.2: Date and time information for the field experiments.

Description	Date at Start	Time at Start	Time at Completion	Duration
Dovre 1	29/10/2020	12:41	14:37	1:55:40.93
Dovre 2	31/10/2020	21:30	23:06	1:35:37.93
Frøya	05/11/2020	13:36	14:21	0:44:51.39
Dolmsund	05/11/2020	17:01	17:44	0:43:01.06
Nærøysund	21/11/2020	20:29	23:38	3:09:13.51
Helgeland	22/01/2021	08:51	11:39	2:48:00.76
Hardanger	11/03/2021	00:27	02:40	2:13:30.04
Måløy	22/09/2021	07:25	10:23	2:57:54.95
Hålogaland	03/01/2022	00:42	03:38	2:56:04.68
Tjeldsund 1	22/01/2022	20:57	21:59	1:02:00.35
Tjeldsund 2	23/01/2022	12:53	14:08	1:15:01.29

*Dates & times are local (Oslo)

7.4 Data handling

Raw files

The files produced by the VBOX on the CF card and saved to the PC in the test vehicle (serial) are in the Racelogic `.vbo` format. This is a human readable text file containing a table of time series preceded by meta data about the system and the names and units for each of the channels. The files written by the VBOX itself are slightly different to those saved by the PC and contain additional information about the configuration of the sensors.

Database files

The raw `.vbo` files are interpreted by a MATLAB script and stored in a structured MATLAB database (named `vbd` denoting **VB**OX **d**ata) and saved to `.mat` files. Each channel in each of the serial and CF files is included as a separate field in the database with the original name as designated by the VBOX/Racelogic software. They are also tagged with `cf` or `srl` to show where the signals came from. This makes the data easy to reference in scripts.

Parameters related to the configuration of the instruments are stored in an excel sheet. They are collected by the MATLAB script that creates the database and stored in the `config` field of the database. This field includes the tyre specification, details of additional installations on the vehicle (in some configurations the roof rack and tools cabinet), the mass properties of the vehicle, the geometry of the vehicle and

placement of instruments, any zero offsets in the instrumentation (for example the angle at which the anemometer is mounted) and the parameters needed to convert the four analogue voltage signals to physical ones (the steering channel and those describing the wind velocity vector).

The `source` field specifies the location and name of the files from which the data was extracted and a summary of how many serial and CF files are referenced. The header from the CF files containing information about the VBOX configuration can also be found here.

The `summary` field contains the date the database was created and an overview of the collective duration of time the time series span. This is from the start of the first serial file to the end of the last serial file.

A field named `bridge_geo` contains the latitude and longitude at the centre points of each set of towers as well as the endpoints of the bridge. This data was manually picked on a map (norgeskart.no) and entered into the database. Typically, the vector graphics in the *land* layer made point-picking easy. In some cases the aerial photography layer was used instead.

The `datetime` vector in the field `utcTime` contains a time vector from the first data point in the first serial file to the last data point in the last serial file. This means that any data from the CF files outside of these bounds is not included. An equivalent vector translated to local time is given in the field `osloTime`. All other vectors include information from all serial or CF sources as a continuous time series from the start to the end of the aforementioned time vectors. `NaN` values are used where no data exists.

It is convenient to have a continuous vector from the start to the finish of the field sessions. The data can then be partitioned according to position, speed, time or any other way the user desires.

7.5 Challenges

Some of the challenges encountered with the instrumentation during the field sessions:

- Establishing a base station was typically challenging, but achievable. The best locations are high in elevation with an unobstructed view of the bridge. If this was not possible then locations at the water's edge were checked next, typically 1-2 km from the bridge. Setup was made easier and quicker by finding locations with existing structures, like fences or railings which the radio mast could be strapped to rather than using guy lines.
- The vehicle-based GNSS antennae appear to have struggled in proximity to the towers. Similarly, the Racelogic Kalman filter could not initiate on the Hardanger bridge because of the two tunnels on either end of the bridge.

There was not enough time spent with a view to satellites for initiation to complete. These problems could be solved by alternative instrumentation (for example vision- or laser-based) or by developing a Kalman filter that uses more a-priori information and does not require an initialisation. An estimator can likely be designed to better handle the disturbances in GNSS signal seen at the towers.

- By mistake, the anemometer was configured with limits on the maximum wind speed that resulted in clipping of some of the wind data. This will be discussed more in Chapters 8 and 14 and has not had a significant impact on the conclusions drawn in the thesis.
- The placement of the anemometer was such that the vehicle's pressure wave does affect the measurements. This will be discussed and characterised in Chapter 8. This has not had a significant impact on the conclusions drawn in the thesis. Placing the anemometer even further ahead or above the vehicle would be challenging to achieve without incurring significant expenses, making the instrumentation difficult to set-up or the vehicle impractical to operate in the field.

Chapter 8

Observations of local flow features

A review of existing studies reveals that the wind has been measured using vehicle-mounted instruments before (see *on-road turbulence* below), yet this thesis appears to be the first work where such measurements have been investigated on bridges. As will be seen in this chapter, there are various local flow features induced by features of the local topography and the geometry of structural elements of the bridge. Namely:

- the turbulence intensity is higher over the segments of the bridge deck where the upstream, non-smooth and complex terrain is at a similar height to the bridge deck,
- the mean wind speed can increase locally over a given segment of the bridge deck where a headland exists underneath or upstream of said segment,
- the towers of suspension and cable-stayed bridges have a shielding effect as the vehicle passes through their wakes leading to an inverse/negative gust,
- the cross-section below the road (of the girder or the topography) and changes to these sections can reduce mean wind speed and increase turbulence intensity, and
- elements of the substructure like piers or counterweights can have a shielding effect as significant as elements above the bridge deck – like the towers – causing an inverse gust.

This chapter begins with a short review of the literature from the multiple areas that are relevant to understanding and identifying the above-mentioned flow features. The wind profiles across the roads and bridges studied here are then presented and discussed.

8.1 A review of literature relevant to the observations

On-road turbulence

Wordley and Saunders [220] (and continued in a second paper [221]) performed a series of field experiments on rural and urban roads with the aim of characterising the turbulence spectrum at an elevation that is relevant for vehicle dynamics. They conclude with estimates of turbulence intensity and turbulence length scales for four different types of upwind terrain.

The *freeway traffic* terrain type was found to create the highest turbulence intensities, mainly caused by the wake of large upwind vehicles. Large vehicles, such as vans, trucks and tractor-trailers can be of a similar length dimension to the width of the towers encountered in the current experiments. Mayer et al. [138] have similarly measured the wind's Power Spectral Density (PSD) from a vehicle on the road.

Cooper [62] presented an analytical approach to estimating the wind's PSD as measured by a moving vehicle following a straight line path. The PSD curve is a function of the driving velocity, the mean wind speed and the angle of the vehicle's straight-line path relative to the mean wind direction. Zhang and Proppe [235] use this analytical approach to perform an accident risk analysis for road vehicles.

Brandt et al. [32] measured the wind environment on a high-speed test track (140-185 kph) and suggested analytical functions as models for various types of gusts. The functions are primarily built using a half and full wavelengths of a sine curve combined with intervals of a constant-value function. A total of 4 gust profiles were proposed.

A 3-second sliding window was used to characterise the size of gusts as the difference between the maximum and minimum wind speed. An order 500 Hamming low-pass filter with a cut-off frequency of 5 Hz was used to filter out smaller scales. Gust amplitudes up to 10.7 m/s in the direction normal to vehicle travel were observed, with most gusts falling in the range 3.4-5.4 m/s.

Complex, rough terrain

Midjiyawa et al. [140] studied the flow characteristics at various locations near the shoreline of coastal fjords in Norway. Winds that had travelled over complex terrain were shown to have significantly higher turbulence intensity in the horizontal direction (up to 0.22) when compared to wind headings along the fjord direction (up to 0.11).

Abedi et al. [11] performed a CFD study to understand the impact of complex, hilly, forested terrain on flow characteristics at multiple wind turbine sites. The resulting plots (Fig. 21 in [11]) illustrate how local topographical peaks topped with forest can lead to a local, downstream increase in turbulent kinetic energy.

The high energy region can extend up to 500 m downstream and remains at a similar elevation to the topographical peak from which it emanates. This gives an example of how non-smooth topographical features can cause local increases in turbulence several hundred meters downstream.

Kim and Patel [110] similarly illustrate the increase in turbulent kinetic energy behind a local topographical peak. Again, the turbulent kinetic energy remains heightened at least 500 m downstream of the peak from which the increase emanates.

Headland

Brooks et al. [33] studied the structure of the ABL along a coastline using aircraft measurements. The results (Fig. 2 in [33]) show how a wind that predominantly follows the coastline *wraps* itself around a prominent headland (protruding 35-40 km from the coastline). The flow is observed to accelerate past the apex of the headland and forms an expansion fan downwind. "*The observed wind field shows that the mean wind speed north of the cape is about 6 m.s*$^{-1}$*, accelerating to a maximum of a little over 20 m.s*$^{-1}$ *downstream of the cape.*"

Vehicle forward pressure wave

Wordley and Saunders [220] illustrate how the forward pressure wave of a forward travelling vehicle can change the wind's vertical velocity profile ahead of the vehicle. A wind tunnel experiment as well as a field study were used to quantify the effect of the pressure wave on the measured wind speed and incidence angle. The probe used for measurements in the field was finally placed 1.0 m in front of the foremost point on the vehicle body at the same height. They concluded that with this setup, no corrections to the wind measurements due to the forward pressure wave were necessary.

Mayer et al. [138] mounted their probe on the hood of the car, slightly behind the foremost point on the vehicle body at a height above the roof of the vehicle. A CFD study was used to position the probe such that the effect of the forward pressure wave was minimised. It was found that the influence on wind magnitude was negligible. However, the yaw angle measurements had to be calibrated in the wind tunnel.

Embankments & deck section

Cheli et al. [44] characterise 6 aerodynamic force coefficients – longitudinal, lateral, vertical, roll, pitch and yaw – as a function of incidence/yaw angle for a heavy road vehicle on flat ground using a wind tunnel experiment. Part 2 of the paper [45] shows how these characteristic curves change when the vehicle is placed on

the deck of a bridge section (viaduct) and an embankment topography. They find that the lateral force and yaw moment are particularly affected by the geometry below the road surface. Noguchi et al. [146] perform a similar experiment in the wind tunnel with train models on an embankment.

Note that because the coefficient curves $C_i(\gamma)$ change (γ – incidence/yaw angle, C_i – aerodynamic coefficient for load i), then this indicates a change in the flow over the composite embankment/viaduct-vehicle geometry and not simply a change to the flow over the topography/viaduct. The most significant changes to the aerodynamic characteristics occurred where the viaduct/embankment has dimensions similar to the vehicle's.

Kim and Patel [110] illustrate by means of CFD the flow structure over a triangular ridge as well as flow measurements from the field over an embankment-shaped hill in Scotland. Zhang et al. [231] use CFD to study the flow over a 3D section of a simplified embankment geometry typically seen below railways.

Dorigatti et al. [71], He et al. [92], Kim et al. [114], Zhu et al. [243] also show that the aerodynamic coefficients of the vehicle vary from the flat ground case when placed on a bridge viaduct. A change dependent on lane/position on the deck is demonstrated in all these works as well. Consistently, four-lane bridge decks are considered throughout the referenced articles.

Camara [38] considers the shielding effect of the viaduct/deck section through a CFD analysis of the Orwell bridge's varying cross-section in his report to Highways England.

Substructure elements

As was the case at the Tjeldsund bridge, there may be elements of the bridge's substructure that look similar to buildings. The flow structure around such bluff bodies is well described in texts like Macdonald [136], Peterka et al. [158], Simiu [177]. More recently, they have been studied by Kim et al. [111], Sumner et al. [193], Wang [215].

The work by Sumner is particularly illustrative for the current experiment and shows through the technique of PIV the full flow separation from the top of a finite square cylinder mounted on a flat surface in a wind tunnel. The aspect ratios studied (height-to-cross-section dimension) are similar (AR= 3) to those seen at, for example, the Tjeldsund bridge (AR$\approx$ 2.5, the finite square cylinder being the counterweight below the bridge deck, see Figure 8.33). A recreation of Sumner's results on the separation of flow over a rectangular prism with an aspect ratio of 3 can be seen in Figure 8.1.

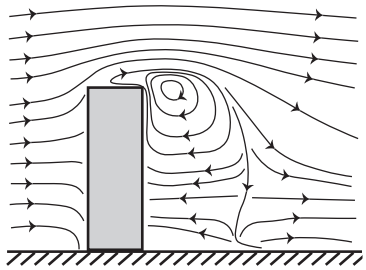

Figure 8.1: A recreation of Sumner's [193] Fig. 5 showing mean streamlines of the flow (Re= 4.2×10^4) over a rectangular prism fixed to the ground plane. The streamlines drawn are those measured (by PIV) in the symmetry plane.

8.2 Processing position and wind measurements

The position and wind measurements recorded in the current field experiments will be used to profile the wind along the road axis. Multiple interesting flow features are observed that can have an adverse effect on vehicle comfort, driver workload and ultimately safety. To this end, it is useful to have accurate and smooth position, heading and velocity signals. This enables:

- the estimation of the wind velocity vector in a global reference frame (the ENU coordinate system) and
- the association of wind flow features to the geometry of the bridge and terrain.

With these interests in mind, a method was used that *snaps* position data to the road centreline and smooths out potential errors. The methodology is described in detail in Appendix E and involves interpolating, extrapolating and smoothing the raw GNSS data to attain better estimates of the position of the vehicle's centre of gravity and the anemometer.

8.3 Wind profiles

After the snapping, smoothing, filtering, filling and translation has been performed, the wind profile along each road considered in this work can be plotted. Figures 8.2 through 8.21 show the raw and transformed wind plotted as a function of a spatial coordinate for each data set.

The profiles are lined up on the horizontal axis with a sketch of the bridge as well as a topographical contour plot of the surrounding terrain. The figures

have been collected here to make interpretations and comparisons easy. Further explanation of the figures is given afterwards.

continues on next page ⟶

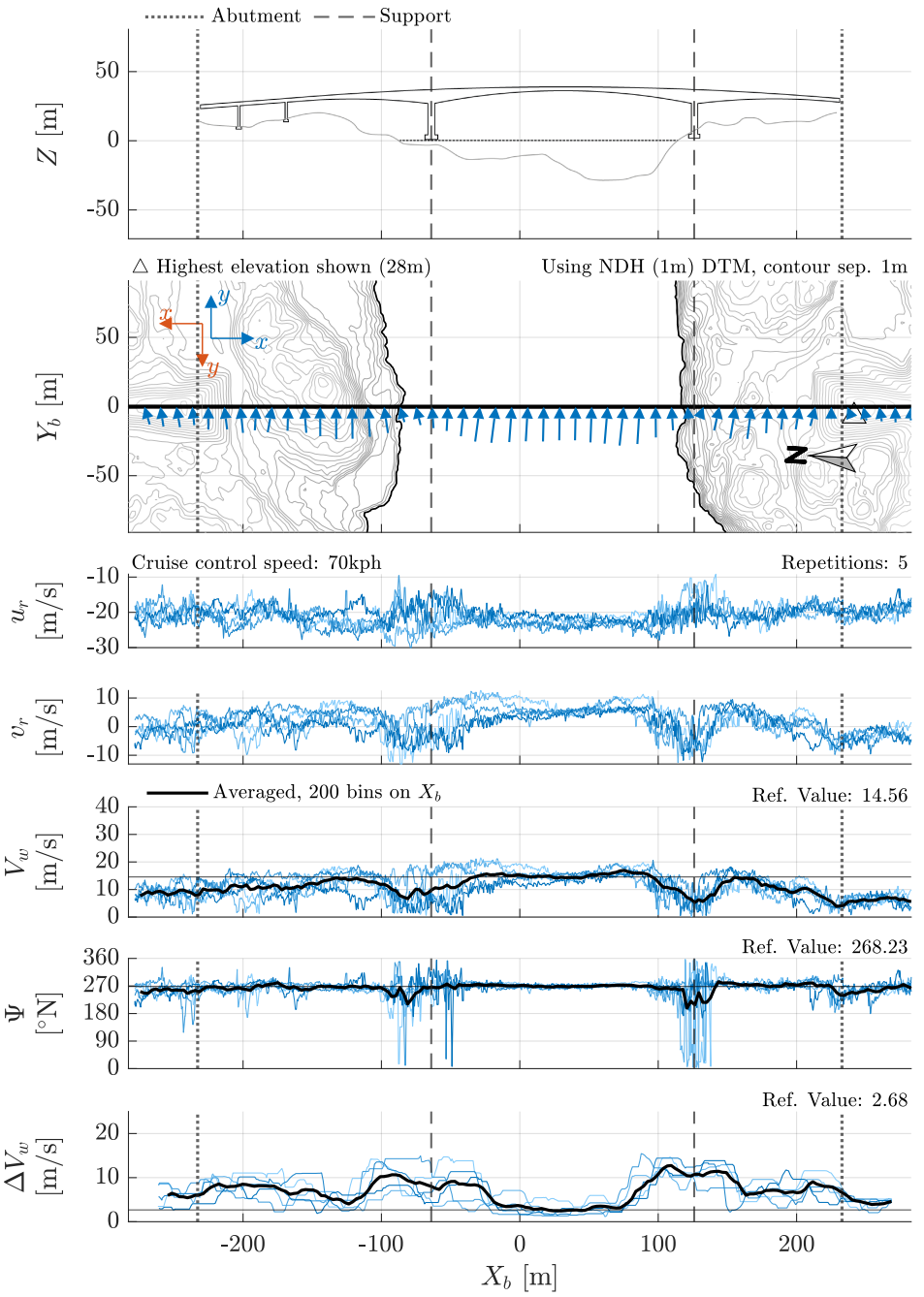

Figure 8.2: Wind profile, Dolmsund bridge, windward lane (vehicle travels left to right), see Section 8.3 for full explanation. ©Kartverket (terrain model & road shape)

u_r and v_r: raw wind in vehicle-fixed anemometer reference frame (see Figure 14.4 for explanation of r), V_w: in-plane wind magnitude in earth-fixed reference frame, Ψ: wind heading from North, ΔV_w: maximum change of V_w within sliding 45 m window

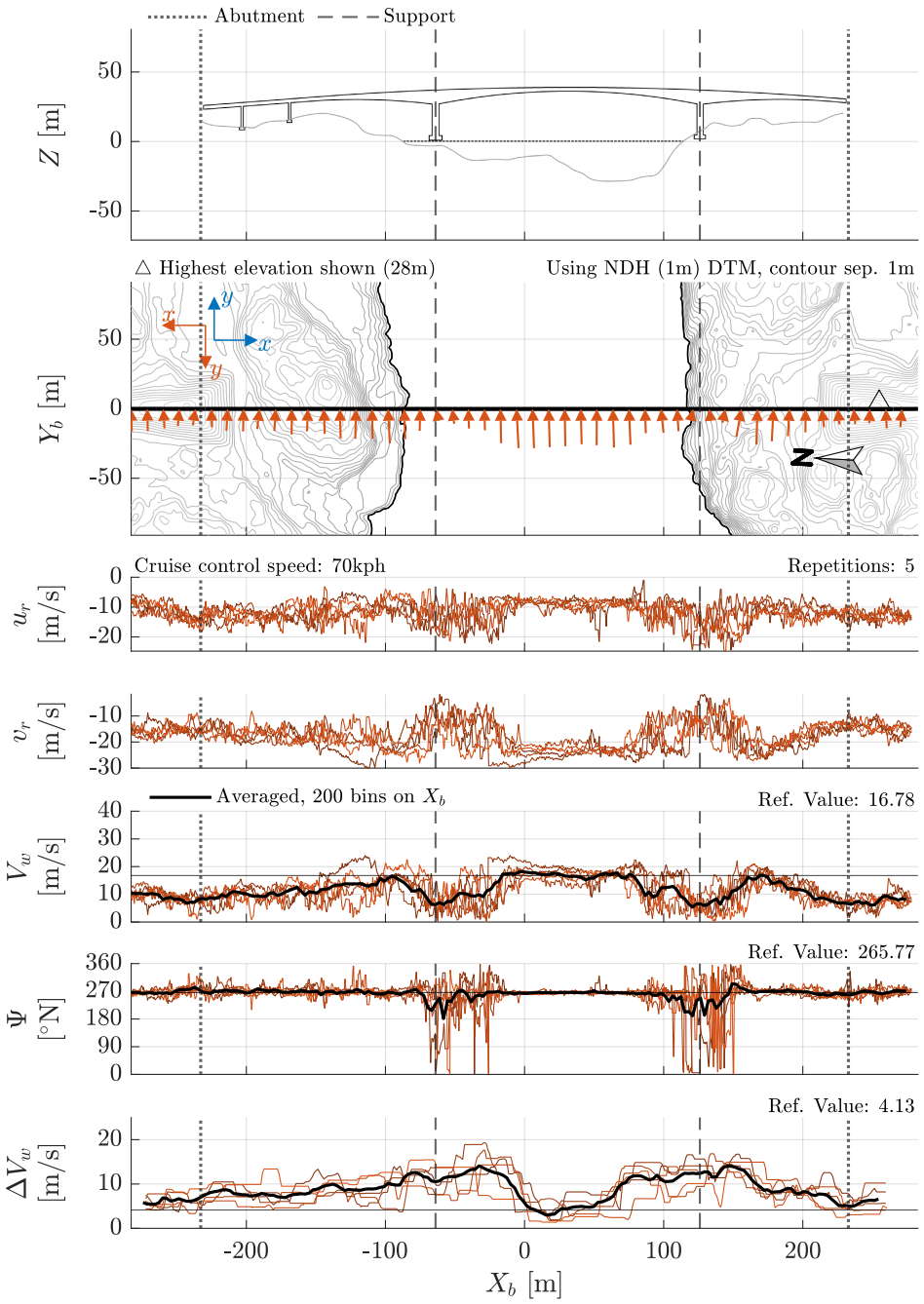

Figure 8.3: Wind profile, Dolmsund bridge, leeward lane (vehicle travels right to left), see Section 8.3 for full explanation. ©Kartverket (terrain model & road shape)

u_r and v_r: raw wind in vehicle-fixed anemometer reference frame (see Figure 14.4 for explanation of r), V_w: in-plane wind magnitude in earth-fixed reference frame, Ψ: wind heading from North, ΔV_w: maximum change of V_w within sliding 45 m window

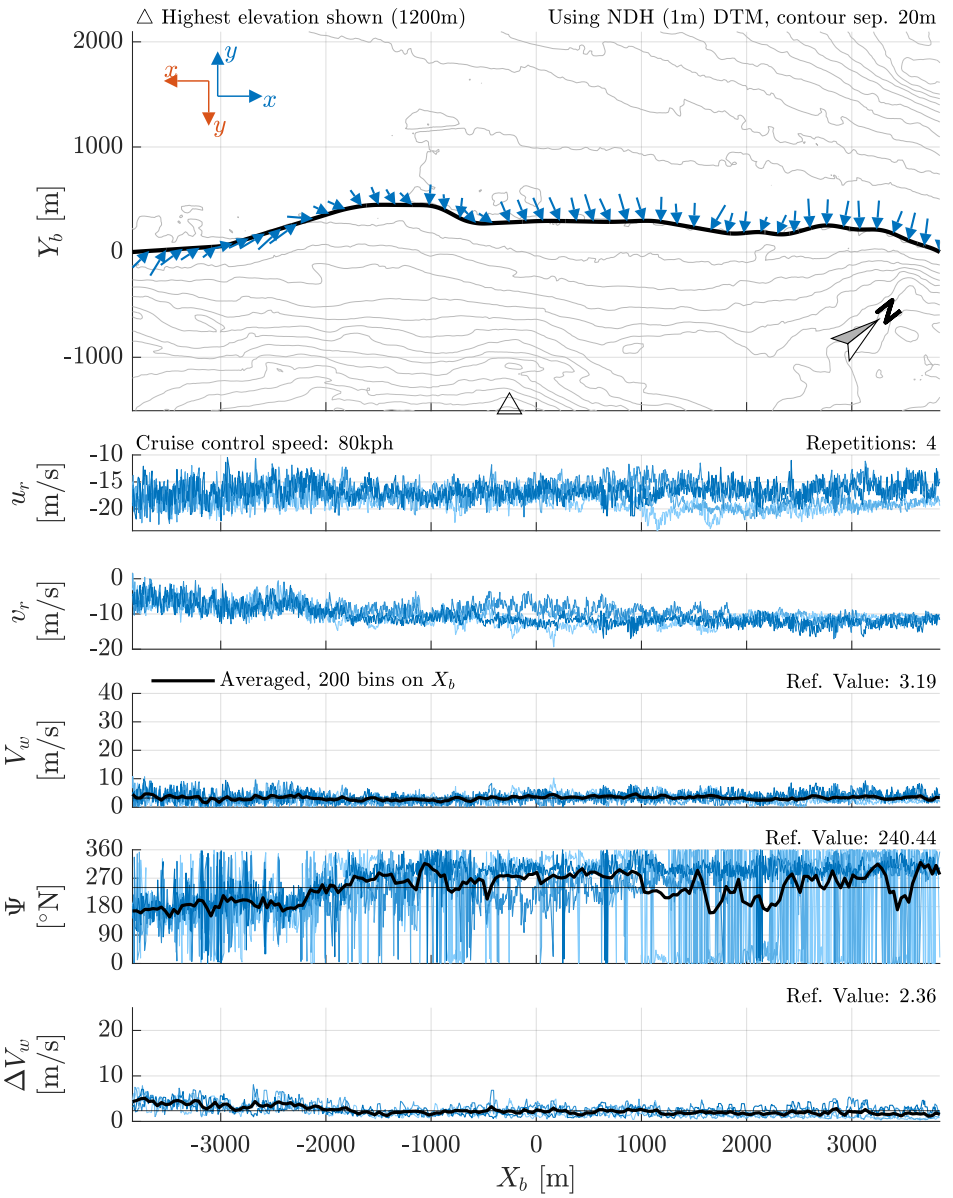

Figure 8.4: Wind profile, Dovre 1, windward lane (vehicle travels left to right), see Section 8.3 for full explanation. ©Kartverket (terrain model & road shape)

u_r and v_r: raw wind in vehicle-fixed anemometer reference frame (see Figure 14.4 for explanation of r), V_w: in-plane wind magnitude in earth-fixed reference frame, Ψ: wind heading from North, ΔV_w: maximum change of V_w within sliding 45 m window

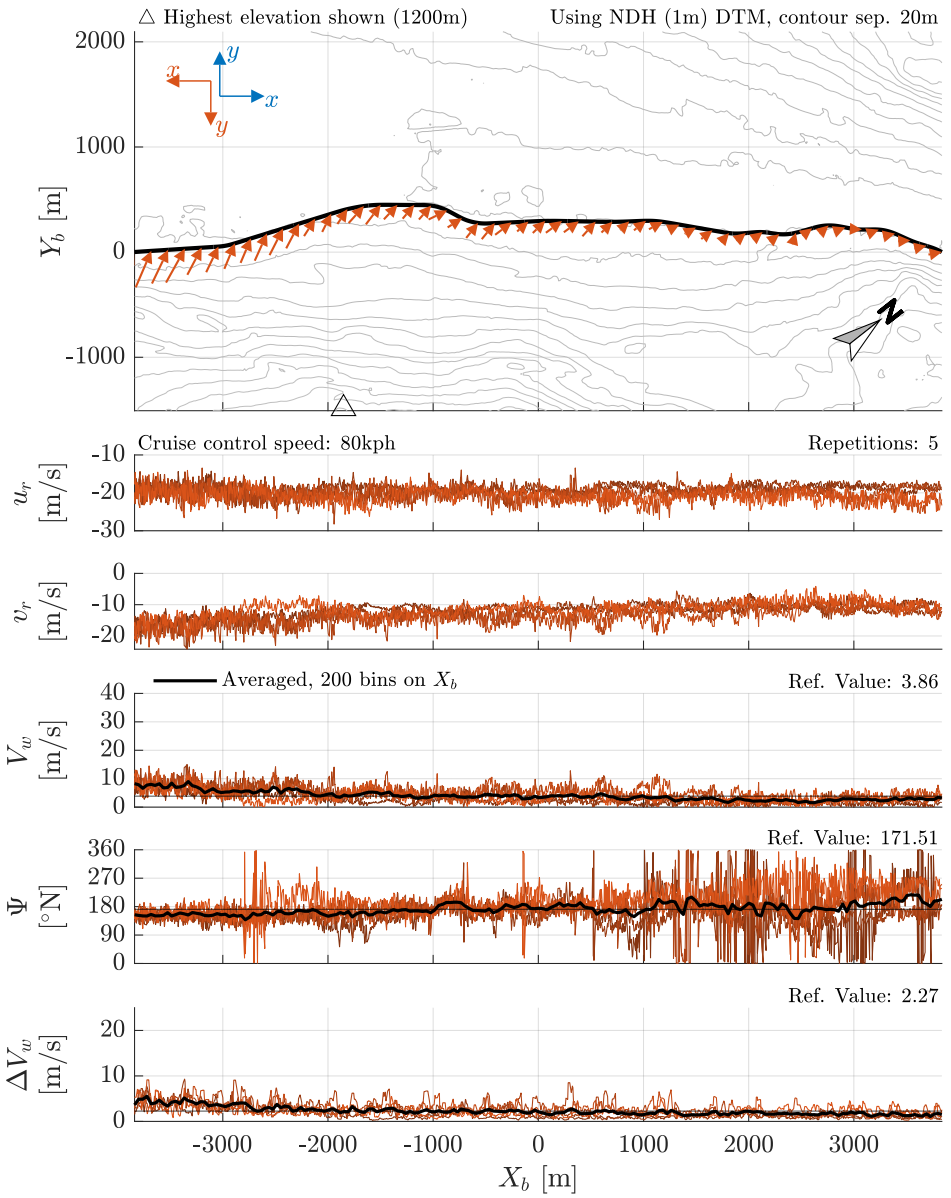

Figure 8.5: Wind profile, Dovre 1, leeward lane (vehicle travels right to left), see Section 8.3 for full explanation. ©Kartverket (terrain model & road shape)

u_r and v_r: raw wind in vehicle-fixed anemometer reference frame (see Figure 14.4 for explanation of r), V_w: in-plane wind magnitude in earth-fixed reference frame, Ψ: wind heading from North, ΔV_w: maximum change of V_w within sliding 45 m window

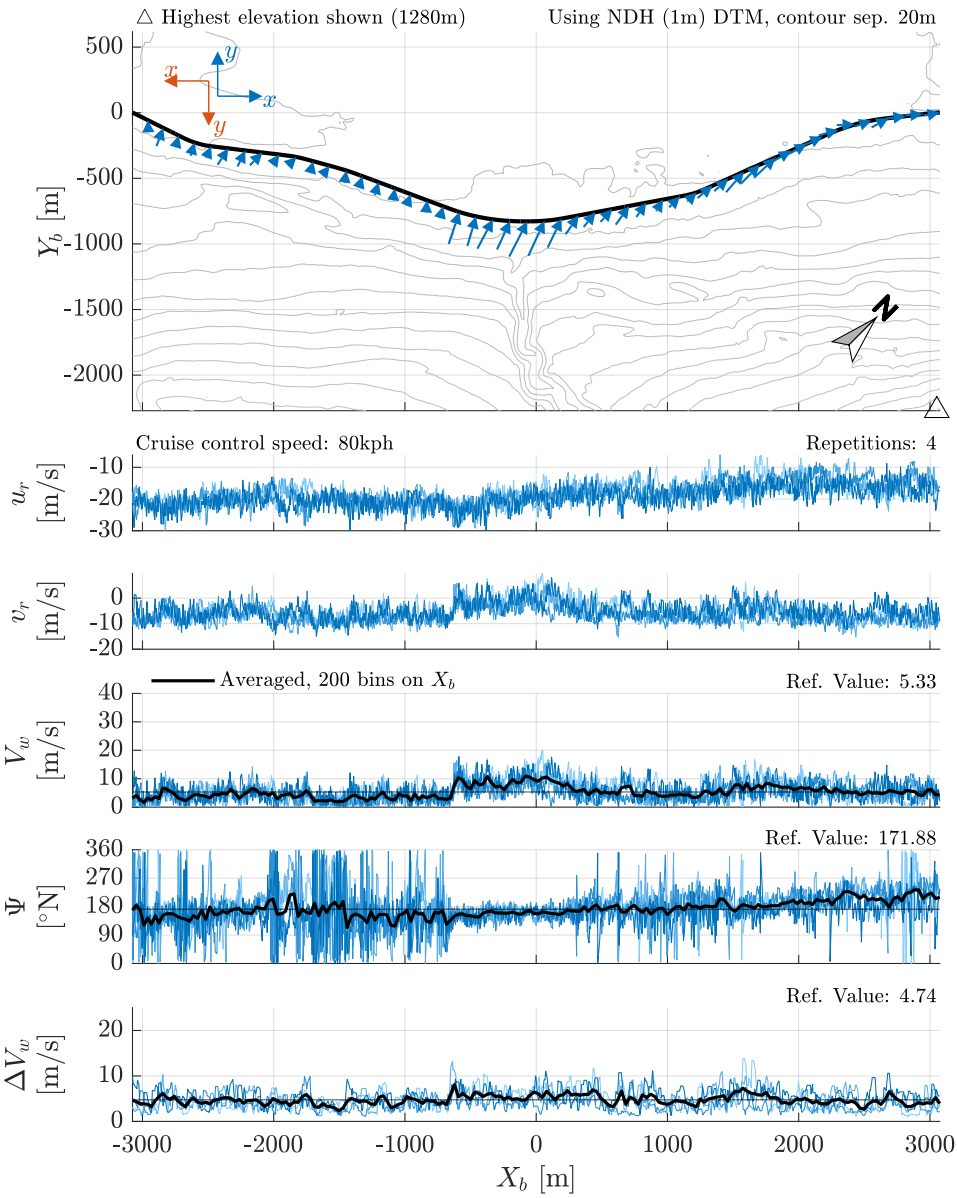

Figure 8.6: Wind profile, Dovre 2, windward lane (vehicle travels left to right), see Section 8.3 for full explanation. ©Kartverket (terrain model & road shape)

u_r and v_r: raw wind in vehicle-fixed anemometer reference frame (see Figure 14.4 for explanation of r), V_w: in-plane wind magnitude in earth-fixed reference frame, Ψ: wind heading from North, ΔV_w: maximum change of V_w within sliding 45 m window

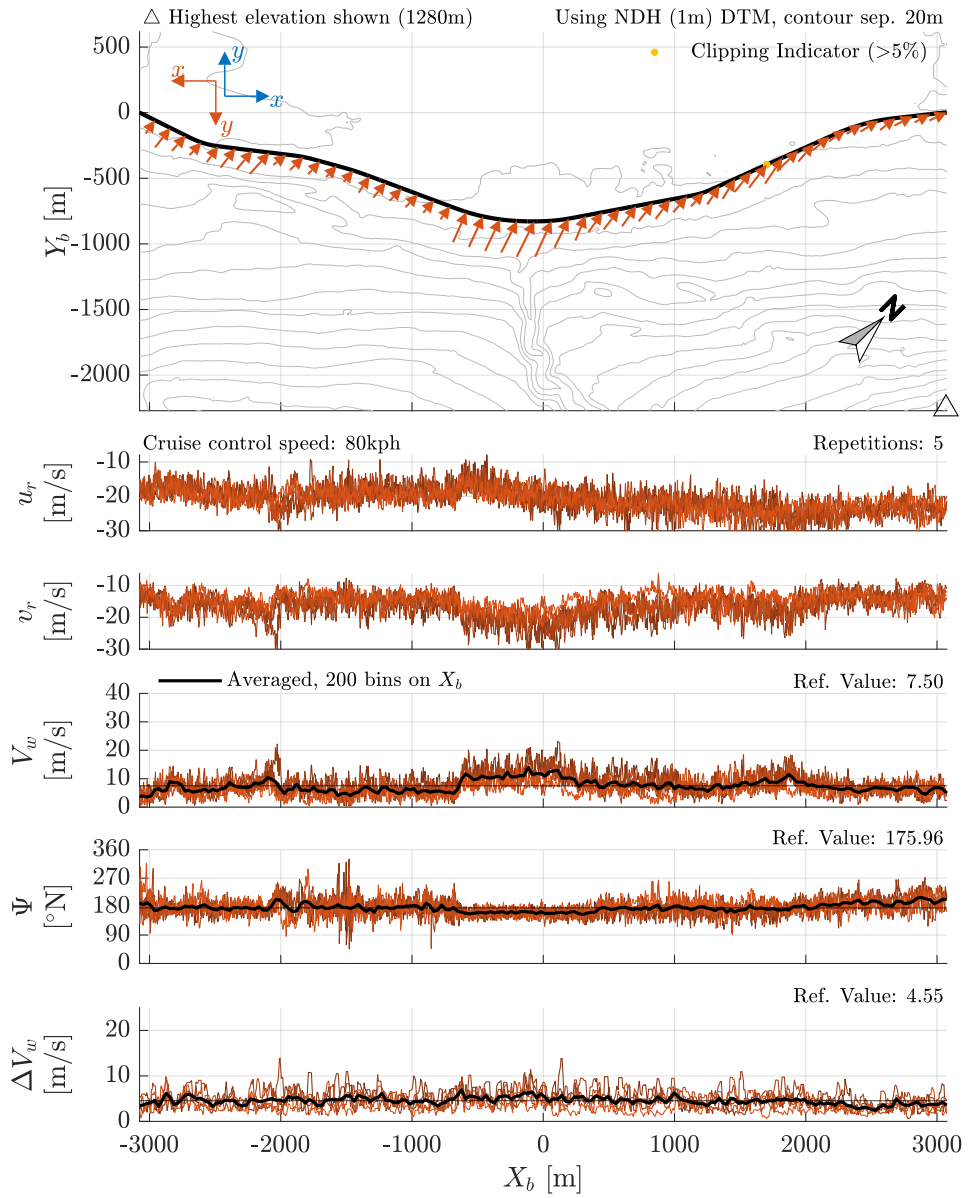

Figure 8.7: Wind profile, Dovre 2, leeward lane (vehicle travels right to left), see Section 8.3 for full explanation. ©Kartverket (terrain model & road shape)

u_r and v_r: raw wind in vehicle-fixed anemometer reference frame (see Figure 14.4 for explanation of r), V_w: in-plane wind magnitude in earth-fixed reference frame, Ψ: wind heading from North, ΔV_w: maximum change of V_w within sliding 45 m window

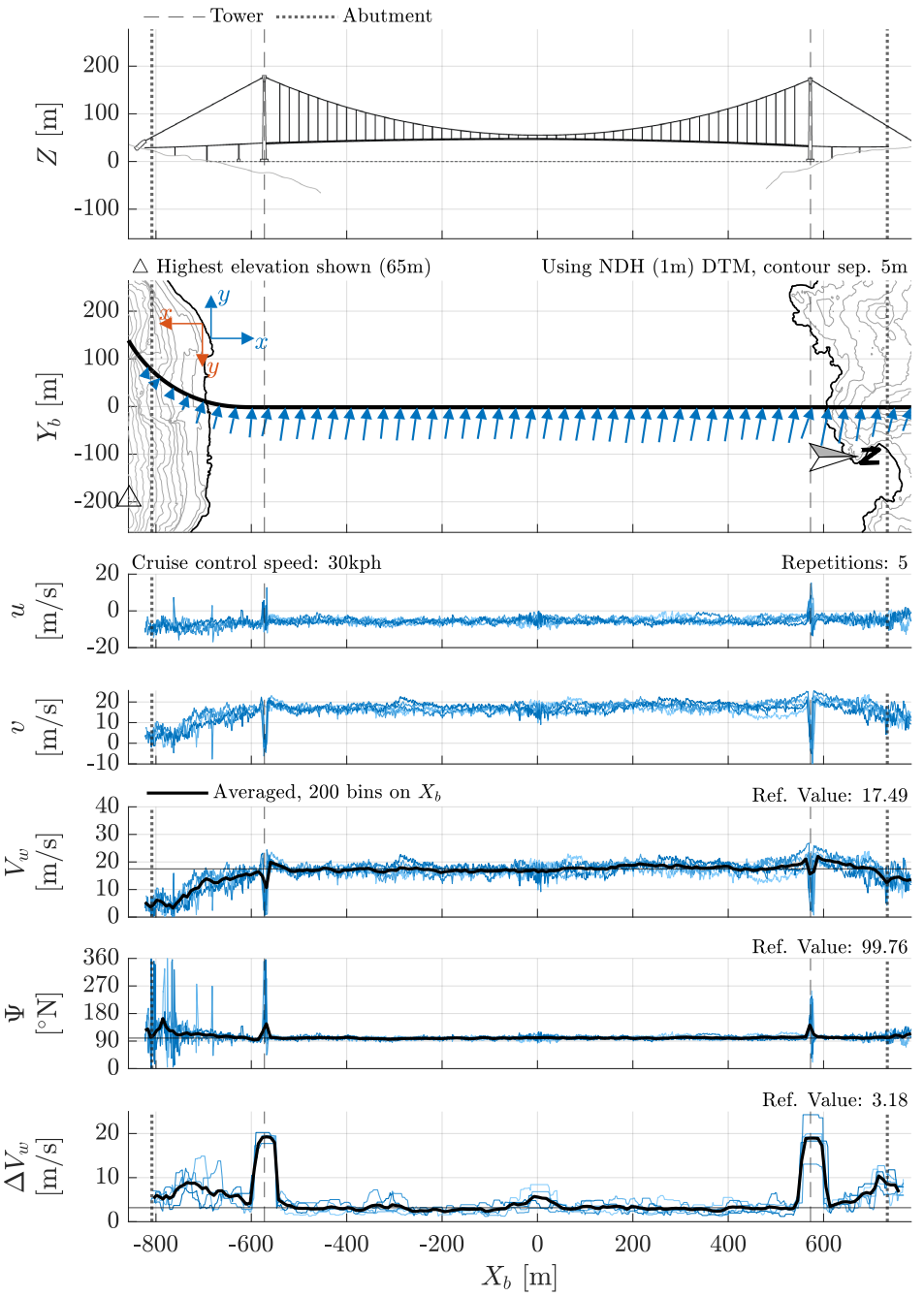

Figure 8.8: Wind profile, Hålogaland bridge, windward lane (vehicle travels left to right), see Section 8.3 for full explanation. ©Kartverket (terrain model & road shape)

u and v: raw wind in vehicle-fixed anemometer reference frame V_w: in-plane wind magnitude in earth-fixed reference frame, Ψ: wind heading from North, ΔV_w: maximum change of V_w within sliding 45 m window

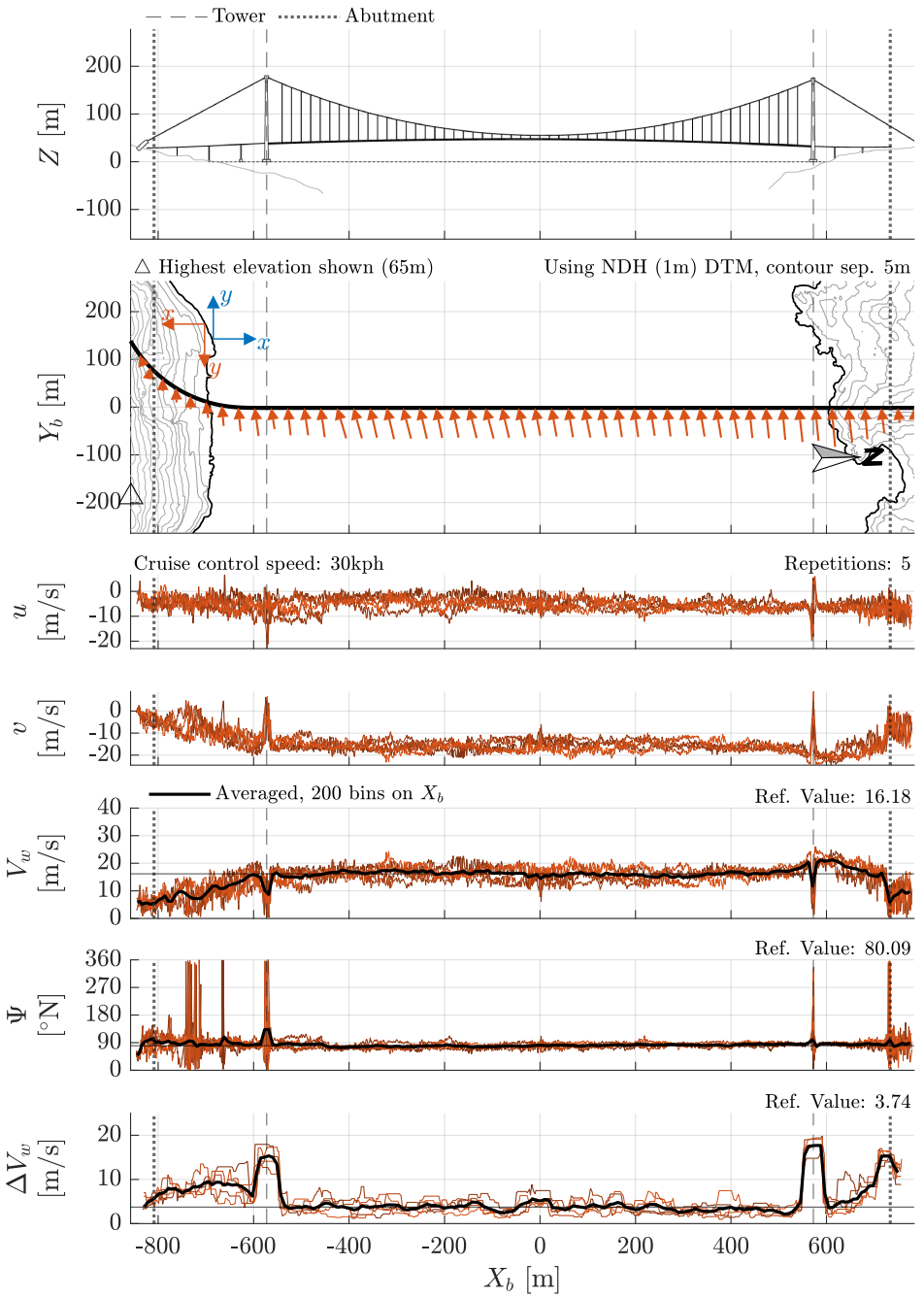

Figure 8.9: Wind profile, Hålogaland bridge, leeward lane (vehicle travels right to left), see Section 8.3 for full explanation. ©Kartverket (terrain model & road shape)

u and v: raw wind in vehicle-fixed anemometer reference frame V_w: in-plane wind magnitude in earth-fixed reference frame, Ψ: wind heading from North, ΔV_w: maximum change of V_w within sliding 45 m window

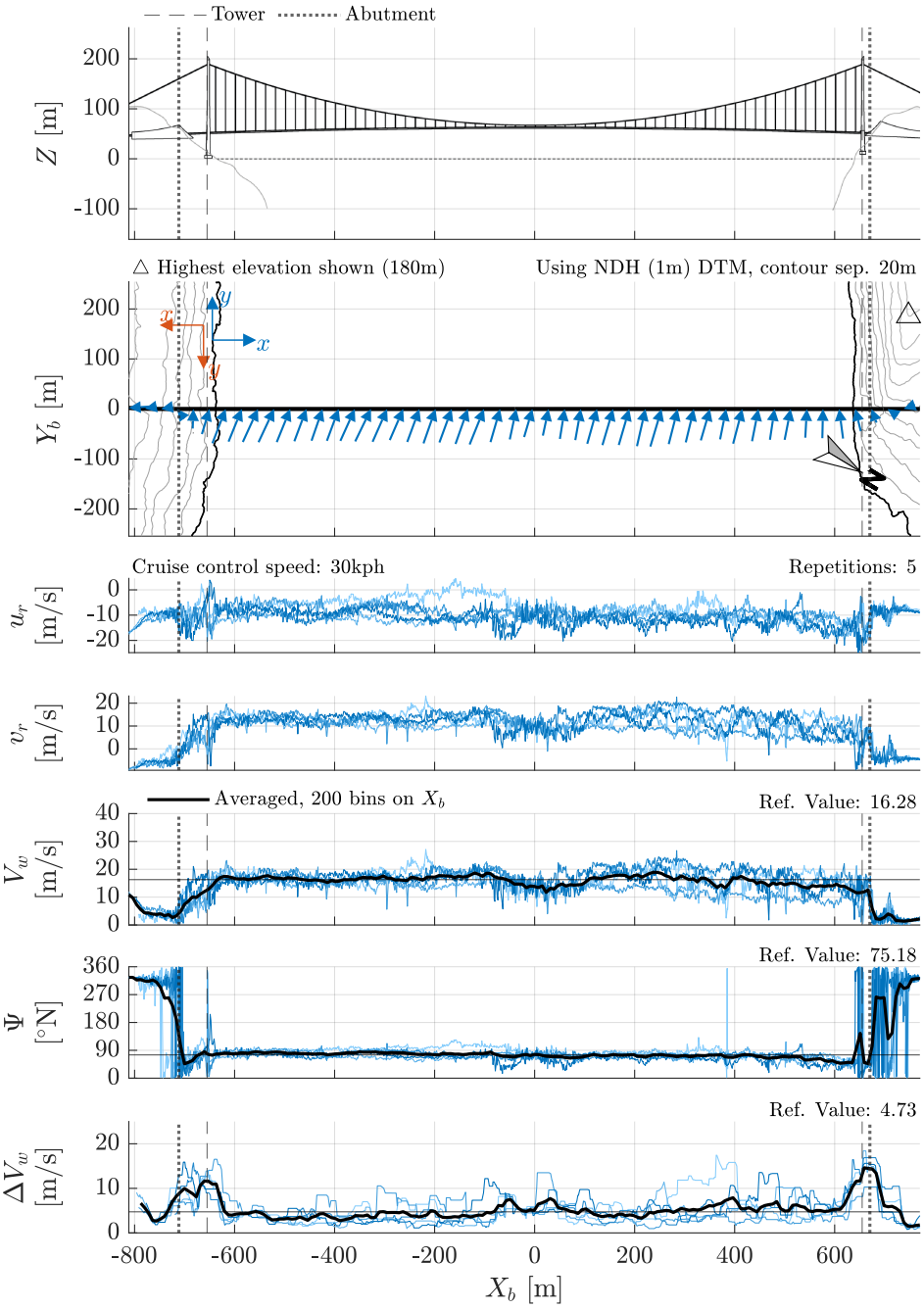

Figure 8.10: Wind profile, Hardanger bridge, windward lane (vehicle travels left to right), see Section 8.3 for full explanation. ©Kartverket (terrain model & road shape)

u_r and v_r: raw wind in vehicle-fixed anemometer reference frame (see Figure 14.4 for explanation of r), V_w: in-plane wind magnitude in earth-fixed reference frame, Ψ: wind heading from North, ΔV_w: maximum change of V_w within sliding 45 m window

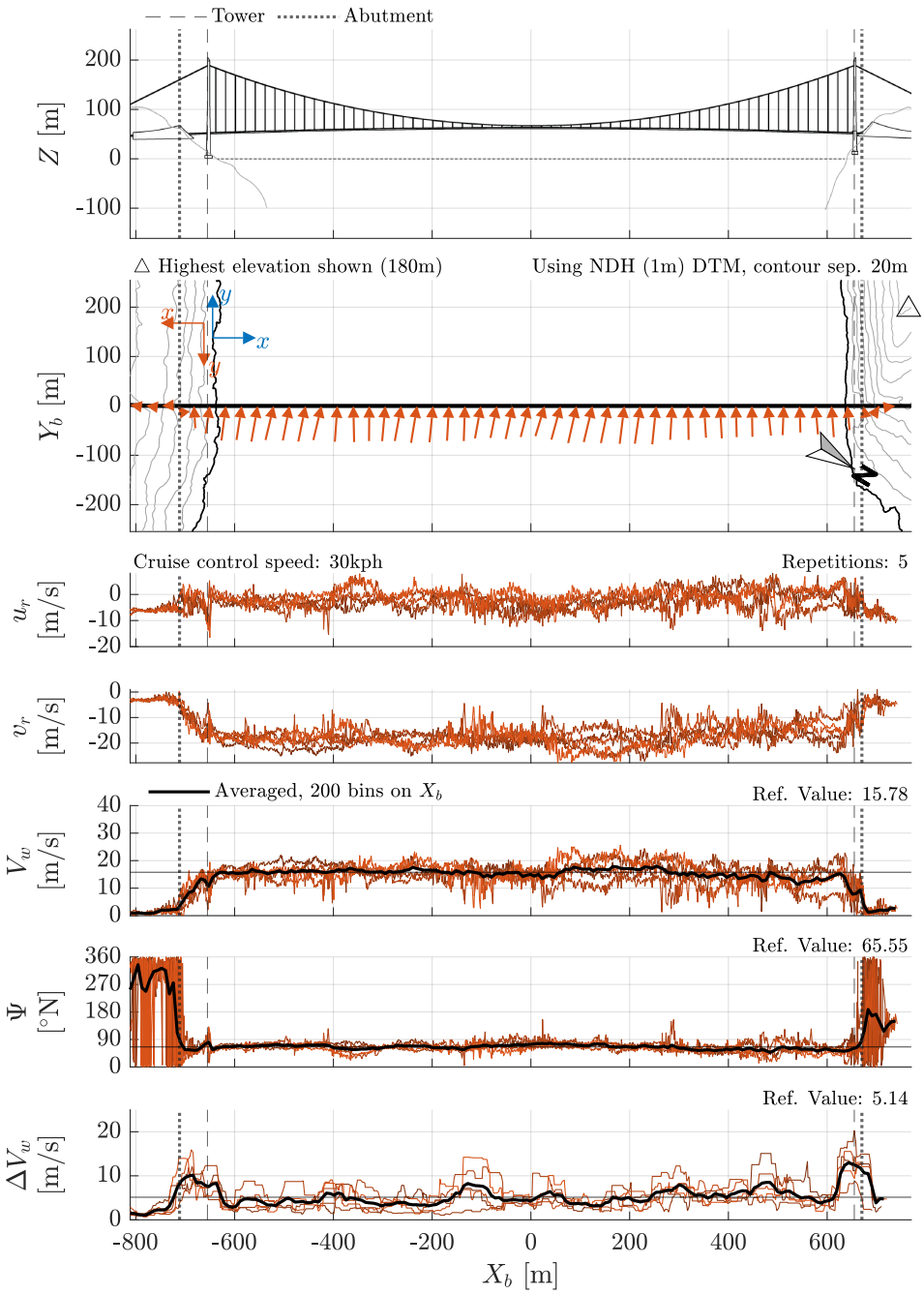

Figure 8.11: Wind profile, Hardanger bridge, leeward lane (vehicle travels right to left), see Section 8.3 for full explanation. ©Kartverket (terrain model & road shape)

u_r and v_r: raw wind in vehicle-fixed anemometer reference frame (see Figure 14.4 for explanation of r), V_w: in-plane wind magnitude in earth-fixed reference frame, Ψ: wind heading from North, ΔV_w: maximum change of V_w within sliding 45 m window

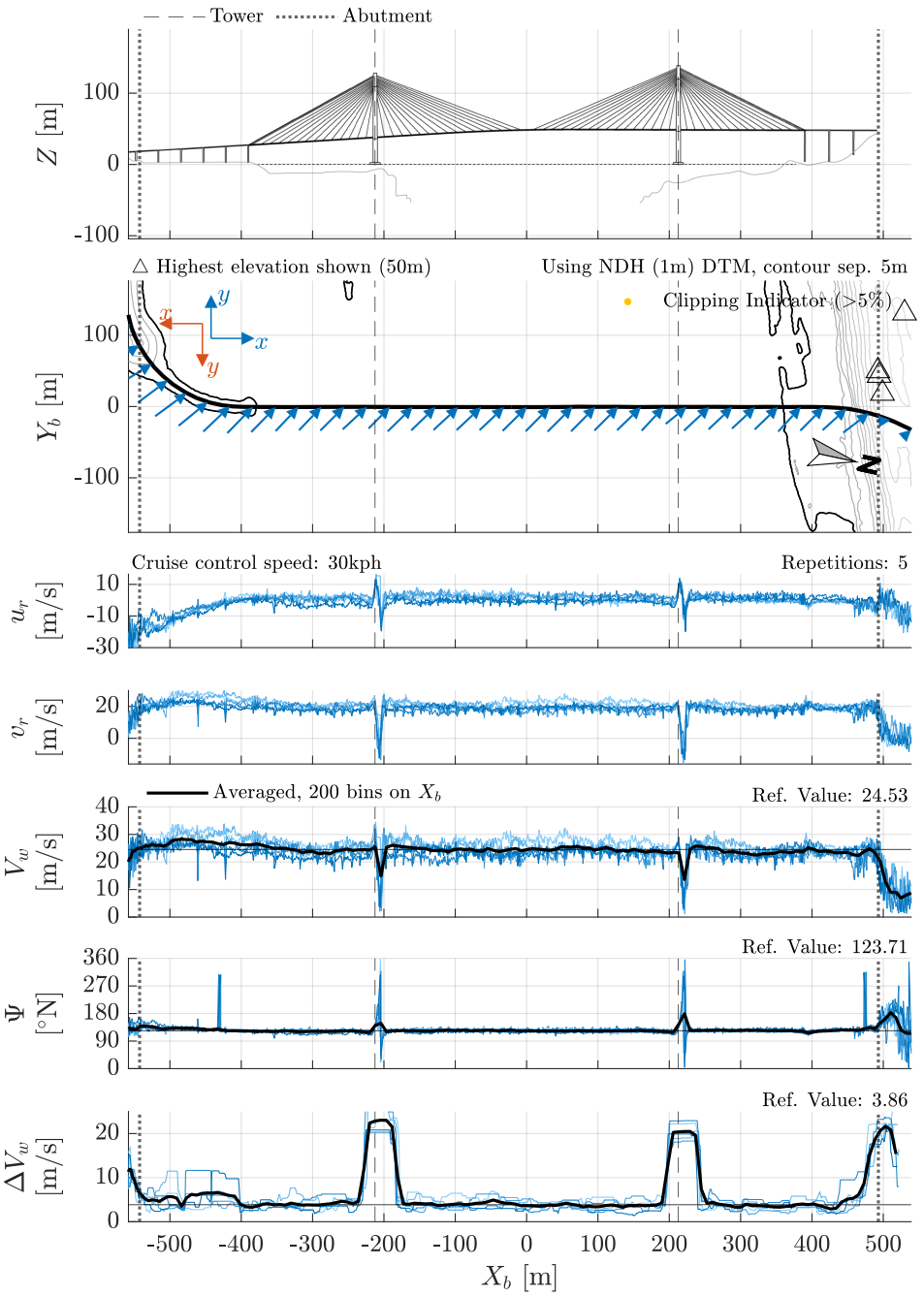

Figure 8.12: Wind profile, Helgeland bridge, windward lane (vehicle travels left to right), see Section 8.3 for full explanation. ©Kartverket (terrain model & road shape)

u_r and v_r: raw wind in vehicle-fixed anemometer reference frame (see Figure 14.4 for explanation of r), V_w: in-plane wind magnitude in earth-fixed reference frame, Ψ: wind heading from North, ΔV_w: maximum change of V_w within sliding 45 m window

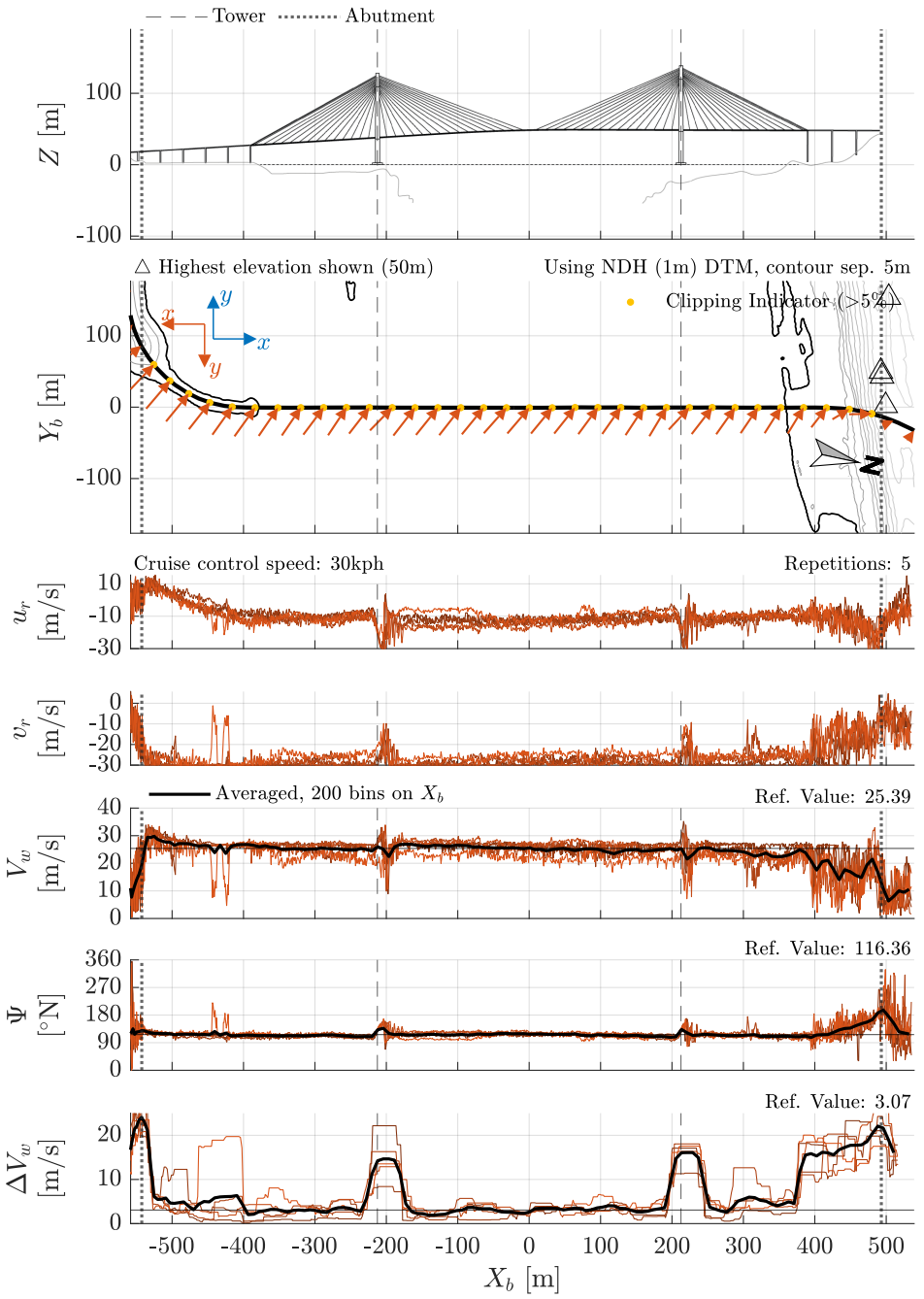

Figure 8.13: Wind profile, Helgeland bridge, leeward lane (vehicle travels right to left), see Section 8.3 for full explanation. ©Kartverket (terrain model & road shape)

u_r and v_r: raw wind in vehicle-fixed anemometer reference frame (see Figure 14.4 for explanation of r), V_w: in-plane wind magnitude in earth-fixed reference frame, Ψ: wind heading from North, ΔV_w: maximum change of V_w within sliding 45 m window

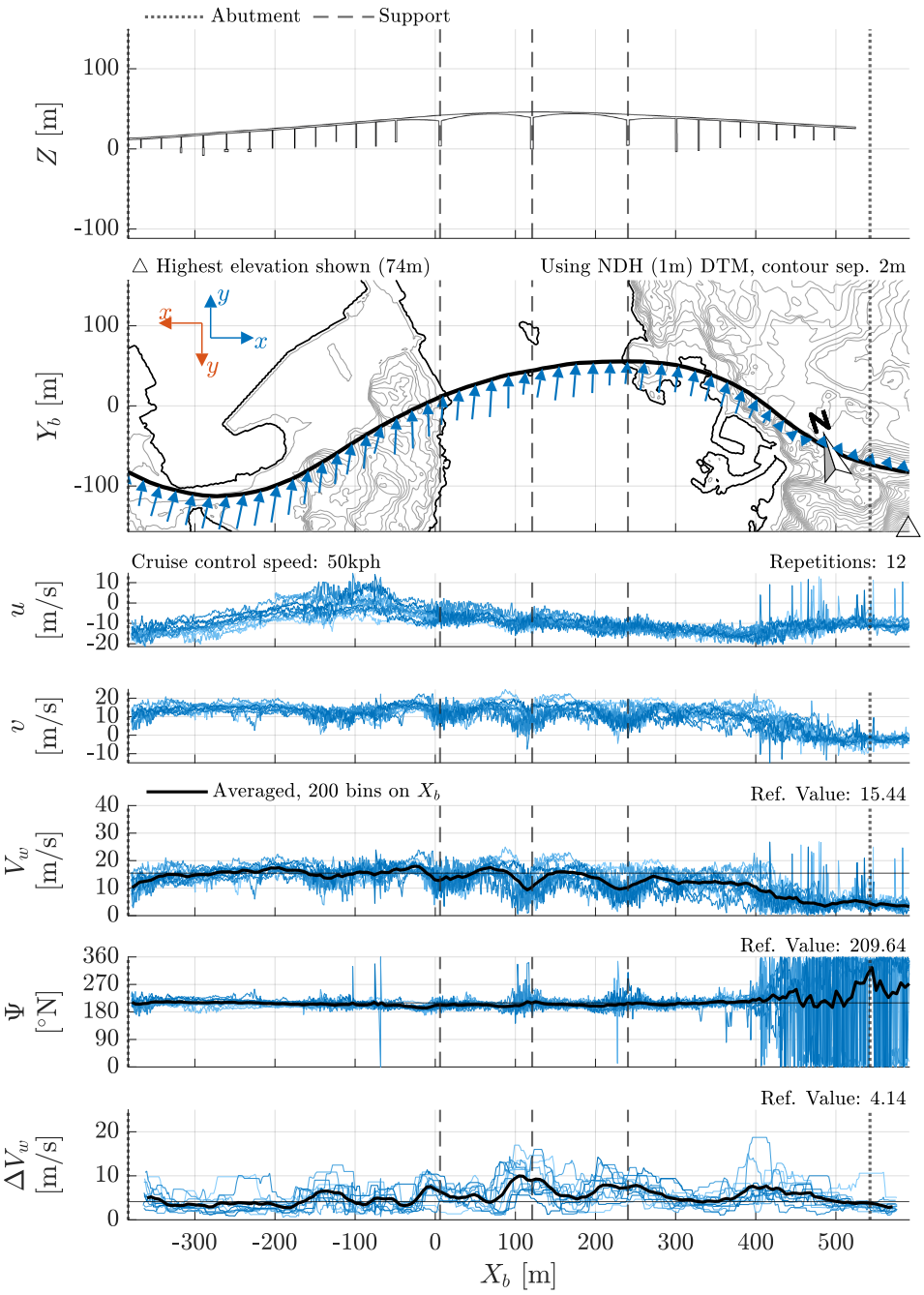

Figure 8.14: Wind profile, Måløy bridge, windward lane (vehicle travels left to right), see Section 8.3 for full explanation. ©Kartverket (terrain model & road shape)

u and v: raw wind in vehicle-fixed anemometer reference frame V_w: in-plane wind magnitude in earth-fixed reference frame, Ψ: wind heading from North, ΔV_w: maximum change of V_w within sliding 45 m window

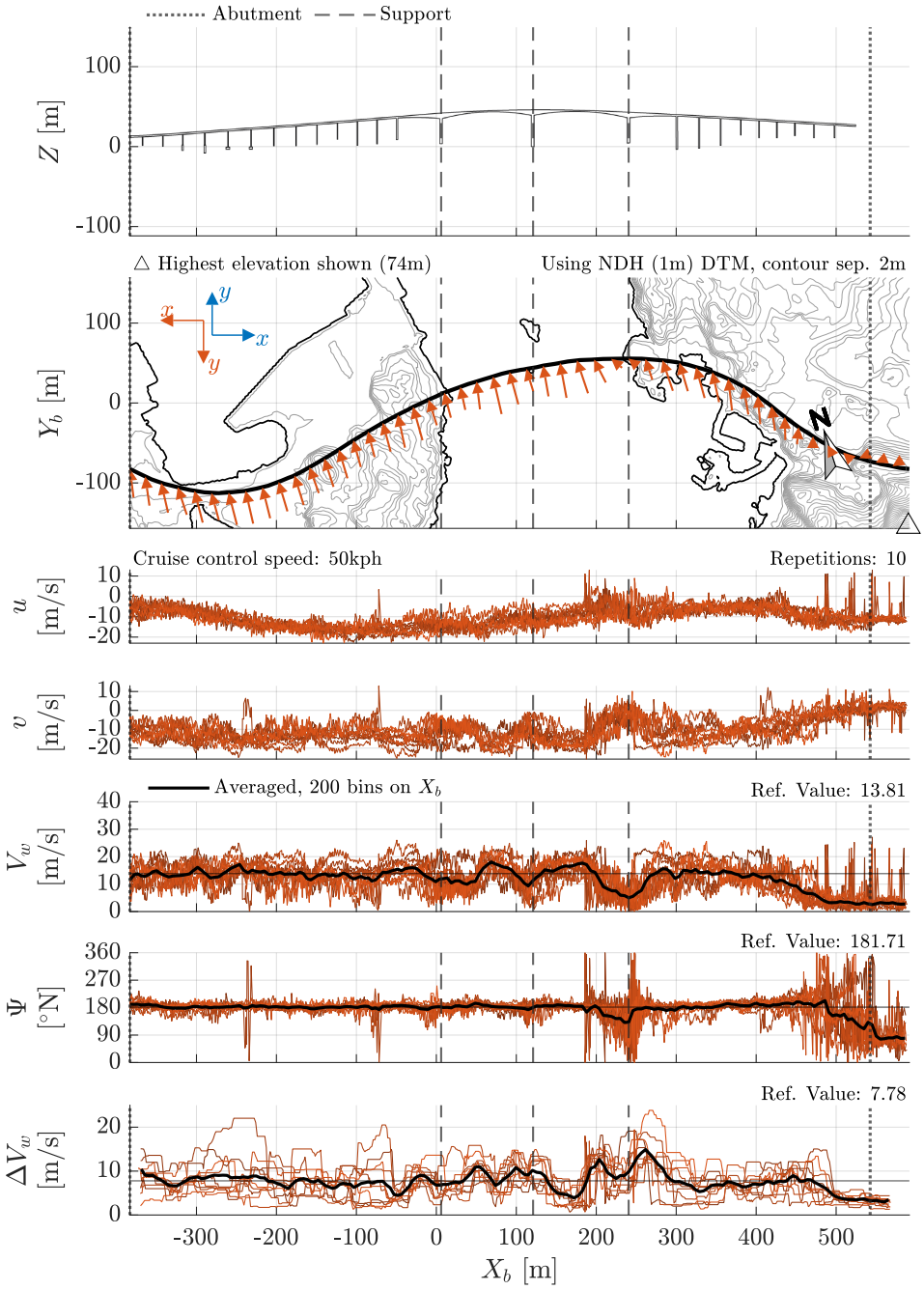

Figure 8.15: Wind profile, Måløy bridge, leeward lane (vehicle travels right to left), see Section 8.3 for full explanation. ©Kartverket (terrain model & road shape)

u and v: raw wind in vehicle-fixed anemometer reference frame V_w: in-plane wind magnitude in earth-fixed reference frame, Ψ: wind heading from North, ΔV_w: maximum change of V_w within sliding 45 m window

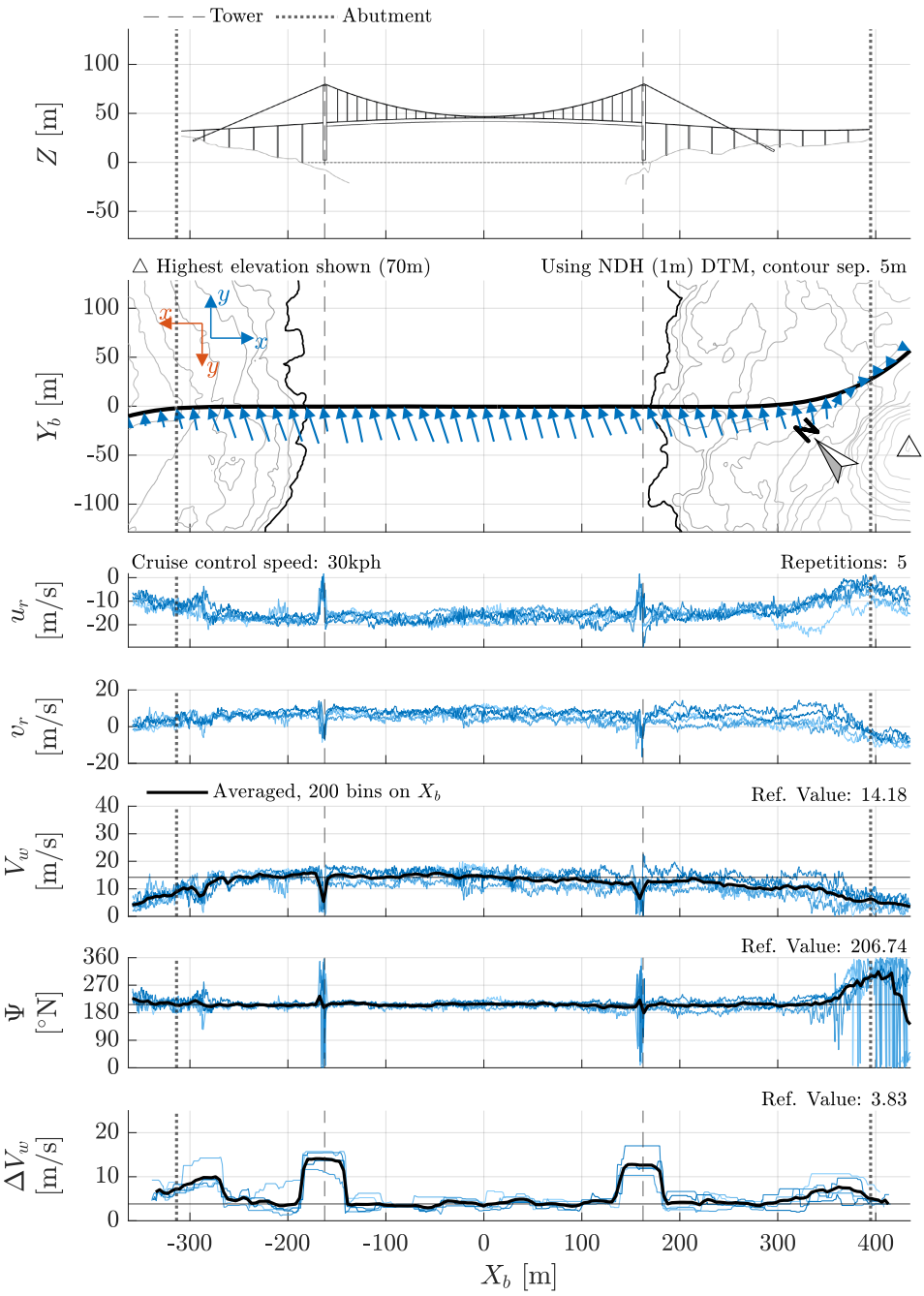

Figure 8.16: Wind profile, Nærøysund bridge, windward lane (vehicle travels left to right), see Section 8.3 for full explanation. ©Kartverket (terrain model & road shape)

u_r and v_r: raw wind in vehicle-fixed anemometer reference frame (see Figure 14.4 for explanation of r), V_w: in-plane wind magnitude in earth-fixed reference frame, Ψ: wind heading from North, ΔV_w: maximum change of V_w within sliding 45 m window

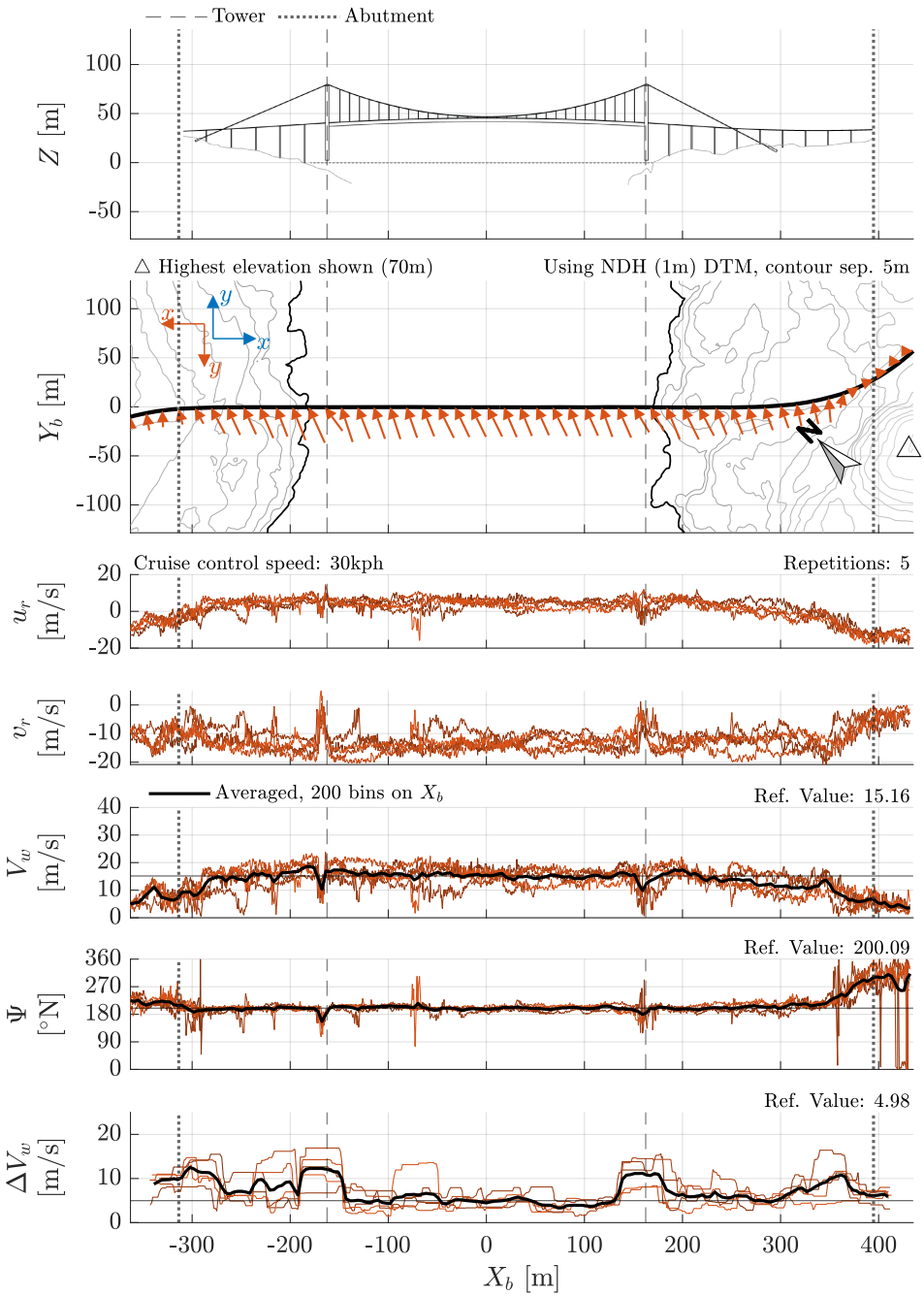

Figure 8.17: Wind profile, Nærøysund bridge, leeward lane (vehicle travels right to left), see Section 8.3 for full explanation. ©Kartverket (terrain model & road shape)

u_r and v_r: raw wind in vehicle-fixed anemometer reference frame (see Figure 14.4 for explanation of r), V_w: in-plane wind magnitude in earth-fixed reference frame, Ψ: wind heading from North, ΔV_w: maximum change of V_w within sliding 45 m window

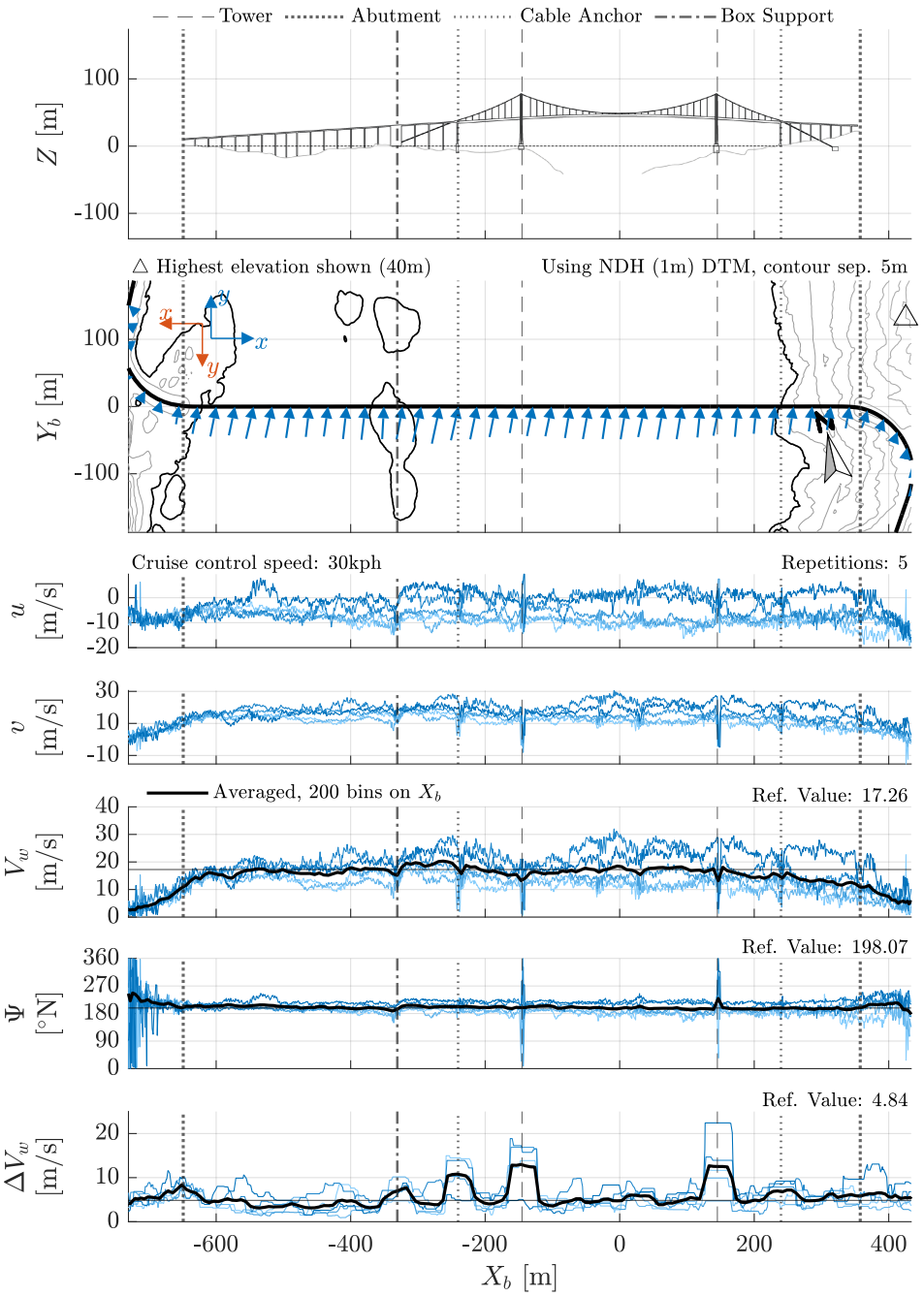

Figure 8.18: Wind profile, Tjeldsund bridge 1, windward lane (vehicle travels left to right), see Section 8.3 for full explanation. ©Kartverket (terrain model & road shape)

u and v: raw wind in vehicle-fixed anemometer reference frame V_w: in-plane wind magnitude in earth-fixed reference frame, Ψ: wind heading from North, ΔV_w: maximum change of V_w within sliding 45 m window

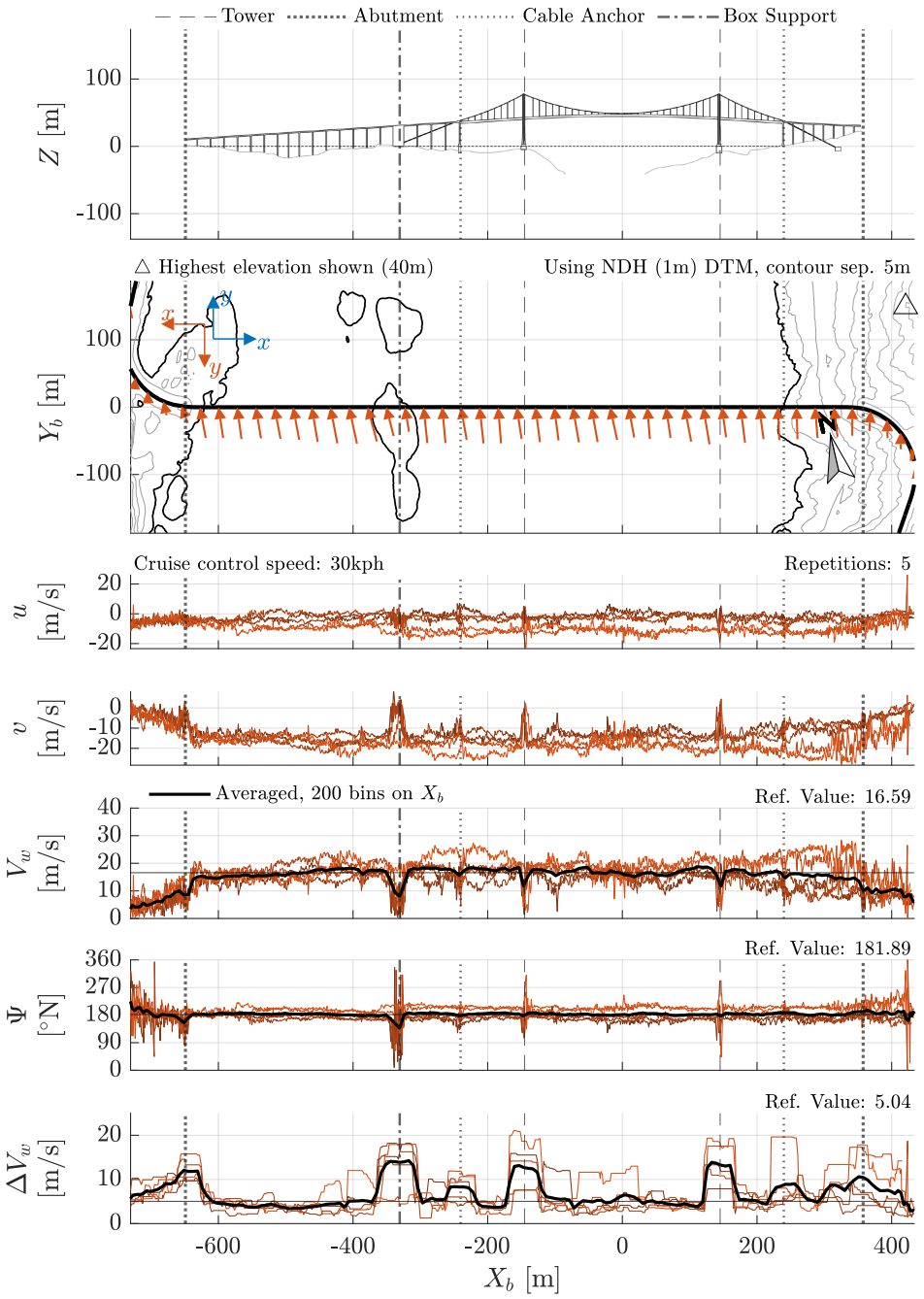

Figure 8.19: Wind profile, Tjeldsund bridge 1, leeward lane (vehicle travels right to left), see Section 8.3 for full explanation. ©Kartverket (terrain model & road shape)

u and v: raw wind in vehicle-fixed anemometer reference frame V_w: in-plane wind magnitude in earth-fixed reference frame, Ψ: wind heading from North, ΔV_w: maximum change of V_w within sliding 45 m window

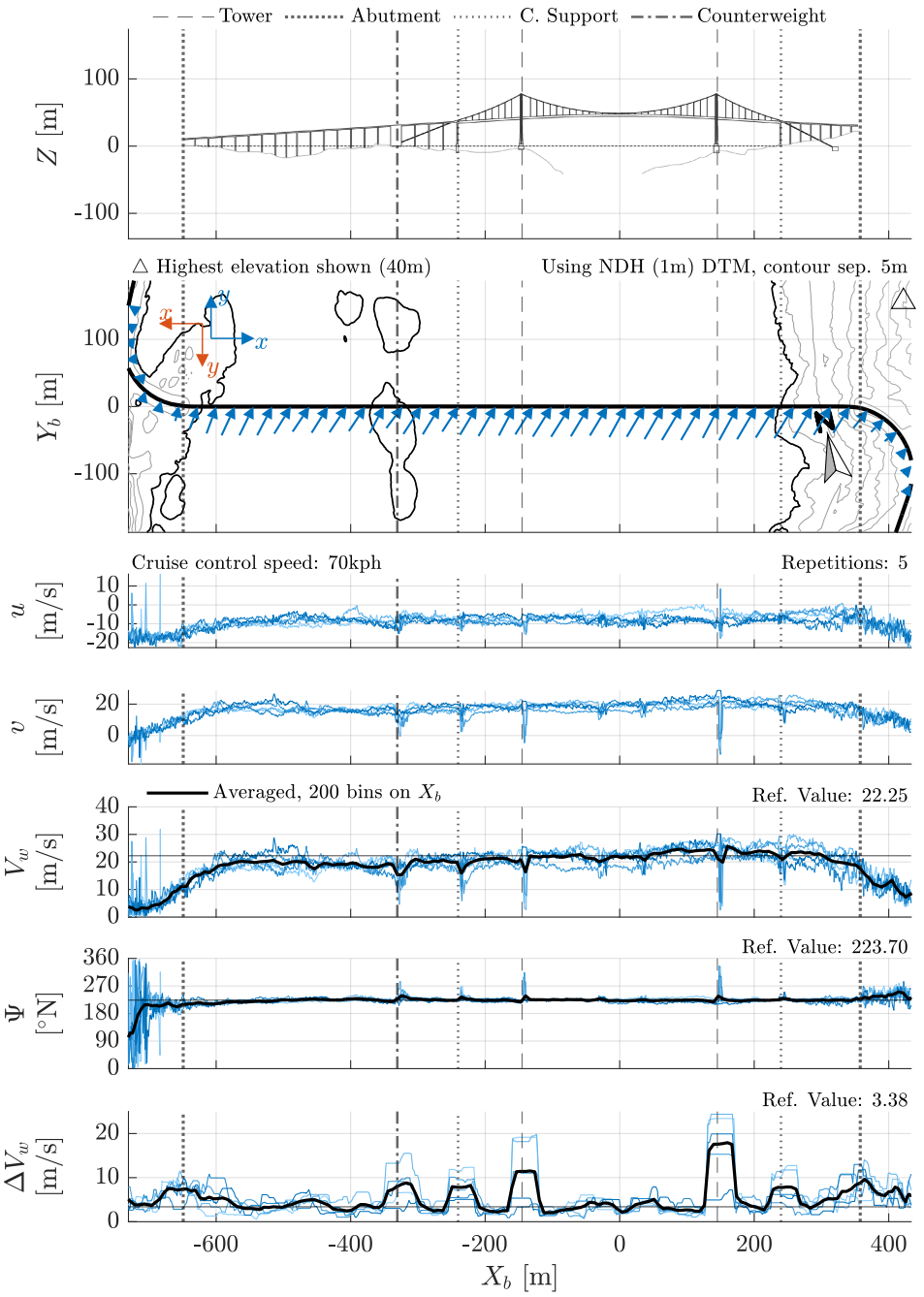

Figure 8.20: Wind profile, Tjeldsund bridge 2, windward lane (vehicle travels left to right), see Section 8.3 for full explanation. ©Kartverket (terrain model & road shape)

u and v: raw wind in vehicle-fixed anemometer reference frame V_w: in-plane wind magnitude in earth-fixed reference frame, Ψ: wind heading from North, ΔV_w: maximum change of V_w within sliding 45 m window

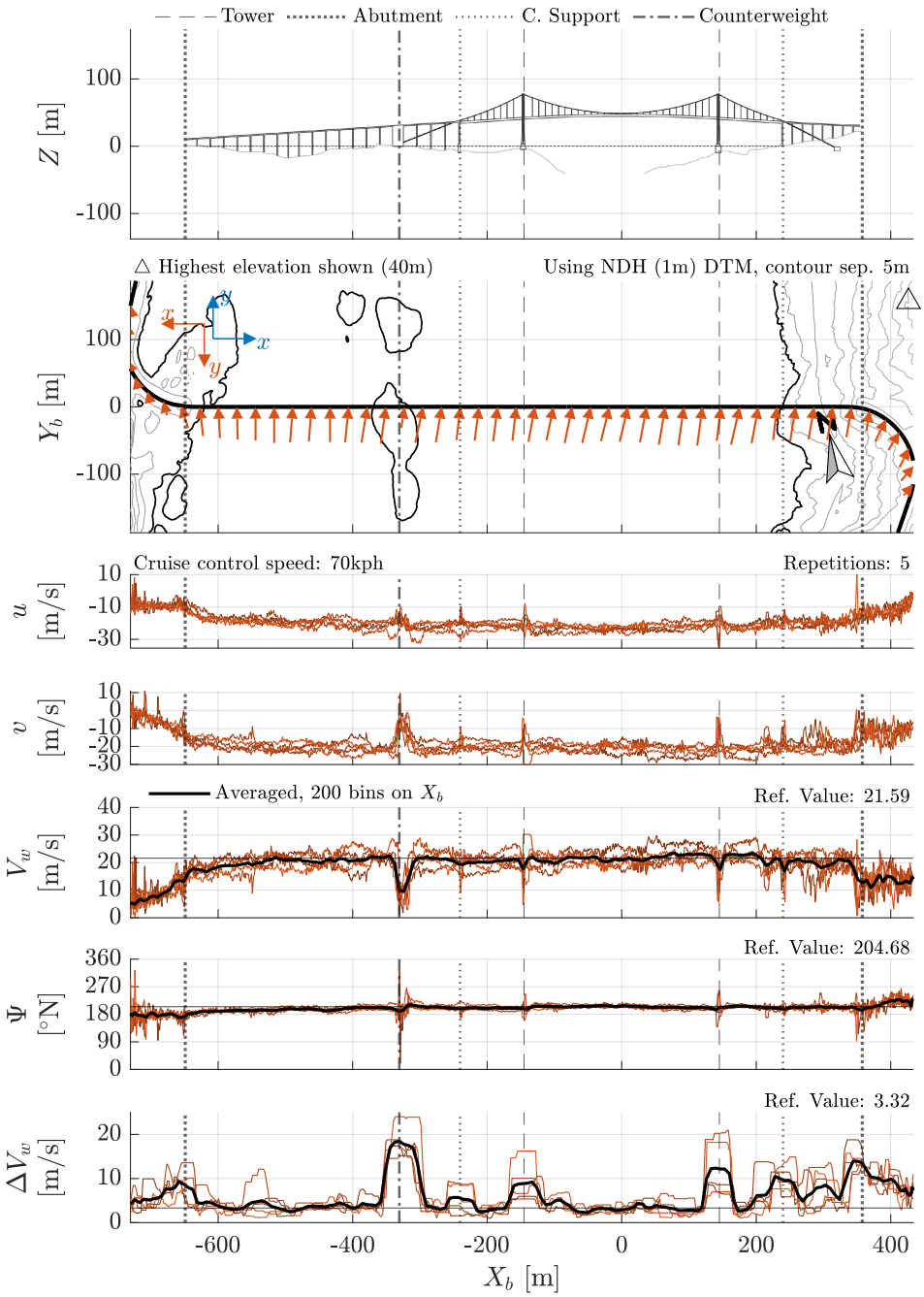

Figure 8.21: Wind profile, Tjeldsund bridge 2, leeward lane (vehicle travels right to left), see Section 8.3 for full explanation. ©Kartverket (terrain model & road shape)

u and v: raw wind in vehicle-fixed anemometer reference frame V_w: in-plane wind magnitude in earth-fixed reference frame, Ψ: wind heading from North, ΔV_w: maximum change of V_w within sliding 45 m window

Map orientation

In these plots, the map on X-Y has been rotated to align with the dominating direction of the road. For the case of suspension and cable-stayed bridges, X_b is aligned to the line connecting the centre-point of the two towers, for example in Figure 8.8. For other bridges and fixed-base roads, the abutments or manually defined endpoints are used for alignment like in Figure 8.2 or 8.4.

Bridge sketches

For each bridge, engineering drawings [185–189, 202, 203] have been used to approximately sketch the profile as would be seen by a viewer looking at the bridge in the positive Y_b direction. For example the Helgeland bridge in Figure 8.12. This corresponds to looking along the predominant wind direction into the page (approximately).

The positioning and scaling of the sketches on the X_b-Z plane has been performed manually and small discrepancies are to be expected. Every effort has been made to relate the features of the sketch to those on the map (for example the intersection between terrain lines and mean sea level or points of curvature) to ensure as accurate a scaling and alignment as possible.

Note that there appears to be a larger discrepancy with the sketch of the Måløy bridge at the eastern end (see Figure 8.14 and 8.15). A projection error due to the curvature of the bridge appears to be the cause. The discussion of the results at this bridge will be centred around the three large supports at the middle of the bridge. Their locations on the sketch relative to the map and line plots has been carefully considered and are believed to be accurate.

Topography

The highest elevations shown by the contours on each map are indicated with an upwards pointing triangle and the elevation at each point in metres is given to the top left of the relevant map. For an example see Figure 8.8. Note that the triangle is placed at a random location along the highest contour. If multiple contours exist at the highest level, then all of them will be marked. See for example Figure 8.12 and 8.13. The separation between the contours in metres elevation is given to the top right. A north arrow is plotted on top of the map in the bottom right corner of the axes.

Line plots

Following the map axes, the upper two line plots show the raw wind measurements as recorded directly from the anemometer. For the earlier data sets, this means u_r

and v_r are plotted (see for example Figure 8.2), where the r indicates that the anemometer was mounted with an angular offset to the x' axis of the vehicle. See Figure 14.4 for reference.

For the more recent data sets, the wind magnitude and direction is output by the anemometer rather than individual components. This data has been translated into the two components u and v aligned with the x' and y' axes of the vehicle. An example can be seen at the Hålogaland bridge in Figures 8.8 and 8.9. The raw wind measurements are provided for traceability and can be used to support any conclusions drawn using the transformed estimates in the Earth-fixed reference frame.

The transformed wind is plotted on the next two axes, with the wind magnitude V_w (in-plane components only) followed by the heading Ψ of the wind in degrees North. This heading follows the convention in meteorology of giving the direction from which the wind originates.

Feature identification, gust amplitude

A simple quantifier is sought to identify and characterise features of the wind that are relevant to safety and comfort. A gust factor is often used in meteorology [156] and typically gives the peak moving-mean wind speed – typically of the order of seconds (e.g. 2 s [156]) – as a proportion of a reference wind speed – typically defined as the mean wind speed over a period of minutes (e.g. 10 min [156]).

The vehicle and driver will be sensitive not only to sudden peak values in wind speed, but also sudden decreases in wind speed, like the inverse gusts created by towers. The maximum change in wind speed within a given temporal window ΔV_w will be used here to identify features that can be uncomfortable and/or make controlling the vehicle more difficult. Brandt et al. [32] found a statistical link between this windowed amplitude-of-change value and what drivers perceived to be instability events. The amplitude-of-change of the wind speed will also be referred to as the gust amplitude in this work.

Schaible [170] concluded that drivers can reduce vehicle motion when disturbed by crosswind gusts in the range $\sim$ 0-0.5 Hz, whereas they amplify the motion in the range $\sim$ 0.5-2 Hz. Above this range the driver has no influence on the vehicle motion. This gives a critical range of time scales of 0.25-2 s. See Chapter 2 for a more complete explanation. Recall also that Sims-Williams [178] gives a range of reduced frequencies $k_f = 0.05$-0.5 for which road vehicles are most sensitive to crosswind gusts.

For the test vehicle ($l_b = 6.8$ m) travelling at 80 kph, the reduced frequency range can be translated into an absolute frequency range:

$$f = \frac{k_f U}{l_b} = \frac{k_f \times 80/3.6}{6.8}, \tag{8.1}$$

giving a range of $f = 0.16$-1.63 Hz for $k_f = 0.05$-0.5. This range overlaps with the range in which drivers are known to amplify wind-induced vehicle response.

Data processing

Theissen [196] filters all his results with a 0.2-second moving mean to remove higher frequency content and the same choice is made here. Content up to 2 Hz will not be significantly attenuated (~ -2.4 dB at 2 Hz).

Two seconds is chosen as the window size for ΔV_w, a round number corresponding to half a wavelength at 0.25 Hz. This will be the relevant value at the speed limit of 80 kph. Assuming flow structures to be *frozen* – something that is valid for features relating to the bridge geometry – the window size can be adjusted to ensure relevant features are captured at slower speeds.

The 2-second value at 80 kph corresponds to a spatial scale of 45 m from which new windows sizes can be proposed for different driving speeds. Table 8.1 shows the window size used for each driving speed represented in the results. The signals will be labelled ΔV_w. This is plotted on the last set of axes in Figures 8.2 through 8.21.

Table 8.1: An overview of window sizes.

Driving speed [kph]	Window size [s]
30	5
50	3
70	2
75	2

Vector visualisation

To make interpretation easier, the wind vectors as they would be observed by a stationary observer are plotted on the map. The vectors show an average of all data (from all repetitions) and are normalised by the largest magnitude vector. The averaging is per bin, where 50 bins have been defined, equally spaced along the road axis. The same averaging procedure is performed to give the *averaged* line on the line plots, this time using 200 bins. See the map in Figure 8.2 for an example.

Lane and direction of travel

The two x-y reference axes (red and blue) in the top left corner of each map in Figures 8.2 through 8.21 indicate the direction of travel of the vehicle and the

offset of the associated lane from the road centreline (see Figure 8.2 for example). The data has been segmented per lane/direction of travel and plotted per lane in separate figures (for example Figure 8.10 is paired with 8.11), with the colour of the lines matching the colour of the relevant reference axes. The blue colour is reserved for the windward lane while the red colour is used for the leeward. The origin of the axes in the corner are offset relative to each other to show that the direction of travel is associated with a lane and a corresponding offset from the road's centreline. Right-hand traffic is practised in Norway.

Note that a slight variation in the shade of the red and blue colours has been used such that individual repetitions/signals can be distinguished more easily in the line plots (see Figure 8.2 for example).

The orientation of the map has been selected such that the driving direction in the windward lane is always left to right on the page. Therefore, for example, the blue colour indicates: (1) travel from left to right on the page, (2) that the vehicle is in the windward lane and (3) that this lane is between the road centreline and the bottom of the page. Consequently, the wind is always blowing predominantly in the positive Y_b direction, or in the upwards direction on the page.

Driving speed

The data plotted in the wind profiles are collected at each respective measurement location at one given cruise control speed. Where repetitions were performed at multiple cruise control speeds, the lowest available speed is chosen to maximise the statistical significance of the data. The cruise control speed is given above the top left corner of the uppermost line plot. See Figure 8.2 for an example. Note that the true driving speed deviates from cruise control speed. The cruise control speed is only used to categorise the data sets.

Clipping

For some of the earlier data sets, the settings on the WindMaster were chosen incorrectly. The wind components u_r and v_r as described in Figure 14.4 were limited to 30 m/s. Some of the data presented in the wind profile plots are therefore subject to clipping.

This is indicated by a yellow dot at the tip of the wind field vectors on the map. If more than 5% of the data in the bin was clipped, then the yellow dot is plotted. The data in the leeward lane at Helgeland (Figure 8.13) is particularly affected.

Axis limits

The vertical axis limits for the bottom three line plots are the same fixed values across all figures. This is done with the intention of making comparisons between

data sets easier and to avoid potential misinterpretations.

Reference values

For comparisons, it will be useful to have reference values for the wind's speed, direction and gust amplitude. The wind on the main span of the bridge is typically fairly uniform and covers a significant portion of the total bridge length. The wind here is typically also the least disturbed (locally) by the surrounding topography. For each bridge, a symmetric interval (given that the origin is defined at the mid-point between the two towers) of the main span is used to give reference values of V_w, Ψ and ΔV_w.

The reference values are plotted as horizontal lines on the relevant line plots in Figures 8.2 through 8.21. An overview of the mean wind vectors in each lane on each bridge is given in Table 8.2.

In the table, U_{ref} is the wind velocity along the bridge axis (the component of the wind speed V_w along X_b, see Figure 1.8 for reference) and is positive from left to right on the page with reference to Figures 8.2 through 8.21. Note that this is the wind speed that would be measured by a stationary observer. V_{ref} is the cross-component of the wind; positive towards the top of the page. The subscripts 1 and 2 denote the windward and leeward lanes respectively such that,

$$U_{\text{ref}} = \frac{U_{\text{ref,1}} + U_{\text{ref,1}}}{2}, \tag{8.2}$$

and the half the difference between the two is denoted $\Delta U_{\text{ref,1-2}}/2$. A positive value therefore indicates that $U_{\text{ref,1}}$ is more positive than $U_{\text{ref,2}}$. Finally, the magnitude of the in-plane wind vector is given as $V_{w,\text{ref}}$. The angle ϕ_{ref} is then,

$$\phi_{\text{ref}} = \tan^{-1}(V_{\text{ref}}/U_{\text{ref}}), \tag{8.3}$$

and gives the angle of the reference flow to the bridge axis. Zero degrees corresponds to flow along the bridge axis in the positive direction (left to right).

8.4 A discussion of local flow features

The results shown in the following plots provide a series of insights into the quality of the data and the utility of the test vehicle as a wind profiler. Most importantly, the results demonstrate the clear and significant effects of certain features of bridge geometry and terrain on the characteristics of the wind field in each lane on the road. The towers have a strong shielding effect and were found to have a significant impact on perceived handling stability. The tower wake will be studied in more detail in Chapters 11 and 13. The discussion here starts with some comments on the vehicle's influence on the wind measurements.

Table 8.2: Mean wind vectors over the main span of each bridge.

Bridge	V_{cr} [kph]	$U_{\text{ref, 1}}$ [m/s]	$U_{\text{ref, 2}}$ [m/s]	U_{ref} [m/s]	$\Delta U_{\text{ref,1-2}}/2$ [m/s]	...
Dolmsund	70	0.29	-0.38	-0.04	0.33	
Hålogaland	30	2.64	-3.16	-0.26	2.90	
Hardanger	30	4.66	1.77	3.22	1.45	
Helgeland	*30*	*17.51*	*15.75*	*16.63*	*0.88*	
Måløy	*50*	*2.59*	*-3.74*	*-0.57*	*3.16*	
Nærøysund	30	-4.05	-6.02	-5.04	0.99	
Tjeldsund	30	2.80	-2.60	0.10	2.70	
Tjeldsund	70	11.31	4.33	7.82	3.49	

...	$V_{\text{ref, 1}}$ [m/s]	$V_{\text{ref, 2}}$ [m/s]	$\Delta V_{\text{ref,1-2}}/2$ [m/s]	V_{ref} [m/s]	$V_{w,\text{ ref}}$ [m/s]	ϕ [°]
	14.50	16.74	-1.12	15.62	15.62	90.16
	17.24	15.74	0.75	16.49	16.49	90.91
	15.21	15.33	-0.06	15.27	15.60	78.11
	17.08	*19.70*	*-1.31*	*18.39*	*24.79*	*47.88*
	14.34	*13.09*	*0.63*	*13.71*	*13.72*	*92.39*
	13.47	13.74	-0.14	13.61	14.51	110.31
	16.32	15.48	0.42	15.90	15.90	89.64
	19.08	21.06	-0.99	20.07	21.54	68.71

8.4.1 The vehicle's forward pressure wave

As expected, the vehicle's forward pressure wave has an effect on the wind measurements. The anemometer would have to be placed far ahead of the front grill in order to avoid this (as in [220]). For the current experiments, the required support structure was deemed too impractical, as explained in Chapter 6. The effect is observable at multiple test locations.

At Dolmsund (Figures 8.2 & 8.3), Hålogaland (Figures 8.8 & 8.9), Hardanger (Figures 8.10 & 8.11), Måløy (Figures 8.14 & 8.15), Nærøysund (Figures 8.16 & 8.17), Tjeldsund 1 (Figures 8.18 & 8.19) and 2 (Figures 8.20 & 8.21) it is clear to see on the map axes that the vectors in the leeward lane (red) point slightly more to the left than those in the windward (blue). This is consistent across the majority of each bridge span. This is believed to be due to the pressure wave in front of the vehicle *pushing* the air forward in the driving direction.

The values of $\Delta U_{\text{ref,1-2}}/2$ in Table 8.2 (introduced in Section 8.3) are an attempt to quantify the scale of this effect. Assuming the effect is equivalent in the two driving directions, then it is expected that the average between the two lanes gives the true component of the wind along the bridge axis U_{ref} and half the difference between lanes/directions to give the magnitude added by the pressure wave in each respective driving direction.

Note that there was significant clipping at Helgeland and that the Måløy bridge is not straight. The same values of $\Delta U_{\text{ref,1-2}}/2$ (as found at other locations) are not expected. To highlight these results they are italicised in the table. The $\Delta U_{\text{ref,1-2}}/2$ value is consistently positive with a mean (ignoring the results from Helgeland and Måløy) of 1.98 m/s and a standard deviation of 1.13 m/s. The pressure wave therefore adds roughly 1-3 m/s to the measurements in the driving direction of the vehicle. This is kept in mind when interpreting the wind profiles, particularly at low wind speeds.

The mean value of $\Delta V_{\text{ref,1-2}}/2$ is -0.19 m/s with a standard deviation of 0.68 m/s. This suggests that there is no consistent bias in the crosswind measurements between the two driving directions.

8.4.2 Topography

Headland

At the Hålogaland bridge (Figures 8.8 and 8.9), the wind speed V_w (third set of axes from bottom) is locally higher near the northern end of the bridge between approximately $X_b = 500$ m to 700 m. The increased wind speed is evident in the magnitude of the plotted vectors on the topographical maps as well (top set of axes).

Table 8.3 shows the peak bin-averaged wind speed for the northern and southern halves of the bridge (split at the origin). The highest wind speed on the northern half is 4.6 and 5.0 m/s higher than the reference value for the windward and leeward lanes respectively. The peaks are found between the northern tower and abutment. The equivalent values for the southern half are 2.4 and 1.4 m/s respectively.

Table 8.3: Peak wind speeds at the Hålogaland bridge.

Lane	Peak V_w [m/s]		$V_{w,\text{ref}}$ [m/s]
	South	North	
Windward (1)	19.9	22.1	17.5
Leeward (2)	17.6	21.2	16.2

It is unfortunate that this flow feature coincides with the location of the northern tower. It will be seen that the shielding effect of the tower effectively creates an inverse gust which the vehicle passes through. The higher wind speed near the tower will increase the size of this gust and is not beneficial to comfort and safety.

The higher wind speed is most likely caused by changes to the ABL due to variations in the shoreline topography. The northern abutment is built on a headland itself as well as being downwind of a similarly sized headland to the east. As described in [33] – albeit for a topography of a larger dimension – an expansion fan has previously been observed downwind of the the tip of a headland, causing a local acceleration of the downstream flow.

Complex, rough terrain

Also on the Hålogaland bridge, there is a segment between the abutment and the northern tower where a particularly uncomfortable level of turbulence was noted during the field session. In Figures 8.8 and 8.9 this is the segment between $X_b = 600$ m and approximately 850 m. The gust amplitude ΔV_w ramps up from a minimum to the right of the tower and up to a peak value in the vicinity of the abutment. The ramp and peak/hat are more pronounced in the leeward lane, but are notably higher than the reference value in both lanes.

Interestingly, ΔV_w is also heightened between the tower and abutment on the curved, southern end of the bridge. This segment was not recorded as being difficult to navigate in the field notes during the experiment.

The peak/hat at the abutment is likely caused by the shielding effect at the end of the finite embankment on which the abutment rests. This will be investigated further under the heading *Embankments* below.

Here, the ramp-like feature of the ΔV_w curve at the northern end and the broad concave curve at the southern end is of interest. These are areas where the peak gust amplitude grows *slowly* with the bridge axis, as opposed to the *fast* changes seen at the towers (or the abutments).

The values of ΔV_w reach a maximum of 9.5 m/s at the southern end (bin-averaged value), leeward lane, compared to a reference value of 3.7. An equivalent value at the northern end is more difficult to obtain due to the ramp being so close to the abutment peak. However, ΔV_w is 8.6 m/s at the top of the ramp before the slope changes ahead of the peak/hat.

The spread (variance) in ΔV_w between individual signals appears to be larger along these approach spans and both the wind speed V_w and direction Ψ signals are visibly more chaotic. This suggests an increase in the general turbulence intensity in the flow. There are no particular features of the bridge that would provide a reasonable explanation for this.

A more likely cause is that the incident wind carried from upstream terrain is simply more turbulent. As outlined in the review of the literature, rough, complex terrain has been shown to increase the turbulent kinetic energy locally in the ABL and can be carried up to 500 m downstream [11]. This might be the cause of the ramp and concave features of the bin-averaged ΔV_w.

For reference, Figures 8.22 and 8.23 show the road/deck axis of the Hålogaland bridge in the surrounding complex terrain. The topography is typically covered by short forest, shrubbery and smaller buildings (cabins and small houses). Two contours that correspond to the approximate minimum and maximum elevation of the road on the bridge – 30 and 50 m respectively – are shown in red in Figure 8.22.

It is thought that rough, complex, upstream terrain at roughly the same height as the bridge deck is the cause of the larger gust amplitudes on the approach spans. Both plots of the terrain show that the regions of increased gust amplitude (ΔV_w) correspond with slices of the upstream terrain ($-750 < X_b < -500$ m and $500 < X_b < 750$ m) that contain the shoreline and elevations similar to or below the bridge deck. In [11], the results suggest that regions of increased turbulent kinetic energy remain within ±25m of the elevation of the peak from which they emanate. This is consistent with the explanation proposed here given the elevation profile of the topography shown in Figures 8.22 and 8.23.

Embankments

The study of the peak/heat feature seen at the abutment is now studied. A similar feature is seen in the ΔV_w curve at at least one of the abutments of the Helgeland (Figures 8.12 and 8.13) and Tjeldsund bridges (Figures 8.18 and 8.19) as well as at Hålogaland (Figures 8.8 and 8.9). The peaks in the bin-averaged ΔV_w signal

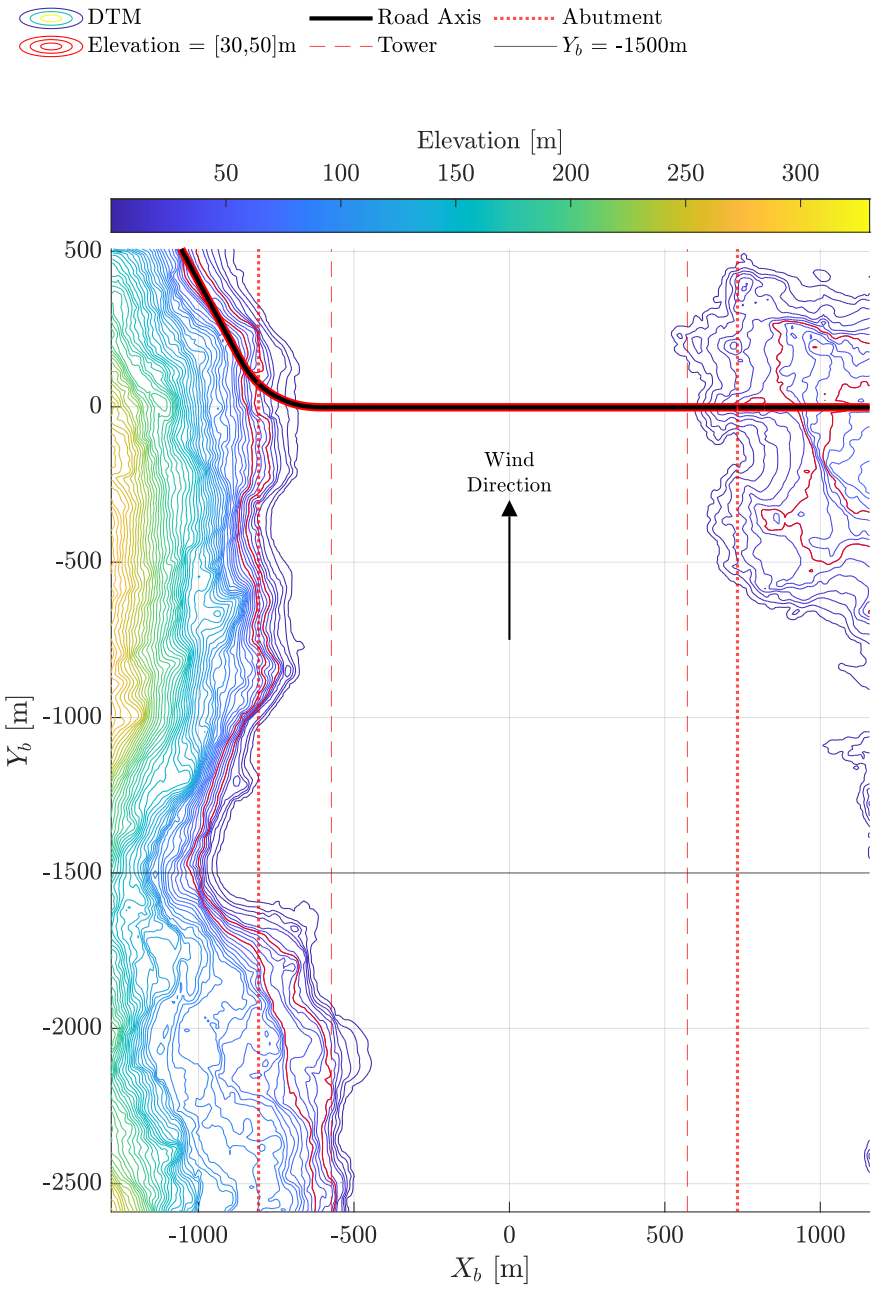

Figure 8.22: Topography at the Hålogaland bridge where the predominant wind is travelling up the page. ©Kartverket (terrain model & road shape)

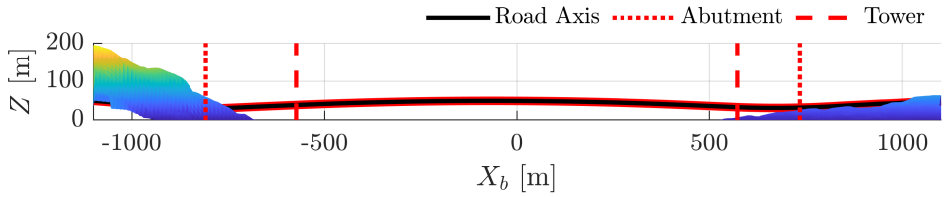

Figure 8.23: A view from $Y_b = -1500$m of the Hålogaland bridge and surrounding terrain where the predominant wind is travelling into the page. ©Kartverket (terrain model & road shape)

have been tabulated in Table 8.4 for each case where a prominent peak/hat can be identified at any of the abutments of the aforementioned bridges. With gusts amplitudes up to 24 m/s it is clear that these are significant features.

The most extreme case is investigated to understand the cause of this feature. This is the peak at the southern end of the Helgeland bridge (Figures 8.12 and 8.13). The peak seen here is the highest of all values given in Table 8.4 and the geometry of the embankment can easily be isolated from the surrounding terrain. The embankment is in fact surrounded only by water and is in the middle of a wide fjord where a stable, low turbulence flow is expected.

Note that the southern peak in ΔV_w in the windward lane on the Helgeland bridge cannot be identified in Figure 8.12 as it is located beyond the limits of the plot. The limits on the X_b axis have been selected carefully in order to avoid having multiple data points from the same time series at the same X_b locations due to the road turning back on itself. The peak can be identified from an alternative rotation of the map as is shown in Figure 8.24.

The Digital Terrain Model (DTM) near the southern embankment has been plotted in three dimensions in Figure 8.25 where regularly spaced in-plane wind vectors have been plotted on a plane offset to $Z = 150$ m for clarity of interpretation. The same X_b-Y_b axes are used as in Figure 8.13 and the road axis has been drawn as a solid black line highlighted in red. The wind plotted as vectors is the wind measured in the leeward lane during the 30 kph passages (the same data as in Figure 8.13). This figure makes clearer the shielding/deflective effect of the embankment.

A set of cross-sectional profiles have been taken from the topography as indicated by the red lines on the DTM. These are taken from planes normal to the 2D projection (on Z=0) of the road line at the points indicated by red dots (plotted on the $Z = 150$ m plane). It is shown that the wind is reduced to a negligible magnitude at approximately the middle of the 5 clustered points on the curved segment of road. Beyond this point – moving away from the bridge – the wind remains low in magnitude and appears to align with the road and embankment geometry.

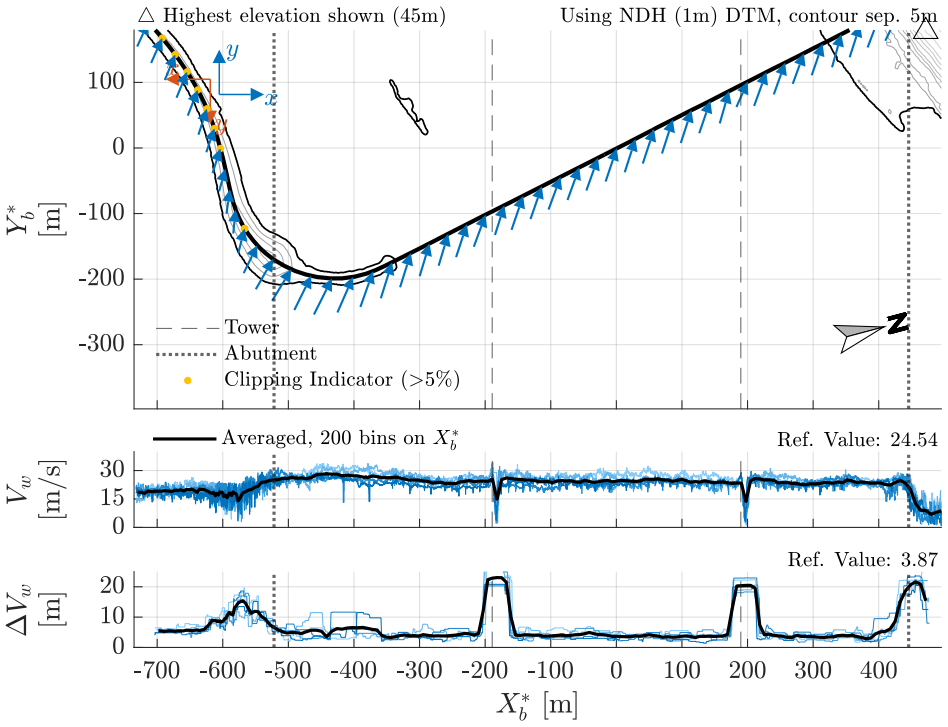

Figure 8.24: Wind profile in the windward lane of the Helgeland bridge (rotated alternative to Figure 8.12). ©Kartverket (terrain model & road shape)

Note: a new coordinate system has been defined, rotated from X_b-Y_b.

Table 8.4: Peak gust amplitudes at the abutments.

Data set	Abutment	Lane	Peak ΔV_w [m/s]
Helgeland	South	Wind-	15.4
		Lee-	24.1
	North	Wind-	21.7
		Lee-	22.1
Hålogaland	North	Wind-	10.4
		Lee-	15.3
Tjeldsund 1	West	Wind-	8.4
		Lee-	12.1
Tjeldsund 2	West	Wind-	7.8
		Lee-	9.4
	East	Wind-	9.6
		Lee-	14.0

The small wind component pointing in the road direction could be the result of the vehicle's forward pressure wave. Moving further from the bridge, towards $Y_b \sim 300$ m, the wind has too high a magnitude for this to be the case and yet its direction still appears to gravitate towards the road's axis.

The cross-sections have been plotted on the bottom set of axes in Figure 8.26 along with the terrain's profile under the road line on the top set of axes. The wind magnitude signals in each lane for all 5 repetitions at 30 kph are plotted on their own respective set of axes.

This makes the shielding effect of the embankment clear to see in both lanes, though more so in the leeward lane. The wind speed over the tallest part of the embankment ($\sim$1150 to $\sim$1220 m on the road axis) is highly variable, indicating a higher turbulence intensity and possibly a flow reversal.

Figure 8.27 shows sketches of a selection of the embankment cross-sections along with some details of the road surface, the test vehicle and the crash barriers on either side of the road lanes. The crash barrier may play a role in causing the higher turbulence and possible flow reversal. It is also noted that the embankment is built up of large rocks and not a smoother surface like grass or soil.

In Figure 8.26 there is a peak in the wind speed in the leeward lane before the steep drop-off due to the shielding effect of the embankment. This peak may have been capped by clipping. Clipping is likely also the reason for the apparent increase in wind speed moving from 1000 m along the positive direction of the axis to the peak. This is simply an artefact resulting from the rotation of the vehicle into a direction that allows a higher resultant wind speed to be measured from the

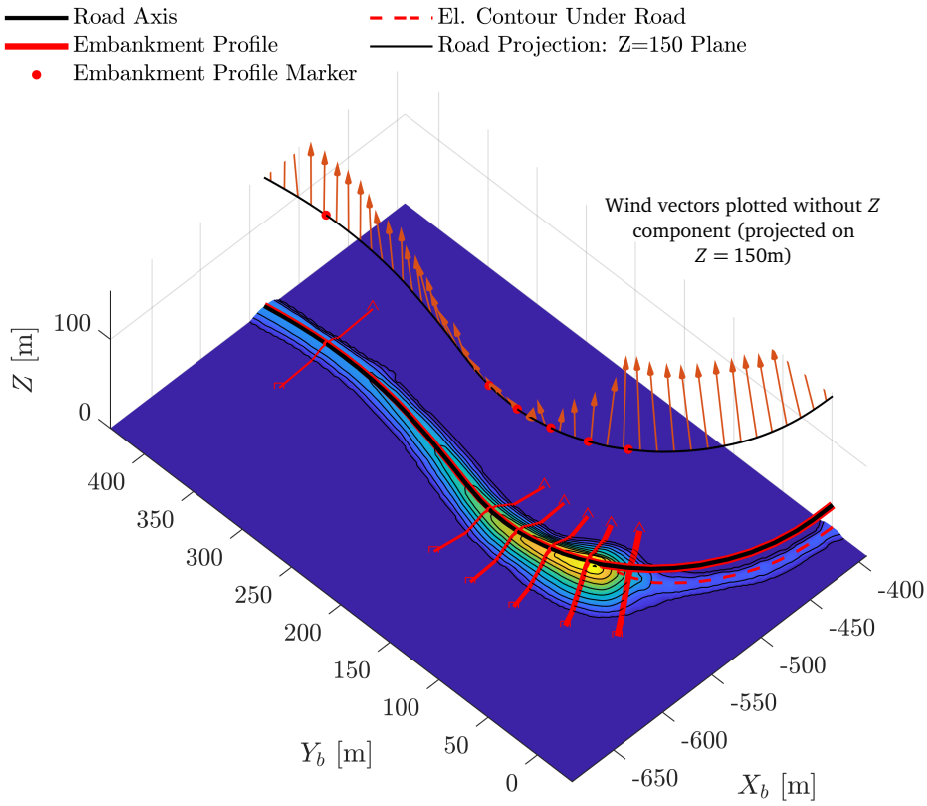

Figure 8.25: A terrain model at the southern abutment of the Helgeland bridge, wind vectors from the leeward lane. ©Kartverket (terrain model & road shape)

The *El. Contour Under Road* shows the road path projected down onto the topography and is drawn in Figure 8.26 using the same colour and style.

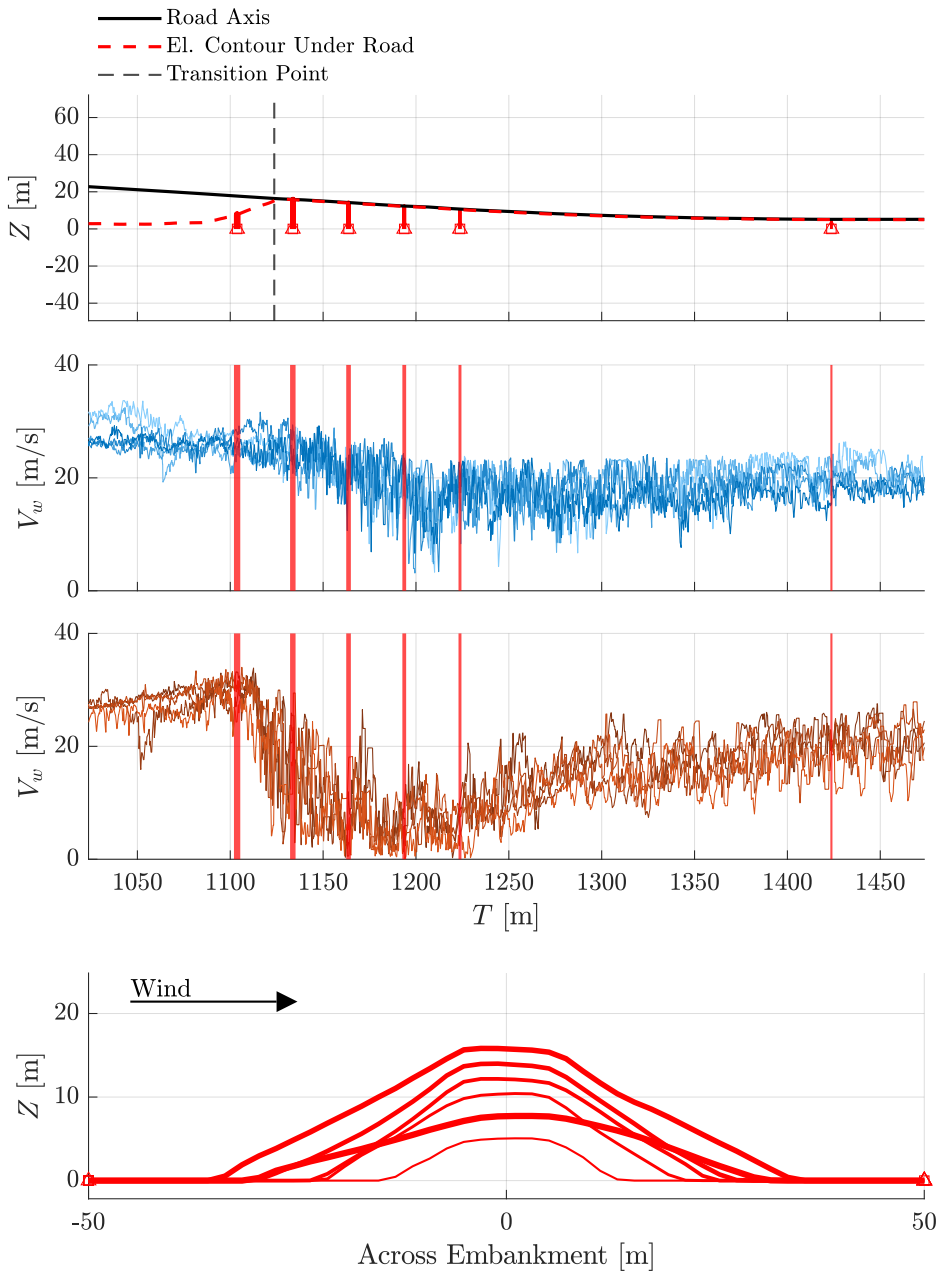

Figure 8.26: Wind profiles at the Helgeland bridge's southern embankment. ©Kartverket (terrain model & road shape)

Note that the curvilinear path of the road on the X-Y plane has been unwrapped onto the T axis.

two components u_r and v_r (i.e. one of the corners of the measurement domain is pointed into the direction of the wind). Similarly, the clipping effect is evident in measurements taken from the windward lane (some signals are clearly capped and remain flat for short intervals).

8.4.3 Bridge geometry

Deck section

The bluffness of the deck section combined with the presence of the vehicle affects the pressure field around the composite girder-vehicle geometry and consequently also the wind magnitude and turbulence seen by vehicles on the road surface. Even a thin deck section has a demonstrable effect. This can be shown by comparing measurements recorded on the VBOX with those recorded by an anemometer fixed to the bridge.

At Hålogaland, a monitoring system has been installed which includes an array of anemometers placed intermittently along the span of the bridge. The system was being tested when the field sessions described here were performed, so only a limited amount of data is available. Nonetheless, concurrent data from the three anemometers designated W10-45-1, W10-47-1 and W10-49-1 is available. Figure 8.28 shows their placement on the bridge structure. The anemometers are mounted approximately 7 m above the deck on mounting arms fixed to the hangers.

As a rough comparison between the bridge-fixed measurement (at ∼7 m above deck) and the vehicle-fixed measurement (at ∼3 m above deck), the mean wind speed and direction over a period of time can be calculated. About 30 seconds of concurrent data is sought to make the comparison statistically significant. At 30kph this corresponds to about 200 m of travel along the bridge axis.

The data between $X_b = 200$ m and 400 m is chosen as this segment is close to the location of the bridge-fixed sensors. Figures 8.8 and 8.9 show that there is little variation in the wind magnitude and direction in this segment and it avoids the supposed headland effect (accelerated flow) seen beyond 400 m. It is assumed that the wind field is homogeneous across this segment and can therefore be compared to concurrent data from the bridge-fixed anemometers (both systems use GPS time). The results can be seen in Figure 8.29.

The first notable feature is that the vehicle-based wind magnitude is consistently lower and follows the variations in the bridge-based measurements. The ratio of VBOX to bridge-fixed wind magnitude is 0.90 mean-averaged across all data points. To 2 significant figures, this value is identical for the windward and leeward lanes.

Do note that there are crash barriers on either side of the road and a fence on the outside of the walkway adjacent to the road on the western edge of the deck. Camara [38] shows in his CFD analysis that the *parapets* on the Orwell bridge have

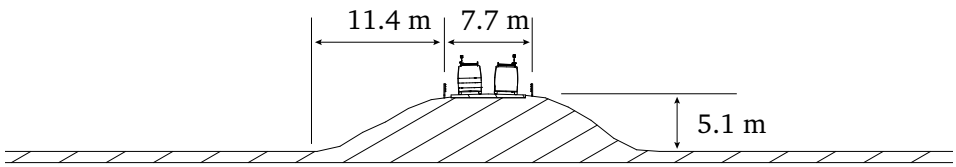

(a) A low prominence embankment profile at $T \sim 1425$ m.

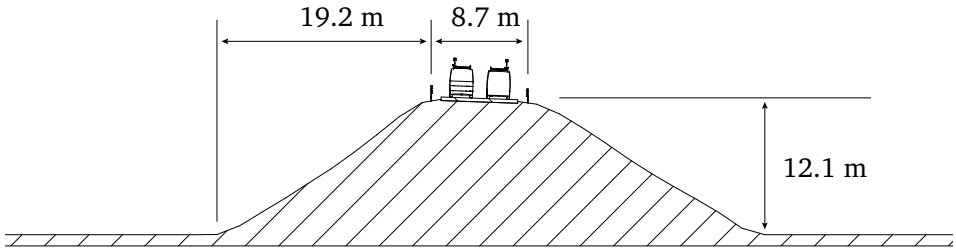

(b) An embankment profile at maximum deflection/shielding at $T \sim 1190$ m.

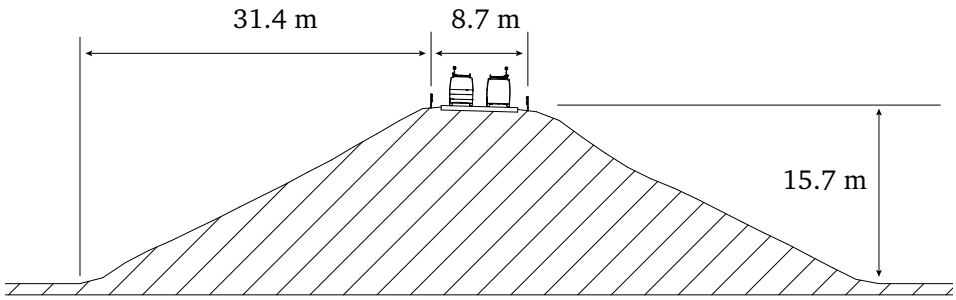

(c) The embankment profile with highest prominence at $T \sim 1130$ m.

Figure 8.27: A comparison of embankments at the southern end of the Helgeland bridge. ©Kartverket (terrain model)

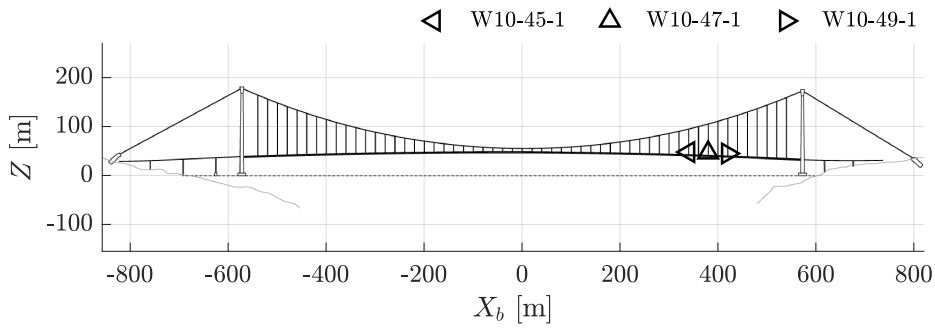

Figure 8.28: Locations of three anemometers on the Hłogaland bridge.

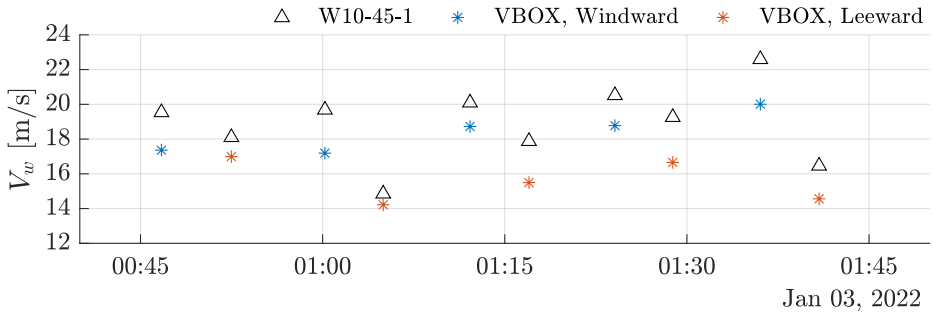

(a) Wind magnitude

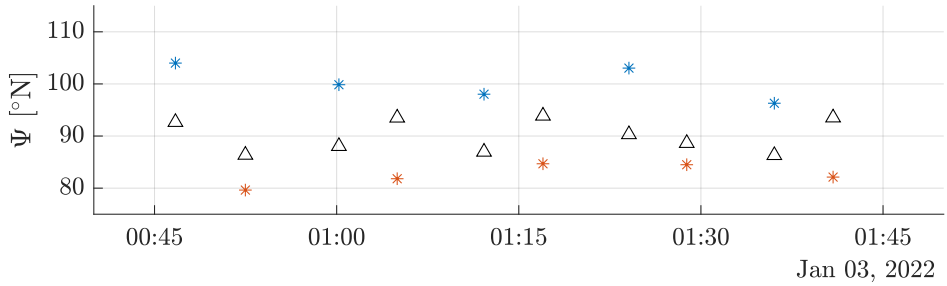

(b) Wind direction

Figure 8.29: A comparison between wind measurements taken from bridge-fixed anemometer W10-45-1 and the anemometer mounted on the moving vehicle (corrected for driving speed).

a significant impact on size of the shielding *bubble* (flow separation from the upper surface of the girder). The barriers and fence on the Hålogaland may have a similar effect. The reduction in wind speed is unlikely to be solely affected by the shape of girder and vehicle alone.

The second plot in Figure 8.29 confirms that the estimated wind direction is dependent on the direction of travel of the vehicle. In the windward lane the direction is consistently higher than the bridge-based measurement while the the opposite is true of the leeward lane. This is consistent with the previously discussed push effect from the vehicle's forward pressure wave.

In summary, no discernable difference is seen between the windward and leeward lanes and the Hålogaland bridge's deck section (with the presence of the vehicle, crash barriers and fencing) has the effect of reducing the wind speed over the deck (at 3 m) by 10% in both lanes compared to the wind measured at 7 m above the deck.

Cantilevered bridges

The Hålogaland bridge has a streamlined cross-section that is approximately uniform across the main span with a maximum depth/thickness of 3.00 m. As can be seen in Figure 8.30, a cantilevered bridge like Dolmsund has a very different cross-sectional profile which varies from 2.75 m to 10.00 m in depth. This cross-sectional shape can be seen on many bridges in Norway including the Måløy bridge and is fairly similar to each of the two adjacent sections on the Orwell bridge [38].

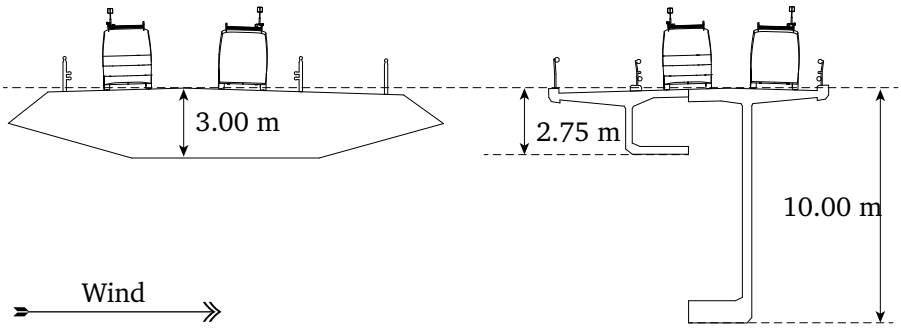

Figure 8.30: A sketch of the cross-sectional profiles at Hålogaland (left) and Dolmsund (right).

The longer main spans are arched with a deck section that varies in depth

whereas the approach spans are shorter with a constant depth. At Måløy, the deck section depth varies between 1.70 m and 7.00 m.

The deeper deck section near the central support piers has a shielding effect as can be seen in both the wind magnitude and the gust amplitude ΔV_w for the Måløy and Dolmsund bridges (Figures 8.14 & 8.15 and 8.2 & 8.3 respectively). There are wide-spanning troughs in both leeward and windward lanes centred at the main supports. At Dolmsund, the deceleration in flow is accompanied by an increase in the bin-averaged gust amplitude ΔV_w.

Table 8.5 gives an overview of the changes to mean wind speed (bin-averaged) and gust amplitude near the support towers of the Dolmsund and Måløy bridges. The Dolmsund cross-section generally has a larger maximum shielding effect with changes from the reference value between -9 and -11 m/s vs. -6 to -9 m/s at Måløy. Note that the maximum depth is 10.0 vs. Måløy's 7.0 m.

Similarly, the maximum bin-averaged gust amplitude is larger for the deeper section with 10 m/s at Dolmsund vs. 6-7 m/s at Måløy.

Table 8.5: Changes in mean wind speed and gust amplitude on cantilevered bridges (all values in m/s).

Data set	Lane	$V_{w,\,\mathrm{min}}$	$V_{w,\,\mathrm{ref}}$	min. - ref.	$\Delta V_{w,\,\mathrm{max}}$	$\Delta V_{w,\,\mathrm{ref}}$	max. - ref.
Dolmsund	Wind-	5.3	14.6	-9.3	12.8	2.7	10.1
	Lee-	5.4	16.8	-11.4	14.1	4.1	10.0
Måløy	Wind-	9.3	15.4	-6.1	10.0	4.1	5.9
	Lee-	5.0	13.8	-8.8	14.9	7.8	7.1

Construction & traffic at Måløy

At both the Dolmsund and Måløy bridges the general shape of the V_w and ΔV_w curves are similar near the supports/deep sections. The wind speed has a v or u shape, while ΔV_w has more of a plateau shape. These shapes are less recognisable in the leeward lane of the Måløy bridge, particularly in the ΔV_w curve. The variability between individual signals is substantial across the span, with certain repetitions seeing gust amplitudes of up to 20 m/s locally.

This was the only bridge where there was a significant amount of traffic during the experiments. In addition to the traffic, there was maintenance work being performed on the bridge. This entailed having various construction materials stored on the bridge deck along a limited segment of the leeward lane. There were also traffic lights to regulate traffic. The materials and scaffolding will likely have affected the wind profile. Also, a consistent speed could not always be held and so certain segments of the bridge are overrepresented in the wind profile.

The wakes of individual vehicles can be observed as individual inverse gusts similar to those seen in the wakes of towers. This has been observed at the Helgeland bridge and will be discussed further in Chapter 10. A continuous flow of traffic is therefore likely to increase the average level of ΔV_w.

Substructure

The best example of how elements of the substructure can affect the wind profile is the Tjeldsund bridge. In general for all profiles at Tjeldsund (Figures 8.18, 8.19, 8.20 and 8.21) there are 3 hat-shaped features in addition to those at the towers. Two are located at the cable support piers while another is evident at the counterweight.

The hat-shaped features in ΔV_w coincide in each case with troughs in V_w and thus present in the same way as the shielding effect in the wake of the towers. The difference here is that these geometries aren't above the bridge deck. There are also support columns under the bridge deck that do not seem to be associated with high amplitude gusts ΔV_w. The reason for this will be discussed under the heading *Cable support piers* & *support columns*.

Table 8.6 gives a summary of the peak bin-averaged values of ΔV_w at the cable support piers, the counterweight and the towers of the Tjeldsund bridge.

The western cable support geometry appears to produce a more severe gust than the eastern one. This could be due to inhomogeneity in the wind (i.e. higher wind speed at the western tower) or could be because the vehicle passed on average at a different lateral position in the lane. There is also not a consistent effect of lane on $\Delta V_{w,\,\max}$ at the cable supports in Table 8.6. At the eastern support, the windward shielding is higher, whereas the opposite is true at the western support.

For the counterweight there appears to be a clear effect of lane on $\Delta V_{w,\,\max}$, which has almost twice the value in the leeward versus the windward lane.

Counterweight

The counterweight has been sketched in Figure 8.33 and has a 16x8 m cross-section with an approximate height of 30 m. It has the same basic shape as a simple building and is a finite rectangular section cylinder with an aspect ratio of 2.5 ($=30\times 2/[16+8]$).

Sumner et al.'s [193] results suggest that the flow is fully separated from the windward edge and across the full top surface of a finite square cross-section cylinder with an aspect ratio of 3 at a Reynold's number of 4.2×10^4. The Reynold's number here is $\sim 1.9\times 10^7$ assuming $\nu = 1.46\times 10^{-5}$ m^2/s (at 0 m elevation in the International Standard Atmosphere [1]) and taking the reference speed $V_{\text{ref}} = 17.3$ m/s from the windward lane.

Table 8.6: Peak gust amplitude near elements of the Tjeldsund bridge.

Data set	Element	Lane	$\Delta V_{w,\,\max}$
Tjeldsund 1	Counterweight	Wind-	7.7
		Lee-	14.3
	Cable Anchor West	Wind-	10.8
		Lee-	8.4
	Tower West	Wind-	13.0
		Lee-	13.2
	Tower East	Wind-	12.7
		Lee-	13.9
	Cable Anchor East	Wind-	7.2
		Lee-	9.0

Figures 8.31 and 8.32 show the wind vectors measured over the counterweight in three dimensions. The vectors are rooted along an approximate line of measurement. It is a straight line that follows the road axis and is offset vertically by the height of the anemometer above the ground (as measured statically in the lab) and horizontally by the average measured lateral position in the lane across all repetitions over the full span of the bridge.

Figure 8.32 shows evidence of the pressure wave/separation bubble over the composite bridge deck-counterweight geometry. The windward vectors have a higher vertical component than those in the leeward lane, and this vertical component is locally raised over the counterweight geometry. The wind in the leeward lane decreases in tact with this local increase in vertical component, providing evidence that the flow at this elevation is separated or re-circulating.

Cable support piers & support columns

The cable support piers are also finite rectangular section cylinders with a width of 1.60 m on the windward face. The supports under the approach spans are circular columns with a diameter of 0.80 m. As can be seen in Figure 8.34, the cable supports meet the deck section at the very edges of the deck and protrude slightly above the road surface. The wake is therefore brought windward to the leading edge of the deck section as well upwards above the road surface. The other support columns are tucked underneath the windward edge, which may be why they do not have an obvious effect on the observed flow.

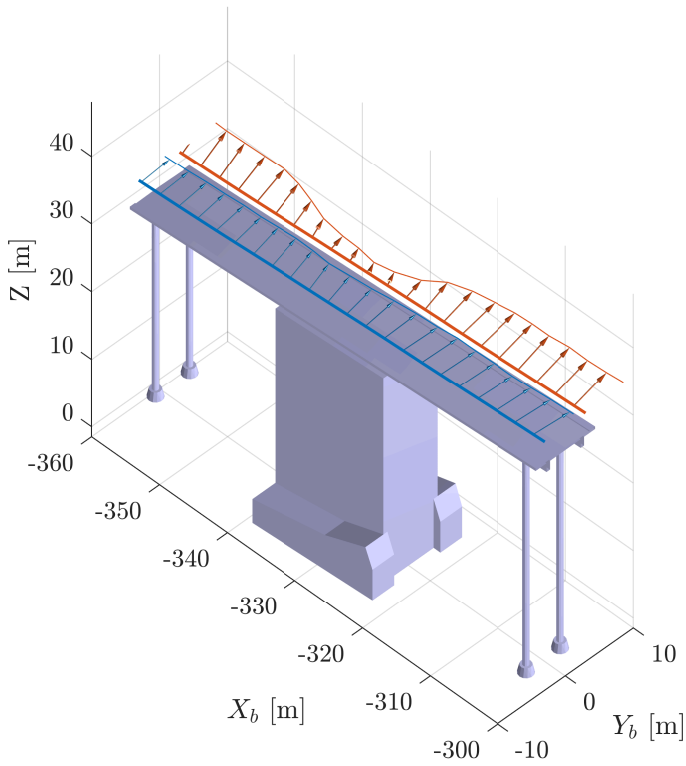

Figure 8.31: General isometric view of flow over Tjeldsund counterweight.

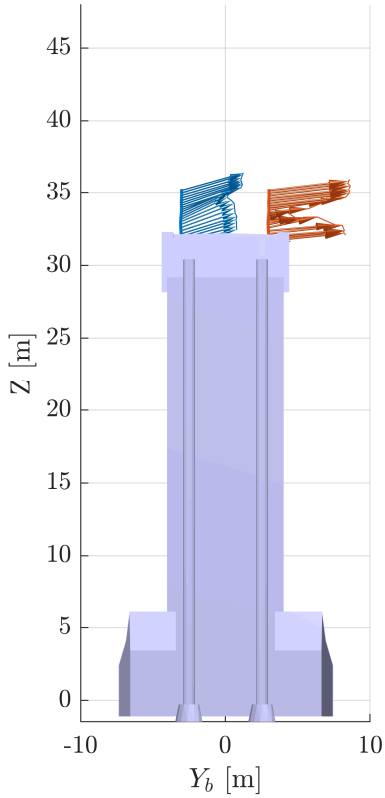

Figure 8.32: View along the road axis of the flow over the Tjeldsund counterweight.

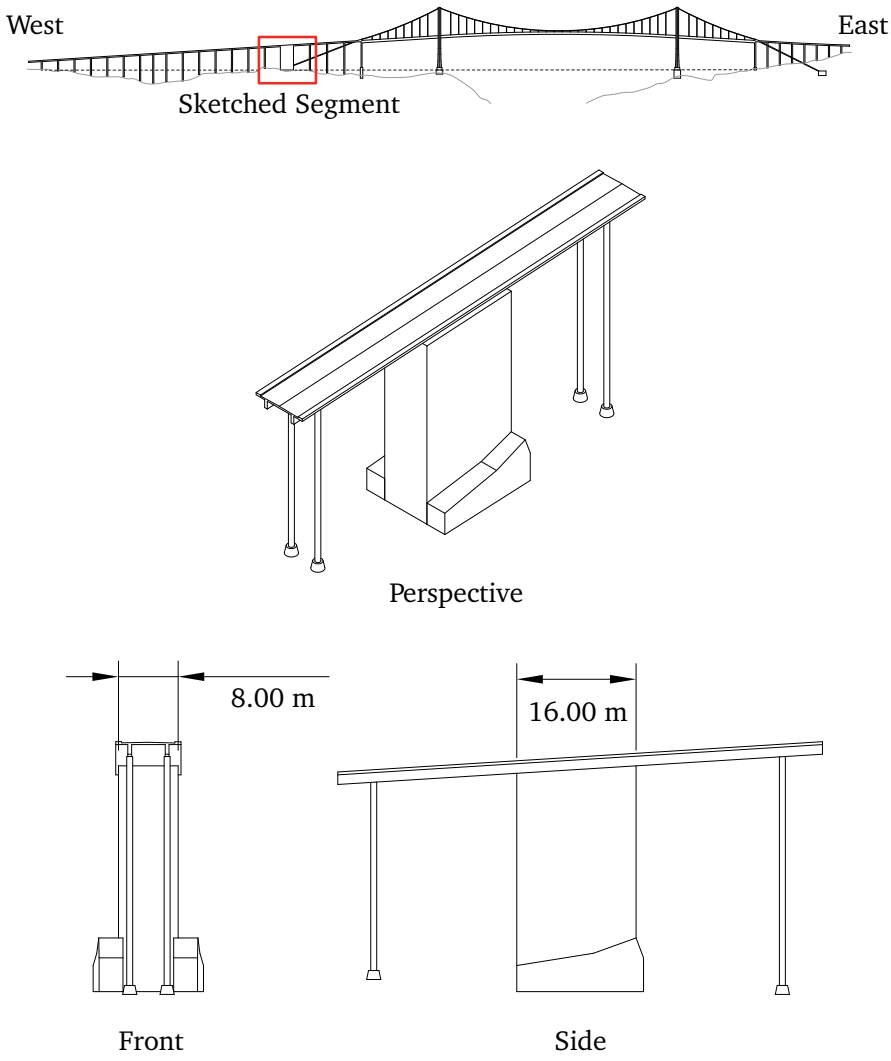

Figure 8.33: A sketch of counterweight at Tjeldsund (1:1000).

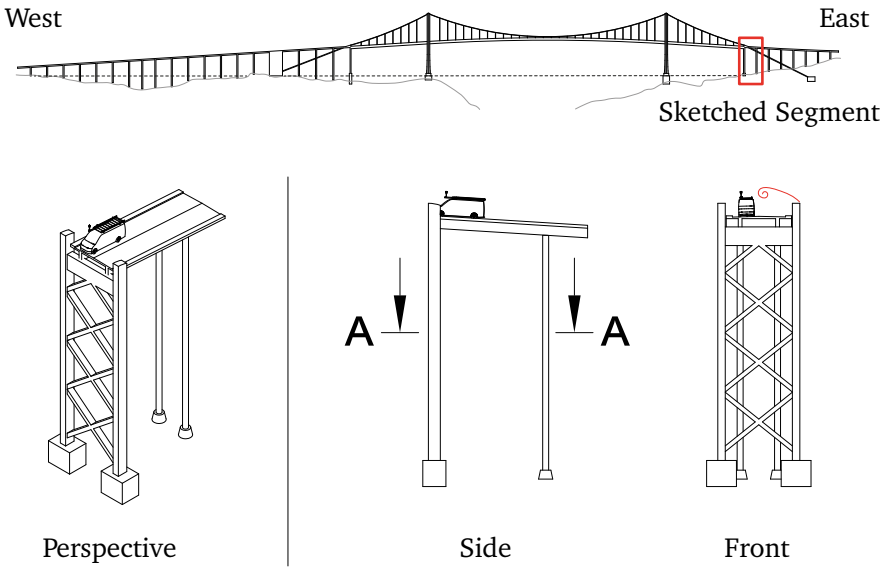

(a) A sketch of a segment near the eastern cable support of the Tjeldsund bridge (1:1000).

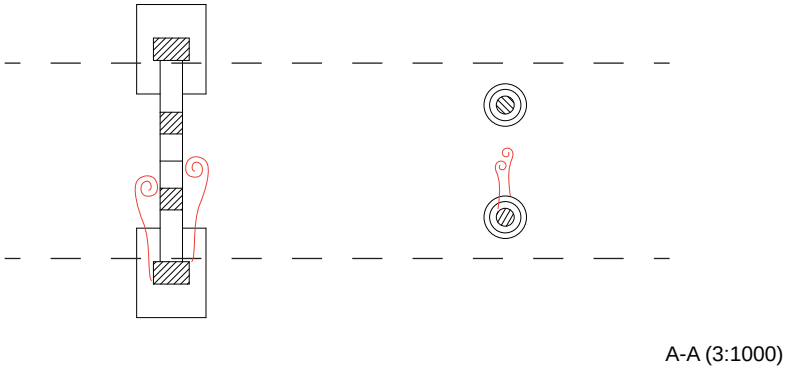

(b) A section view of the cable support and columns.

Figure 8.34: A sketch of the cable support piers and support columns at Tjeldsund.

Helgeland support columns

The wakes of the three support columns under the northern approach span of the Helgeland bridge are apparent in the leeward lane measurements shown in Figure 8.13. Between $X_b = 375$ m and 500 m there is more turbulence in V_w along with a step increase in gust amplitude ΔV_w. The bin-averaged gust amplitude remains above 16 m/s for $X_b > 375$ m.

The bin-averaged V_w curve presents with troughs where the minima are consistently 10-20 m to the right (north along the bridge axis) of the support columns. This is consistent with the theory that these are the wakes of the support columns given the wind's skew incidence angle (approximately 45°). For reference, the columns have a rectangular section with a high aspect ratio. The column closest to the main span has a dimension 5.0×1.2 m and the two columns north of this have a dimension of 3.6×1.2 m.

Unlike the supports under the northern approach span, the supports on the southern end of the bridge do not seem to form an observable wake over the bridge deck. There are two conceivable explanations for this:

1. The bridge deck on the southern end descends towards the embankment. The descent angle may be such that the wake forms below the bridge deck.
2. There is a steep topographical drop just leeward of the northern approach span. It may be that this gives the wind a vertical component that pushes the wake over the bridge deck.

Cables & hangers

In the windward lanes of the Helgeland and Hålogaland bridges (Figures 8.12 and 8.9) there are sharp, low magnitude troughs at regular intervals. These intervals correspond with the spacing between the cable stays and hangers respectively. A closer inspection reveals that the troughs line up well with the sketched cables and hangers as well. This is both an interesting feature to capture and gives evidence of the good quality of the data.

There could be several reasons for why these features are not seen in the windward lanes of all the suspension bridges. The most important are likely the diameter of the cables as well as their proximity to the driving lane. On some bridges there is a bicycle lane and/or pedestrian walkway between the road and the leading edge. This increases the distance from the cables to the points of observation of the anemometer on the test vehicle.

The main cable's wake is also evident in the windward lanes of the Hålogaland and Hardanger bridges. At Hålogaland there is a bulge in the gust amplitude at the middle of the bridge (see Figure 8.8) whereas at Hardanger there are two peaks

either side of the midpoint (see Figure 8.10). The main cable increases the level of turbulence at the centre of the main span.

8.5 Conclusions

Several local wind features have been observed at the various bridges visited during the field sessions. These features are characterised by changes to the wind magnitude and the 45 m gust amplitude averaged across at least 5 repetitions. The gust amplitude has been defined as the maximum minus the minimum value of the 0.2 s moving mean wind speed within a temporal window approximately equivalent to 45 m of travel along the road/bridge axis. This measure is believed to capture changes that are relevant to safety and comfort. A summary of the most important observations:

- The wind speed is observed to accelerate around the headland topography upwind and below the northern abutment of the Hålogaland bridge. At it's peak, this acceleration adds 5 m/s to the reference wind speed measured over the main span. This bulge in wind speed in the vicinity of the headland is coincident with the northern tower. As a result, the inverse gust caused by the shielding effect of the towers is amplified.
- The non-smooth terrain upwind (up to 1500 m) of the approach spans of the Hålogaland bridge are at an elevation similar to that of the road axis. The gust amplitude over the southern approach span is heightened across the 200 m span and reaches a maximum of 9.5 m/s versus the reference value of 3.7 m/s over the main span.
- Gust amplitudes up to 24 m/s are observed at the southern embankment of the Helgeland bridge. An investigation of the measured wind speed in the windward lane showed that the embankment has the effect of shielding and deflecting the flow. A similar step change in wind speed and peak gust amplitude is seen at the Hålogaland and Tjeldsund bridges as well.
- The slender cross-sectional shape of the main-span girder of the Hålogaland bridge combined with the presence of the vehicle has the effect of reducing the wind speed close to the bridge deck. The measurements taken at $\sim$ 3 m over the deck (anemometer mounted on the vehicle) are on average 10% lower than those measured by anemometers at $\sim$7 m over the deck (attached to the hangers).
- The girders of cantilevered bridges like Dolmsund and Måløy vary in depth and the shielding effect – that slows the mean wind speed – changes in tact with this variation in depth. At Dolmsund, where the section reaches a maximum depth of 10 m, the mean wind speed is reduced by up to 11 m/s against

the reference value over the main span. This is accompanied by an increase in gust amplitude of up to 10 m/s versus the reference value.

- Traffic on the Måløy bridge is found to have a significant effect on gust amplitude with values of up to ∼20 m/s observed locally in individual repetitions.
- At Tjeldsund it is clear that elements of the substructure can also have a shielding effect, creating an inverse gust similar to those seen at the towers.
  - The counterweight under the western approach span looks like a simple rectangular cross-section finite cylinder. As described in the literature [193] at a lower Reynold's number than is present in the field, the flow is completed separated across the top surface. A plot of the wind vector on the wind- and leeward lanes here suggest a similar flow structure where the shielding effect has the appearance of an inverse gust. The inverse gust has an average amplitude of 14 m/s.
  - The cable support piers on either side of the towers are also built such that their wake creates an inverse gust over the deck. The columns protrude from the outer edges of the girder. The result is a maximum gust amplitude of up to 11 m/s.
  - The supports on the northern approach span of the Helgeland bridge were also placed in an arrangement in the incident wind such that their wake/pressure wave is observable in the leeward lane. In this case, the average gust amplitude remained above 16 m/s for more than 200 m of the approach span.
- The cable stays on the Helgeland bridge and the hangers on the Hålogaland bridge form wakes that are observable in the wind speed plots. These appear simply as artefacts and are not believed to affect safety and comfort given the small width/dimension of the inverse gust. This will be investigated further in Chapter 11.

Chapter 9

Vehicle-driver response profiles

Observations and analysis of the vehicle-driver response to wind gusts will be presented in the next chapters (from the current one through to Chapter 12) using data that describes the vehicle's motion. The lateral acceleration A_y, yaw rate ω_z and roll rate ω_x signals will be presented as a function of X_b (bridge axis) for each bridge/road segment visited in the field. The use of an amplitude-of-change operator Δ on the signals reveals some interesting features of the vehicle-driver response that can be related to the flow features discussed in the previous Chapter (8). Here, the location of these features will be pointed out on the vehicle-driver response profiles while the causes and a qualification of the response observed will be discussed in the chapters that follow (10 through 12).

9.1 Processing response measurements

The time series of lateral acceleration, yaw rate and roll rate have been processed to make comparisons with the reference values extracted from the literature (Chapter 3) as useful as possible.

Low-pass filter

Brandt et al. [32] applied a low-pass filter with a cut-off of 5 Hz to the response data. Correspondingly, Figure 2.3 (from Chapter 2) shows that the most significant wind-induced responses will be below 5 Hz (see critical frequency ranges and frequency response function). This cut-off frequency may be revisited in future work, but is applied to all response data shown in this chapter. A 7^{th}-order Butterworth filter is used and is applied forwards and backwards to cancel phase shifts introduced by the filter.

Amplitude of change Δ

The amplitude-of-change of each signal A_y, ω_z and ω_x within a 2-second sliding window is also calculated. These signals are denoted ΔA_y, $\Delta\omega_z$ and $\Delta\omega_x$.

The 2-second value is consistent with the window sizes defined in Table 8.1 for the driving speeds of 70, 75 and 80 kph (used in Chapter 8). The definition of the amplitude-of-change signals Δ is also consistent with the method used by Brandt et al. [32], except for the size of the window. This allows for a more or less direct comparison, where the smaller window used here filters out some of the slightly slower changes that are retained in Brandt's wider window.

Resultant response

The term *resultant response* will be used to indicate that the recorded response is the resultant vehicle response after control input from the driver. Using the terminology vehicle-driver response can be misleading as it is only the vehicle's motion that is described.

9.2 Response profiles

Figures 9.1 through 9.16 describe the resultant response of the vehicle-driver system at each of the experiment locations. The figures are formatted and presented in the same way as the wind profiles in Chapter 8. In the interest of saving space on the page, the two first axes have been combined with both the bridge sketch and the birds-eye view of the road axis being plotted on one set of axes.

The sketch and road map axes are followed by the low-pass filtered signals A_y, ω_z and ω_x and the amplitude-of-change of each of these respectively. At the bottom of the page is the raw speed of GNSS antenna A, which is approximately the driving speed V_x of the vehicle.

Only data from the sessions performed at the highest driving speeds at each location are plotted. The Måløy bridge has been omitted because there was a temporary traffic light on the bridge and only one lane was open for a part of the bridge. The vehicle was not driven across the bridge at a smooth, near-constant speed as was done at the other bridges. The data from Frøya has been plotted in Appendix F for completeness, but has not been plotted here for lack of relevance.

continues on next page ⟶

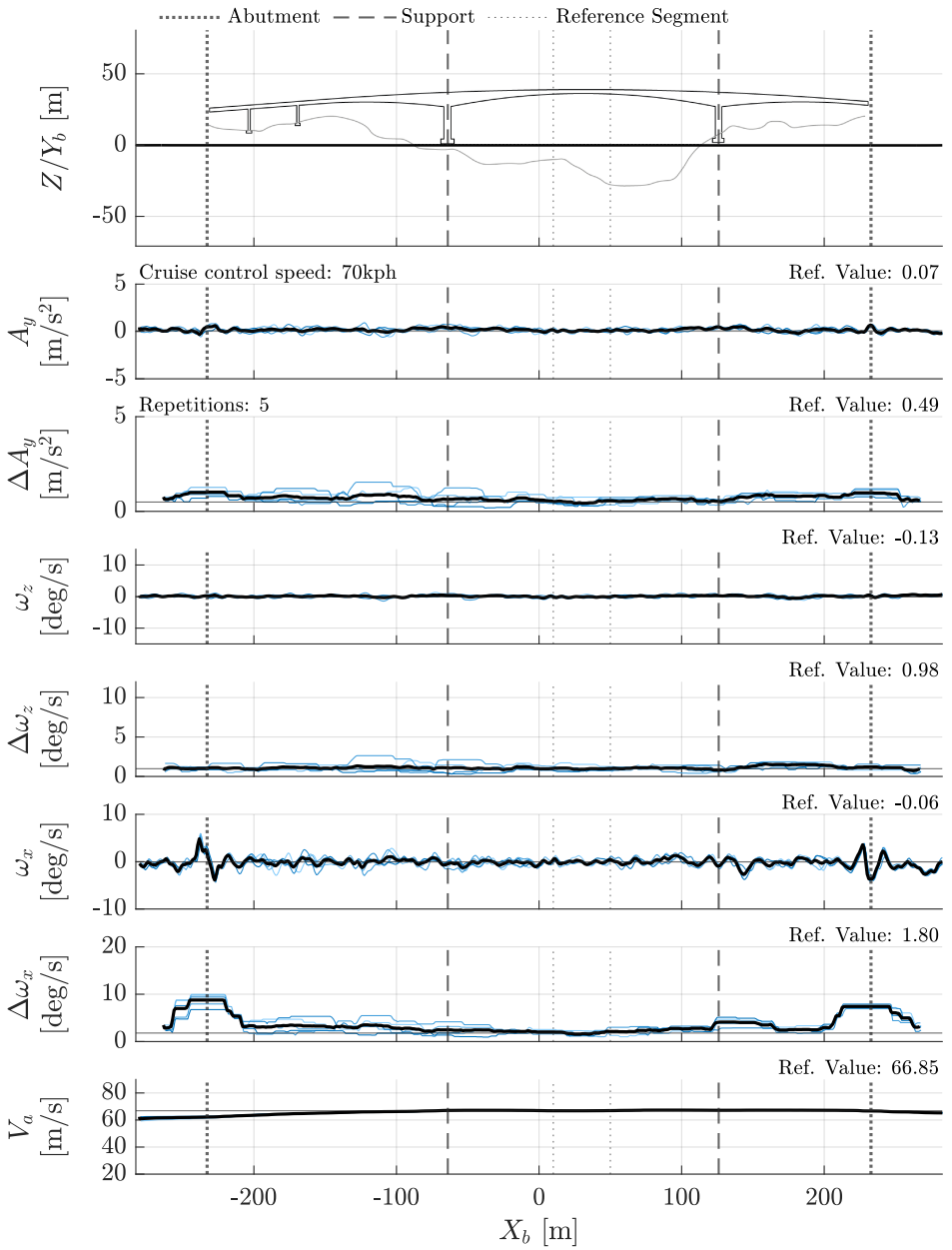

Figure 9.1: Response profile, Dolmsund bridge, windward lane (vehicle travels left to right), see Section 9.2 for full explanation. ©Kartverket (terrain model & road shape)

All signals measured by Inertial Measurement Unit and filtered by a low-pass Butterworth filter with a cut-off of 5 Hz, A_y: lateral acceleration, ω_z: yaw rate, ω_x: roll rate, $\Delta(i)$: maximum minus minimum of signal i within 2-second sliding window, V_a: GNSS speed measured at antenna A (see Figure A.3).

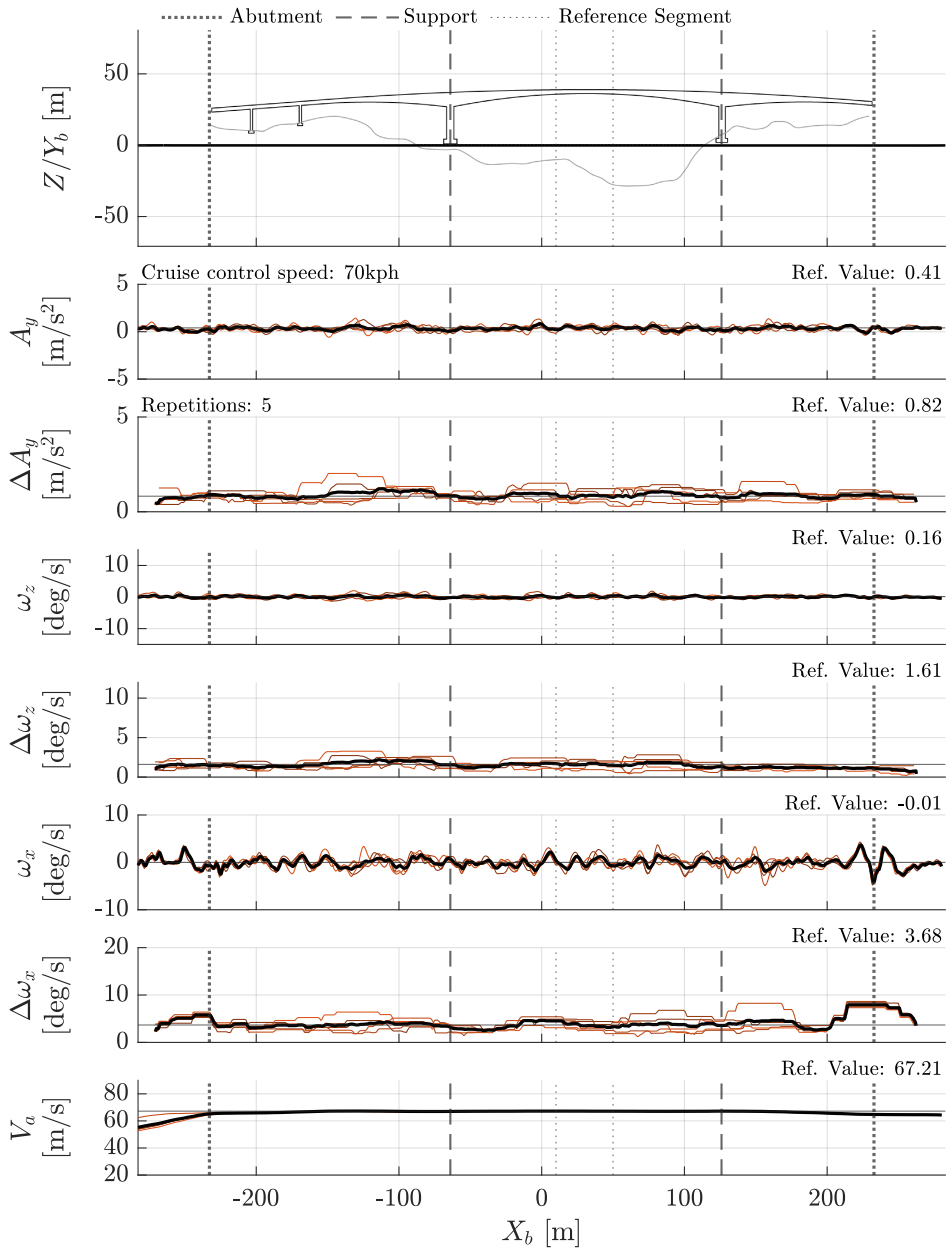

Figure 9.2: Response profile, Dolmsund bridge, leeward lane (vehicle travels right to left), see Section 9.2 for full explanation. ©Kartverket (terrain model & road shape)

All signals measured by Inertial Measurement Unit and filtered by a low-pass Butterworth filter with a cut-off of 5 Hz, A_y: lateral acceleration, ω_z: yaw rate, ω_x: roll rate, $\Delta(i)$: maximum minus minimum of signal i within 2-second sliding window, V_a: GNSS speed measured at antenna A (see Figure A.3).

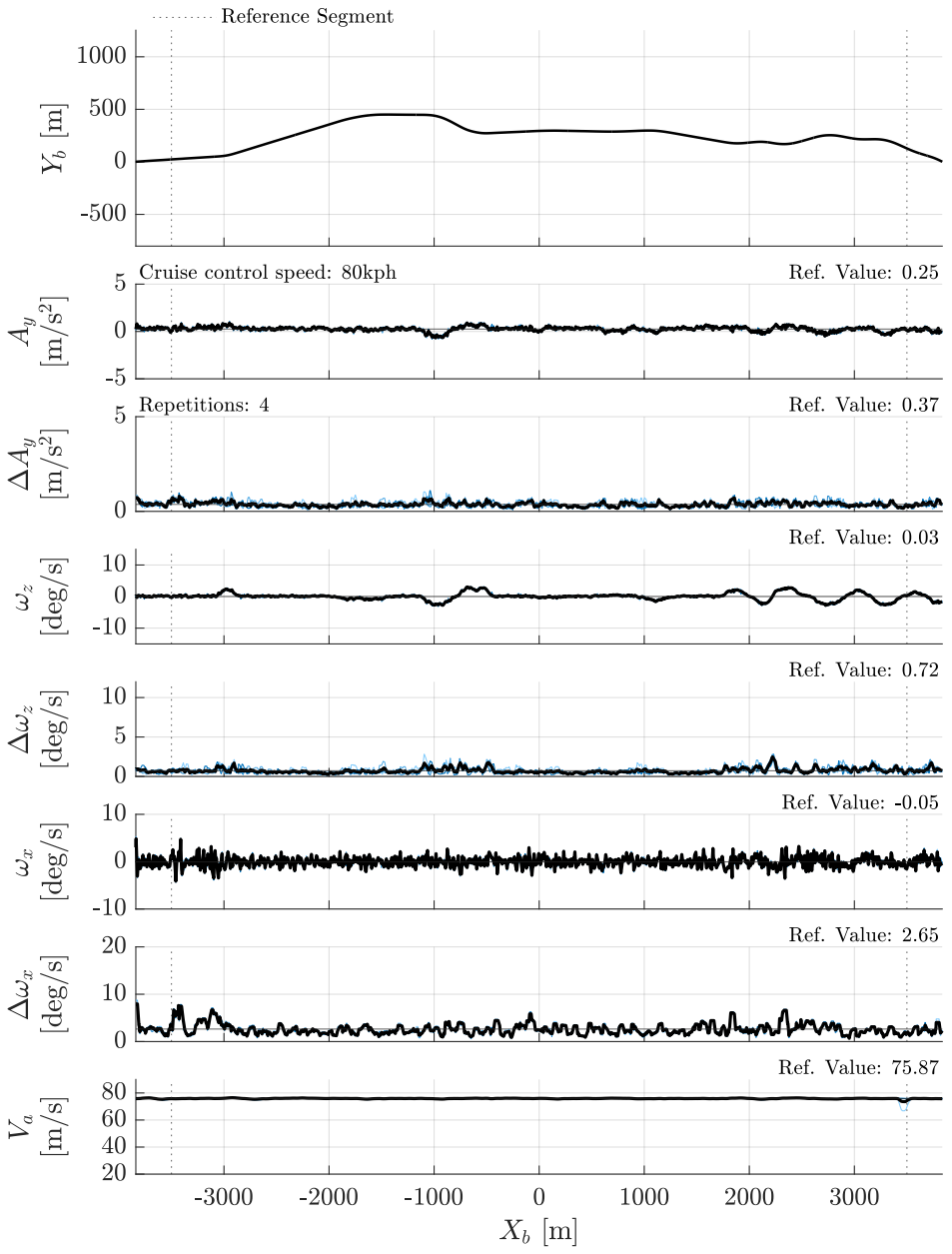

Figure 9.3: Response profile, Dovre 1, windward lane (vehicle travels left to right), see Section 9.2 for full explanation. ©Kartverket (terrain model & road shape)

All signals measured by Inertial Measurement Unit and filtered by a low-pass Butterworth filter with a cut-off of 5 Hz, A_y: lateral acceleration, ω_z: yaw rate, ω_x: roll rate, $\Delta(i)$: maximum minus minimum of signal i within 2-second sliding window, V_a: GNSS speed measured at antenna A (see Figure A.3).

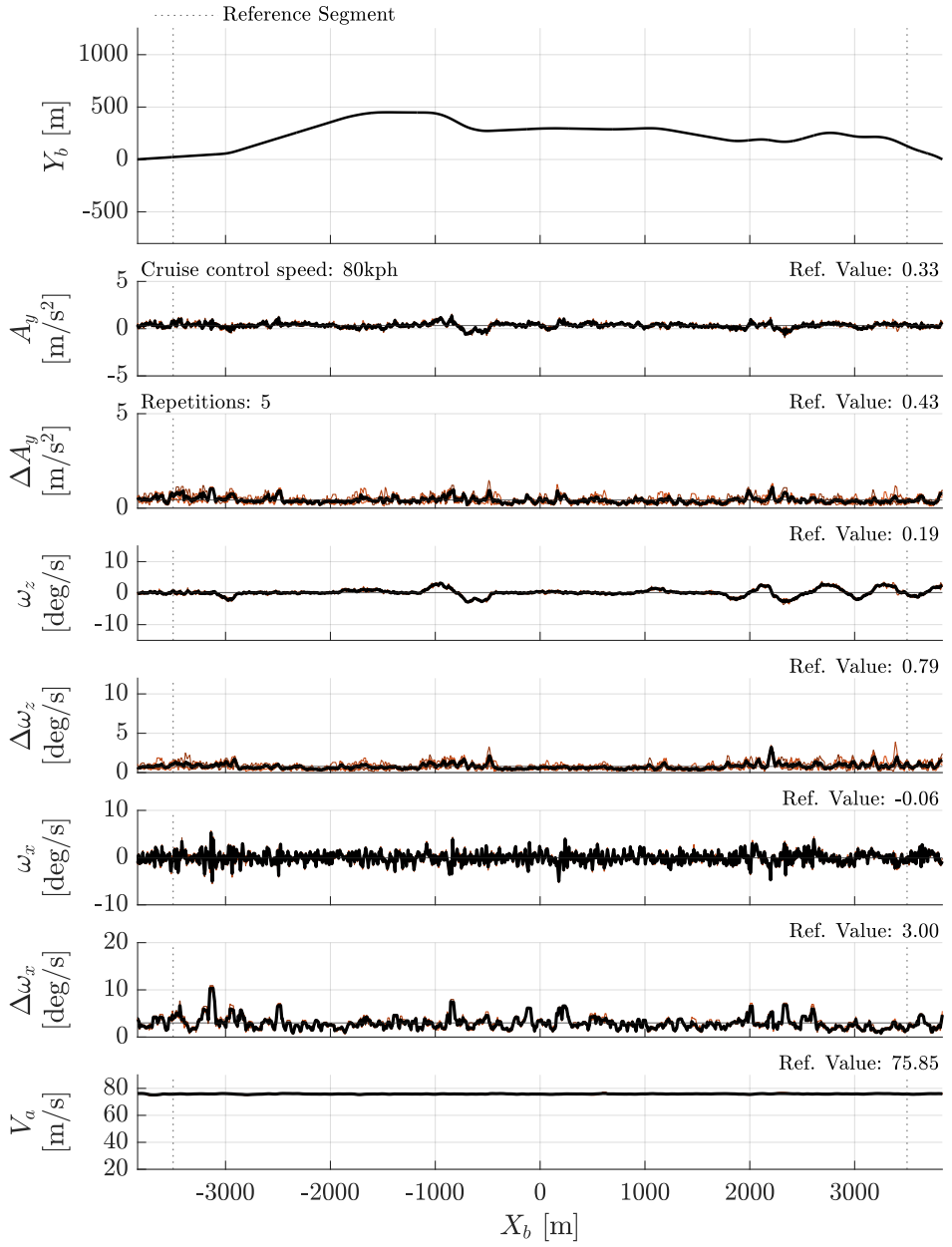

Figure 9.4: Response profile, Dovre 1, leeward lane (vehicle travels right to left), see Section 9.2 for full explanation. ©Kartverket (terrain model & road shape)

All signals measured by Inertial Measurement Unit and filtered by a low-pass Butterworth filter with a cut-off of 5 Hz, A_y: lateral acceleration, ω_z: yaw rate, ω_x: roll rate, $\Delta(i)$: maximum minus minimum of signal i within 2-second sliding window, V_a: GNSS speed measured at antenna A (see Figure A.3).

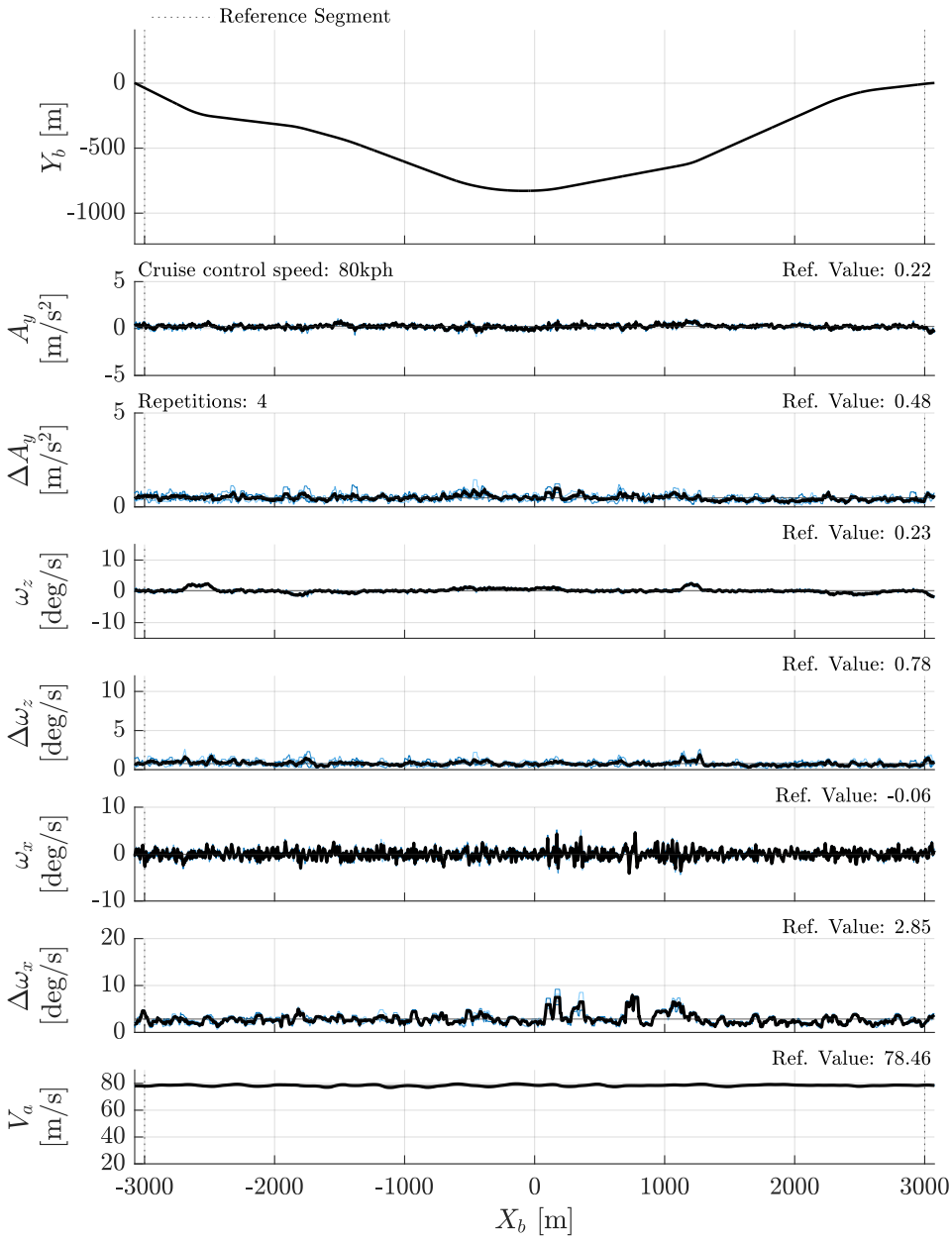

Figure 9.5: Response profile, Dovre 2, windward lane (vehicle travels left to right), see Section 9.2 for full explanation. ©Kartverket (terrain model & road shape)

All signals measured by Inertial Measurement Unit and filtered by a low-pass Butterworth filter with a cut-off of 5 Hz, A_y: lateral acceleration, ω_z: yaw rate, ω_x: roll rate, $\Delta(i)$: maximum minus minimum of signal i within 2-second sliding window, V_a: GNSS speed measured at antenna A (see Figure A.3).

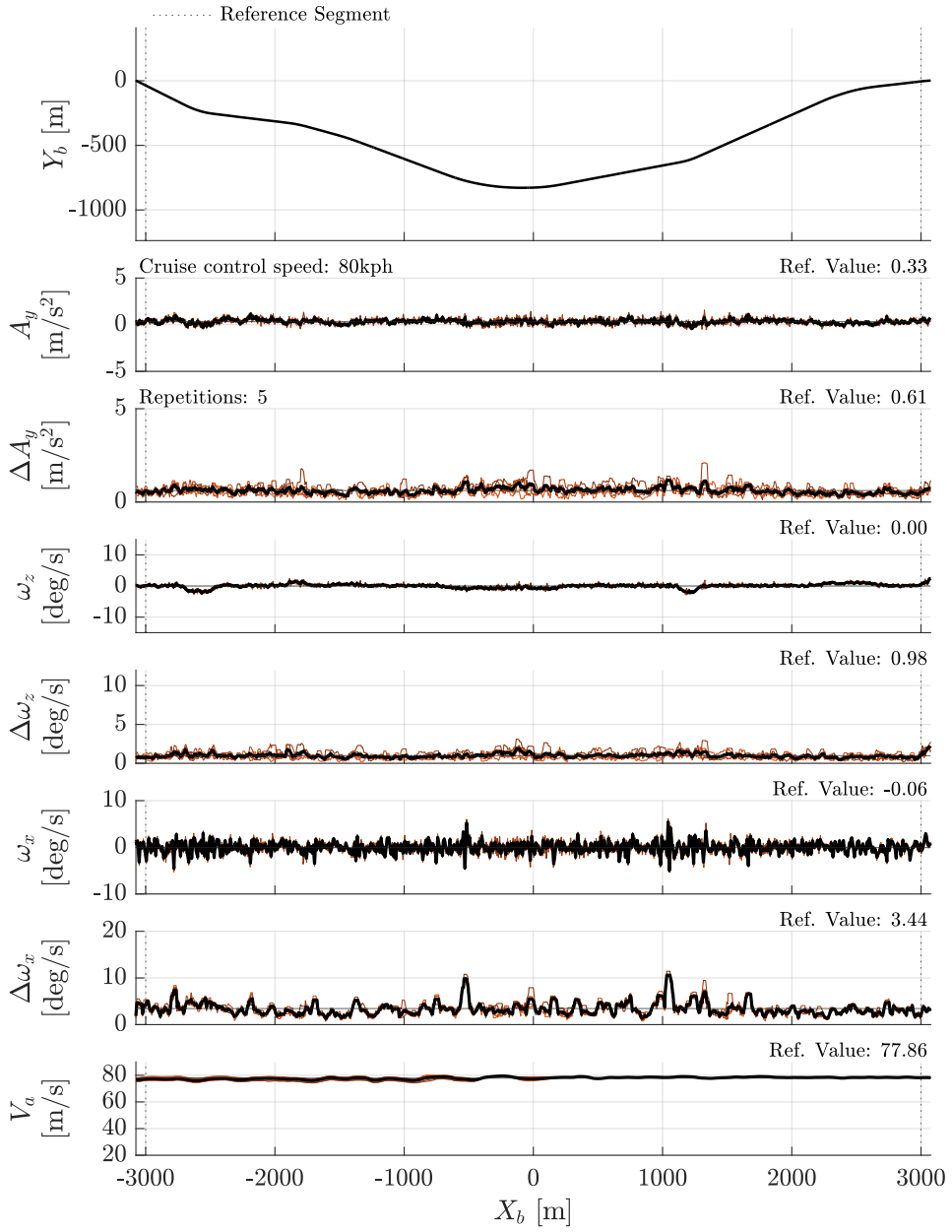

Figure 9.6: Response profile, Dovre 2, leeward lane (vehicle travels right to left), see Section 9.2 for full explanation. ©Kartverket (terrain model & road shape)

All signals measured by Inertial Measurement Unit and filtered by a low-pass Butterworth filter with a cut-off of 5 Hz, A_y: lateral acceleration, ω_z: yaw rate, ω_x: roll rate, $\Delta(i)$: maximum minus minimum of signal i within 2-second sliding window, V_a: GNSS speed measured at antenna A (see Figure A.3).

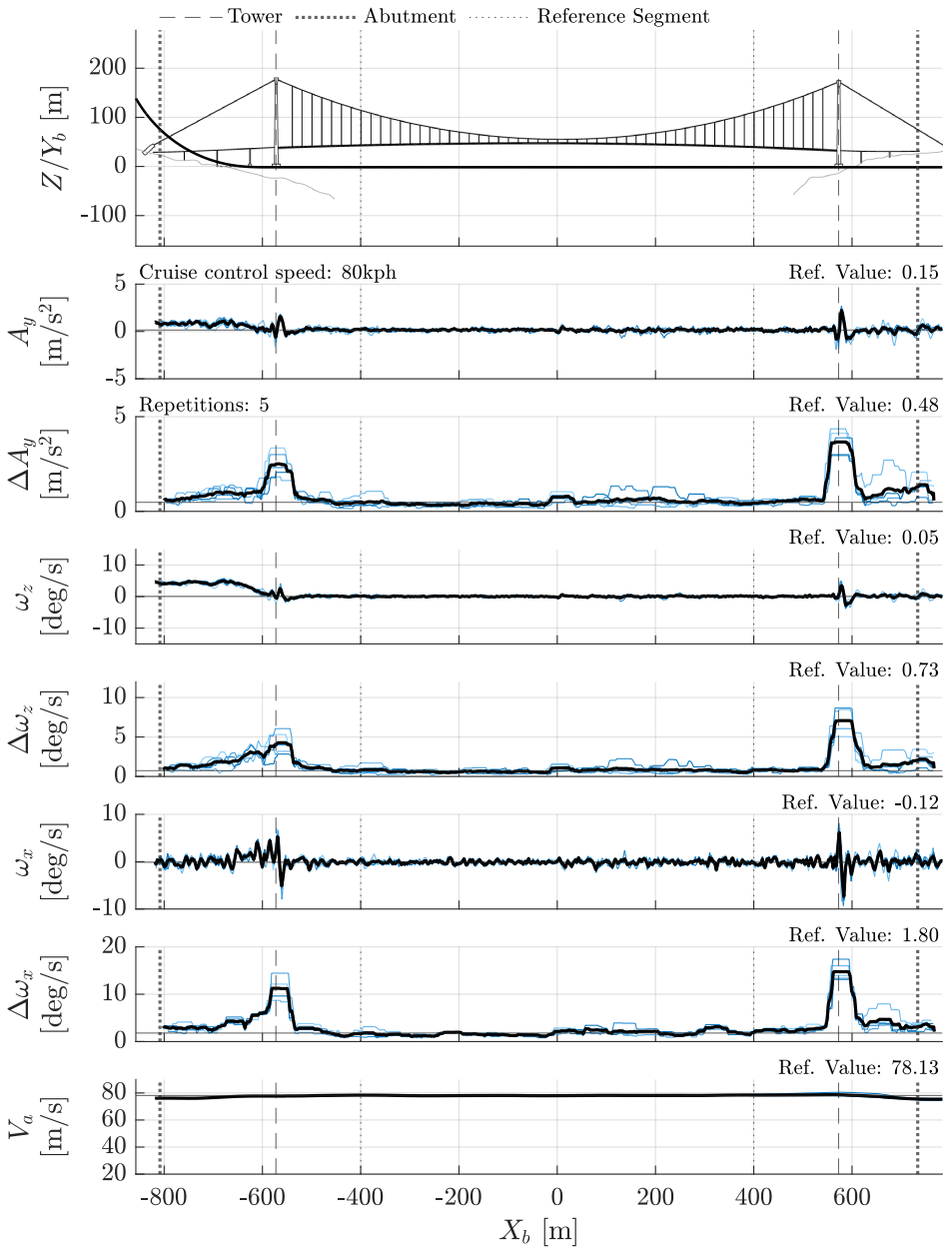

Figure 9.7: Response profile, Hålogaland bridge, windward lane (vehicle travels left to right), see Section 9.2 for full explanation. ©Kartverket (terrain model & road shape)

All signals measured by Inertial Measurement Unit and filtered by a low-pass Butterworth filter with a cut-off of 5 Hz, A_y: lateral acceleration, ω_z: yaw rate, ω_x: roll rate, $\Delta(i)$: maximum minus minimum of signal i within 2-second sliding window, V_a: GNSS speed measured at antenna A (see Figure A.3).

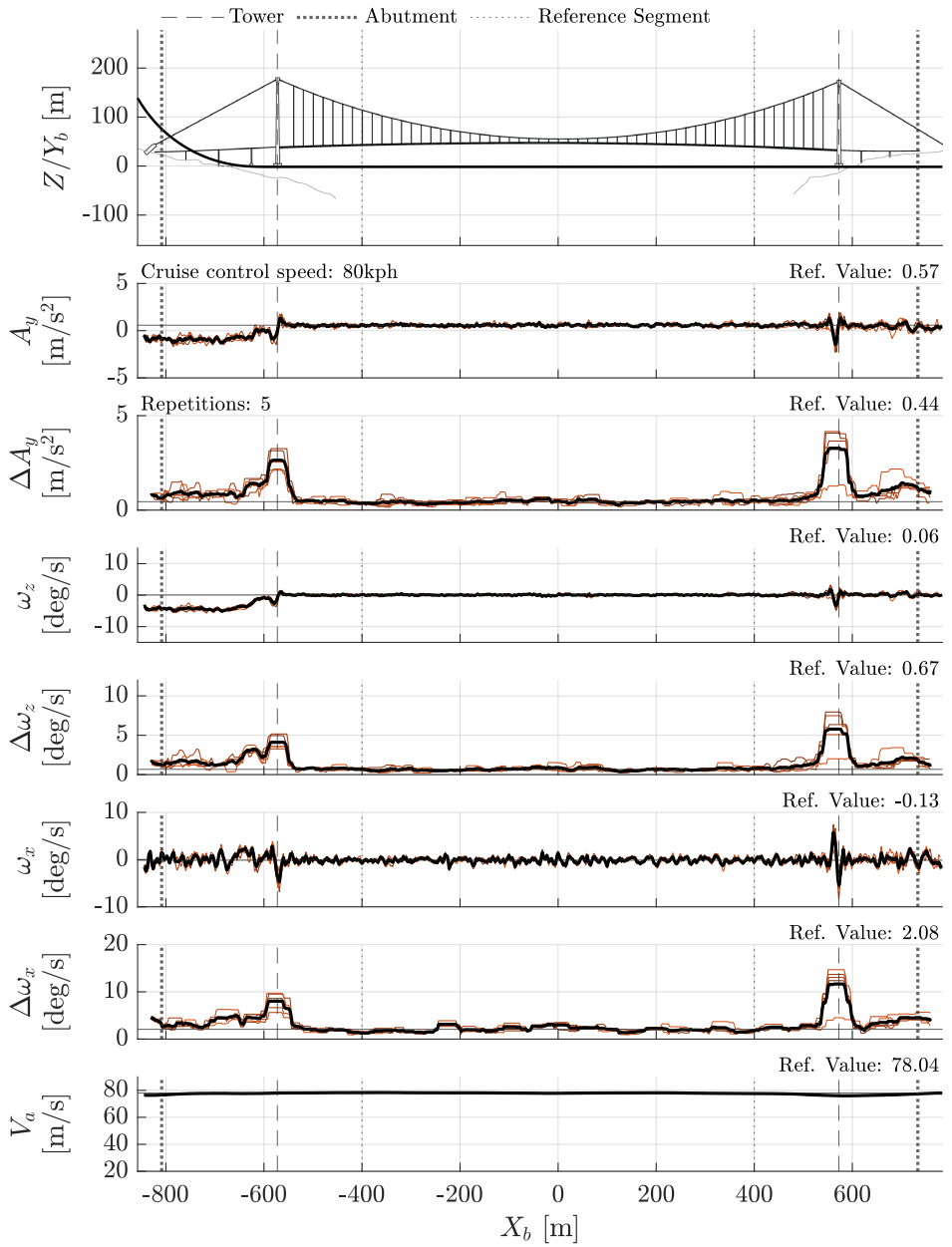

Figure 9.8: Response profile, Hålogaland bridge, leeward lane (vehicle travels right to left), see Section 9.2 for full explanation. ©Kartverket (terrain model & road shape)

All signals measured by Inertial Measurement Unit and filtered by a low-pass Butterworth filter with a cut-off of 5 Hz, A_y: lateral acceleration, ω_z: yaw rate, ω_x: roll rate, $\Delta(i)$: maximum minus minimum of signal i within 2-second sliding window, V_a: GNSS speed measured at antenna A (see Figure A.3).

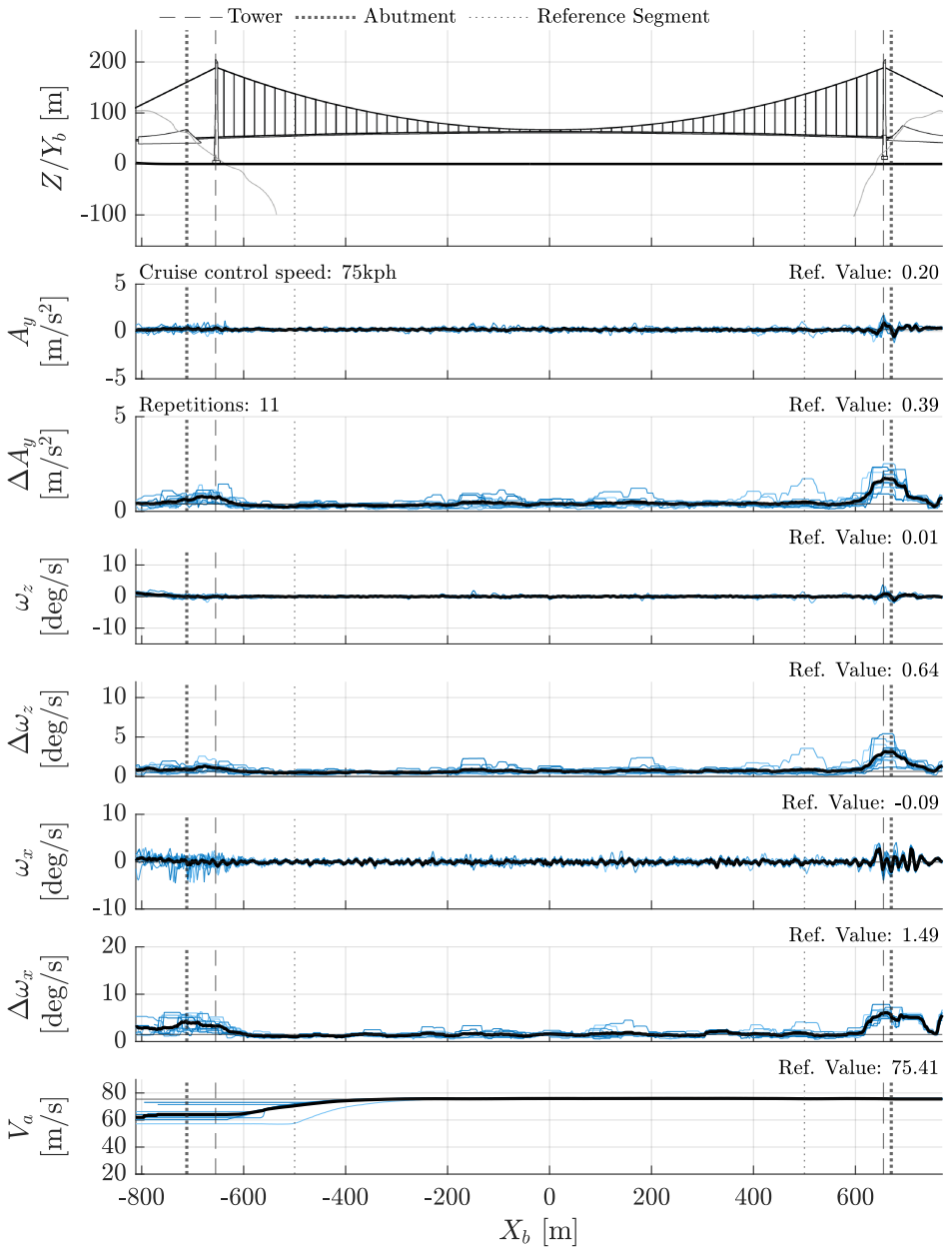

Figure 9.9: Response profile, Hardanger bridge, windward lane (vehicle travels left to right), see Section 9.2 for full explanation. ©Kartverket (terrain model & road shape)

All signals measured by Inertial Measurement Unit and filtered by a low-pass Butterworth filter with a cut-off of 5 Hz, A_y: lateral acceleration, ω_z: yaw rate, ω_x: roll rate, $\Delta(i)$: maximum minus minimum of signal i within 2-second sliding window, V_a: GNSS speed measured at antenna A (see Figure A.3).

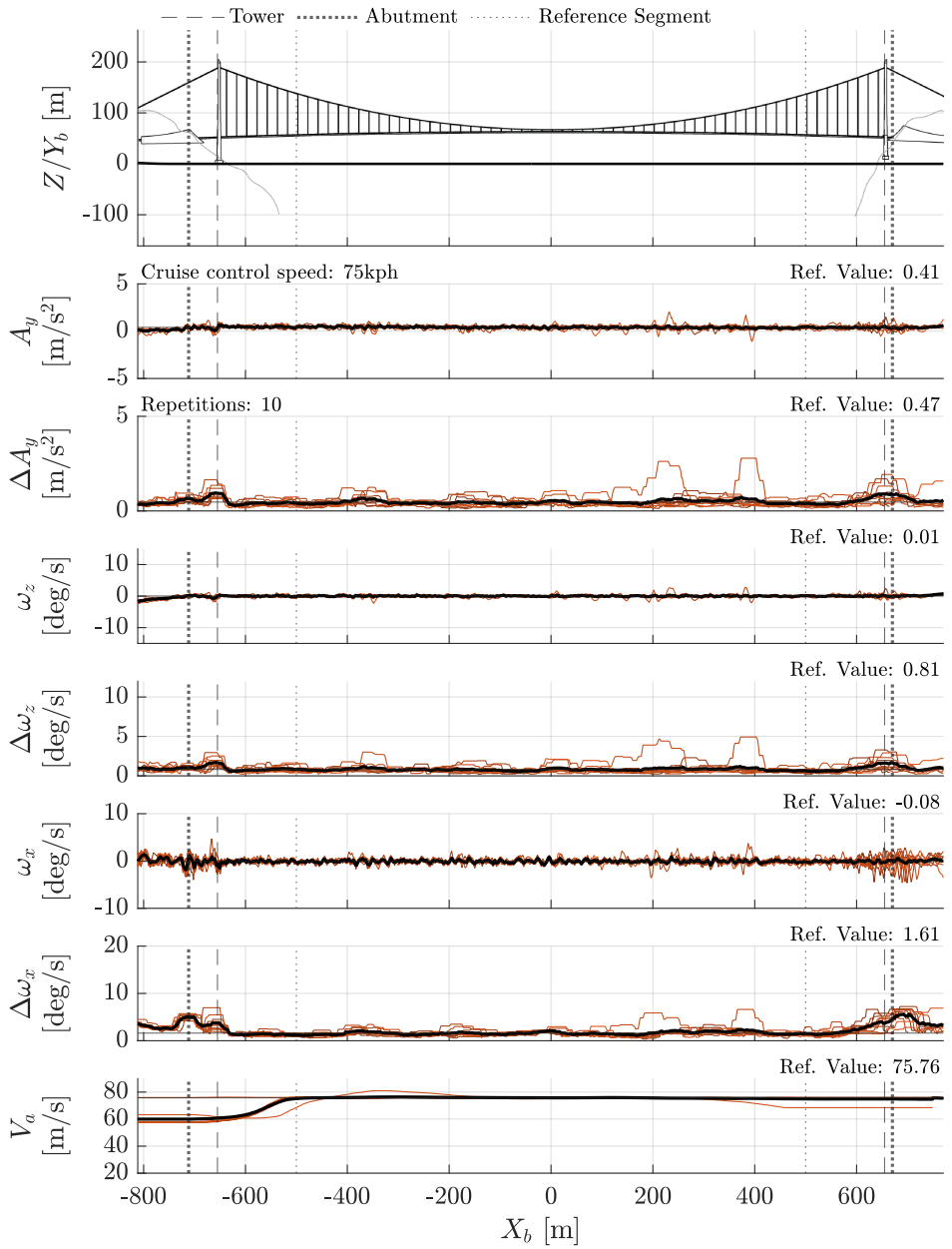

Figure 9.10: Response profile, Hardanger bridge, leeward lane (vehicle travels right to left), see Section 9.2 for full explanation. ©Kartverket (terrain model & road shape)

All signals measured by Inertial Measurement Unit and filtered by a low-pass Butterworth filter with a cut-off of 5 Hz, A_y: lateral acceleration, ω_z: yaw rate, ω_x: roll rate, $\Delta(i)$: maximum minus minimum of signal i within 2-second sliding window, V_a: GNSS speed measured at antenna A (see Figure A.3).

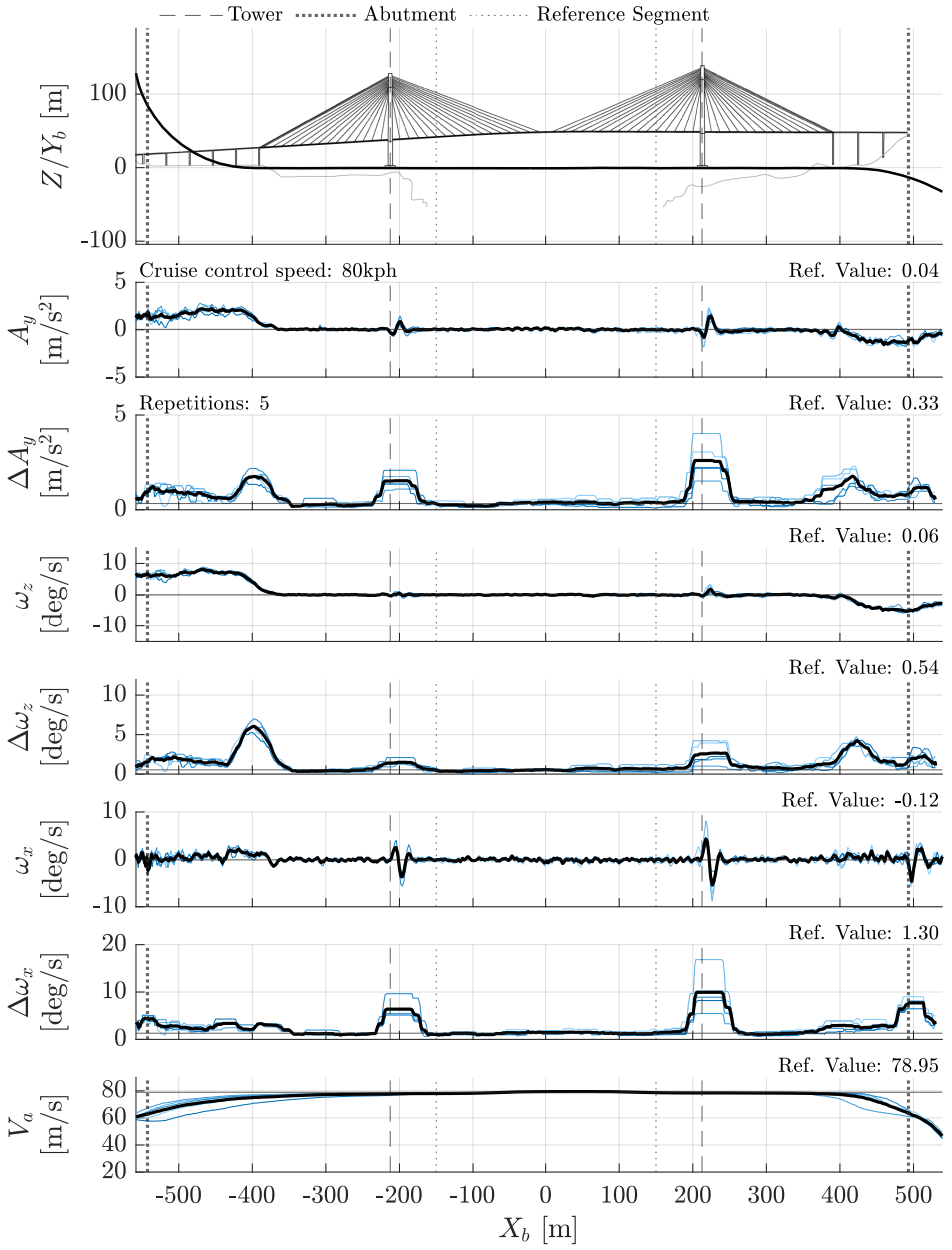

Figure 9.11: Response profile, Helgeland bridge, windward lane (vehicle travels left to right), see Section 9.2 for full explanation. ©Kartverket (terrain model & road shape)

All signals measured by Inertial Measurement Unit and filtered by a low-pass Butterworth filter with a cut-off of 5 Hz, A_y: lateral acceleration, ω_z: yaw rate, ω_x: roll rate, $\Delta(i)$: maximum minus minimum of signal i within 2-second sliding window, V_a: GNSS speed measured at antenna A (see Figure A.3).

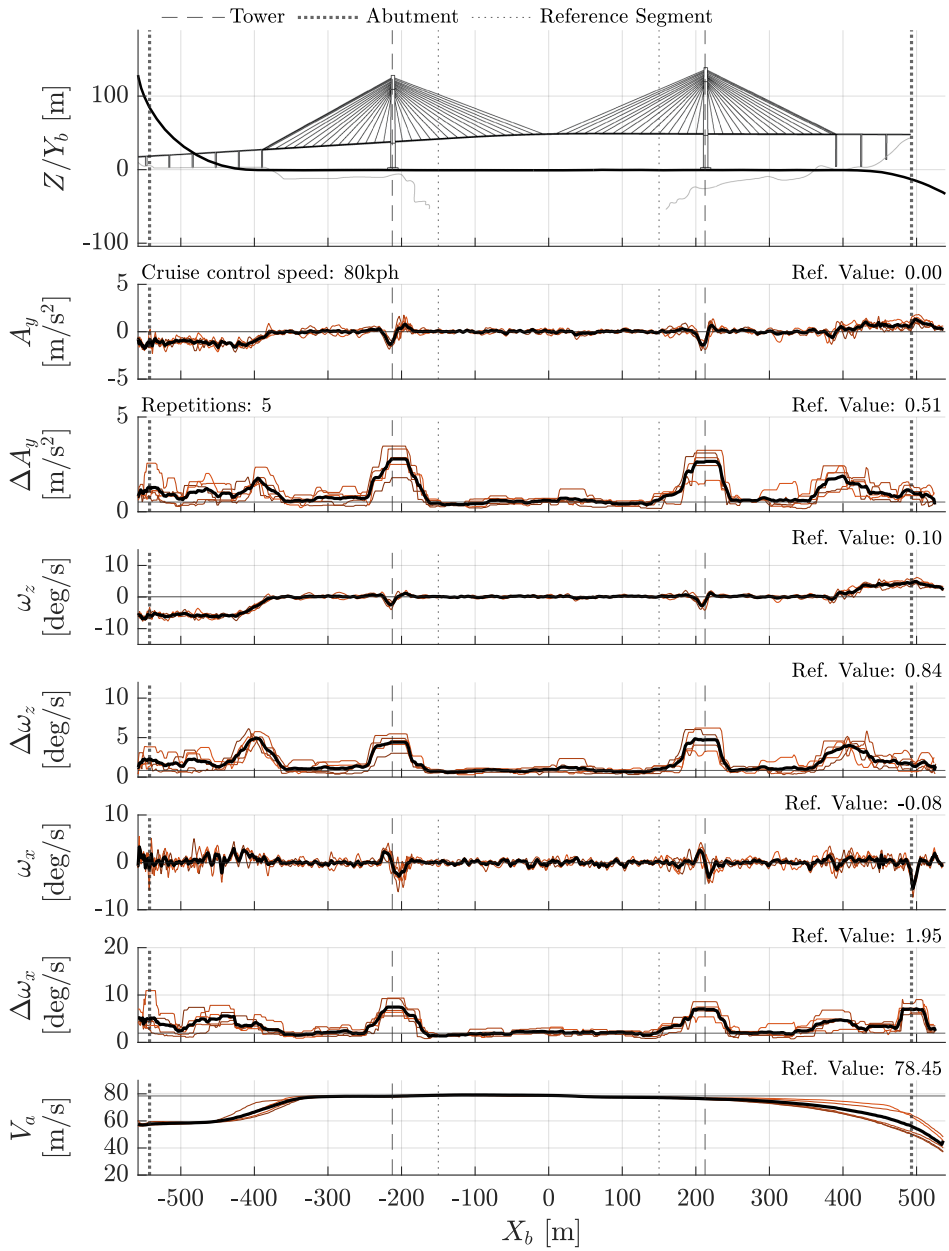

Figure 9.12: Response profile, Helgeland bridge, leeward lane (vehicle travels right to left), see Section 9.2 for full explanation. ©Kartverket (terrain model & road shape)

All signals measured by Inertial Measurement Unit and filtered by a low-pass Butterworth filter with a cut-off of 5 Hz, A_y: lateral acceleration, ω_z: yaw rate, ω_x: roll rate, $\Delta(i)$: maximum minus minimum of signal i within 2-second sliding window, V_a: GNSS speed measured at antenna A (see Figure A.3).

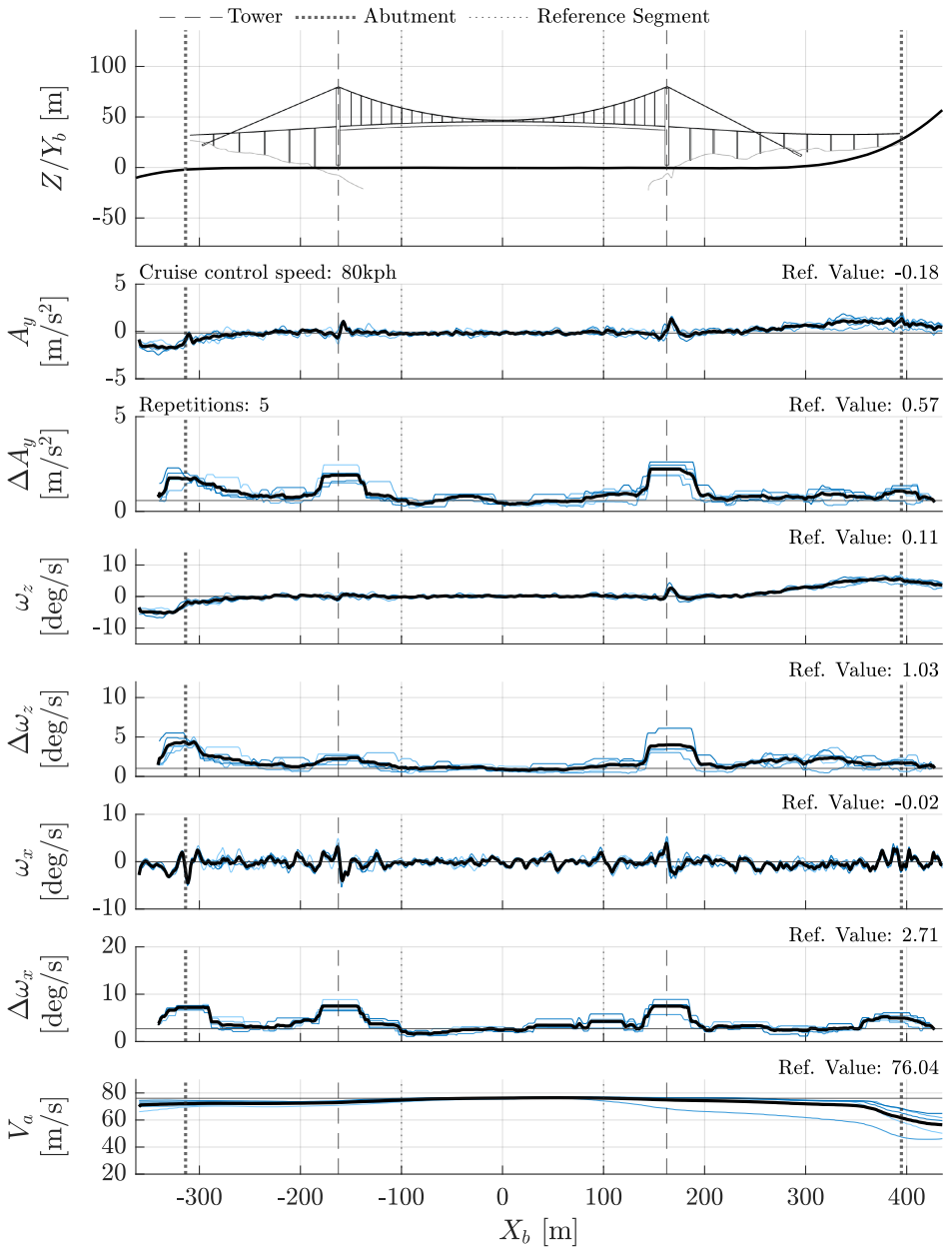

Figure 9.13: Response profile, Nærøysund bridge, windward lane (vehicle travels left to right), see Section 9.2 for full explanation. ©Kartverket (terrain model & road shape)

All signals measured by Inertial Measurement Unit and filtered by a low-pass Butterworth filter with a cut-off of 5 Hz, A_y: lateral acceleration, ω_z: yaw rate, ω_x: roll rate, $\Delta(i)$: maximum minus minimum of signal i within 2-second sliding window, V_a: GNSS speed measured at antenna A (see Figure A.3).

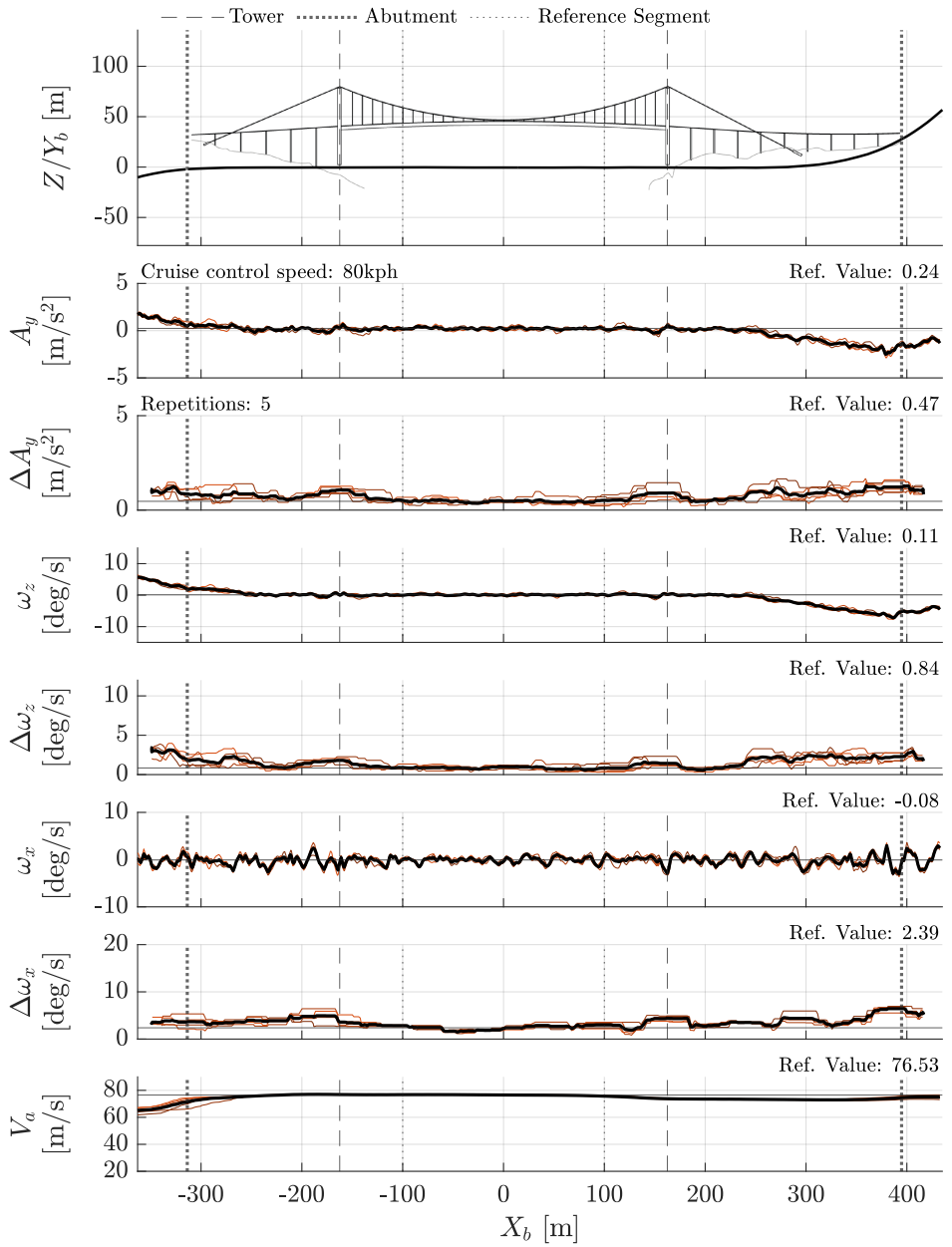

Figure 9.14: Response profile, Nærøysund bridge, leeward lane (vehicle travels right to left), see Section 9.2 for full explanation. ©Kartverket (terrain model & road shape)

All signals measured by Inertial Measurement Unit and filtered by a low-pass Butterworth filter with a cut-off of 5 Hz, A_y: lateral acceleration, ω_z: yaw rate, ω_x: roll rate, $\Delta(i)$: maximum minus minimum of signal i within 2-second sliding window, V_a: GNSS speed measured at antenna A (see Figure A.3).

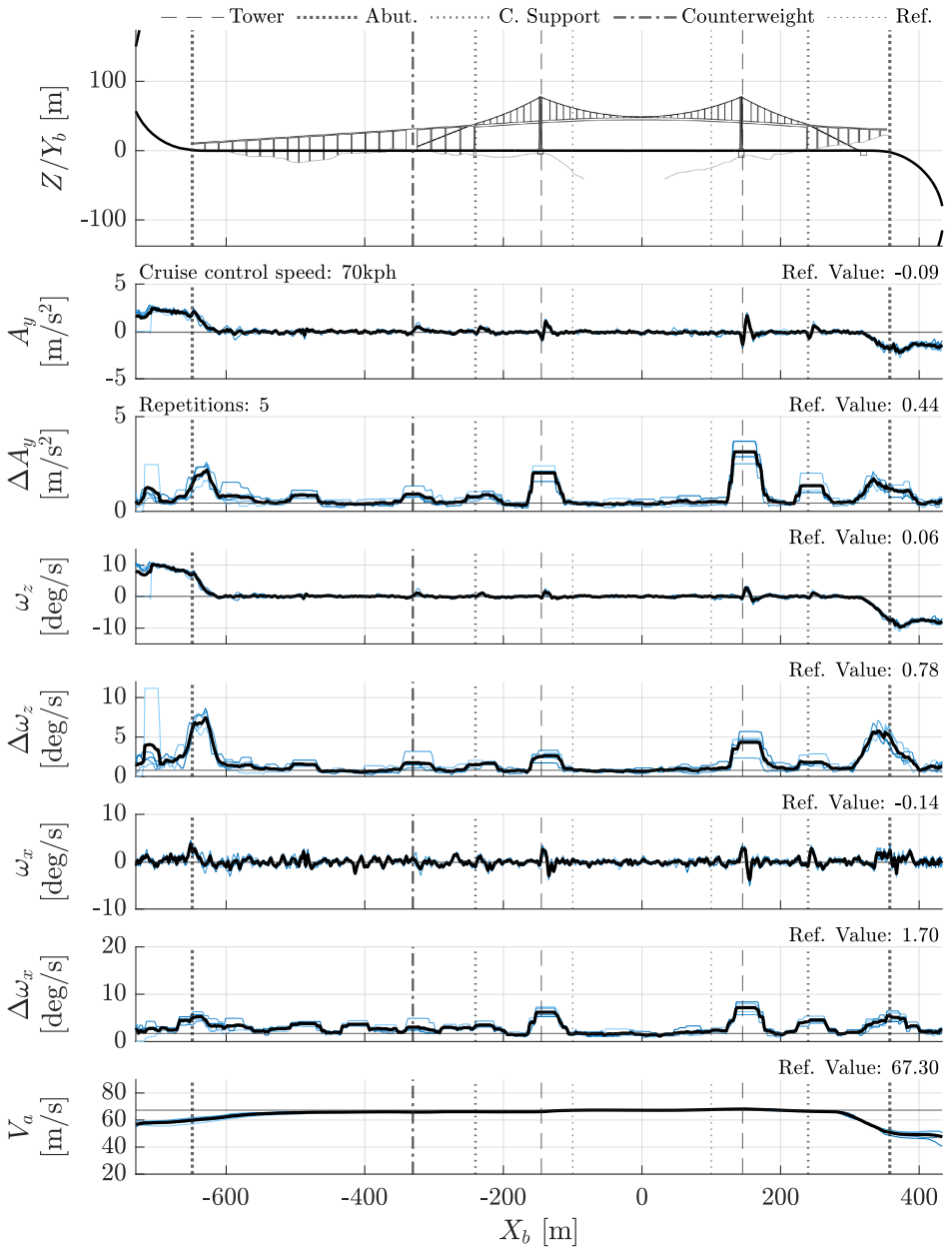

Figure 9.15: Response profile, Tjeldsund bridge 2, windward lane (vehicle travels left to right), see Section 9.2 for full explanation. ©Kartverket (terrain model & road shape)

All signals measured by Inertial Measurement Unit and filtered by a low-pass Butterworth filter with a cut-off of 5 Hz, A_y: lateral acceleration, ω_z: yaw rate, ω_x: roll rate, $\Delta(i)$: maximum minus minimum of signal i within 2-second sliding window, V_a: GNSS speed measured at antenna A (see Figure A.3).

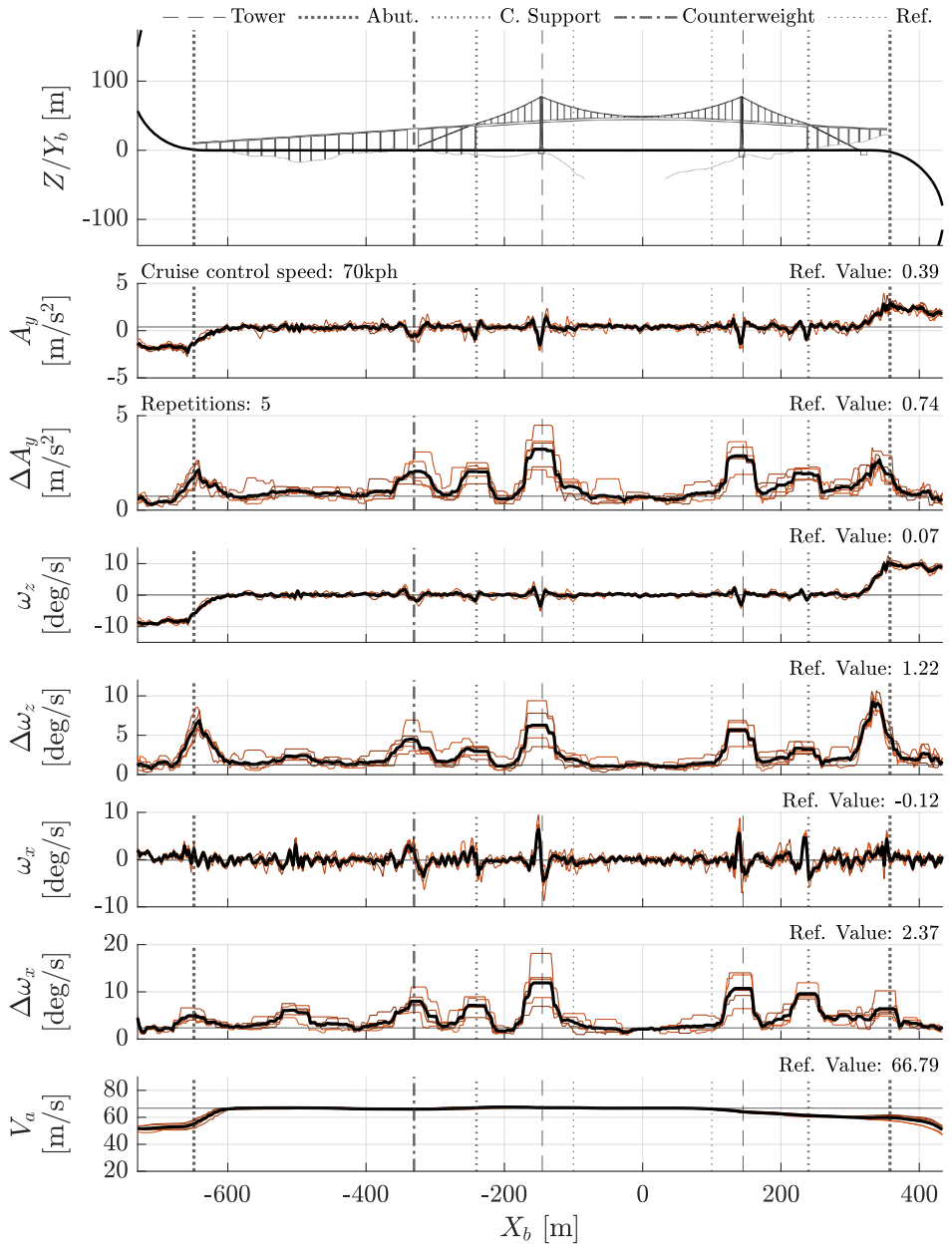

Figure 9.16: Response profile, Tjeldsund bridge 2, leeward lane (vehicle travels right to left), see Section 9.2 for full explanation. ©Kartverket (terrain model & road shape)

All signals measured by Inertial Measurement Unit and filtered by a low-pass Butterworth filter with a cut-off of 5 Hz, A_y: lateral acceleration, ω_z: yaw rate, ω_x: roll rate, $\Delta(i)$: maximum minus minimum of signal i within 2-second sliding window, V_a: GNSS speed measured at antenna A (see Figure A.3).

9.3 Discussion

Response on the main spans

In general, there are not many notable features of the response on the main spans. Particularly at the cable-supported bridges – Hålogaland in Figures 9.7-9.8, Hardanger in 9.9-9.10, Helgeland 9.11-9.12, Nærøysund in 9.13-9.14 and Tjeldsund in 9.15-9.16 – A_y and ω_z show some small oscillations, but reference values of ΔA_y (mean value across the drawn reference segment) are low (typically ~ 0.5 m/s^2 which corresponds roughly to peak values of 0.25 m/s^2 in A_y). This indicates that wind perturbations of the vehicle-driver system are not severe and certainly less significant than those seen in response to the predictable gusts discussed next (at the tower and other obstructions to the wind). Nonetheless, there are some consistent effects of lane/direction and driving speed on the mean and peak response that will be discussed in Chapter 10. There are also some outliers:

- There are hat-shaped features in all three amplitude-of-change signals Δ at $X_b \approx 400$ m for one repetition on the Hardanger bridge in the leeward lane (Figure 9.10). This was caused by a sudden step-shaped gust and was described as a front-axle skid event in the field notes.
- It has not been plotted (because it was recorded at 60 kph), but similar hat-shaped features have been observed at the Helgeland bridge in response to driving past a pair of tractor-trailers (with the test vehicle in the leeward lane).

These outliers will also be discussed in more detail in Chapter 10.

Response to predictable gusts

There are some repeated hat-shaped features – that are visible in the mean signals and not just individual repetitions – at each of the bridges as well. The most obvious ones are those seen at the towers (see Figures 9.7 and 9.8 of Hålogaland for an example). At Tjeldsund (Figures 9.15 and 9.16), the hat shape is evident at the cable support piers (indicated by vertical lines in the figures) and at the counterweight. The response looks slightly different in each repetition, but there is a similar response in each and all the individual signals lie close to the mean curve. These predictable gusts will be discussed further in Chapter 11. It will be shown that these structural elements of the bridge create gusts of a similar scale and that a certain range of gust scales is critical to vehicle-driver crosswind sensitivity (as posited in Chapter 2).

There are also hat-shaped features in the $\Delta\omega_x$ signals in the windward lane at Dolmsund (Figure 9.1). This is thought to be associated with the transition from

fixed-base road to bridge girder. The hat shape is evident in ΔA_y as well, albeit less clearly. This would appear to be a less critical wind feature given that the response is primarily in roll and is not so severe in handling. It will be shown that the step-shaped gusts observed at abutments are in some cases of a critical scale. This will be discussed further along with the gusts seen at the cable stays and suspension hangers in Chapter 11.

Response to stochastic gusts

The front-axle skid event that was observed at the Hardanger bridge was also experienced at Dovre (unfortunately this was not during one of the recorded sessions) and at the Dolmsund bridge. In all of these cases, the cause was not a predictable gust like those just described. Instead, it will be shown that there was a higher level of turbulence – increasing the likelihood of observing significant (high amplitude) gusts of a critical scale – at certain locations. At Hardanger it is argued that the higher proportion of critical gusts is caused by the *far-away* (>1 km) complex terrain causing an increase in atmospheric turbulence.

At Dolmsund, it is argued that there is a higher proportion of critical gusts due to the separation of the flow over the bridge's bluff girder cross-section. In fact, the difference between the windward (where separation is unlikely to perturb the vehicle) and the leeward lane (where separation is more likely to perturb the vehicle) is clear to see by comparing Figures 9.1 (windward) and 9.2 (leeward). The difference is directly evident in the variability between repetitions (particularly in A_y) and is also reflected in the reference values (0.82 in the leeward versus 0.49 in the windward for ΔA_y).

The increased likelihood of encountering severe stochastic gusts that are of a critical scale will be discussed further in Chapter 12.

Chapter 10

Response on the main spans

In this chapter, observations of the response of the vehicle to *natural* wind turbulence on the main spans of the bridges is presented. It is shown – under the strong crosswinds observed during the field experiments – that the vehicle response sometimes exceeds the upper limit of the small-signal range (0-0.5 m/s^2), but generally remains within. The effects of driving direction/lane and driving speed are discussed and some examples of extreme response on the main span are described. These observations add to a general, evidence-based understanding of wind-related risks to vehicles on the main span of bridges.

10.1 Background

As evidenced by the systematic literature mapping in Chapter 4, there is an interest in describing and predicting the aerodynamic loads acting on vehicles travelling on bridge girders. Some key conclusions from the literature relevant to the current chapter are:

- The static aerodynamic coefficients – as a function of yaw angle – for a vehicle on a bridge girder are different to the coefficients for the same vehicle on the ground. The coefficients are further dependent on the lateral placement of the vehicle on the girder (i.e. which lane the vehicle is in). The girder has the effect of slowing the flow down relative to the free-stream (at vehicle height above the upper deck surface). See [38, 46, 71, 92].
- Certain incidence angles of skew winds (winds that are not perpendicular to the bridge) are critical with respect to the magnitude of aerodynamic loads on the vehicle. This will be a function of the driving speed, driving direction and the girder geometry. See [38, 113].
- Reducing vehicle speed can be an effective method to reduce undesirable vehicle response on bridges [113].

- The non-trivial aerodynamic behaviour when two oncoming vehicles pass one another on a bridge can induce large changes in aerodynamic loads on the vehicle, in some cases comparable to passing through the wake of a bridge tower. See [132, 133].

10.2 Mean/peak wind and response on main spans

In Chapter 8, a segment of the road on each bridge was defined to provide reference values of wind speed and direction. On bridges, the reference segment is a symmetric portion (about the midspan) of the main span. On fixed-base roads, the reference segment is almost the entirety of the road used during the field sessions.

The flow in the reference segment is assumed to have the characteristics of what Sims-Williams [178] calls *natural wind turbulence*. The flow is influenced by local topography and bridge geometry to a lesser degree than, for example, in proximity to the abutments or the towers respectively. On fixed-base roads, it is assumed that the collection of obstructions to the wind alongside the road form a homogeneous group. The fixed-base roads are included in the current analysis for reference.

Figure 10.1 shows the mean and peak wind speeds in the reference segments at each location, driving speed and lane of travel in the first plot (10.1a) followed by the mean wind direction (10.1b). The grey, dashed lines separate the clusters of data sets by location. Generally, the graph shows that the mean and peak wind speeds in the reference segments were consistent during the measurement period (stationary between the repetitions at each driving speed). This is evidenced by the general consistency in bar height within each cluster. An exception is the case of Helgeland (both lanes) and Nærøysund (windward lane) where clipping is evident and gives the impression that the wind speeds were lower at the higher driving speeds (where clipping has the most impact on the results).

Note that there is no data set where there was truly no wind. The Dovre 1 data set is the closest, yet even here the mean wind speed was between 3-4 m/s and there were gusts up to 10-15 m/s. Figure 8.4 shows that the higher wind speeds were fairly localised between ~ -4000 and ~ -2000 m. It was concluded in Chapter 8 that the forward pressure wave of the vehicle could be responsible for 1-3 m/s.

Consequently, the Dovre 1 data set will be considered a still-wind case. The weather was clear on the day of testing and no other sources of perturbations were observed (other than road undulations). The vehicle was driven using cruise control in the same manner as in the collection of all other data series. The stretch of highway driven is a typical example of a Norwegian rural highway ($\sim$ 7.5 m wide with 1 m shoulder) with a speed limit of 80 kph. The vehicle was driven according to the speed limit and no incidents of instability or particular discomfort were noted. The data from Dovre 1 shows what a typical lateral response is to un-

perturbed (no wind) driving on a typical Norwegian road. Many of the roads that cross the bridges visited during the field sessions are of a similar type to Dovre 1 (the E6 between Vålåsjøen and Dombås).

Figure 10.2 shows the mean and peak change-of-amplitude of the handling response signals (ΔA_y and $\Delta\omega_z$) for each of the test locations clustered by driving speed and separated by lane/direction of travel. Brandt et al.'s [32] threshold values for driver perceived instability events are plotted as horizontal lines along with the peak value at Dovre 1 (still-wind, comfortable). Assuming that peak values are about half the amplitude-of-change value for straight-line driving (i.e. the response to perturbations look like single oscillations with equal magnitude above and below the zero-axis), then the upper limit of the small-signal range is $\Delta A_y = 1$ m/s^2. This line has also been plotted to give a rough indication as to the classification of the response into the small-signal or linear range. Note that the response is typically below the upper limit of the small-signal range (A_y = 0-0.5 m/s) which is the expected range of response for straight-line driving according to [164].

10.3 Effect of direction/lane

There is a consistent difference in the mean values recorded in the leeward and windward lanes within each location cluster. For example, at Helgeland the leeward lane is more critical at each speed with the red bars being about twice the height of the blue ones at 60 and 70 kph in ΔA_y. At Nærøysund the opposite is true; the windward lane is critical.

Interestingly, Nærøysund seems to be an outlier in that the windward response is definitively higher than the leeward. The blue bars at Hålogaland and Tjeldsund 1 are also higher than their red counterparts – and at Hålogaland consistently so between driving speeds – though the difference is very small.

Generally, the peak value is higher in the lane where the mean value is higher and vice versa. The few examples where this is not the case are where the mean values are very similar in value, for example at Tjeldsund 1 or Hålogaland at 30 kph (in both ΔA_y and $\Delta\omega_z$). With respect to the effect of lane/direction, the results are consistent between the lateral acceleration and the yaw rate.

There is therefore typically one lane or direction of travel in which the mean and peak change-of-amplitude in handling response is higher. This is likely the result of different wind loading resulting from the presence of different wind conditions in the two parallel lanes as well as the contribution from the driving speed. If the wind is skew (not perpendicular to the road axis), then an amplification of the resultant wind vector is expected in one direction (driving partly into the wind) and an attenuation in the opposite direction (driving partly with the wind).

The most significant differences between lanes are seen at Helgeland, Nærøysund and Dolmsund. At Helgeland and Nærøysund the wind is skew, with a refer-

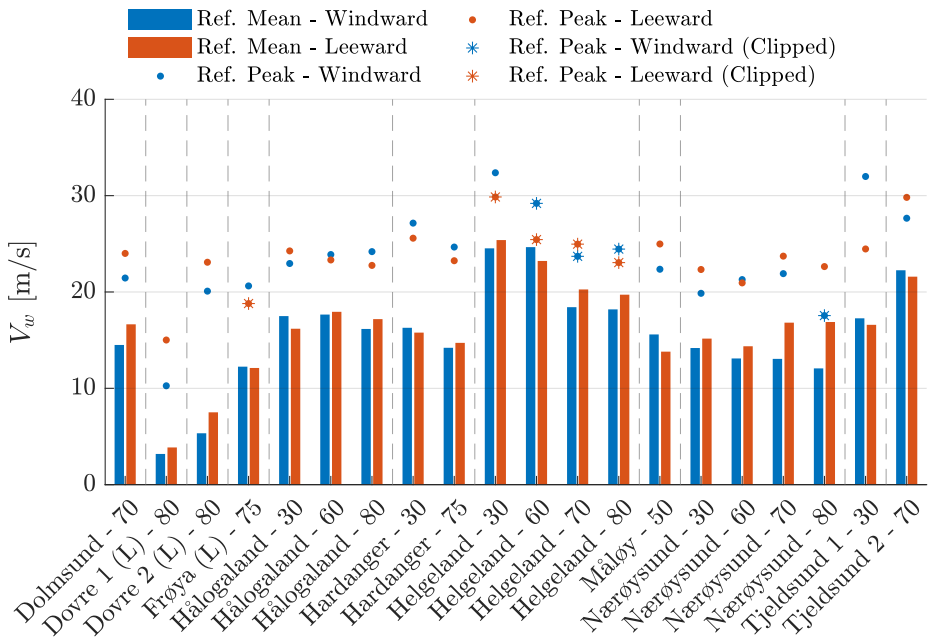

(a) Wind speed

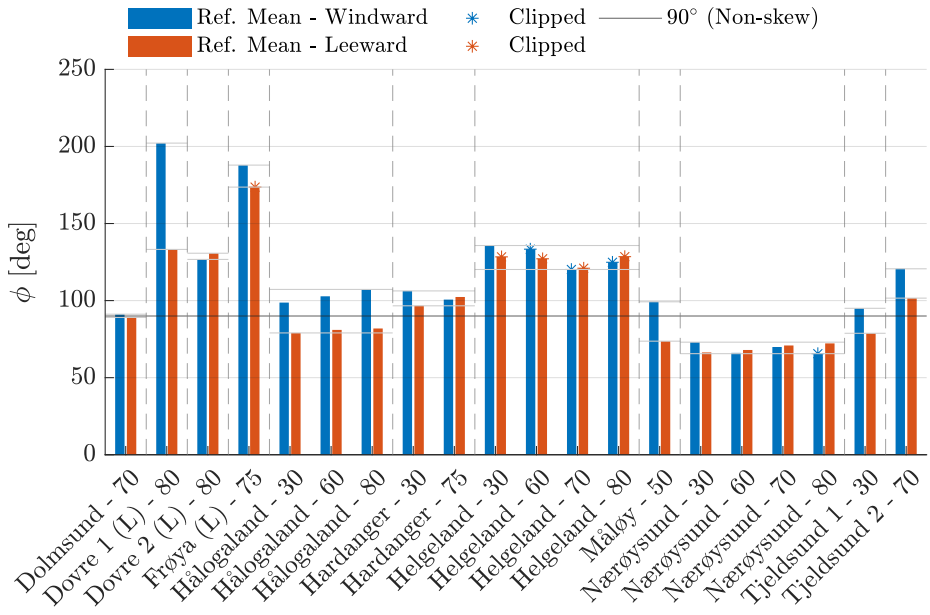

(b) Wind incidence angle

Figure 10.1: A comparison of wind measurements within the reference segments at each test location. The letter L is used to indicate fixed-base roads as opposed to bridges.

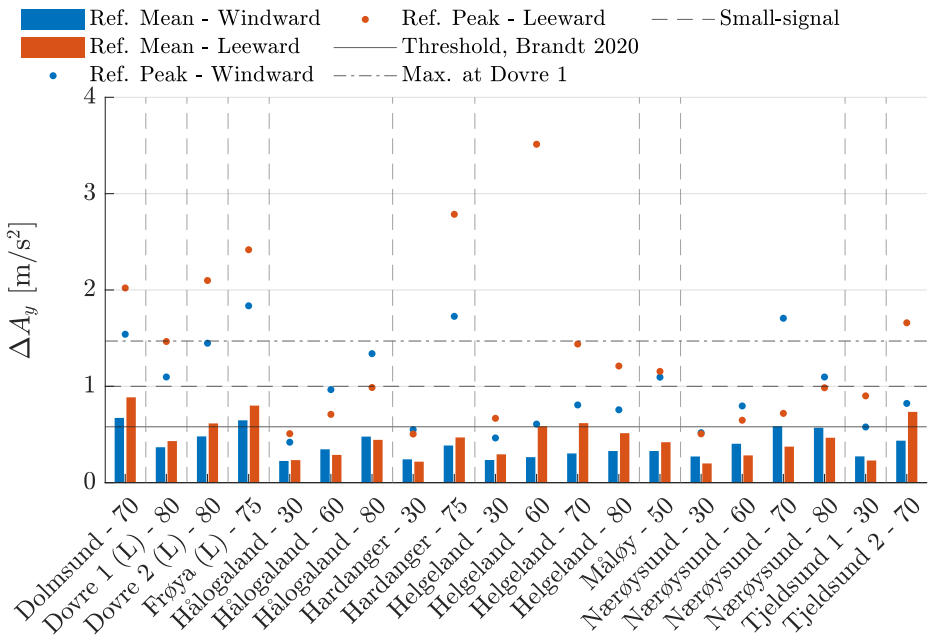

(a) Lateral acceleration

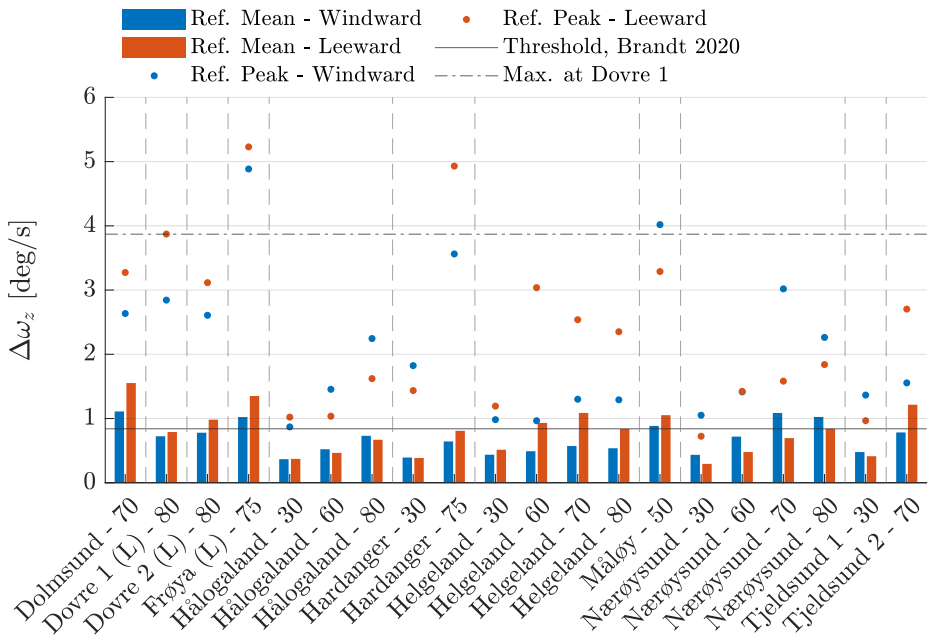

(b) Yaw rate

Figure 10.2: A comparison of mean and peak handling response within the reference segments at each test location. The letter L is used to indicate fixed-base roads as opposed to bridges.

ence segment mean angle of incidence to the bridge axis of 120-135° (lower bound subject to clipping, the true value is likely higher) and 65-70° respectively (see Figure 10.1b). The skewness is likely a big contributor to the difference in response between the two lanes. At Nærøysund at 70 kph, there is a difference in mean ΔA_y between the two lanes of 104% and at Helgeland (70 kph) the value is 57%.

At Dolmsund the wind was not skew, but in fact very close to perpendicular. Nonetheless, the statistics show a difference between the two lanes (32% in ΔA_y at 80 kph) and particular note was made of this during the field session. The experience of driving the vehicle in the leeward lane was described as much less stable/controllable. In Chapter 8, it was shown that cantilevered bridges like Dolmsund have thick, bluff cross-sections of varying thickness that can have a significant impact on the wind characteristics over the bridge deck. It could be that the wind characteristics (turbulence) simply vary significantly from the leeward to the windward lane and that this explains the difference in handling response. The effect of separation-induced turbulence (from the girder) on response will discussed further in Chapter 12.

10.4 Effect of driving speed

Within each cluster in Figure 10.2 the effect of driving speed is fairly clear. Both handling responses – lateral acceleration ΔA_y and yaw rate $\Delta \omega_z$ – increase in mean value with speed. In most cases, the relationship is a monotonically increasing one. The exceptions are the critical lanes at Helgeland (leeward, red) and Nærøysund (windward, blue) where the mean response appears to peak at a similar value (just below Brandt et al.'s threshold in ΔA_y and just above in $\Delta \omega_z$) and at 70 kph. Interestingly, for the subset of bridges only (ignoring fixed-based measurements), these mean values are also among the highest, approximately matching a third high value in the leeward lane at Tjeldsund 2.

There is nothing to indicate that the characteristics of the wind were different in the 70 kph case looking at Figure 10.1 of wind speed and direction. Though a potential difference at Helgeland would be masked by clipping, it cannot conclusively be stated that the wind was not different at 70 kph compared to the crossings at the other speeds.

Another factor that may explain the maximum value at 70 kph is the order of execution of the crossings. At Helgeland, the 70 kph crossings were executed first. The driving style may have changed during the field session. An attempt to maintain stricter control was likely used at the start that changed into a more passive driving style towards the end. In Chapter 2 it was explained that Schaible [170], Wagner and Wiedemann [205] and MacAdam et al. [135] all suggest that trying to maintain strict control could have the effect of amplifying the lateral motion of the vehicle.

On the other hand, at Nærøysund the 70 kph sessions were performed at the end of the session. In this case the response may have worsened as a result of driver tiredness. The experiments ran from 20:30 through to midnight immediately following a 5-6 hour journey to the bridge.

These are possible explanations for why 70 kph appears like a critical driving speed at two of the bridges where a generally high response was observed. Note that the road surface at Nærøysund was notably of a poorer condition than at Helgeland. This might explain the relatively high response despite the mean wind speed being significantly lower ($\sim$15 m/s at Nærøysund vs. $\sim$25 m/s at Helgeland, omitting clipped values).

In every case where the 30 kph speed was used, the mean and peak response values are consistently low with peaks only just exceeding Brandt et al. [32]'s threshold values (see Helgeland - 30 and Tjeldsund 1 - 30 in ΔA_y and all 30 kph bars in $\Delta\omega_z$). The effect of lane also seems to be reduced at the driving speed of 30 kph. Comparing peak ΔA_y at 80 kph (or 75) with 30 kph at locations where both are available:

- Hålogaland: 1.34 vs. 0.51
- Hardanger: 2.79 vs. 0.55
- Helgeland: 1.21 vs. 0.67
- Nærøysund: 1.10 vs. 0.52
- Tjeldsund (Data set 2 vs. 1): 1.66 vs. 0.90

Increases between 80% (Helgeland) and 407% (Hardanger) in peak ΔA_y have therefore been observed between driving at 30 kph and 80 kph.

The mean values of ΔA_y at each bridge lie within the small-signal range and there are only 7 data points from bridge data (i.e. not including the land-based measurements at Dovre and Frøya) where maximum values of ΔA_y exceed the upper boundary of this range ($\Delta A_y = 1$ m/s^2). At Dolmsund (80 kph) and Hardanger (75 kph) the peak values exceed this range in both lanes, suggesting perhaps that the high values are not simply outliers (some of which will be discussed in Section 10.6: *Extreme Values*). It will be seen in Chapter 12 that there was a higher level of turbulence at these bridges due to the far-field upstream topography (Hardanger) and the bluff shape of the cross-section (Dolmsund).

10.5 Roll response

Figure 10.3 shows the variance in the roll response between repetitions. As discussed in Chapter 3, the roll rate signal is typically repeatable over a given stretch of road in the still-wind case. Any variance between repetitions would therefore suggest that there is another perturbing force (i.e. aerodynamic forces).

Accordingly, in Figure 10.3 the Dovre 1 results are the absolute lowest ($\text{var}(\omega_x) \approx 0.02$ deg/s), reinforcing the theory that the variance between roll response repetitions is a good indicator of aerodynamic perturbation. The difference between Dovre 1 and Dovre 2 (≈ 0.13 deg/s) highlights this even more. While they are different segments of the same road, they are adjacent to one another and of a similar consistent quality of road and composition of curves. The difference between them in terms of variance in roll response is very likely due to wind-induced perturbations.

The effect of speed and lane in $\text{var}(\omega_x)$ appears to be consistent with the handling response plots. There is always a critical lane and the amplitude-of-change values increase monotonically with driving speed apart from in the critical lanes of Helgeland and Nærøysund where the peaks lie at 60 and 70 kph respectively.

Dolmsund, Helgeland, Nærøysund and Tjeldsund stand out as the critical cases. Dolmsund looks like an outlier with almost twice the value of the next highest values at Nærøysund and Tjeldsund. The wind-induced response was significant at this bridge due to the bridge's blunt cross-section.

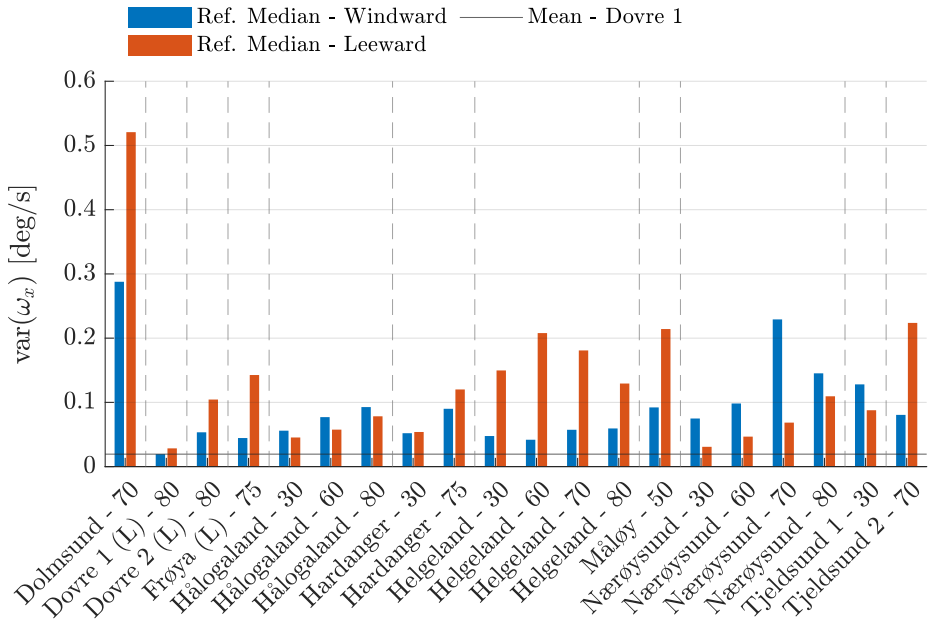

Figure 10.3: A comparison of variability in the roll rate within the reference segment at each test location. The letter L is used to indicate fixed-base roads as opposed to bridges.

10.6 Extreme Values

There are some extreme values in the bar charts just presented. Firstly, there is the high peak value of $\Delta A_y \approx 3.5$ m/s^2 in the leeward lane of Helgeland 60, which is much higher than it's windward counterpart and therefore looks like an outlier. An inspection of the response profile (not plotted, as only the data from 80kph is plotted in Figure 9.12) reveals the repetition where this peak was recorded. The change-of-amplitude of wind ΔV_w and the response ΔA_y and $\Delta \omega_z$ look like they do at the towers (a hat shape) and there are two of them closely spaced (<50 m). These have been identified as the wake of two tractor-trailers driving in succession (as was noted in the field notes). It will be seen in Chapter 11 that $\Delta A_y \approx 3.5$ m/s^2 is closer to the expected value of response to inverse gusts in the wake of bridge towers rather than that expected on the main span.

Below the outlier at Helgeland 60, there is a second highest maximum value in the leeward lane of Hardanger 75 with $\Delta A_y \approx 2.8$ m/s^2. This repetition was also noted in the field notes, in this case because a front-axle skid was observed. According to the test driver and an accompanying passenger, the front wheels slipped a short distance laterally before regaining traction. In this case, traction – and steering control – was regained quickly before the vehicle struck the safety barrier. In fact, from observation, the vehicle remained quite well within the driving lane and far from the barrier. Nonetheless, from a traffic safety perspective, this event is unacceptable. It was very uncomfortable and could have had dire consequences given a different traffic situation. It is also plausible that some drivers may respond unfavourably in such situations. A rear-axle skid (oversteer) could have had even more severe consequences.

A brief investigation of the front-axle skid event

The repetition where this occurred has been isolated and plotted in Figure 10.4. The cause of the slip event is clear to see at X_b =400 m where a sharp step-change in wind speed is seen ($\Delta V_w = 18$ m/s). This appears to be an eddy/gust in the oncoming wind and has no apparent relation to any geometrical feature of the bridge or be the result of an obvious feature of the local topography.

The lateral position of the vehicle has been plotted on the second to last set of axes. Only raw position data is available at the Hardanger bridge (the Racelogic Kalman filter cannot be initialised when travelling between two tunnels). Therefore, the position data is rather noisy and it seems to be particularly noisy around the slip event. It is difficult to say if the vehicle was shifted laterally by a significant amount (>0.5 m) from this gust. The heading angle on the last set of axes does show that the yaw/rotation of the vehicle changed by about 2° as a result of the gust.

The wind data in Figure 10.4 shows that the wind dropped to zero immediately preceding the sharp increase in wind speed (recall that the vehicle drives from right to left in the figure in the leeward lane). The natural driver reaction is to straighten the wheels as there is no longer a need to counteract the force from the crosswind. This is evident in the plot of wheel angle δ shown on the last set of axes where the 1.5 to 2.0 degrees needed to balance the crosswind and drainage angle is reduced to 1 degree (drainage angle only) immediately preceding the gust. The sharp wind then strikes while the front tyres are at a low slip angle and unable to produce the necessary lateral steering force to counteract the lateral aerodynamic force.

10.7 Conclusions

The response of the test vehicle to crosswinds on the main span of bridges has been observed to be a function of the driving direction, the lane (lateral position on the girder) and the driving speed:

- The mean resultant response of the vehicle-driver system on the main span of a bridge is a function of the driving direction when winds are skew.
  - The skew winds at Helgeland (120-135°) lead to a difference of 57% in mean ΔA_y between the two lanes at a driving speed of 70 kph.
  - At Nærøysund (65-70°), the equivalent value is 104% at the same driving speed.
- The mean resultant response is sometimes also a function of lane (windward/leeward position on the girder), especially where the girder has a bluff section.
  - At Dolmsund, a difference of 32% in mean ΔA_y was found between the windward and leeward lanes most likely due to increased turbulence in the leeward lane caused by separation of the flow over the deck.
- In general, the mean and peak response (both ΔA_y and $\Delta \omega_z$) values increase monotonically with speed.
  - Driving at 80 kph has been seen to increase the mean ΔA_y by between 80% (Helgeland) and 407% (Hardanger) compared to 30 kph. This corresponds well with expectation derived from the theory on vehicle-driver crosswind sensitivity presented in Chapter 2. Crosswind sensitivity increases with driving speed.
  - The effect of driving speed is less pronounced between 60, 70 and 80 kph.

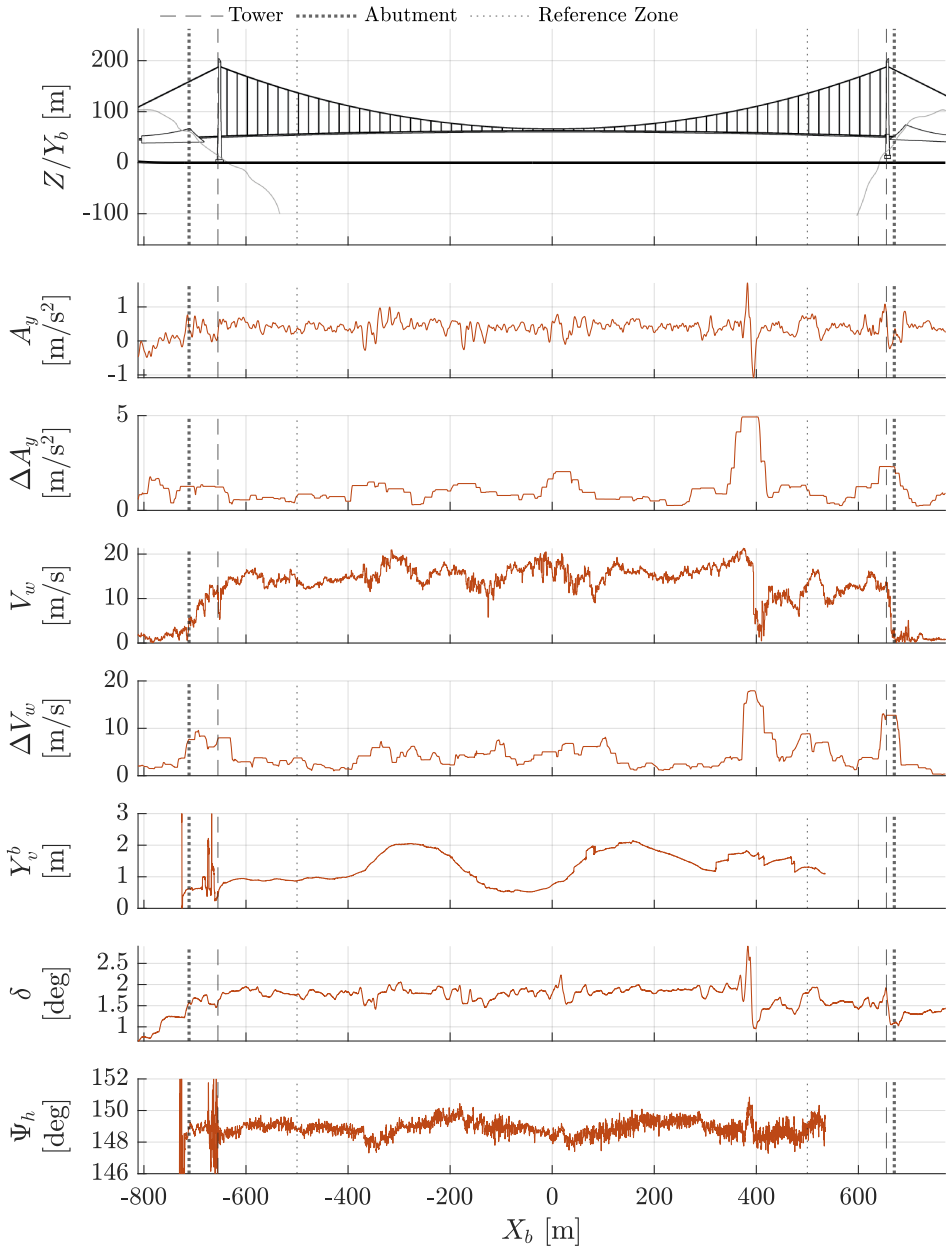

Figure 10.4: An example of a tyre slip event at the Hardanger bridge.

Note: A_y signal has been low-pass filtered with a Butterworth filter with a cut-off frequency of 5 Hz.
Y_v^b: lateral position of vehicle on Y_b axis.

- A front-axle skid event was observed on the Hardanger bridge where $\Delta A_y = 2.8$ m/s^2 was observed ($\Delta\omega_z = 4.9°$/s).
  - The skid event was caused by a sudden 18 m/s step-increase in wind speed that followed shortly after the wind speed fell close to zero.
- A high response ($\Delta A_y = 3.51$ m/s^2, $\Delta\omega_z = 3.03°$/s) was observed at the Helgeland bridge in response to the inverse gusts created in the wakes of two oncoming tractor-trailers passing in the windward lane.
- The variance in the roll rate signal between repetitions was shown to be a good proxy for wind-induced resultant response (as opposed to road-induced).
  - The variance for the still-wind case at Dovre 1 was 0.02 deg/s. Values higher than this may therefore indicate the presence of wind perturbations.

Some conclusions can be drawn from a regulatory perspective if traffic regulations are to be dependent on measured wind conditions. Based on the empirical evidence presented in this chapter:

- It is important to consider the skewness of the wind and its effect on the resultant response in each driving direction.
- The girder-induced turbulence may make certain lanes more critical than others.
- The driving speed can have a significant impact on resultant response (up to a 4x increase in average response from 30 to 80 kph).
- Vehicles in the windward lanes of a bridge act like obstacles to the wind. Their wakes can induce a significant vehicle-driver response for those travelling in the leeward lanes.
- A sudden, high amplitude gust has been observed to cause a front-axle skid. This will be followed up in Chapter 12 where it will be seen that critical gusts could potentially be predicted by in-situ monitoring of wind statistics.

Chapter 11

Response to predictable gusts

In Chapter 2, it was posited that drivers struggle to compensate for aerodynamic perturbations within a certain frequency range (0.5 to 2 Hz, [170]) and that the reduced frequency range from 0.05 to 0.5 is critical to the crosswind sensitivity of road vehicles [178]. In this chapter, the *inverse gusts* observed in the wakes of towers, cable support piers and a counterweight structure (a unique feature of the Tjeldsund bridge) are used to study the frequency- and reduced frequency-dependency of vehicle-driver response. These gusts caused some of the highest resultant response values seen in the current data sets. This is evident from the hat-shaped features in the signals ΔA_y, $\Delta\omega_z$ and $\Delta\omega_x$ in Figures 9.1 through 9.16.

It will be shown that the identified inverse gusts at towers, support piers and the counterweight are typically within the critical frequency range when driving at the speed limit on Norwegian road bridges. On the other hand, gusts observed at the abutments (step-shaped) or in the wake of cables and hangers (inverse gusts) are typically further from the limits of the critical range (or near the outer bounds) and do not induce an equally significant response. The case of the Tjeldsund bridge is also discussed, where – due to the design of the bridge – there is a clustering of multiple critical gusts across multiple short segments of the girder. Driving across the Tjeldsund bridge was experienced as being on the limit of handling stability during the field session.

11.1 Response to identified gusts

The peak values of $|A_y|$, $|\omega_z|$, $|\omega_x|$ and peak values of ΔA_y, $\Delta\omega_z$ and $\Delta\omega_x$ (quantities defined in Chapter 9) have been collated and sorted by speed for each repetition/signal when the vehicle passed one of the towers, counterweights or cable support piers . The peaks are calculated as the maximum value within 50 m either side of the centre-point of each bridge feature (tower, counterweight or cable sup-

port pier). A peak gust amplitude ΔV_r is defined in the same way for each case as well.

The absolute peaks have been plotted as a function of amplitude-of-change (Δ) peaks in Figure 11.1. The relationship *Peak = Max./2* is derived from this – which is logical for oscillations about zero – and allows for an approximate comparison of MacAdam et al.'s results (presented as peak values) and Brandt et al.'s results (presented as amplitude-of-change). MacAdam et al. [135] ranked the controllability of a vehicle in response to a crosswind *gauntlet* and Brandt et al. [32] found the minimum level of response necessary to classify the response to a given gust as an *instability event*.

MacAdam et al.'s 4/10 response ratings ($|A_y|$, $|\omega_z|$) have each been translated to an equivalent amplitude-of-change (ΔA_y, $\Delta\omega_z$) using a linear fit between peak value and amplitude-of-change (see *4/10 Equiv.* in Figure 11.1). The same translation has been done for the P_{CT} line, which describes the minimum roll-only response necessary to cause discomfort to seated railway passengers in a transition curve (used here for lack of a better reference value on roll rate).

Placing the front-axle skid event

As an additional reference, the peak absolute values of A_y, ω_z, and ω_x and peak values of ΔA_y, $\Delta\omega_z$ and $\Delta\omega_x$ during the front-axle skid event at the Hardanger bridge are plotted as horizontal lines in Figures 11.1 and 11.2 respectively (labelled *F. Skid*). The skid lines lie close to both of the MacAdam 4/10 lines (A_y and ω_z) and the $P_{CT} = 1$ line in Figure 11.1. This means that a vehicle configuration that was deemed 4/10 uncontrollable through an artificial crosswind gauntlet had the same peak response as the current test vehicle did during a front-axle skid event on the Hardanger bridge. This is surprising, as 4/10 suggests there is a 60% margin to driver-perceived complete loss of control. Perhaps this indicates that 4/10 on MacAdam et al.'s scale is already too high a value to be classified as safe under straight-line driving.

Response as a function of gust amplitude

The amplitude-of-change peaks have been plotted as a function of the gust amplitude ΔV_r for each of the towers, counterweight and cable support piers in Figure 11.2. Brandt et al.'s [32] values and MacAdam et al.'s [135] equivalent 4/10 controllability values have been plotted for reference as horizontal lines.

Figure 11.2 shows that there is generally a positive relationship between gust amplitude and the response values ΔA_y, $\Delta\omega_z$ and $\Delta\omega_x$, though there is a significant amount of scatter. For steady aerodynamics and linear handling dynamics it could be hypothesised that the response – which is a function of aerodynamic loading – will grow with the square of the gust amplitude (using basic aerodynamic

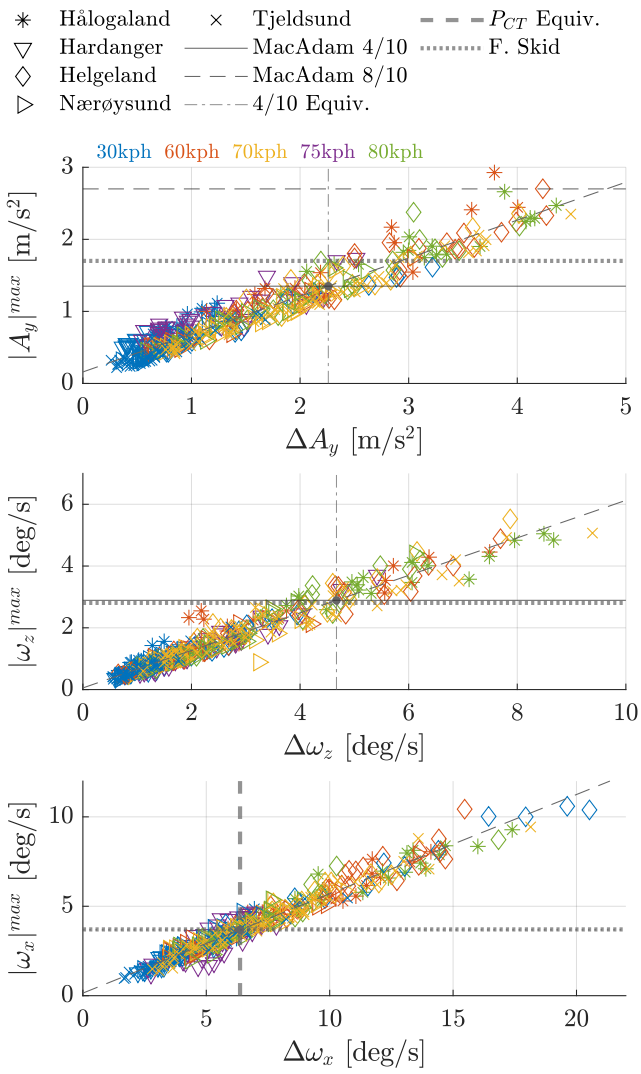

Figure 11.1: A comparison of gust amplitude with peak absolute response at the towers.

MacAdam et al. [135] ranked controllability on a scale from 0 – *no wind effect*, to 10 – *uncontrollable*. The $P_{CT} = 1$ line shows the level of pure roll motion necessary for 1% of seated passengers to feel discomfort on a railway transition curve according to [6].

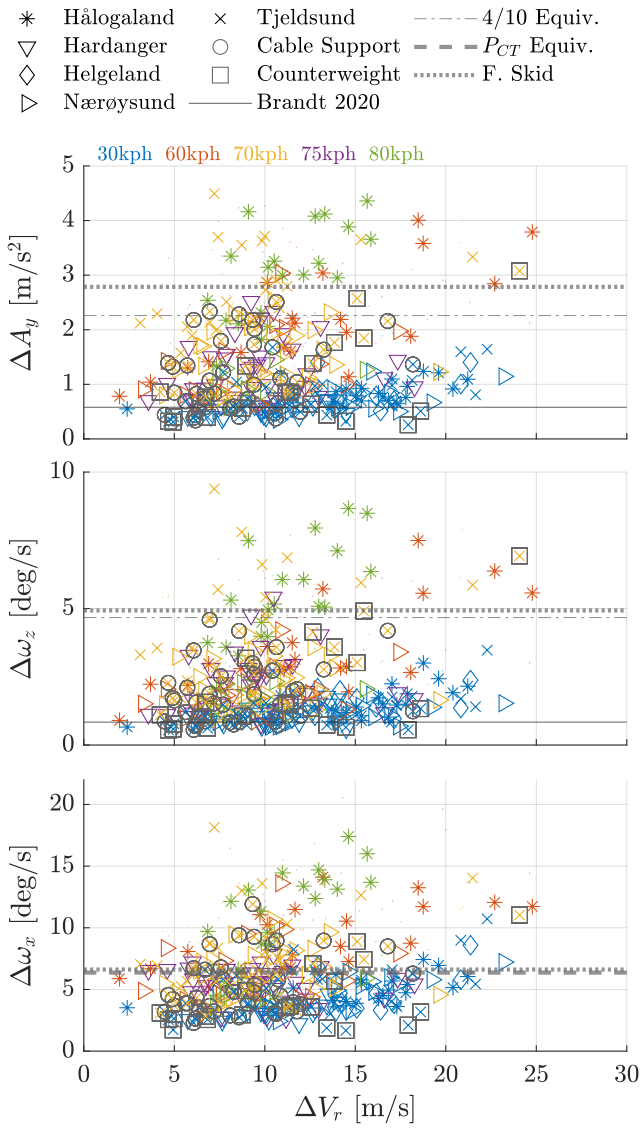

Figure 11.2: A comparison of gust amplitude with response amplitude-of-change at the towers.

Brandt et al. [32] found the level of ΔA_y and $\Delta\omega_z$ at which test drivers of a modern SUV on a test track in natural winds identified "instability events". MacAdam et al. [135] ranked controllability on a scale from 0 – *no wind effect*, to 10 – *uncontrollable*. The $P_{CT} = 1$ line shows the level of pure roll motion necessary for 1% of seated passengers to feel discomfort on a railway transition curve according to [6]. Where more than 5% of the anemometer data within a given repetition is clipped, the data point is plotted with a reduced marker size which appears like a small dot.

coefficient theory [19]). This is explained further and tested in Section 11.3. It is thought that unsteady aerodynamics and driver steering input are responsible for some of the scatter and that this becomes apparent as a function of frequency and reduced frequency.

It is noted here for later reference that the highest values of ΔA_y, $\Delta\omega_z$ and $\Delta\omega_x$ are generally seen in response to gusts above 5-7 m/s in amplitude. In ΔA_y, there are no data points below the front skid line on the vertical axis that are also below $\Delta V_r =\sim 7$ m/s on the horizontal axis. The same can be stated of $\Delta\omega_z$ for both the front skid line and MacAdam's 4/10 equivalent.

11.2 A possible sensory threshold

In Brandt et al.'s study, the drivers were actively looking to identify instability events. The resulting values that were proposed to identify such events could be interpreted as the lower threshold for which crosswind effects can be identified by human drivers. In other words, Brandt et al. [32] found the sensory threshold.

Using this proposed classification and Figure 11.2, it is almost exclusively at 30 kph that the effect of the crosswind gust is under this sensory threshold. In fact, 74 of 84 data points below the $\Delta A_y = 0.58$ m/s^2 threshold were observed at 30 kph (and 43 of 52 points below the $\Delta\omega_z = 0.84$ threshold at 30 kph).

This corresponds well with the collective experience from the field experiments. The effect of the inverse gust at the towers was almost always felt unless driving at 30 kph. At this low driving speed, the effect of the tower could generally not be sensed from the vehicle's motion, but rather from audiovisual cues (i.e. wind-induced cabin noise and visually observing the tower as it passes). It would appear from Figure 11.2 that some 30 kph data points are above the sensory threshold (ΔA_y), but generally only when ΔV_r is above 10-15 m/s (very high).

11.3 Wakes: towers & support structures

The 396 recordings of inverse gusts seen in wake flows captured during the current field experiments provide a unique opportunity to study the unsteady dynamics of the vehicle-wind-driver system. The inverse gusts observed in the wake of the towers, counterweight and cable support piers are fairly consistent in shape and can be approximated by a single, two-piece cosine as can be seen in Figure 11.3a.

For each data point in Figures 11.1 and 11.2 (i.e. for each case where the vehicle passed through an inverse gust caused by the obstruction of the flow by a geometrical feature of the bridge), the wind magnitude is plotted and a semi-automated fitting procedure is followed (to be explained next). The red curves f_i

in Figure 11.3 are defined by 6 parameters v_{1-6} for a discrete domain x_i (see Figure 11.3a for the definitions of v_{1-6}):

$$f_i = \begin{cases} v_4 & v_1 - w_l \leq x_i < v_1 \\ v_5 + \frac{v_4 - v_5}{2}\left(1 - \cos\left[\frac{\pi(v_2 - x_i)}{v_2 - v_1}\right]\right) & v_1 \leq x_i \leq v_2 \\ v_6 + \frac{v_5 - v_6}{2}\left(1 - \cos\left[\frac{\pi(v_3 - x_i)}{v_3 - v_2}\right]\right) & v_2 < x_i \leq v_3 \\ v_6 & v_3 < x_i \leq v_3 + w_l \\ \text{NaN} & x_i < v_1 - w_l \text{ and } x_i > v_3 + w_l \end{cases} \tag{11.1}$$

where w_l is the width of a constant value lip at the beginning and end of the two-piece cosine. MATLAB's `fmincon` optimisation function is used to find values of v_{1-6} that minimise the root-squared error between the fit and the measured gust profile. A simple GUI is designed for manual adjustment of the fit whereby:

- the initial parameters of the optimisation can be changed v_{1-6}, and
- the width of the lips can be varied w_l. The widths of the lips w_l are fixed for each optimisation, but can be adjusted to obtain a new optimisation result.

Adjustments sliders and a live-updating plot are used to manually find initial parameters and a lip width that give acceptable optimisation results. Generally, little to no improvement can be achieved through adjustment, though in a few cases an appropriate fit can be achieved where the initial optimisation fails to do so. The fit quality (acceptable or not) is then manually evaluated for each of the 396 fits. Only those considered acceptable were used further.

Figure 11.3a shows an example of a very good fit. Figure 11.3b shows an example of where the anti-spike algorithm in the WindMaster anemometer has affected the measurements. The approximation in Figure 11.3b is deemed acceptable as the period $v_3 - v_1$ is a fairly good estimate of the period of the gust. Figure 11.3c shows an example of a situation where the fit is deemed unacceptable.

The timestamps at v_1 and v_3 are used to estimate the period of the gust and the reciprocal of this period gives a heuristic for the frequency of the gust from the moving vehicle's perspective. Of the 396 possible fits, 280 are deemed acceptable.

Normalisation of acceleration

The resultant responses ΔA_y to each gust can be normalised by the gust amplitude. Aerodynamic loads are typically characterised by coefficients [19]:

$$C_F = \frac{F}{\frac{1}{2}\rho U^2 A}, \tag{11.2}$$

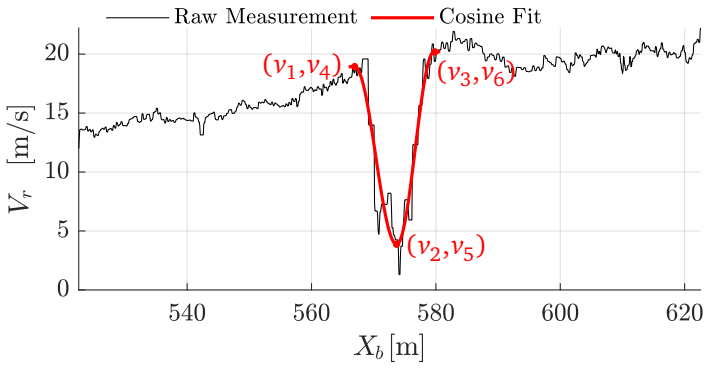

(a) A good fit at Hålogaland, Right Tower (North), Windward Lane, at 30 kph.

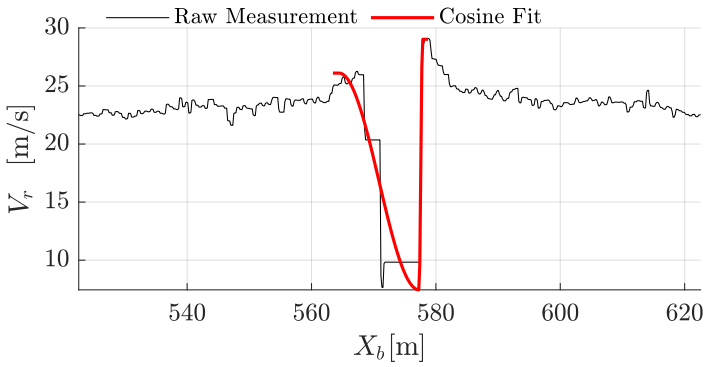

(b) An acceptable fit at Hålogaland, Right Tower (North), Windward Lane, at 60 kph.

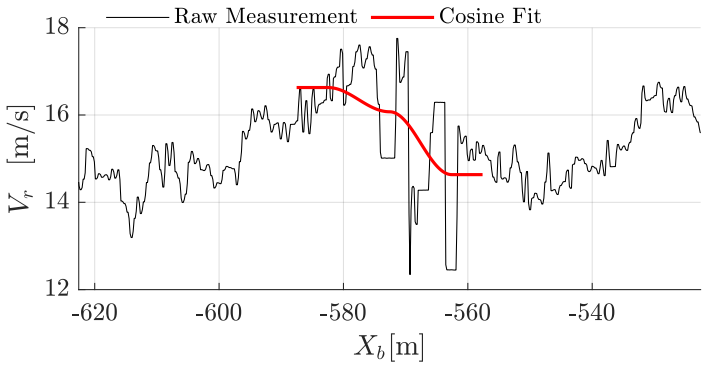

(c) An non-fit at Hålogaland, Left Tower (South), Windward Lane, at 60 kph.

Figure 11.3: Examples of fitting a two-piece sinusoidal gust to the measured data.

where C_F is the aerodynamic force coefficient for the force F, ρ is the density of the fluid, U is the freestream velocity and A is a chosen characteristic area for the object in the flow. For a fixed density (which can typically be assumed) and a fixed geometrical dimension (length scale/area of an object or feature of the flow) the force F scales with the coefficient and the square of the wind speed. For road vehicles, it has been shown that the aerodynamic coefficient is a function the incident yaw angle (see for example Baker [22]). For small angles, the coefficients have an approximately linear relationship with said incidence angle (up to about 40° for the side force coefficient).

By normalising the resultants plotted in Figure 11.1 and 11.2, it is expected that effects that do not scale with the incoming velocity will be recovered – for example the incident yaw angle and frequency dependencies. A non-dimensional resultant change in lateral acceleration is defined:

$$\Delta\hat{A}_y = \frac{m\Delta A_y}{\frac{1}{2}\rho(\Delta V_r)^2 A_s}, \tag{11.3}$$

where m is the vehicle's mass (2,780 kg), $\rho = 1.225$ kg/m^3 and A_s is the projected area of the side of the vehicle ($A_s = 13.4$ m^2).

Critical frequency range

The normalised change of lateral acceleration $\Delta\hat{A}_y$ for each of the inverse gusts has been plotted as a function of both the absolute frequency f as well as the reduced frequency k_f in Figures 11.4 and 11.5 respectively.

Frequency

The majority of the data points in Figure 11.4, representing the response in the wake of the towers, cable support piers and the counterweight, lie in the critical range for driver control. These wake-induced responses are some of the highest values (most extreme) of ΔA_y, $\Delta\omega_z$ and $\Delta\omega_x$ in the response profiles of Figures 9.1 through 9.16. The fact that the majority (216 of 280) of these *extreme* responses lie in the range 0.5 to 2 Hz supports the suggestion that this range is critical for wind-induced vehicle-driver handling response. The four highest values of $\Delta\hat{A}_y$ are fairly closely spaced on the frequency axis (approximately centred about 1.25 Hz), showing that gusts near this frequency are perhaps even more critical.

The grey bars drawn behind the scatter plot (Figure 11.4) show the maximum value plotted within each 1/4 Hz bin. The majority of bars that are higher than the 95$^{\text{th}}$ percentile value (of all data points) are within the critical range (5/7). The remaining two bars fall in the range 2.25-2.75 Hz, which was not posited as part of

the critical range in Chapter 2. It is now clear that these higher frequencies should not be disregarded.

Schaible [170] concluded that the driver has no effect on the handling response to perturbations above 2 Hz and in Chapter 2 it was assumed that perturbations above 2 Hz would be negligible in magnitude (due to the low amplitude gain of the vehicle's handling frequency response function and the decay of turbulent wind energy with smaller scales). In reality, these higher frequency perturbations are not negligible and the driver's compensatory steering (which is limited to lower frequencies according to Schaible [170]) is not sufficient to avoid a high resultant response (i.e. to avoid attaining values in the top 5% of the overall data set presented here).

Additional data points across the plotted frequency domain are needed to draw more concrete and statistically significant conclusions. There are only 45 data points above 1.75 Hz. The comparison between different bins would be further convincing with more data points and/or an even distribution across the frequency domain. This should be prioritised in future studies.

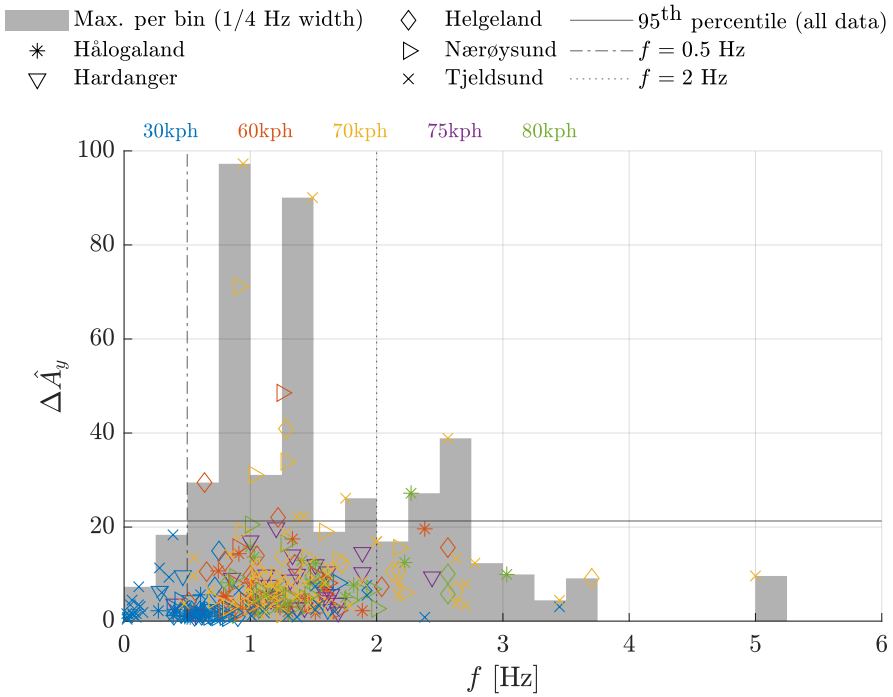

Figure 11.4: Non-dimensional resultant amplitude-of-change of lateral acceleration as a function of the absolute frequency of gusts (in wake flow).

Reduced frequency

Figure 11.5 shows the same data points as shown in Figure 11.4 plotted against a reduced frequency axis k_f instead of absolute frequency f. Just above half of the data points (154/280) are within the previously identified range for critical turbulence length scales: 0.05 to 0.5 ([178], see Chapter 2). However, there are also a significant number of points (120/280) above $k_f = 0.5$ and many of these are associated with a high response ($\Delta\hat{A}_y > 10$).

Again, grey bars have been drawn to show the maximum value observed within bins ($1/8^{\text{th}}$ width). There are 2 bars that extend above the 95^{th} percentile value within the proposed critical range (0.05 to 0.5) and 3 bars that lie above $k_f = 0.5$ in the range 0.5 to 1. This would suggest that the range 0.5 to 1 is also critical to vehicle-driver crosswind sensitivity. The 2 bars within the proposed critical range span the k_f-axis from 0.25 (4 vehicle lengths) to 0.5 (2 vehicle lengths), giving an overall critical range of 0.25 to 1 (or 1 to 4 vehicle lengths) based on 95^{th} percentile values of the current data.

This does not necessarily contradict the summary conclusion presented by Sims-Williams [178] discussed in Chapter 2. He concluded that the crosswind sensitivity of vehicles is critical in response to gusts with length scales between 2 to 20 vehicle lengths. The wind's spectral energy is high at these scales, vehicle response is not quasi-steady, aerodynamic loads may be unsteady and the suspension natural frequency typically lies in this range as well. While all these statements may hold true, the effect of the driver is not considered, nor is the unique, inhomogeneous wind field that has been observed on bridges in this thesis. From the current results with a driver, it would appear that gusts of higher reduced frequencies (up to 1, or down to length scales of 1 vehicle length) may also be important and that the larger length scales (from 4 to 20 vehicle lengths) are less so.

As was noted in the discussion of frequency effects above, it would be useful to have a more even distribution of points along the horizontal (k_f) axis. This is difficult to achieve using field experiments like the ones presented in this work as it requires finding gusts of specified dimensions in the field. It may be possible to predict gust dimensions based on geometrical details (of the towers, support piers, or similar as will be discussed in Chapter 13) and to find the required scales on bridges in Norway. This is an opportunity for further study.

Based on the current results attained with a real driver in the field, the most critical (95^{th} percentile) handling responses to wind perturbations are due to gusts with length scales between 1 and 4 vehicle lengths.

Driver contribution

The absolute highest points ($\Delta\hat{A}_y$) in Figure 11.5 are from the left-hand (western) tower at the Tjeldsund bridge. It will be discussed in Section 11.6 that the driver

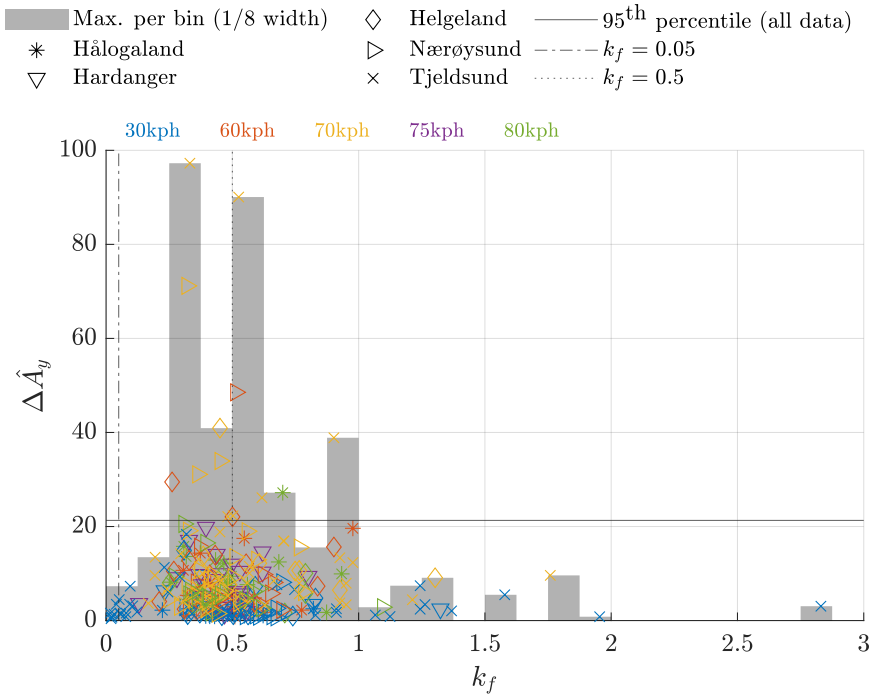

Figure 11.5: Non-dimensional resultant amplitude-of-change of lateral acceleration as a function of the reduced frequency of gusts (in wake flow).

is under increased workload between $X_b = -400$ and -100 m due to the close proximity of the tower, cable support piers and counterweight to one another along the girder. The driver input could therefore be a significant contributor to the high resultant response seen here.

The next two highest points are from the Nærøysund bridge. There is no reason to believe that the aerodynamic forces were higher here than at any of the other towers at the same frequency (noting caution here, because angle of incidence of the wind has not been considered in the analysis).

However, the Nærøysund field session was the first one that involved driving through the wakes of bridge towers. Therefore, it could the inexperienced test driver that made a significant contribution to the high resultant responses recorded at Nærøysund. There is also an expansion joint at each of the towers, which was noted to induce a vehicle response in addition to the aerodynamic perturbation.

Gust amplification by headland effect

A local effect that was characterised at the northern approach to the Hålogaland bridge in Chapter 8 was the acceleration of flow around the headland below/upstream of the bridge deck. This had the effect of increasing the mean wind speed near the northern tower and the gust amplitude resulting from the tower's wake. The result is a response that is significantly higher on passing the northern tower in comparison to the southern tower.

Figures 9.7 and 9.8 show that in ΔA_y the mean value at the North tower is 3.23 m/s^2 versus 2.23 m/s^2 at the South in the windward lane. In the leeward lane the respective values are 2.99 versus 2.79. The response is high at both towers, but the headland acceleration of the flow increases the response at the North tower by 20-40%, having the biggest effect in the windward lane.

In fact, the four data points above MacAdam et al.'s equivalent 4/10 value ($\Delta\omega_z$) from the Hålogaland bridge in Figure 11.2 are all from the North tower. These are also some of the absolute highest values seen across all data sets (in ΔA_y and $\Delta\omega_z$). This demonstrates the importance of inhomogeneities in the wind field across the bridge span to evaluations of vehicle safety.

Summary on unsteady dynamics

The current analysis, using a heuristic to establish the frequency of observed gusts supports the theory that there are critical ranges of frequency f and reduced frequency k_f for vehicle-driver crosswind sensitivity. There is strong evidence to support the conclusions of Schaible [170], that drivers have a tendency to respond adversely to perturbations in the frequency range from 0.5 to 2 Hz and have little to no effect on response beyond 2 Hz. It has been shown here that the most severe

handling responses (95th percentile) to inverse gusts behind towers, support piers and a counterweight structure are seen between 0.5 and 2.75 Hz.

A slightly different reduced frequency range to that proposed by Sims-Williams [178] has been found to be critical for the test vehicle on the bridges visited in this work. He suggested that 2-20 vehicle lengths can generally be considered the range in which vehicles are most sensitive to crosswinds. For the real vehicle-driver system used here, the most severe handling responses are observed for gusts of 1-4 vehicle lengths.

11.4 Wakes: cables & hangers

In the windward lanes at Helgeland and Hålogaland (Figures 8.12 and 8.8), there are small dips in the wind magnitude that have been identified as the wakes of the cable stays and hangers respectively. Due to the limited spatial resolution of the signals, it is difficult to estimate the spatial dimension of these inverse gusts. An approximate value of 1 m has been determined based on a series of manual inspections of the signals at each bridge. The frequency and reduced frequency of these gusts can thus be approximated:

- At 30 kph, $f = 8$ Hz, $k_f =\sim 7$
- At 80 kph, $f = 22$ Hz, $k_f =\sim 7$

At both driving speeds, the frequency and reduced frequency are therefore well above the upper limits of each respective critical range. Upon inspection of the raw (unfiltered) lateral acceleration, yaw rate and roll rate signals, there is no identifiable response of the vehicle to these wakes. This reinforces the theory that the identified ranges of reduced frequency k_f and frequency f are indeed critical.

11.5 Gusts at the abutments

In Chapter 8, a heightened value of ΔV_w was characterised at a number of the abutments. An abutment is where the roadway transitions from the bridge deck to a fixed base. Typically, a finite, artificial embankment exists (on the land-side of the abutment) and has the effect of shielding the wind such that there is a step in the wind magnitude across the abutment. This can be shown to look like a half-period of a cosine, which allows for a similar characterisation of the gust frequency as the inverse gusts discussed above.

Figure 11.6 shows an example of the half-cosine gust profile seen at the northern abutment of the Helgeland bridge. The topography in this example is not the typical artificial embankment described above, but instead the girder makes landfall at the top of a steep slope.

Regardless of the specific topography, the roadway transitions from a fixed-base – where the surrounding topography, fauna and structures provide a shielding effect – to an elevated bridge girder – where the wind can flow both above and below the road surface. A step change in wind speed is often observed at such a transition from land to girder-based road independent of the specific local topography (embankment, cliff, steep drop-off or otherwise).

Gust fitting at the abutments

A similar fitting procedure to the one in Figure 11.6 is applied to the wind speed at each abutment in all data sets. The results are tabulated in Table 11.1 where only the fittings that are deemed acceptable have been included. For the case of the abutment fitting procedure, the fit is deemed acceptable if the half-cosine step can be clearly distinguished from the variations in wind speed surrounding the abutment.

For each acceptable case, the width of the step (or the half-period of the cosine) $D_{\text{gust}}/2$ is taken from the half-cosine fit as well as the amplitude (from peak to trough) A_{gust}. The typical vehicle speed over the abutment (which may differ from the speed limit due to the curvature of the road or the need to accelerate from a start point near the abutment) is estimated by inspection at the abutment location using Figures 9.1 to 9.16.

A single frequency f and reduced frequency k_f is then calculated in each row of Table 11.1 based on the dimension of the gust D_{gust} and the vehicle speed V_x. Next to these values are binary numbers that indicate whether or not f and k_f are within the critical ranges identified in Chapter 2. As can be seen by inspection of the table, 5 out of 9 are within both critical ranges, and so a wind-related response feature is expected at these abutments.

It is assumed that the gusts do not change in spatial dimension within the duration of the experiments (stationarity). Consequently, the gust fitting is performed using the 30 kph data, to take advantage of the higher spatial resolution, and the temporal period (and frequency) is calculated using the driving speed indicated in the table.

Analysis

Next to the column of binary indicators, there are three columns describing whether or not a distinct response can be seen at the abutments in the signals A_y, ω_z and ω_x (at the indicated driving speed). For example, at the Hålogaland bridge, an oscillatory response can be seen in both A_y and ω_x immediately to the left of the abutment in Figure 9.8. The oscillations are visible in the mean curve (suggesting repeatability) and are clearly distinguishable from the signals nearby.

Table 11.1: Characterisations of gusts and response observed at the abutments.

Data set	Lane[1]	Abutment[2]	$D_{\text{gust}}/2$ [3] [m]	A_{gust} [m/s]	V_x [4] [m/s]	ID	...
Hålogaland	LW	R/North	14.14	8.74	80	a.	
Hardanger	WW	R/North	17.28	9.02	80	b.	
Hardanger	LW	R/North	4.69	5.80	80	c.	
Hardanger	LW	L/South	24.98	5.34	60	d.	
Helgeland	WW	R/North	22.34	15.16	60	e.	
Helgeland	LW	R/North	25.26	15.84	60	f.	
Helgeland	LW	L/South	74.15	21.71	60	g.	
Nærøysund	WW	L/West	13.54	2.67	70	h.	
Tjeldsund 2	LW	L/West	8.48	8.27	50	i.	

...	ID	f [Hz]	k_f	Threshold[5] f/k_f	Lateral[6] A_y	Yaw[6] ω_z	Roll[6] ω_x
	a.	0.79	0.24	1/1	Yes	Likely	Yes
	b.	0.64	0.20	1/1	Likely	Likely	Likely
	c.	2.37	0.72	1/1	Unclear	No	Unclear
	d.	0.33	0.14	0/1	Likely	No	Yes
	e.	0.37	0.15	0/1	Likely	No	Yes
	f.	0.33	0.14	0/1	Likely	No	Yes
	g.	0.11	0.05	0/0	Unclear	Unclear	Unclear
	h.	0.72	0.25	1/1	Yes	Likely	Yes
	i.	0.82	0.40	1/1	Yes	No	Yes

[1] LW - leeward, WW - windward.
[2] R/L indicates right/left in the profile plot (Figures 9.1 to 9.16).
[3] The half-period of the cosine fit.
[4] Taken to the nearest 10kph from inspection of Figures 9.1 to 9.16.
[5] 1 - indicates value is within critical f/k_f range ($0.5 < f < 2.0$ and $0.05 < k_f < 0.5$), 0 - indicates values lies outside critical range.
[6] A (damped) oscillatory response starting at or near the abutment can be identified upon inspection of the appropriate Figure (9.1 through 9.16).

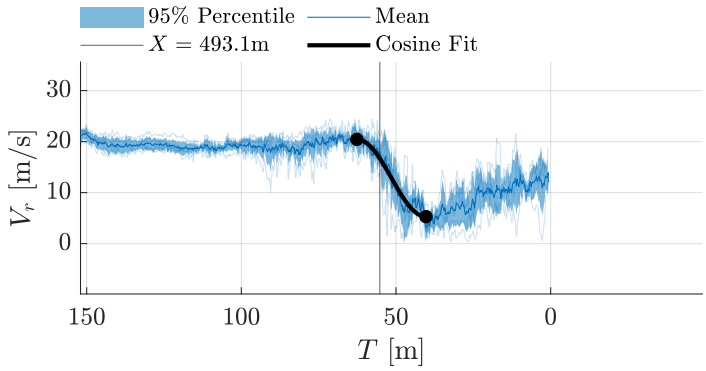

Figure 11.6: Fitting a half-cosine to the wind profile at the right, northern abutment of the Helgeland bridge (wind measured at 30 kph).

Note that T is the distance along the roadway (a curvilinear axis) and is in this case defined such that $T = 0$ m near the abutment shown to the right (north) in Figure 9.12. The location of the abutment is indicated using a solid vertical black line. Instead of performing the fitting on each individual repetition, a mean curve has been used and the 95% confidence interval has been plotted as a shaded region.

This is suggestive of a response to an impulse-like perturbation at the abutment given that the driving direction is from right to left in Figure 9.8 (the oscillatory response follows the perturbation). This is very clear in the lateral acceleration and roll rate signals, but less so in the yaw rate. There are no expansion joints, or similar undulations in the roadway at any of the tabulated abutments. It is expected that the perturbation causing the oscillatory response in each case is an aerodynamic one.

It can be seen from the table that the binary indicators are fairly good predictors of a distinct yaw rate response. Where the indicators read 0/0 or 0/1, the yaw column shows *No* or *Unclear* and where the indicators read 1/1 the yaw column more often shows *Likely* (for 3 of 5 cases of 1/1). A roll response is evident in almost all cases (*Yes* in 6 of 9 rows), suggesting that there is an aerodynamic perturbation in most cases, yet it is only those within the critical frequency range where the yaw response is likely to be significant. The lateral acceleration response is also more clearly distinguishable (more likely to be *Yes*) if the frequency is critical (3 of 5 in the critical range versus 0 of 4 outside).

Note that the 2 of 5 critical range cases that are marked *Likely* or *Unclear* instead of *Yes* are at the Hardanger bridge, where the step change in wind speed results from entry/exit from a tunnel and is in close proximity to the tower wake. The tower's wake is in such close proximity that it is difficult to distinguish between a response induced by the tower wake and one induced by a step change at the abutment.

In the *Helgeland, LW, L/South* row (g.) the responses are marked *Unclear*. The

reason why is given by looking at Figure 11.7 where each response is plotted along the road axis. The nature of the response certainly changes across the abutment line, but there is no distinct, repeatable oscillatory behaviour. Instead, there is generally more stochastic oscillation on the right side of the abutment line than on the left. Looking at Figure 8.26, there is an increase in turbulence in addition to the step change in mean wind magnitude (at very low frequency, 0.11 Hz with $k_f = 0.01$). This likely explains the change in the behaviour of the vehicle response signals.

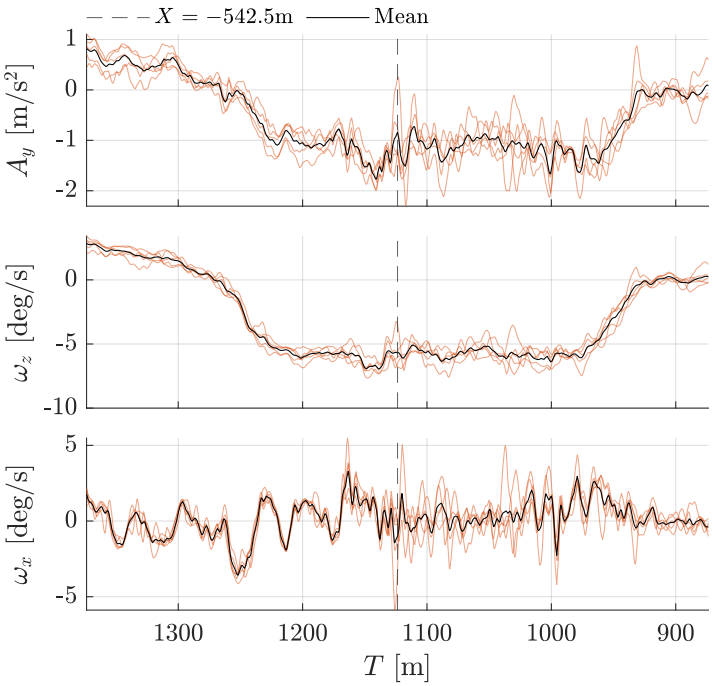

Figure 11.7: A closer look at the response at the southern abutment of the Helgeland bridge.

Note: raw signals have been low-pass filtered with a Butterworth filter with a cut-off frequency of 5 Hz.

Summary

There are few clear examples of the half-cosine step change in wind magnitude (9 out of a possible 28) and even fewer that are isolated from other aerodynamic influences like the tower wake or increased turbulence. Nonetheless, Table 11.1

suggests that the clearest examples of adverse, wind-induced handling response are within the proposed critical frequency range.

In the current data set, the clearest examples of oscillatory handling response resulting from a half-cosine step change in wind magnitude (i.e. rows with *Yes-Likely-Yes* in the last three columns) are observed at the northern abutment of the Hålogaland bridge and the western abutment of the Nærøysund bridge where $f = 0.79$ and 0.72 Hz and $k_f = 0.24$ and 0.25 respectively.

11.6 Clustering of critical gusts at Tjeldsund

The Tjeldsund bridge is the bridge that was felt to be the least safe to cross during the field sessions. It was noted by the test driver that the vehicle was on the verge of losing stability on multiple occasions. The bridge was closed shortly after the measurements presented in this work were recorded because the wind speed increased further (beyond the 32 m/s threshold set for the Tjeldsund bridge). The closure of the bridge was viewed as appropriate in response to the increase in wind speed at the time of the experiment.

The highest values of $\Delta A_y = 4.49$ m/s^2 and $\Delta\omega_z = 9.39$ deg/s recorded in all data sets (at any point on the bridges) were recorded at the Tjeldsund bridge in response to a gust with a mere amplitude of 7.2 m/s. In fact, there are high resultants (above the equivalent of MacAdam et al.'s 4/10 controllable rating and the front-axle skid line) in response to gust amplitudes ranging from 7 m/s to 25 m/s. One possible explanation for this wide range could be the contribution of the driver to the resultant response.

Figure 11.8 shows the PDF of the amplitude-of-change of the lateral acceleration and yaw rate for the wakes at the Hålogaland bridge (behind both towers in each of the lanes at 80 kph) versus those on the Tjeldsund bridge (including the towers, the counterweight and cable support piers at 70 kph). The mean of the distribution is in fact higher at Hålogaland than at Tjeldsund even though the Tjeldsund bridge was perceived as much more difficult to cross.

The sequence of events at Tjeldsund are very different to those at Hålogaland. Comparing Figures 9.7 and 9.8 from Hålogaland with 9.15 and 9.16 from Tjeldsund there are some key differences. At Hålogaland there are no significant features in the amplitude-of-change signals (peaks or hat-shaped impulses) other than those at the towers. The bridge is long and the time spent driving between the towers is approximately 50-60 seconds at 70 kph.

At Tjeldsund there are in fact 7 significant features, two at the towers, two at the cable support piers, one at the counterweight as well as two more at the transition from the curved road (at the abutments) to the straight roadway on the bridge deck (the peak in the amplitude-of-change signals here is a result of the short-radius road curvature). Between the left (western) tower, cable support pier and counterweight

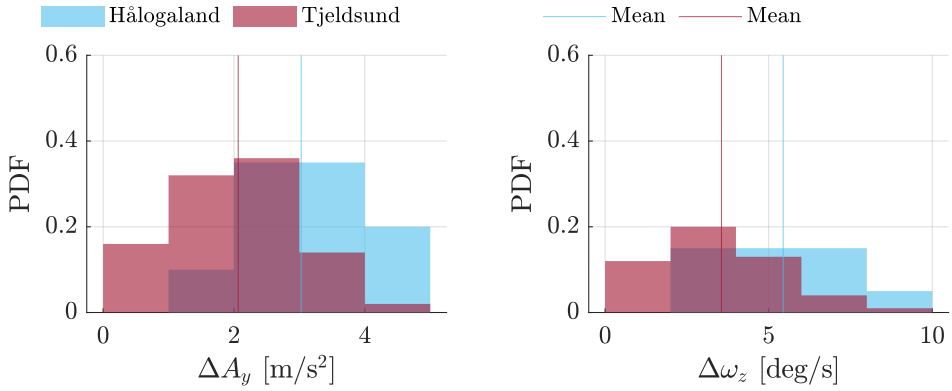

(a) Lateral acceleration

(b) Yaw rate

Figure 11.8: A comparison of the response in the Hålogaland and Tjeldsund wake flows.

there is a spacing of roughly 90 m between each, giving approximately 4.5 seconds of recovery time between each at 70 kph. The time between the towers is also relatively short at 13 s, while the 4.5 s value also applies between the eastern tower and cable support pier. The peak at the western transition curve is in turn only 5 s beyond this. The repeated and successive clusters of peaks is likely to require significant concentration and energy to navigate and might explain why the vehicle was perceived as less controllable on the Tjeldsund bridge in contrast with Hålogaland. It may simply be a matter of excess workload on the driver.

It is also noted that the gusts at the bridge towers are more likely to be expected perturbations. The counterweight is not visible from the bridge deck and so the inverse gust above it comes as a surprise when crossing the bridge.

11.7 Conclusions

Gusts have been identified and characterised in the wakes of bridge towers, a counterweight structure, cable support piers, stay cables, suspension hangers as well as at abutments. The frequency of each of the gusts have been estimated using appropriate fitting procedures. The resultant response ΔA_y to each gust has been normalised by gust amplitude to reveal the effect of frequency f and reduced frequency k_f on resultant vehicle-driver response. The highest responses (95$^{\text{th}}$ percentile) – and those most adverse to safety – are seen in response to gusts with a frequency f within the range $0.5 < f < 2.75$ Hz and the reduced frequency range $0.25 < k_f < 1$.

The bridge towers, the counterweight and the cable support piers typically create gusts that are critical in dimension. The cable stays and suspension hangers are too small to be critical and the abutments create gusts that are on the lower limits of the critical ranges due to the large dimensions of the gusts. The step-shaped gusts seen at the abutments could be a bigger threat to vehicle-driver stability at higher driving speeds. Higher driving speeds would lead to higher frequencies.

The Tjeldsund bridge is constructed such that critical gusts form at 5 locations along the girder. These are the locations of the towers, the cable support piers and the counterweight. The spacing between the gusts is small (about 4.5 s at 70 kph on either side of the bridge) and – along with the added challenge of navigating the short-radius curves at either end of the bridge – makes the driving task difficult.

Chapter 12

Response to stochastic gusts

It has already been seen that a random, step-shaped gust caused a front-axle skid event on the Hardanger bridge. The gust appears to have been part of the *natural* wind and cannot be related to any specific local topographical feature or feature of the bridge geometry. Front-axle skids have been observed on multiple other occasions, including:

- on the main span of the Dolmsund bridge, and
- while driving on the Dovre mountain pass (Dovre 2).

Unfortunately, these other events were observed in transit to and from testing. Consequently, no wind or response data was recorded to describe them. Nonetheless, it is believed that the gusts that induced these skid responses were also a feature of the *natural* break up of eddies in the atmospheric boundary layer as opposed to being discrete, identifiable gusts like the inverse gusts in the wake of bridge towers. In addition to topography-induced turbulence, it appears that the separation of flow over the top surface of girders with bluff cross-sections can also introduce turbulence scales that are critical to the stability of the vehicle-driver system.

In this chapter, the turbulence observed in the field will be described and related to measurements of the response of the vehicle-driver system. It is shown that the number of critical gusts on a bluff-section girder (on a cantilevered bridge like Dolmsund or Måløy) is likely to be higher than on a more streamlined girder (for example Hardanger or Hålogaland). Similarly, certain topographies can increase the proportion of critical gusts observed along certain segments of the visited bridges.

12.1 Turbulence at Hardanger

The Hardanger bridge is located in complex terrain where the easterlies have previously been observed to be more turbulent than westerlies [82]. Note that the wind

comes predominantly from these two directions due to the shape of the fjord. It is thought that the mountainous terrain upstream of the bridge is the cause of the increased levels of turbulence that come with the easterly wind [82].

The statistics of the turbulence can be described with the current data using the Probability Density Function PDF (as a histogram) of the amplitude-of-change of wind speed ΔV_w. This can be seen for a selection of data sets in Figures 12.1 through 12.5. The 2-second window allows gusts with a period up to 4 seconds to be characterised by the amplitude-of-change value (down to 0.25 Hz).

What distinguishes the Hardanger case from the distribution at other bridges is the length of the right-hand tail (further distributions from other bridges are plotted in Figures 12.3 through 12.5). Compared to Dovre 2 for example (Figure 12.2), there is slightly more area under the part of the distribution above 10 m/s. This makes up 1.8% of the data in the leeward lane of the Hardanger bridge versus 0.8% in the leeward at Dovre 2. These are small proportions of the overall data sets, but the likelihood of meeting a gust larger than 10 m/s at Hardanger is twice that at Dovre 2. This long, narrow right-hand tail is also evident in the distribution of response ΔA_y (Figure 12.1b).

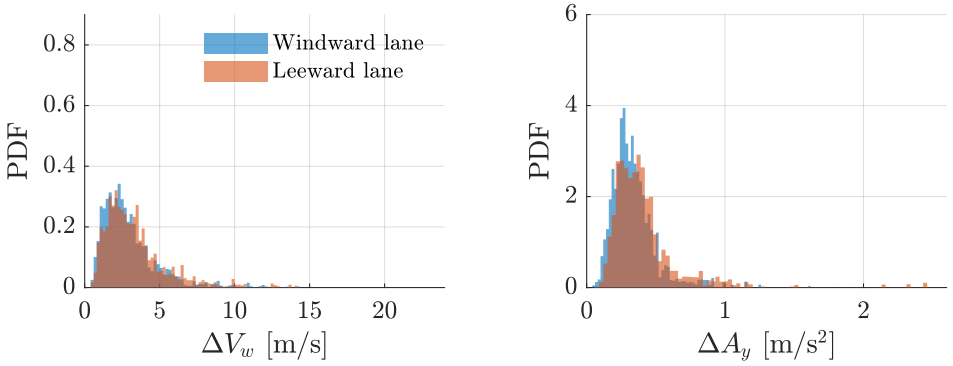

(a) Gust amplitude (30 kph)

(b) Lateral acceleration (75 kph)

Figure 12.1: Distributions of amplitude-of-change in wind magnitude and lateral acceleration in the reference segment on the Hardanger bridge.

Road conditions

It should be noted that part of the reason for the front-axle skid event at Hardanger could be the road surface conditions. Notes on the road conditions were not recorded, though the weather stations at Fv7 Ålvik Aust, Fv572 Eddegjelet and Kvamsøy (located near the Hardanger bridge and in the Eidfjord) show that the temperature was between 4-6°C during the experiment on 11/03/2021 between

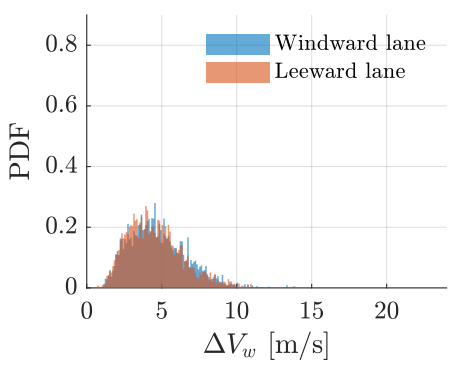

(a) Gust amplitude (80 kph)

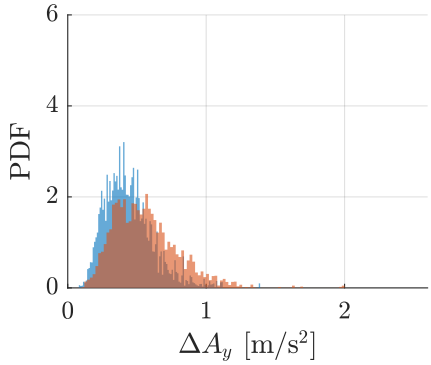

(b) Lateral acceleration (80 kph)

Figure 12.2: Distributions of amplitude-of-change in wind magnitude and lateral acceleration in the reference segment at Dovre 2.

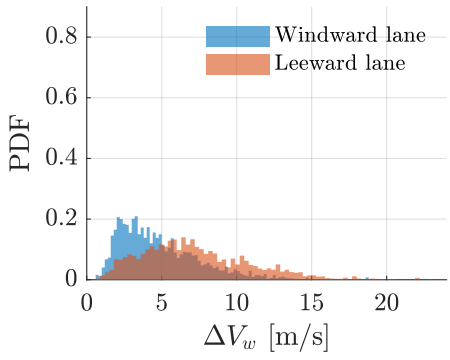

(a) Gust amplitude (50 kph)

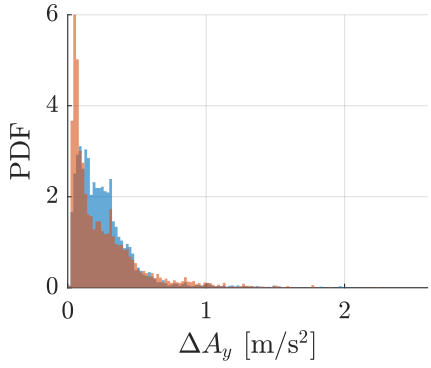

(b) Lateral acceleration (50 kph)

Figure 12.3: Distributions of amplitude-of-change in wind magnitude and lateral acceleration in the reference segment of the Måløy bridge. *The reference segment has been expanded to $-300 < X_b < 450$m to include the majority of the bridge span.

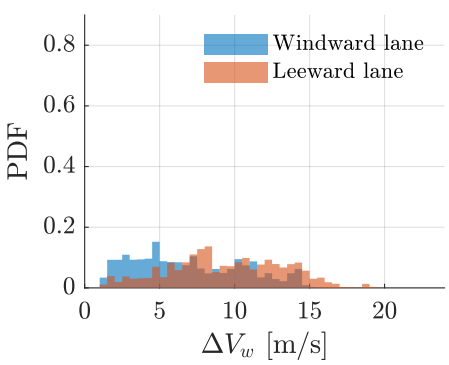

(a) Gust amplitude (70 kph)

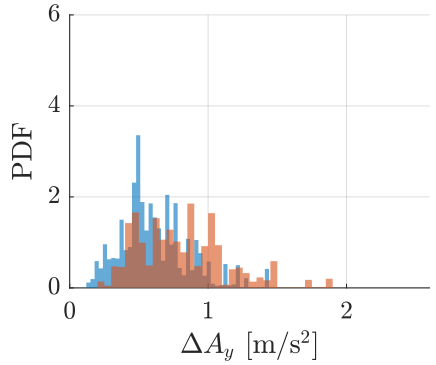

(b) Lateral acceleration (70 kph)

Figure 12.4: Distributions of amplitude-of-change in wind magnitude and lateral acceleration in the reference segment on the Dolmsund bridge. *The reference segment has been expanded to $-200 < X_b < 200$m to include the majority of the bridge span.

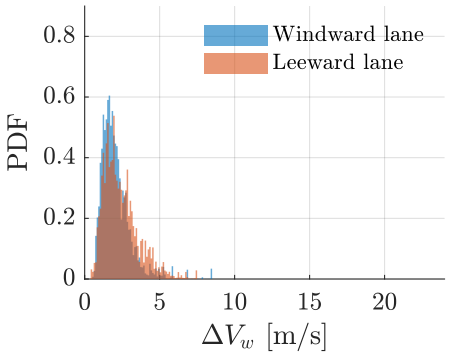

(a) Gust amplitude (30 kph)

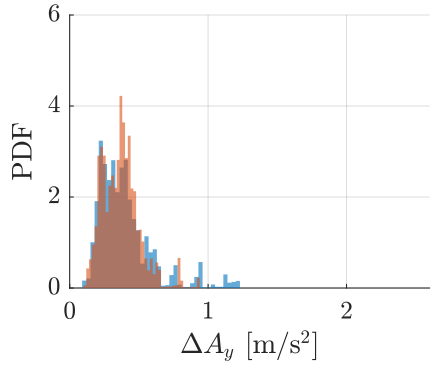

(b) Lateral acceleration (80 kph)

Figure 12.5: Distributions of amplitude-of-change in wind magnitude and lateral acceleration in the reference segment on the Hålogaland bridge.

00:00 and 03:00 (seklima.met.no, 21.07.2022, CC BY 4.0). Fv7 Ålvik Aust and Kvamsøy recorded 0.4 and 0.2 mm respectively of rainfall within that period and similarly light rain between 14:00 and 19:00 the previous day. The road surface was cold and most likely slightly wet. The road conditions are likely to have contributed to the cause of the observed skid event.

12.2 Turbulence generated by complex, rough terrain

In Chapter 8, the increased turbulence at each of the approach spans of the Hålogaland bridge was attributed to the complex and rough upstream terrain. The effect of this on the response can be seen in Figure 12.6, which shows the variance between repetitions of each response signal as a function of X_b. Other than the peaks at the towers, there is clearly an elevated variance (relative to the main span) in each response signal across both approach spans.

The surface quality is not notably different between the main span and the approach spans. In fact, the bridge was completed in late 2018 and the road surface is still of a high standard from abutment to abutment. Even if the road surface were to be irregular, it has been shown that this would lead to a fairly repeatable pattern of response. The variance seen here is the result of aerodynamic perturbations and the increased turbulence that exists locally over the approach spans has an appreciable effect on the repeatability of the response.

Correspondingly, the mean values (from the mean curve) of ΔA_y, $\Delta\omega_z$ and $\Delta\omega_x$ are higher than the reference value over the approach spans in both Figures 9.7 (windward) and 9.8 (leeward). For example, at peak in the windward lane, ΔA_y is 1.07 m/s^2 over the northern approach span versus a reference value of 0.40 and 1.10 versus 0.37 in the leeward lane. The effect of this localised increase in turbulence places the response above the sensory threshold ($\Delta A_y = 0.58$ m/s^2), but comfortably below MacAdam's 4/10 uncontrollable configuration ($\Delta A_y = 2.43$ m/s^2).

12.3 Turbulence generated by flow separation from bridge girders

It was noted in Chapter 8 that the deck's cross-section can induce an increase in turbulence and consequently increase the reference value of gust amplitude. It was particularly the cantilevered bridges where the gust amplitude was found to be higher and the wind profile visibly more turbulent (see the wind profile plots, Figures 8.2 to 8.21).

The distribution of gust amplitude ΔV_w and ΔA_y at Måløy and Dolmsund can be seen in Figures 12.3 and 12.4 respectively. The less streamlined concrete cross-

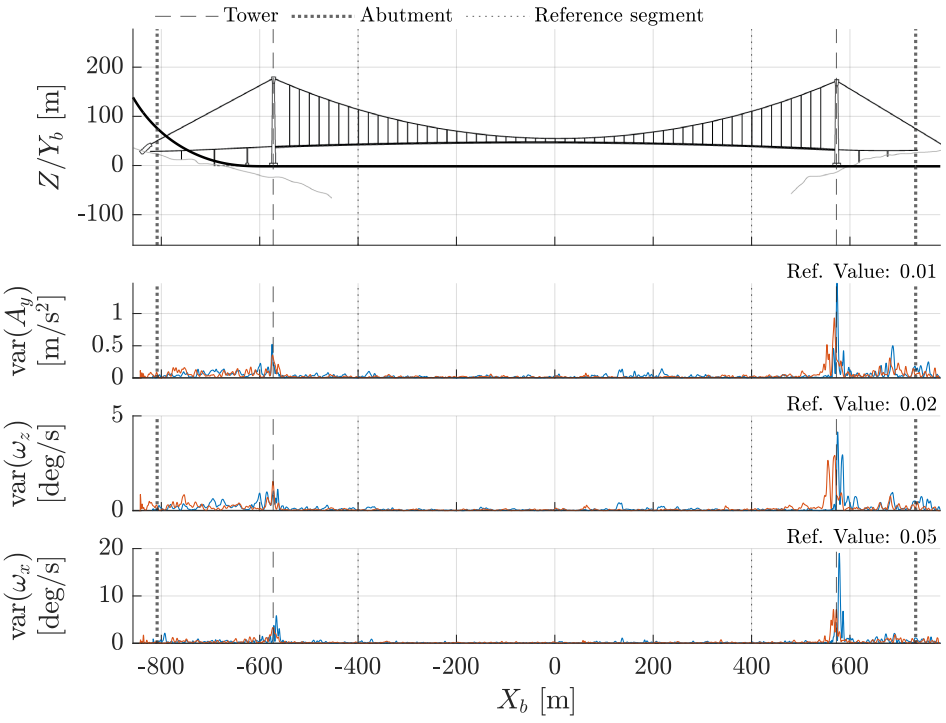

Figure 12.6: Variability between measurements of lateral acceleration, yaw rate and roll rate at the Hålogaland bridge at 80 kph.

Note: raw signals have been low-pass filtered using a Butterworth filter with a cut-off frequency of 5 Hz.

sections at Måløy and Dolmsund result in much flatter distributions of gust amplitude than those seen at the Hardanger bridge just discussed. Note that the reference segment has been extended to include the majority of the bridge span. The distributions therefore capture the influence of the varying cross-sectional depth of the cantilevered bridges (as well as the wake/pressure wave of the piers).

It is particularly in the leeward lane of the Dolmsund bridge that the distribution is wide and stretches all the way to approximately 18 m/s. The PDF is also fairly symmetric (based on this limited dataset) in comparison to for example Hålogaland and Hardanger (Figures 12.5a and 12.1a respectively). The Måløy distributions are similarly flat, with the distribution in the leeward lane being fairly symmetric. The windward lane is more skew, yet has a much thicker tail compared to, for example, the Hardanger bridge.

Table 12.1 summarises some key statistics of the data sets. The percentage of gust amplitudes above 7 m/s is much higher at both the Dolmsund and Måløy bridges (the value is ≥20% in both lanes) compared to the more streamlined sections at the cable-supported Helgeland, Hålogaland and Hardanger bridges (with a maximum value of 5.8% in the leeward lane of the Hardanger bridge).

Table 12.1: A comparison of reference segment distributions.

Bridge Name	Lane[1]	Speed [kph]	$\Delta V_w > 7$m/s %	$\Delta A_y > 0.58$m/s^2 %
Dolmsund	WW	70	45.2	49.0
Dolmsund	LW	70	73.4	72.9
Hålogaland	WW	80	0.9	13.9
Hålogaland	LW	80	1.3	6.5
Hardanger	WW	75	5.0	6.5
Hardanger	LW	75	5.8	14.0
Helgeland	WW	80	0.0	1.9
Helgeland	LW	80	3.3	22.1
Måløy	WW	50	19.4	6.9
Måløy	LW	50	46.1	9.5

[1] WW - Windward, LW - Leeward

The value of 7 m/s is chosen as an illustrative boundary because no lateral responses ΔA_y above MacAdam's 4/10 controllability line are observed below this gust amplitude in Figure 11.2. It was suggested in Chapter 11 that MacAdam's 4/10 controllability score may already be indicative of an unsafe level of crosswind response. The likelihood of a wind-induced traffic accident may therefore increase with the number of gusts above the 7 m/s threshold. More studies relating driver evaluations of control and stability to measures of vehicle response are needed to

better define an appropriate threshold.

At Dolmsund, the higher proportion of gusts above 7 m/s has a clear effect on the percentage of lateral response values ΔA_y above the sensory threshold. The lowest value at Dolmsund (49.0% in the windward lane) is more than twice the next highest value of 22.1 in the leeward lane at Helgeland.

The leeward lane at Dolmsund stands out in the field notes as being particularly uncomfortable for a sustained period of time (the entire span of the bridge) as opposed to the local discomfort typically seen at the towers of cable-supported bridges. This corresponds well with the finding that the response is above the sensory threshold for 70% of data points. Having such a high proportion of the response above the sensory threshold is likely to be more tiresome for certain drivers or could even be overwhelming for others.

As mentioned previously, a front-axle skid event was also observed at the Dolmsund bridge. The separation-induced turbulence at Dolmsund may therefore increase the likelihood of wind-induced incidents by two mechanisms:

1. increasing the chance of observing a skid-inducing gust, and
2. increasing the number of gusts observed above the sensory threshold, thereby placing continuous physical and mental strain on the driver.

Note that the effect of mean wind speed has not been considered in this analysis. It is also possible that the terrain upstream of the Dolmsund bridge contributes to the high number of large-magnitude gusts observed. However, the difference between the windward and leeward lanes (45.2% versus 73.4% above 7 m/s) suggests that the girder has a strong effect.

12.4 Conclusions

Observations from the current field data show that critical turbulence – defined as high values of the change-of-amplitude $\Delta V_w > 7$ m/s – can be caused by both complex terrain as well as the separation of flow over the top surface of bridge girders. Gusts resulting from both sources of turbulence have been observed to cause a front-axle skid event with the test vehicle.

Separation of the flow from the girder surface appears to place more gusts above a 7 m/s threshold than the effect of complex terrain does. The percentage of gusts above 7 m/s in amplitude varied between 20% and 70% on the bluff-sectioned girders of cantilevered bridges (Måløy and Dolmsund) versus 0 to 6% on streamlined girders (Helgeland, Hardanger and Hålogaland). Correspondingly, the percentage of the ΔA_y signal above Brandt et al.'s [32] sensory threshold (0.58 m/s^2) is higher at Dolmsund and Måløy (7-73%) compared to the cable-supported bridges (2-22%).

Chapter 13

Tower wake profiles

The inverse gusts resulting from the shielding effect of bridge towers has been shown in Chapter 11 to create a hazardous situation for drivers. The gust dimensions and driving speeds are typically such that the gust is experienced at a frequency that is adverse to a driver's ability to maintain a straight path. Consequently, it is useful for bridge designers and owners to be able to predict the dimensions of the inverse gust – most importantly its amplitude and spatial period – such that the risk posed to drivers can be characterised and mitigation strategies can be developed.

In this chapter, wind speed profiles are plotted for each of the bridge towers observed in the field campaign. Similar profiles have been observed in the wind tunnel by a number of researchers previously. The geometry of the towers observed here and the flow conditions do not perfectly match those used in previous wind tunnel experiments. Nonetheless, it will be seen that there are similarities between the current field observations and results presented in the literature. The wind tunnel is likely to be a dependable tool in predicting gust profiles behind towers on existing and new bridges, though new studies are needed.

13.1 State of knowledge: mean flow in tower wakes

Using the database presented in Chapter 4, the existing list of relevant literature can be queried for studies describing the wind profile in the wake of bridge towers. A search for the key term *tower* in the metadata, followed by a skim reading of the resulting articles, quickly filters the list down to 7 entries.

Each text contains original results that illustrate the effect of bridge towers on the local, surrounding wind field and/or the aerodynamic loads on vehicles. Only the wind characteristics are of interest in this chapter. Consequently, Argentini et al. [20], Ma et al. [132, 133], who present only information about aerodynamic loads

rather than the local wind profile are not considered further.

The 4 remaining texts each present span-wise wind profiles describing the flow in the wake of various bridge tower geometries. The key features of the methodology, results and conclusions of the studies are presented next to allow for a comparison with the current experimental campaign.

Methodology

A brief summary of the studies that present span-wise wind profiles:

- Rocchi et al. [166] measured the near-tower span-wise wind profile in a wind tunnel. A series of static tests were performed with a vehicle model being placed at successive locations along a modelled girder in a quasi-static re-enactment of the tower passing manoeuvre. The wind was measured through pressure tappings on the vehicle model. The authors argued that the use of a series of vertically distributed tappings could be used to average out vertical variations in wind speed above the bridge deck. It is hoped that this will give a profile that can be used to numerically model aerodynamic loads on the vehicle as accurately as possible.
- Charuvisit et al. [42] performed a similar test in the wind tunnel. Critically, the profile was measured directly over the bridge girder using a split-film probe rather than indirectly through pressure tappings on a vehicle model. Measurements for the profile were taken at the half-height of a pre-defined scale vehicle model.
- In Zhou and Zhu [236] – another similar study – the profile was measured directly with an array of vertically distributed pitot-static tubes instead of the split-film probe. The vertical wind profile was used to calculate an equivalent wind speed (that maintains the same aerodynamic force on the vehicle) from which multiple measurements along the girder were used to estimate the span-wise profile. The results were compared to a CFD study as well.
- Wang et al. [209] also present near-tower span-wise wind profiles. However, being a conference article, the methodology is not fully explained and so this text will not be referred to further.

On the test vehicle used in the current experimental campaign, an anemometer is used to measure the wind speed directly and it is placed above the vehicle's bonnet (see Chapter 6 for a diagram and further details). In contrast to the studies in the literature, a vertical profile is not measured (nor averaged) and the single-point measurement is not at the mid-height of the vehicle.

Data extraction and projection

Data sets from Charuvisit et al. [42], Rocchi et al. [166] and Zhou and Zhu [236] have been extracted and plotted in Figure 13.1. The data points are manually picked from raster images of the relevant plots in each respective article.

In contrast to the other two studies, in Charuvisit et al. [42] the girder/tower model was rotated in the wind tunnel such that the tower column was placed at an incidence to the flow (see α in Figure 13.1). Four non-zero incidence angles were considered in addition to the zero-case considered in the other articles. Note the following with regards to [42]:

- The tower modelled in the wind tunnel was composed of a single rectangular column. The cable-stayed and suspension bridges driven across during the field experiments all have towers made up of two columns, one on either side of the girder.
- The incidence angles considered are $\alpha = 0°$, 30°, -30°, 60° and -60°. Only the positive values will be presented here (due to symmetry in the results).

The span-wise wind profiles are projected onto an axis perpendicular to the mean wind vector (dashed line labelled *Proj.* in Figure 13.1) to make comparisons between measurements at different wind incidence angles more insightful. Spatial coordinates are normalised by the projected width of the tower D which translates all positions to a non-dimensional plane x^*-y^*. A comparison of all span-wise wind profiles from the identified literature can be seen in Figure 13.1 along with sketches of the bridge tower cross-sections.

Experimental parameters

The aspect ratio AR of the tower cross-section, the cross-section's orientation/incidence angle to the flow α (AR and α are defined in Figure 13.2), the Reynolds number of the flow Re and the location of the measurement line (i.e. where the traffic lane and girder lie in the wake) are tabulated in the first columns of Table 13.1.

It appears that the flow conditions and geometry were similar in only two data sets. The $\alpha = 0°$ case by Charuvisit et al. [42] and the test by Rocchi et al. [166] consider the same incidence (0°), similar cross-sections (compare AR) and similar Reynold's numbers (Re). On the other hand, there is a difference in the parameter y^*_Δ, the positioning of the measurement line in the wake. In addition, the two different measurement approaches (direct wind measurement [42] vs. indirect measurement using a scale vehicle model [166]) may influence the results.

It is difficult to draw comparisons between data sets because the experimental parameters are so different. However, it will be seen that the results from the literature have similarities between themselves as well as with the results from the experimental campaign.

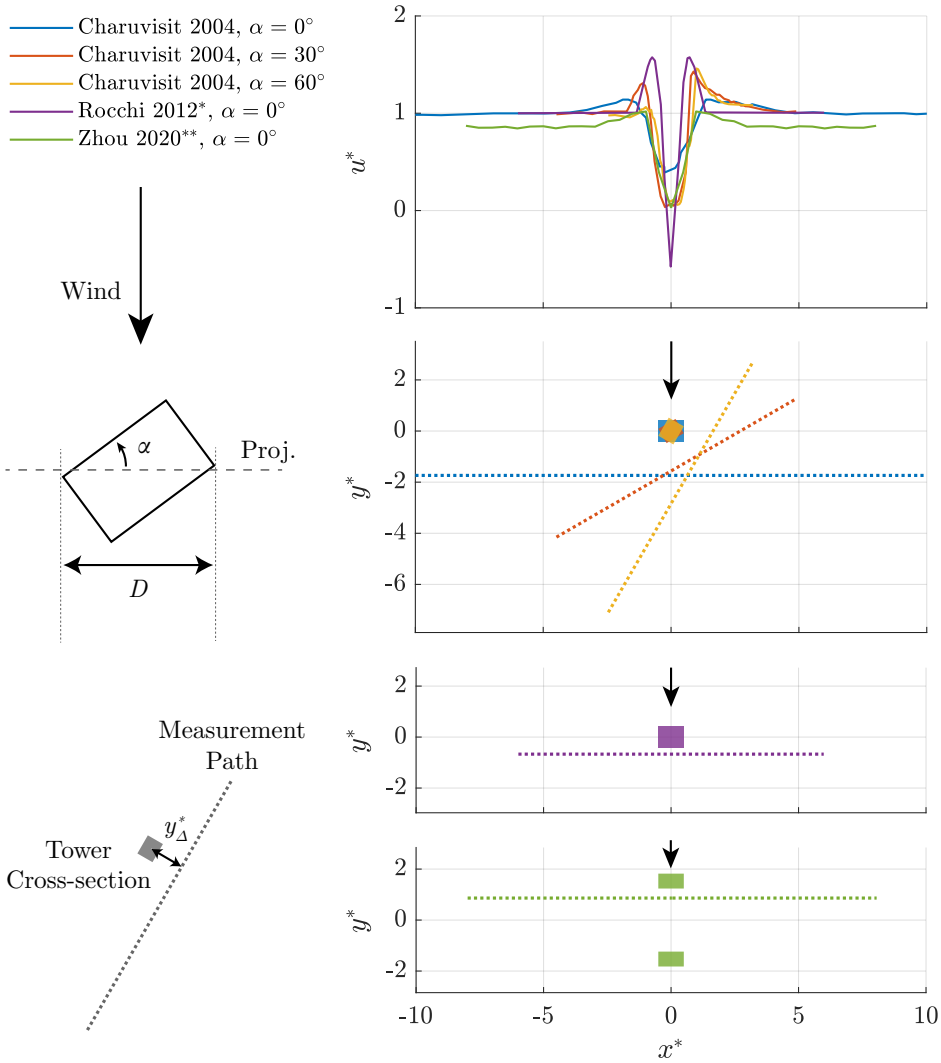

Figure 13.1: Overview of span-wise wind profiles in the literature.

The dashed lines show the measurement path in relation to the tower sections that are drawn as coloured patches. The concave edges of the Rocchi et al. profile have been simplified as straight lines.

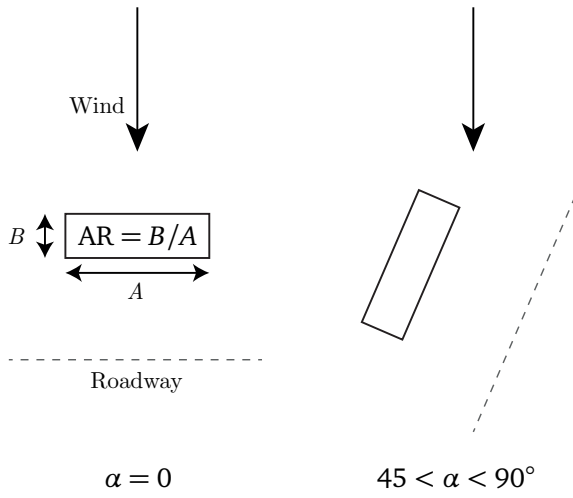

Figure 13.2: Convention used for defining aspect ratio and incidence angle.

The incidence angle is defined as zero when the in-plane wind vector is perpendicular to the roadway. Side B is defined as the side parallel to the wind vector at $\alpha = 0$ (thus always perpendicular to the roadway). The aspect ratio is then AR $= B/A$ such that low aspect ratios describe bluff bodies and high aspect ratios describe a more streamlined body at $\alpha = 0$. The incidence angle can vary between -90 and 90° such that bluff body becomes a streamlined one close to -90 and 90° and the wind vector becomes aligned with the roadway.

Discussion of results

Despite the wider difference in experimental parameters, it is in fact the results from Charuvisit et al. [42] and Zhou and Zhu [236] that look most comparable to one another in Figure 13.1 and Table 13.1. Noting some important differences between the two data sets:

- The *equivalent* wind speed presented by Zhou and Zhu [236], and used to draw the profile, is a root-mean-square value over the height of the vehicle normalised by the free-stream mean wind speed.
- The wind speed measured by Zhou and Zhu [236] is only the component normal to the bridge girder's axis, whereas Charuvisit et al. [42] present the in-plane magnitude of the wind vector.
- Charuvisit et al. [42] measure the wake behind a single, vertical column, whereas Zhou and Zhu [236] measure the wake between two vertically inclined columns that come together to form a single tower structure.

The first two points explain why the profile by Zhou and Zhu [236] tends to a value below 1 far away from the tower.

The shapes of the profiles by Charuvisit et al. [42] and Zhou and Zhu [236] are nonetheless similar even though the peaks and trough for [236] are sharper and the trough goes all the way to zero. The closer proximity of these measurements to the tower (small y^*_Δ) may at least partly explain this discrepancy, but also the difference in cross-section geometry (Charuvisit et al. [42]'s single rectangular section vs. Zhou and Zhu [236]'s rectangular section pair, see Figure 13.1).

The results by Rocchi et al. [166] differ more significantly from the other two studies. The width of the wake is narrower and the peaks higher. The trough extends into negative values. Some possible explanations:

- The tower cross-section is not perfectly rectangular in the Rocchi et al. [166] wind tunnel model (each side *bulges* with concave curvature).
- The measurement line's proximity to the tower y^*_Δ is smaller than in the other two studies.
- The profile is indirectly calculated - rather than directly measured - by solving an optimisation problem. The optimisation uses force estimates calculated from pressure measurements to estimate wind speeds.

As stated by the authors, the wind profile generated through this optimisation method should lead to more accurate force estimates using their model for the aerodynamic loads on the vehicle. The resulting wind profile is not necessarily an accurate characterisation of the true wind field.

It may also be that the presence of the vehicle in close proximity to the tower has a significant effect on the near-tower flow. Rocchi et al. [166] consider a tractor-trailer with a significant length dimension in comparison to the width of the tower (the ratio of vehicle length to tower width is approximately 1.6). Future studies may look to understand the effect of the presence of the vehicle on the span-wise wind profile near the tower.

Table 13.1: Key parameters of the span-wise wind profiles from the literature.

Data	AR	α [°]	y^*_Δ [1]	Re	...
Charuvisit et al. [42]	0.83	0	1.74	0.98×10^5	
Charuvisit et al. [42]	0.83	30	1.74	1.26×10^5	
Charuvisit et al. [42]	0.83	60	1.74	1.20×10^5	
Rocchi et al. [166]	0.58[2]	0	0.67[4]	2.38×10^5	
Zhou and Zhu [236]	0.56[3]	0	0.85[4]	3.13×10^5	

Left peak		Right peak		Trough		Skew.[5]
(x^*, y^*)	u^*	(x^*, y^*)	u^*	x^*	u^*	
(-1.8,-1.7)	1.14	(1.5,-1.7)	1.14	-0.26	0.39	0.00
(-1.1,-2.2)	1.31	(0.9,-1.1)	1.43	-0.23	0.04	0.04
(-1.0,-4.5)	1.06	(1.0,-1.1)	1.46	0.25	0.06	0.16
(-0.7,-0.7)	1.58	(0.7,-0.7)	1.58	-0.01	-0.58	0.00
(-1.0,-0.9)	1.19	(1.0,-0.9)	1.19	0.00	0.03	0.00

[1] y^*_Δ is the distance measured perpendicular to the girder from the profile path to the centre of the (leading) tower. (see Figure 13.1)
[2] The cross-section is not fully rectangular, but has concave sides.
[3] The tower cross-section is a pair of rectangular sections rather than a single section.
[4] Values are approximate due to limited information given in the referenced articles.
[5] Skewness is defined on a linear scale from 0 to 1, where 0 corresponds to equal left and right hand peaks (u^*) and 1 corresponds to the case where one value is zero and the other non-zero (Skewness= $0.5|u^*_l - u^*_r|/|\text{mean}([u^*_1, u^*_1])|$, where u^*_l and u^*_r are the left and right peaks).

Key observations

Some key observations from the wind tunnel data presented in the literature (refer to Figure 13.1 and Table 13.1):

1. Universally, the profiles have three extreme values with one trough near $x^* = 0$ that is straddled by two peaks.

2. At zero incidence, Zhou and Zhu [236]'s results show that the wind speed falls almost to zero $u^* = 0.03$. Charuvisit et al. [42]'s results show only a 60% drop in wind speed at the trough ($u^* = 0.39$) at zero incidence compared to values closer to zero at 30° and 60° ($u^* = 0.04, 0.06$). Note that $y^*_\Delta = 1.74$ in [42] in contrast with $y^*_\Delta = 0.85$ in Zhou and Zhu [236]. This means that the measurement line is about twice as far away from the tower centre in Charuvisit et al.'s [42] study.
3. The non-zero incidence cases from Charuvisit et al. [42] give non-symmetric profiles with skewness values of 4% and 16% at 30 and 60° respectively. The highest peak is found on the side where the measurement line is more windward (i.e. y^* is more positive). See the notes in Table 13.1 for the definition of skewness used here.
4. The magnitude of the highest peak appears to increase with incidence α based on Charuvisit et al. [42]'s results.
5. The non-dimensional lateral location (x^*) of the highest peak is consistent for both non-zero incidence angles, $\alpha = 30, 60°$ (0.9 and 1.0). The absolute location on the girder will be different.
6. At incidence, the vehicle path (or girder) passes through the $y^* = 0$ axis into positive values of y^*. Beyond this point, the path leads the tower in the flow and the vehicle is forward of the tower wake. The vehicle will still be in a flow region that is influenced by the tower (pressure wave). This is demonstrated by the data from Charuvisit et al. [42] at $\alpha = 60°$ on the right-hand side of the plane. The profile does not return to the mean wind speed, $u^* = 1$. In this case, the measurement line was not sufficiently long to capture the full influence of the tower on the flow (i.e. capture the return to $u^* = 1$).
7. At $\alpha = 0°$ there is fairly good agreement in the peak value of u^* between [42] and [236] with a 14% and 19% increase from mean wind speed. Note the different cross-sectional aspect ratios of 0.83 and 0.56 respectively. The peak can be up to 58% higher than the mean wind speed (see Rocchi et al.'s case).
8. All the left peaks from the data sets extracted from the literature lie in the range $-1.8 < x^* < -0.7$ and the right peaks within $0.7 < x^* < 1.5$.

13.2 Results from the experimental campaign

Reference values of wind speed and direction have been used to calculate the incidence α at each bridge tower observed in the field (using the definition of the reference segment given in Chapter 8). Note that one value is used for each bridge (averaged for both lanes) such that any local variations in the mean flow near the towers have not been accounted for.

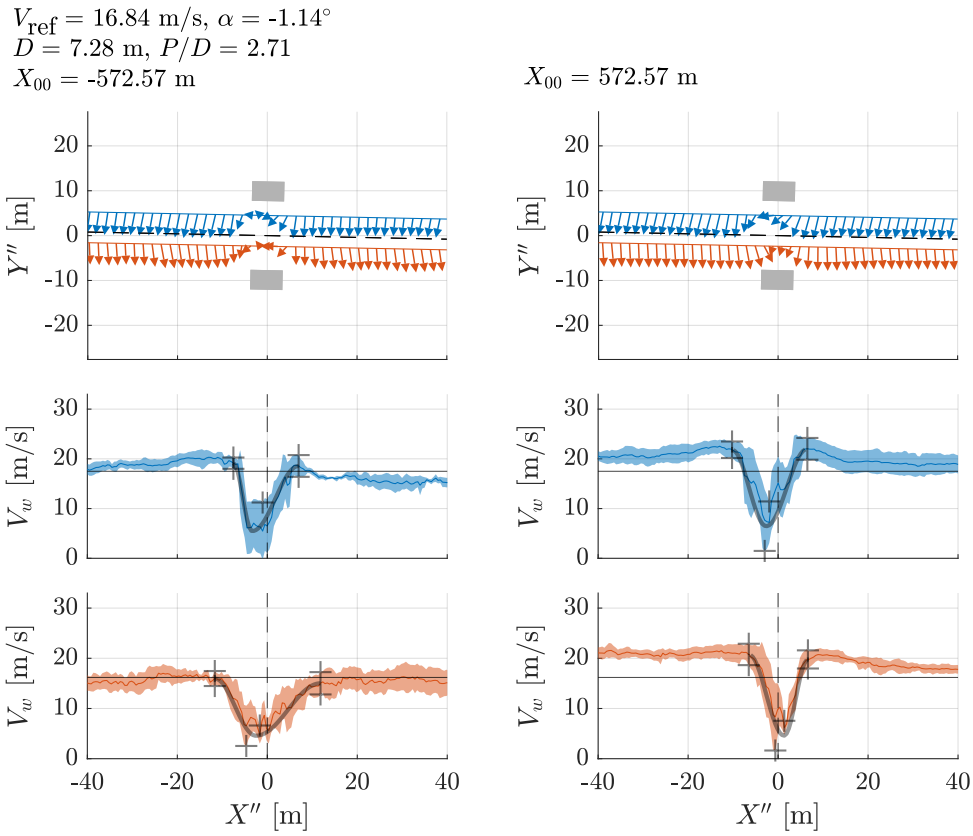

(a) South tower (b) North tower

Figure 13.3: Two-piece harmonic inverse gusts at Hålogaland towers.

Windward lanes are plotted in blue and leeward in red in keeping with wind and response profile plots in Chapters 8 and 9. The solid lines of V_w are bin-averaged curves calculated from all available signals recorded at 30 kph (typically 5). The bins are 0.5 m wide. The shaded regions are 95% confidence intervals. The black lines are two-piece cosine fits to the mean curve. The markers show the extremes of the 95% confidence interval at the end points of the two-piece cosine. The markers at the trough are simply the minima of the top and bottom 95% interval curves. X_{00} is the position on X_b that is taken as the origin for the X''-Y'' plane.

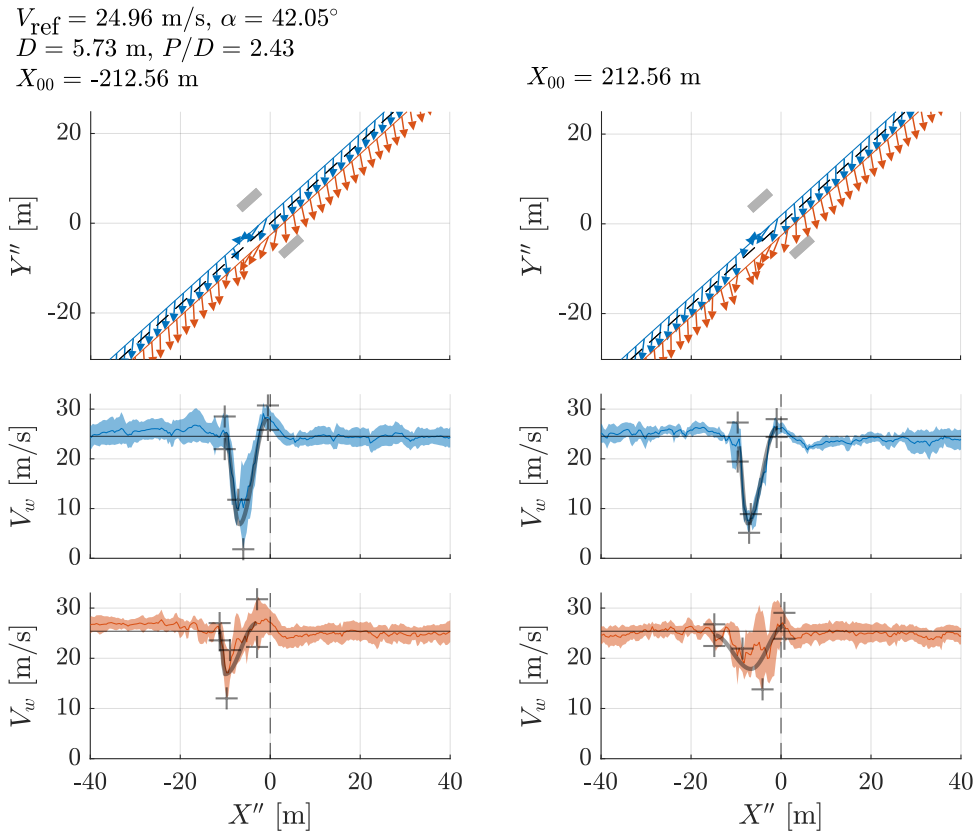

(a) South tower (b) North tower

Figure 13.4: Two-piece harmonic inverse gusts at Helgeland towers.

Windward lanes are plotted in blue and leeward in red in keeping with wind and response profile plots in Chapters 8 and 9. The solid lines of V_w are bin-averaged curves calculated from all available signals recorded at 30 kph (typically 5). The bins are 0.5 m wide. The shaded regions are 95% confidence intervals. The black lines are two-piece cosine fits to the mean curve. The markers show the extremes of the 95% confidence interval at the end points of the two-piece cosine. The markers at the trough are simply the minima of the top and bottom 95% interval curves. X_{00} is the position on X_b that is taken as the origin for the X''-Y'' plane.

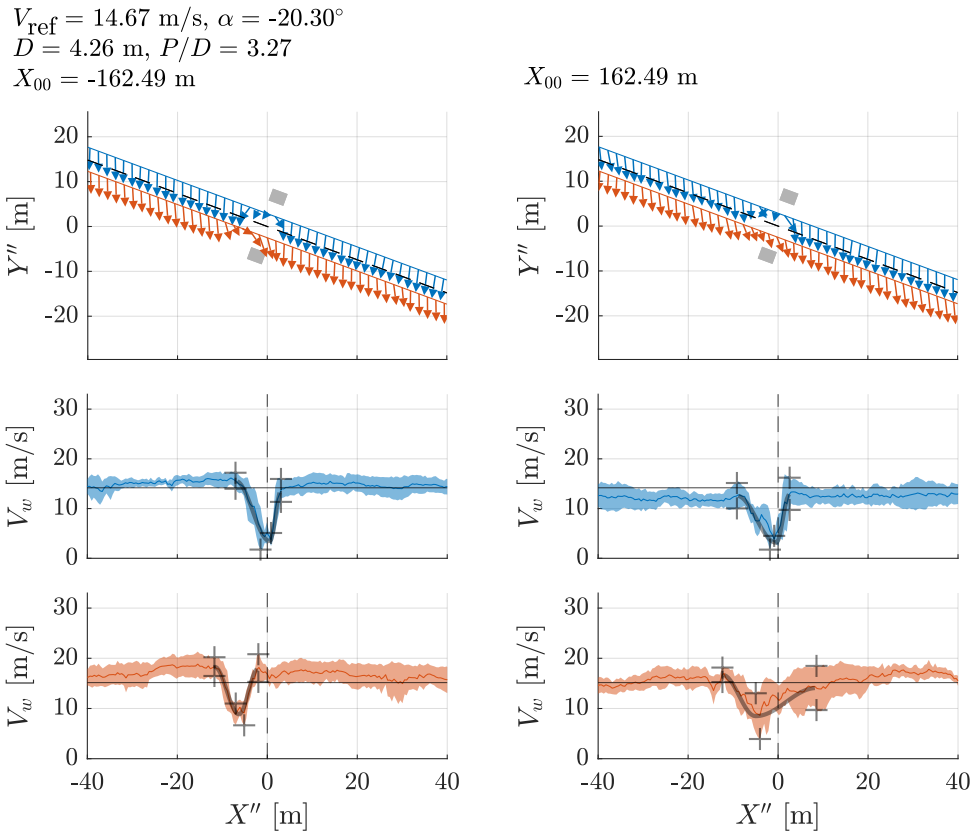

(a) North tower (b) South tower

Figure 13.5: Two-piece harmonic inverse gusts at Nærøysund towers.

Windward lanes are plotted in blue and leeward in red in keeping with wind and response profile plots in Chapters 8 and 9. The solid lines of V_w are bin-averaged curves calculated from all available signals recorded at 30 kph (typically 5). The bins are 0.5 m wide. The shaded regions are 95% confidence intervals. The black lines are two-piece cosine fits to the mean curve. The markers show the extremes of the 95% confidence interval at the end points of the two-piece cosine. The markers at the trough are simply the minima of the top and bottom 95% interval curves. X_{00} is the position on X_b that is taken as the origin for the X''-Y'' plane.

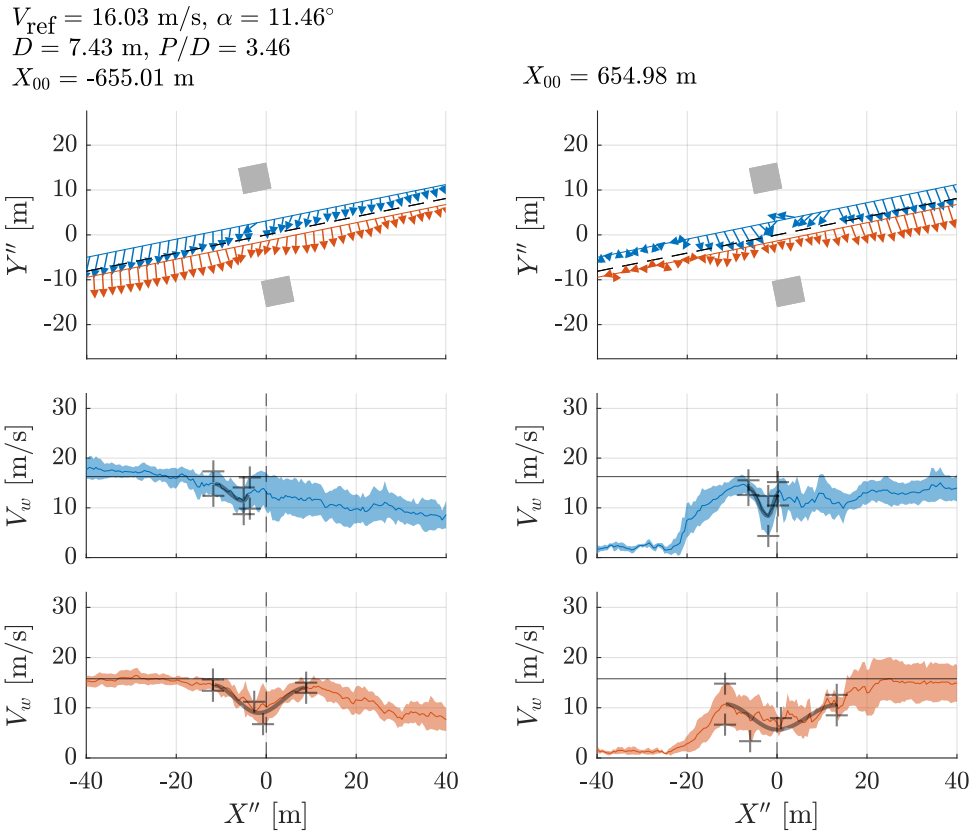

(a) South tower *Note that a tunnel entrance exists to the right of the tower on X_b.

(b) North tower *Note that a tunnel entrance exists to the left of the tower on X_b.

Figure 13.6: Two-piece harmonic inverse gusts at Hardanger towers.

Windward lanes are plotted in blue and leeward in red in keeping with wind and response profile plots in Chapters 8 and 9. The solid lines of V_w are bin-averaged curves calculated from all available signals recorded at 30 kph (typically 5). The bins are 0.5 m wide. The shaded regions are 95% confidence intervals. The black lines are two-piece cosine fits to the mean curve. The markers show the extremes of the 95% confidence interval at the end points of the two-piece cosine. The markers at the trough are simply the minima of the top and bottom 95% interval curves. X_{00} is the position on X_b that is taken as the origin for the X''-Y'' plane.

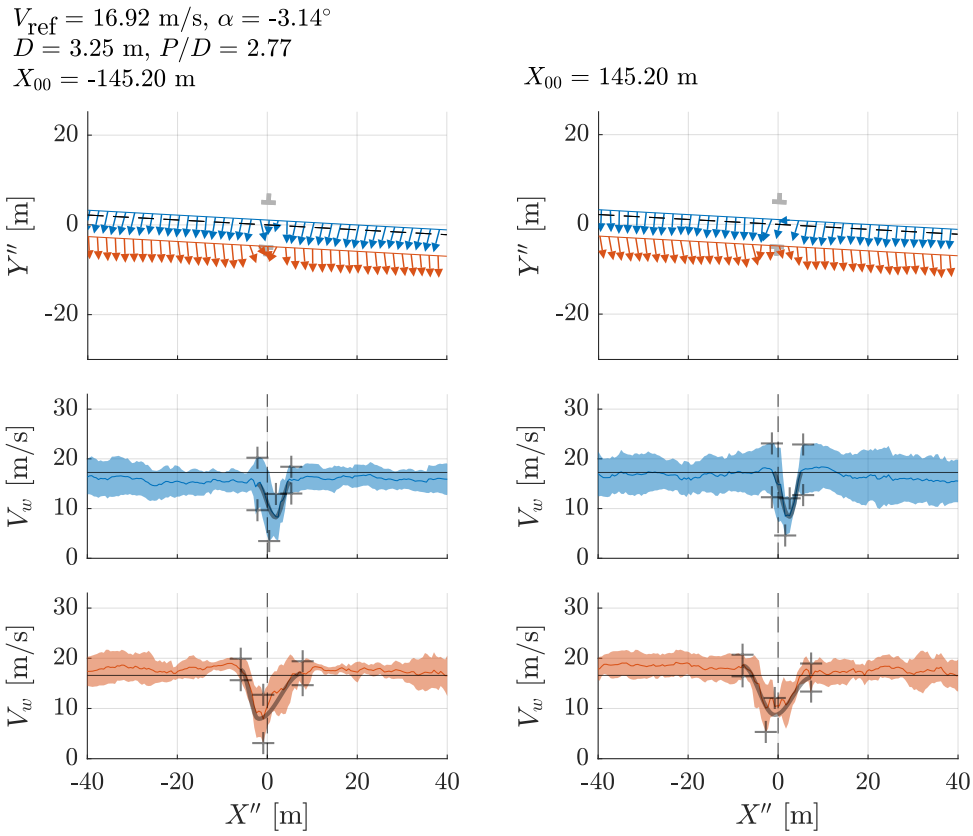

(a) West tower (b) East tower

Figure 13.7: Two-piece harmonic inverse gusts at Tjeldsund towers.

Windward lanes are plotted in blue and leeward in red in keeping with wind and response profile plots in Chapters 8 and 9. The solid lines of V_w are bin-averaged curves calculated from all available signals recorded at 30 kph (typically 5). The bins are 0.5 m wide. The shaded regions are 95% confidence intervals. The black lines are two-piece cosine fits to the mean curve. The markers show the extremes of the 95% confidence interval at the end points of the two-piece cosine. The markers at the trough are simply the minima of the top and bottom 95% interval curves. X_{00} is the position on X_b that is taken as the origin for the X''-Y'' plane.

The projection of the tower perpendicular to the flow D (see Figure 13.1) is calculated and used to normalise the data in the same manner as the data from the literature. Table 13.2 shows the Reynold's number (based on D), the incidence α and the aspect ratio AR of the tower sections for each bridge.

The distance from the centre of the leading tower to the measurement path y^*_Δ is calculated using a reference value (averaged on a portion of the main span) of the vehicle's measured lateral displacement from the centreline in each lane and is tabulated appropriately in Table 13.2. Note that the true path during each repetition may vary locally from the average y^*_Δ.

In Tables 13.2 and 13.3, each tower (at either end of each bridge) is given a reference index from a to t which refers to a specific tower and measurement line (lane) at each individual tower (2 lanes and 2 towers makes 4 combinations at each bridge). This allows for cross-referencing between Tables 13.2 and 13.3.

A sketch of the tower cross-section, the measurement path and averaged in-plane wind vectors can be seen in Figures 13.3 through 13.7. The sketches have been oriented such that the reference wind vector points down the page. A local coordinate system X''-Y'' has been defined at the centre-point of each tower's respective cross-section and is aligned such that negative Y'' is in the reference wind direction.

The locations of the towers are point-picked from the mapping service norgeskart.no and the absolute positioning of the GNSS has not been verified. Consequently, there is no guarantee of perfect alignment between the sketched cross-sections and the position data (see for example Figure 13.7 from the Tjeldsund bridge where it looks like the vehicle's leeward path crosses through the leeward tower). A good alignment is expected in most cases nonetheless given the advertised accuracy of the GNSS system (5 mm positional accuracy using the RTK algorithm as shown in Chapter 6).

Normalised coordinates are not used, yet the limits on the X'' axes are consistent between all figures such that tower and gust scales can be observed and compared. Recall that the gust dimension is relevant for the transient development of aerodynamic loads as explained in Chapter 11.

The two-piece cosine fitting procedure introduced in Chapter 11 is used to define the spatial period of the gust D_{gust} as well as the wind speed at the peaks and trough. Further details are given in the descriptions under Figures 13.3 through 13.7.

The location x^* and wind speed u^* in the normalised domain (spatial information normalised by D and wind speed by reference wind speed) for the peaks and the trough are tabulated in Table 13.3 along with the normalised gust dimension $D^*_{\text{gust}} = D_{\text{gust}}/D$ and skewness.

P is the distance between the two centre-points in the pair of sections that make up one tower cross-section (see Figure 14.1). The ratio P/D describes the spacing

Table 13.2: Parameters of the measured span-wise wind profiles.

Bridge	Re ($\times 10^6$)	P/D	α [°]	AR	Lane	y^*_Δ	Ref.[1]	Tower Idx./Loc.
Hålogaland	8.4	2.71	-1.14	0.61	1	0.74	a	1/N
							b	2/S
					2	1.68	c	1/N
							d	2/S
Hardanger	8.2	3.46	11.46	0.92	1	1.32	e	1/N
							f	2/S
					2	1.91	g	1/N
							h	2/S
Helgeland	9.8	2.43	42.05	0.34	1	0.97	i	1/N
							j	2/S
					2	1.56	k	1/N
							l	2/S
Nærøysund	4.3	3.27	-20.30	0.80	1	1.00	m	1/N
							n	2/S
					2	2.19	o	1/N
							p	2/S
Tjeldsund 1	3.8	2.77	-3.14	-[2]	1	1.21	q	1/W
							r	2/E
					2	3.01	s	1/W
							t	2/E

[1] An index value that can be used to find the corresponding row in Table 13.3.
[2] The Tjeldsund section is non-rectangular and so AR is not defined.

Table 13.3: A characterisation of the measured span-wise wind profiles. Values are given for fitted two-piece cosines.

Ref.[1]	Left peak		Right peak		Trough		D^*_{gust}	Skewness[2]
	x^*	u^*	x^*	u^*	x^*	u^*		
a	-1.41	1.30	0.89	1.31	-0.87	0.38	2.30	0.01
b	-1.03	1.14	0.96	1.10	-0.74	0.32	1.99	0.02
c	-0.90	1.23	0.91	1.17	-0.64	0.27	1.81	0.03
d	-1.60	0.95	1.62	0.89	-0.63	0.27	3.23	0.04
e	-0.86	0.88	0.03	0.80	-1.18	0.52	0.90	0.12
f	-1.58	0.93	-0.49	0.81	-1.59	0.71	1.11	0.38
g	-1.56	0.67	1.79	0.66	-0.71	0.35	3.41	0.02
h	-1.59	0.91	1.19	0.87	-1.15	0.56	2.84	0.05
i	-1.68	0.94	-0.17	1.05	-1.07	0.28	2.04	0.08
j	-1.77	1.01	-0.09	1.13	-1.04	0.27	2.26	0.08
k	-2.59	0.99	0.13	1.06	-2.09	0.72	3.66	0.12
l	-1.96	1.01	-0.51	1.08	-1.95	0.67	1.96	0.09
m	-1.66	1.06	0.71	0.93	-0.53	0.23	2.53	0.09
n	-2.15	0.86	0.60	0.88	-0.47	0.21	2.94	0.02
o	-2.76	1.25	-0.47	1.23	-2.14	0.60	2.45	0.02
p	-2.91	1.14	2.01	0.96	-2.06	0.58	5.24	0.19
q	-0.67	0.88	1.64	0.93	-2.50	0.48	2.32	0.05
r	-0.42	1.05	1.71	1.05	-2.54	0.49	2.14	0.01
s	-1.82	1.05	2.42	1.01	-2.51	0.47	4.24	0.04
t	-2.43	1.10	2.26	0.96	-2.76	0.51	4.70	0.14

[1] An index value that can be used to find the corresponding row in Table 13.2.
[2] Skewness is defined on a linear scale from 0 to 1, where 0 corresponds to equal left and right hand peaks (u^*) and 1 corresponds to the case where one value is zero and the other non-zero.

between the two tower columns and will be seen in the next chapter (14) to affect the vortex shedding properties of paired cylinders. The parameter will likely have an effect on the mean wake profile as well.

13.3 A comparison of field and wind tunnel results

Each observation from the data extracted from the literature under the *Key observations* heading in Section 13.1 can now be compared to the current field data (see Tables 13.2 and 13.3 and Figures 13.3 through 13.7). Point for point:

1. The general two-peak, one-trough shape is observable in the field data (it is less clear in the windward lane of the Hardanger bridge in Figure 13.6, likely due to the towers' proximity to tunnel entrances/exits at either abutment). Unlike in the wind tunnel data, the peaks do not always exceed $u^* = 1$. This may be because the reference speed – taken from the main span – does not match the true mean wind speed in the vicinity of the towers. The wind speed may be lower towards the ends of the bridge near terrain. The field data may also be noisier (there is less data on which to take an average) and more prone to error (for example GNSS position errors or errors caused by the anemometer's anti-spike algorithm) than the wind tunnel data. The combination of noise and errors make the peaks difficult to characterise correctly.
2. At the trough, in the data extracted from the literature at zero incidence $\alpha = 0$:

   - Charuvisit et al. [42] found $u^* = 0.39$ with measurement line $y^*_\Delta = 1.74$
   - Zhou and Zhu [236] found $u^* = 0.03$ with measurement line $y^*_\Delta = 0.85$

   The incidence was near-zero at Hålogaland ($\alpha = -1.14°$) and Tjeldsund 1 ($\alpha = -3.14°$) with the following results at the trough:

   - Hålogaland lane 1: $u^* = 0.38$ and 0.32 (N & S respectively), $y^*_\Delta = 0.74$
   - Hålogaland lane 2: $u^* = 0.27$ and 0.27 (N & S respectively), $y^*_\Delta = 1.68$
   - Tjeldsund 1 lane 1: $u^* = 0.48$ and 0.49 (W & E respectively), $y^*_\Delta = 1.21$
   - Tjeldsund 1 lane 2: $u^* = 0.47$ and 0.51 (W & E respectively), $y^*_\Delta = 3.01$

   The results from the field are closer to Charuvisit et al. [42]'s results with flow reductions to values of u^* no lower than 0.27. The data extracted from the literature suggests that an increased distance from a single section y^*_Δ can increase u^* at the trough. It is logical to argue that there is more shielding closer to the leeward side of a single section. The results for the paired sections at Hålogaland and Tjeldund 1 suggest the opposite here. There may

be an interaction between the leeward section's forward pressure wave and the windward section's wake.

3. The skew cases in the measured data are the Helgeland (42.0°) and Nærøysund (-20.3°) bridges. At Helgeland the skewness is most pronounced with values between 8% and 12% (compare to Charuvisit et al. [42]'s 4% and 16% at 30° and 60°). The data extracted from the literature and the measured results are therefore complementary in this instance. At Nærøysund there are values between 2% and 19%. This latter value results from a poor two-piece cosine fit (see Figure 13.5b, South tower) and looks like an outlier. There may be another flow feature affecting the profile. A vortex street was observed in the wakes of each tower at Helgeland and will be discussed in Chapter 14. At the Helgeland towers as well as the North tower at Nærøysund, the highest peak is the leeward one which is in agreement with Charuvisit et al. [42]'s results. High values of skewness are observed at Hardanger (up to 39% as seen in Table 13.3). This may be due to the proximity of the towers to the fjord walls and tunnel entrance/exits. Such configurations/topographies have not been modelled in the wind tunnel and so comparisons cannot be made to the Hardanger case.
4. It is difficult to conclude from the numbers in Table 13.3, but a comparison of Figures 13.4 (Helgeland) and 13.5 (Nærøysund) reveals that the windward peak (most positive in y^*) is more pronounced at Helgeland (42°) than Nærøysund (-20°). This complements the observation from the wind tunnel data that the peak increases in magnitude with incidence (at least up to 60° – the highest case in [42]).
5. There is little consistency in the lateral position x^* of the windward peaks at Nærøysund and Helgeland, unlike that observed in the wind tunnel data. The sections at Helgeland have a uniquely low aspect ratio (0.34) and at high incidence (42°) create a sort of channel that pushes the flow to the left in Figure 13.4. This shifts the entire profile significantly to the left (the trough is at $-2 < x^* < -1$). The single sections from Charuvisit et al. [42] and the paired sections observed here at Helgeland cannot be compared.
6. In the wind tunnel data it is possible to pick a point far away from the tower where u^* returns to 1. The tower's pressure wave has ostensibly negligible effect further away from this point on the measurement line. Such a point is difficult to determine with the measured data here. As previously mentioned, there may be span-wise variations in the mean wind vector and the signals here are polluted with noise and errors. More data for averaging could improve future results.
7. The majority of peaks in Table 13.3 are in fact close to or below 1. Again, this is likely due to noise, errors and the inappropriate choice of reference wind

speed. Nonetheless, the highest value at any of the peaks is $u^* = 1.31$. This at the Hålogaland bridge at α =-1.1°. For comparison, zero incidence peaks in the wind tunnel data are 1.14 [42] and 1.19 [236].

8. All peaks in the wind tunnel data lie in $0.7 < |x^*| < 1.8$ compared to $0.4 < |x^*| < 2.9$ in the experimental campaign. There is more variation in the field data. It should also be noted that the right-hand peak in the windward lane of the Helgeland bridge lies in the left-hand plane meaning the entire two-piece cosine shape has been shifted across the $x^* = 0$ line. These observations suggest the lateral position of the peaks are not easily predicted using current wind tunnel results.

13.4 Summary

The wind speed profiles observed in the wake of the towers at the Hålogaland, Hardanger, Helgeland, Nærøysund and Tjeldsund bridges have been compared to wind tunnel data extracted from the literature. It is overall encouraging that there are concrete similarities between the wind tunnel data and the field data even though there are some fundamental parameter differences:

- The field cases were all paired sections in comparison to majority single sections in the wind tunnel data.
- The Reynold's numbers are an order of magnitude higher in the field.
- The aspect ratios are reasonably similar with 0.6-0.9 in the field (apart from Helgeland at 0.34) versus 0.6-0.8 in the wind tunnel.
- Two cases in the field are close to zero incidence – for which there are three cases in the literature – while the others were at 11°, 20° and 42°, different to the remaining 30° and 60° presented in the literature.
- The measurement line distance y^*_Δ for the field varies between 1.0 and 3.0 while the wind tunnel values (literature) are 0.9-1.8.

Some comparative observations:

- The general shape of the profiles seen in the field correspond well with findings from the wind tunnel experiments. There is a trough straddled by two peaks.
- It is difficult to obtain equally illustrative data in the field due to instrumentation errors and a lack of repeatability. Measures can be taken in future experiments to maximise the amount of data and account for local variations in mean wind speed across the span and/or time variations (i.e. non-stationarity).

- Unlike in the wind tunnel data – where values up to 97% have been presented – no tower was found to have a shielding effect that reduced the wind speed by more than 79% (Nærøysund, Lane 1, Tower 2/S).
- Skewness values in the wind profile up to 12% have been observed in the field at $\alpha = 42°$ compared to up to 16% found at $\alpha = 60°$ in the literature. This does not include the Hardanger bridge, where the proximity of the towers to the steep fjord walls and tunnel entrances/exits lead to skewness in this inverse gust of up to 38%.
- The observation from wind tunnel data that the windward peak is the highest peak appears to hold true in the field.
- The lateral location x^* of the peaks was seen to vary widely in the field observations ($0.4 < |x^*| < 2.9$). At Helgeland the right-hand peak was even observed in the left-hand plane.
- The highest peak seen in the field is a 31% increase at zero incidence (α =-1.1° at Hålogaland) compared to 46% at $\alpha = 60°$ in the literature.
- The general two peaks and one trough shape was observed at the Hardanger bridge, though the inverse gusts were of a much lower amplitude than elsewhere. The proximity of the towers to the fjord wall and the entrances/exits to the tunnels are likely to make wind tunnel studies and predictions more difficult.
- A general result from Table 13.3 is that the spatial periods of the gusts D_{gust} are between 0.9 and 5.2 times the projected width of the tower D.

The wind tunnel studies are also varied in the method used to estimate the wind profiles. None of the wind tunnel studies observed the wind speed at the equivalent height of the anemometer used in the field campaign and some of the wind tunnel studies performed an averaging or equivalencing procedure on the vertical wind profile.

13.5 Conclusions

The similarities between the results – combined with the merits of each method independently – suggest that both the wind tunnel and field results are plausibly good descriptions of the averaged wind profile along a measurement line in the wake of bridge towers. This would make the wind tunnel a promising tool that can be used to characterise the wakes behind existing and new bridge towers. In addition, the instrumented vehicle is a valuable calibration and validation tool. Put together, both tools can help bridge designers and owners better characterise the wind field on bridges and enhance wind-related traffic risk assessments.

The following is suggested for future work:

1. A parameter study can be performed in the wind tunnel with paired cross-section cylinders to study the effect of AR, P/D, α and y^*_Δ on the wind profile.
2. Three-dimensional effects have not been considered. The bridge girder may have an effect as well as any taper or inclination of the tower columns. These can also be studied in the wind tunnel.
3. The effect of the fjord walls and tunnel entrances/exits on the wind profiles in the wake of the Hardanger bridge towers should be studied in more detail.
4. One improvement to the field observations would be to resolve the issue of the anti-spike algorithm of the anemometer. This can be resolved either by de-activating the algorithm (if possible) or choosing alternative instrumentation.
5. A second improvement could be to perform dedicated experiments where the full experiment time is spent driving at 30 kph near the bridge towers such that as much data as possible is collected.

Chapter 14

The vehicle's response to tower vortex shedding

An interesting phenomenon was observed during the field sessions in the leeward lane (southward travel) on the Helgeland bridge. At the lowest driving speed - with the cruise control set at 30 kph - the vehicle oscillated violently about its roll axis in approach to the towers. It was hypothesised during the sessions that there was a sizeable coherent vortex street in the wake of the tower.

This type of roll response was not observed elsewhere during the field campaign. The excessive roll response did not make it difficult to control the vehicle, though it did have a significant impact on the ride comfort.

The measured wind and roll response in the vortex street will be described in this chapter. A systematic review of wind tunnel studies describing vortex streets in the wake of high aspect ratio cylinders is presented first. This will aide in the discussion on whether or not similar vortex-induced responses are likely to be observed on other bridges in Norway.

14.1 State of knowledge: oscillating flows in the wakes of high aspect ratio cylinders

The flow around high aspect ratio cylinders (or in some literature, 2D cylinders) has been studied and is a simplified case of the flow around a real, fully-featured three-dimensional bridge tower column. The aspect ratio is defined as the length of the cylinder as a proportion of a sectional dimension, such that high aspect ratios describe long, line-like cylinders. The term cylinder is used to describe geometries with any cross-sectional shape, not just a circular one.

Figure 14.1 shows a selection of some of the cross-sectional shapes and cylinder arrangements that have been studied. The simplest of which has been studied

extensively and is the case of a single circular cross-section cylinder (Figure 14.1a). For a thorough explanation of the flow around a circular cylinder and how the flow develops with Reynold's number see Anderson [19]. The oscillatory flow has been studied in the wind tunnel by, amongst others, Bearman [31], Achenbach and Heinecke [13] and Schewe [171].

Flow changes with Reynold's number – circular cylinder

The authors of this last work [171] plot the Strouhal number – based on the frequency of lift coefficient fluctuations – as a function of Reynold's number in the range 2.3×10^4 to 7.1×10^6. The Strouhal number shows Reynold's number independence up to a critical Re $\approx 3.5 \times 10^5$. Here there is a sudden increase in Strouhal number associated with a sudden decrease in drag coefficient. This can be explained by fundamental changes to the structure of the boundary layer and its separation from the cylinder's surface.

From this critical Reynold's number and into the supercritical regime, there is a slight negative slope up to Re $\approx 10^6$. Here there is another sudden change in St, in this case a drop in value. Schewe refers to this as the upper transition. Further increase in Reynold's number is then associated with a recovery of the Strouhal number in what Schewe refers to as the transcritical regime.

The above description of the different flow regimes for the circular cylinder demonstrates the sensitivity of the wake oscillations, or vortex structures, to Reynold's number. The details of the flow structure will not be reviewed here. However, it is important to understand that the wake flow trailing cylinders can be sensitive to Reynold's number even at high values up to the order of 10^7 (observed in this work).

Rectangular cylinder

For rectangular cylinders - as bridge tower columns often are - the geometry of the cross-section will also have an effect on the vortex structures. The aspect ratio AR (of the cross-section) and the angle of incidence fully describe the geometry of the cylinder relative to the oncoming flow (see Figure 14.1d for a non-skew/non-leaning cylinder). Note that the aspect ratio is defined as the long side as a proportion of the short side in this chapter (in contrast to the previous chapter) to be consistent with the literature. If present, the flow will also be affected by the presence of additional cylinders and their arrangement relative to one another.

Paired cylinders

The case of a suspension or cable-stayed bridge tower is typically what is shown in Figure 14.1g. The rectangular cross-sections are parallel to one another, yet in-

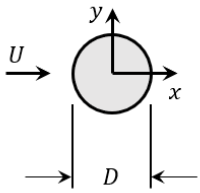

(a) Single circular cross-section

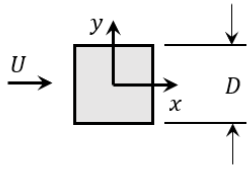

(b) Single square cross-section

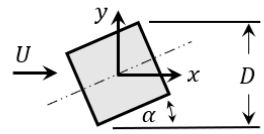

(c) Single square cross-section at incidence

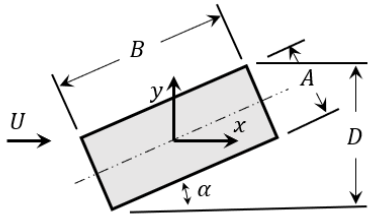

(d) Single rectangular cross-section at incidence

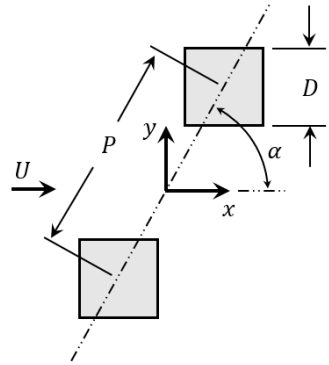

(e) Staggered square cross-sections without incidence

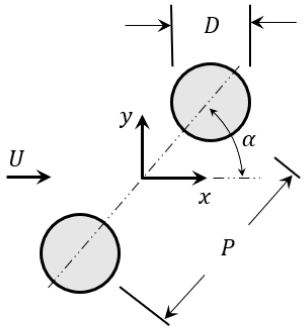

(f) Staggered circular cross-sections

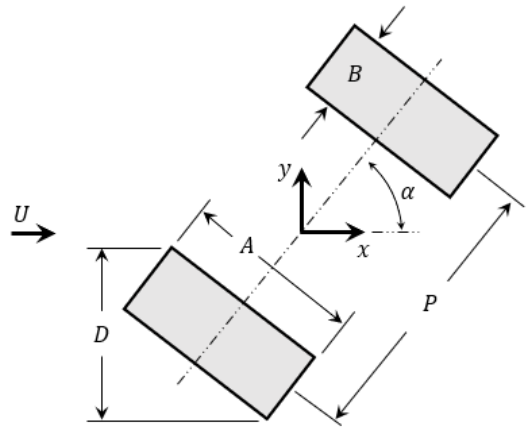

(g) Staggered rectangular cross-sections at incidence

Figure 14.1: Cross-sectional arrangement of cylinders.

clined and staggered in relation to the mean wind vector. The aim here will be to seek and review any literature that can shed light on the wake that forms behind this shape and arrangement of cylinders. It will be seen that this case has not been considered directly, and so the strategy taken is to look at individual parameters independently. The effect of the rectangular shape, it's aspect ratio and the presence of a paired cylinder.

Note that the high Reynold's number seen in the field has not been recreated in laboratory experiments. Additionally, the placement of sensors – and the type of sensors – used to measure the frequency of oscillation varies between studies and differs from the case of the experimental campaign presented here where the test vehicle is traversing through the wake.

In the fully three-dimensional case, each cylinder may be inclined to the vertical and/or tapered along the long axis as well. There is also a girder between the two tower columns. These effects from the 3D geometry of the tower and girder will not be considered, but present an opportunity for further study. Some existing studies on the topic were found during the literature search.

Targeted search

The following search phrase was used to find relevant titles. The phrases used to filter out certain results – those preceded by the NOT operator, for example *wall-mounted* or *control* – were chosen in an iterative process upon review of the search results. These phrases were found to reduce the search results to a manageable list for more detailed review without losing important entries. Note that the methodology used here is unlikely to be as robust as that used for the mapping presented in Chapter 4. The goal here is not to achieve a fully representative list of literature, but rather to find sufficient data and evidence to compare with the current experimental results. The search was performed on the 25th of May, 2021 using the Web of Science database. Only one database was chosen for the sake of simplicity. The particular database used here was found to be easy to use and give a significant number of results without being tied to any particular publisher.

> TI = ((square OR rectangular) AND cylinder AND (wake OR flow) NOT "low reynolds" NOT "wall mounted" NOT wall-mounted NOT suppression NOT control)

This gave 175 results from which 57 were identified as relevant based on a review of the data and conclusions presented in the articles. These have been arranged according to the Reynold's number, cross-section shape and arrangement of cylinders considered in the research in Table 14.1. They have then been screened for interesting data and the key findings have been plotted in Figure 14.2. Here,

interesting data is that which clearly demonstrates the effect of geometric parameters on the frequency content of shedding vortices; preferably at higher Reynold's numbers.

Rectangular cross-section

Figure 14.2a shows St as a function of angle of incidence for square and rectangular cross-section cylinders. See Figures 14.1c and 14.1d for a visual description of each respective geometry and the parameters used to describe them. Some observations from the data include:

- The Strouhal number in the wake of a rectangular cross-section cylinder is strongly dependent on it's orientation in the flow – the incidence angle α.
- For all the data sets, there is less incidence-dependence in the range starting from $\alpha \approx [10, 15]^\circ$ to $\alpha \approx [60, 70]^\circ$.
- Between $\alpha \approx 30^\circ$ and $\approx 60^\circ$ (*mid-range*) the results from Norberg [147] (AR = [1,2,3]) show that St is roughly constant (≈ 0.17) and equal for all values of aspect ratio.
- The left-hand peak Strouhal number for the square cylinder is found at an incidence of 15° and is consistent between the two studies with AR= 1.
- From Norberg [147], the effect of increasing the AR from 1 to 2 is to lower the left-hand peak Strouhal number (from ~ 0.18 to ~ 0.17) and the incidence angle at which it occurs (from 15° to 10°).
- Increasing AR to 3 further lowers the incidence at peak St (to 5°) and increases the peak value (to ~ 0.19).
- The right-hand peak for AR = 2 occurs at a higher incidence 70° vs. 60° for AR = 1, with a higher value ~ 0.18 vs. ~ 0.17, showing the inverse trend to the left-hand peaks.
- It appears that the higher Reynold's number in Huang et al.'s study results in a higher left-hand peak and a higher constant value in the mid-range of incidence angles.

Note again that the location at which the Strouhal number has been measured has not been checked for each study. This may have an influence on the results and change the observations given above. A significant missing piece to understanding this data is the Reynold's number dependency. Nonetheless, the following is kept in mind for future analysis:

- The Strouhal number in the wake flow of a rectangular cylinder is sensitive to incidence angle α.

Table 14.1: A map of the literature on the wake of square and rectangular cylinders.

Re[1]	Cross-section	Arrangement[2,3,4,5]	Presented in
10^5	rectangular	single	[180, 213]
10^5	square	inline	[182]
10^5	square	single	[97]
10^4	rectangular	single	[86, 147, 197]
10^4	square, plate	single, s-by-s	[88]
10^4	square	inline	[72, 112, 126, 210, 218, 227]
10^4	square	s-by-s	[91, 142, 184]
10^4	square	s-by-s array	[117]
10^4	square	single	[96, 201]
10^4	square	staggered	[17]
10^3	rectangular	single	[143, 150]
10^3	square	inline	[174, 183]
10^3	square	s-by-s	[152]
10^3	square	single	[75, 128, 129]
10^2	rectangular	s-by-s	[149]
10^2	rectangular	single	[57, 141]
10^2	square	inline	[58, 104, 121, 176, 181]
10^2	square	inline array	[101]
10^2	square	inline, staggered	[118]
10^2	square	s-by-s	[14, 16, 56, 155]
10^2	square	s-by-s array	[9, 100]
10^2	square	single	[76, 175, 198, 228, 229]
10^2	square	staggered	[12, 102, 145, 240]
10^1	square	inline	[43]
10^1	square	s-by-s	[15, 169]

[1] Maximum Reynold's number considered.
[2] single: see Figure 14.1a, 14.1b, 14.1c.
[3] s-by-s (side-by-side): see Figure 14.1f at $\alpha = 90°$.
[4] inline: see Figure 14.1f at $\alpha = 0°$.
[5] staggered: see Figure 14.1f at $\alpha \neq 0, 90°$.

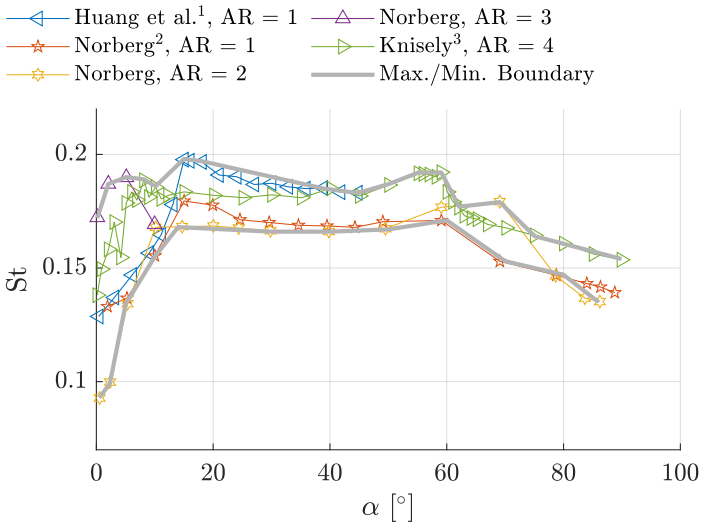

(a) Rectangular cross-section cylinders

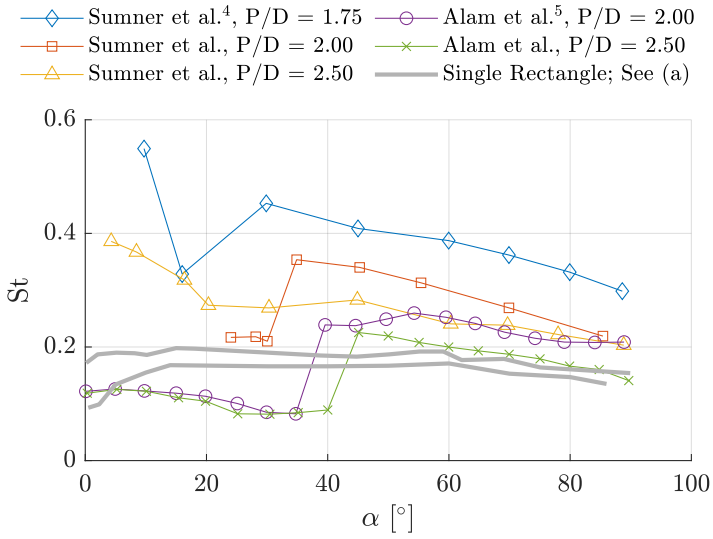

(b) Staggered cylinders (upstream St)

Figure 14.2: Strouhal number as a function of incidence presented in the literature.

[1] Huang et al. [97]; rectangle; measured by hot-wire anemometer; $Re = 9.4 \times 10^4$
[2] Norberg [147] square; measured by hot-wire anemometer; $Re = 5 \times 10^3$.
[3] Knisely [116] rectangle; measured by hot-wire anemometer; $Re \approx 10^4$.
[4] Sumner et al. [192] circle; measured by hot-wire anemometer; $Re = 7.2 \times 10^4$.
[5] Alam et al. [17] square; measured by hot-wire anemometer; $Re = 1.3 \times 10^4$.
Note: some data is missing/approximate where data series were indistinguishable.

- The sensitivity is acute at angles close to 0° and 90°.
- The aspect ratio of a rectangular cylinder can affect the peak Strouhal number and the incidence angle at which this occurs.
- The aspect ratio can also affect the range of incidence angles across which the Strouhal number is roughly constant. The approximately constant St range is wider with higher AR.
- Higher peak Strouhal numbers are found for AR$= [3, 4]$ when compared to AR$= [1, 2]$.

This summarises the observations and gives some interim conclusions about the effect of angle of incidence and aspect ratio on the Strouhal number measured in the wake flow of rectangular cylinders. The next step is to consider the effect of the presence of a second, identical cylinder in close proximity to the first.

Staggered cylinders

Figure 14.2b shows the variation of St with angle of incidence as measured behind the leading - or upstream - cylinder of a pair of staggered cylinders. The data by Alam et al. [17] results from a series of experiments with pairs of square cross-section cylinders. The cylinders are kept at $\alpha = 0°$ (using the definition of α given by Figure 14.1c), yet are placed at a stagger apart from each other as shown in Figure 14.1e. The incidence α therefore defines the line passing through the centre-point of each cylinder rather than the orientation of each respective square cross-section. Even though it was not found as part of the targeted literature search, data from Sumner et al. [192] is also presented for the case of a staggered pair of circular cylinders. This data is plotted in order to give additional opportunities for comparison.

Data sets from experiments on staggered circular cylinders are more accessible due to the review paper by Sumner [191]. This article – which includes many of the results given by the same authors in a previous paper [192] – reviews thoroughly the wake structure, forces and frequency content of wake flows behind pairs of circular cylinders in series (one behind the other), in parallel (side by side) and in the staggered configuration. A set of flow patterns (or regimes) are identified/defined for a range of Reynold's numbers and geometrical configurations.

These will not be reviewed in depth here, yet it is important to note that the appearance of any given regime is sensitive to geometrical parameters and Re. For example, when sufficiently close (small P, see Figure 14.1 for definition) and at certain incidence angles α, the two cylinders may act as a single bluff body. In this and other regimes there can be a dominating coherent oscillatory flow characterised by a single Strouhal number. In other configurations – for example for larger P and sufficiently large α – there may be two distinct Strouhal numbers. The

two wakes may be interacting, or the presence of one cylinder in the wake of the other may disturb the upstream wake. There are even configurations where it is difficult to determine the Strouhal number because there is no coherent oscillatory flow structure at all.

In the case of the Helgeland bridge tower, for which a clear and significant oscillatory wake flow was observed in the field, the spacing ratio P/D is ≈ 2.5.

Figure 14.2b shows select plots from configurations close to the Helgeland bridge case. The full data sets for both leading and trailing cylinders have not been plotted. In Alam et al. [17] (square cylinders) it is clear that there is one Strouhal number at the lower incidence values with a bifurcation into two distinct numbers at around 45°. The higher Strouhal number corresponds to the wake flow behind the leading cylinder (note that no statement is made here about cases other than $P/D = 2.00$ and $P/D = 2.50$). Intuitively, it is the wake behind the leading tower that will be observed by a vehicle driving between the two columns of the bridge tower.

Even though both branches are not plotted in Figure 14.2b, the bifurcation is still evident in each plotted data set from Alam et al. [17]. There is a clear discontinuity. There is also evidence for this in the data from the circular cylinders. It is not as clear as in the case of the square cylinders. This is because the plots presented in [192] included so much data, especially at the lower incidence angles, that it was difficult to pick out individual data points. The data points plotted in 14.2b are therefore approximate and the resolution along the horizontal axis is significantly lower than in the original paper.

As with the study of the effect of the cross-sectional aspect ratio and incidence of rectangular sections, some tentative conclusions can be drawn that are relevant to the current study:

- The flow around a pair of cylinders in a staggered configuration is sensitive to incidence angle.
- Various flow regimes may occur, where the spacing and angle of incidence (stagger) influences the degree to which the wakes behind each cylinder interact. This in turn affects the frequency content of the wake and how this is distributed in space.
- For configurations where P/D = 2.00 or 2.50, a bifurcation occurs at around $\alpha = 45°$. A significantly higher Strouhal number is found in the wake of the leading cylinder at values of incidence larger than this.
- This Strouhal number can be significantly higher than that for a single rectangular or circular cylinder.

14.2 Observed wind and roll response in the field

Before proceeding with the analysis of the observed vortex shedding at Helgeland, it is worth noting that some of the data collected by the anemometer on the Helgeland bridge has been clipped. The settings for the internal WindMaster digital-to-analogue conversion of the wind components u_r and v_r were incorrect by mistake. Measurements are limited to [-30, 30] m/s. Consequently, the full wind vector is not known at all points in time.

Nonetheless, the observed phenomenon is so compelling that a description of the wind field using the clipped data is still attempted. The wind measurements are strongly supported by the observed roll response.

The clipping is particularly problematic in the leeward (southward) lane as there was a significant component of the wind in the direction of travel of the vehicle. Figure 14.4 shows the approximate wind direction that would be measured by a stationary test vehicle in the leeward lane. Clearly, the addition of a negative wind component in u from the driving velocity of the vehicle would lead to high-magnitude negative component along x' (axis points in the forward vehicle direction in the S-frame – refer to Figure 1.6 for definition).

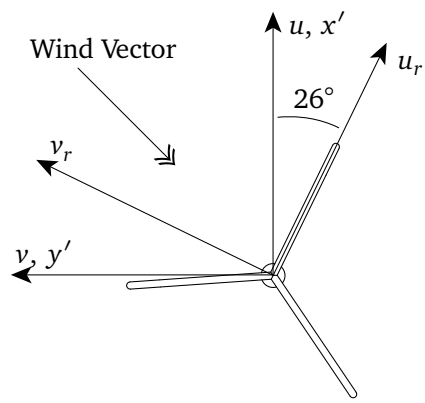

Figure 14.4: A sketch illustrating the offset angle of the anemometer. The anemometer is shown from the top with the North spar aligned with the u_r axis of the rotated anemometer.

Luckily, during the Helgeland session, the WindMaster was mounted with a 26° offset as can be seen in the sketch. This means that the u_r axis remained close to perpendicular to the mean wind vector. The degree of clipping in u_r is therefore limited.

The following analysis will depend more on u_r than v_r even though it is directed almost perpendicular to the mean wind. Spectra will be plotted for the u_r component only, yet the time series of v_r are presented as well in order to demonstrate the correlation between the two in the vortex street. This is believed to be a coherent aerodynamic wake structure where the two components u_r and v_r are strongly correlated.

Some of the clearest evidence of the vortex street and not least the consequences for vehicle safety is seen in the roll response of the vehicle. This data comes from the IMU and is a signal that is not subject to clipping. As will be seen, the measured roll response strongly supports the theory that there is an oscillatory aerodynamic force exciting the vehicle about its roll axis.

Full bridge profile

Figure 14.5 shows the the wind signals and the roll response across the span of the bridge. The wind component u_r and the roll rate of the vehicle ω_x are characterised by significant variation from the mean in the region immediately preceding the towers. This is clear to see in the lower two plots in Figure 14.5. The variation in the roll response is larger here than anywhere else along the bridge axis.

In the case of the wind component, there is significant variation around X_b = -450 to -350 m in addition to that near the towers. This has been attributed to the wake of the support piers below the deck in Chapter 8. Another obvious feature in u_r is the change in mean in the region $X_b > 400$ m. This is attributed to the curvature of the road. Note that the wind speeds plotted are measured in a vehicle-fixed reference frame.

The curves on the v_r vs. X_b axis show that a sizeable portion of the data has been subject to clipping. Some of the signals also have spikes in v_r at $400 < X_b < 500$ and $-300 < X_b < -250$ respectively. This is the result of passing through the wake of oncoming vehicles in the windward lane.

There are no visible geographical features that could cause the increase in variation near the towers. Figure 14.6 gives a map of a larger geographic area around the bridge. With the south-easterly wind that was present during the field session, there is nothing but water in the 2-3 km upwind of the towers. The phenomenon seen at $X_b \approx -200$ m and $X_b \approx 240$ m is almost certainly associated with the towers.

Amplitude spectra of roll and wind speed

The thick dotted lines in Figure 14.5 delimit the reference segment as first defined in Chapter 8. Note that the placement of the reference segment is slightly different to that used previously. The limits have been chosen to separate the roll signal affected by the vortex shedding from that on the main span. The reference segment is

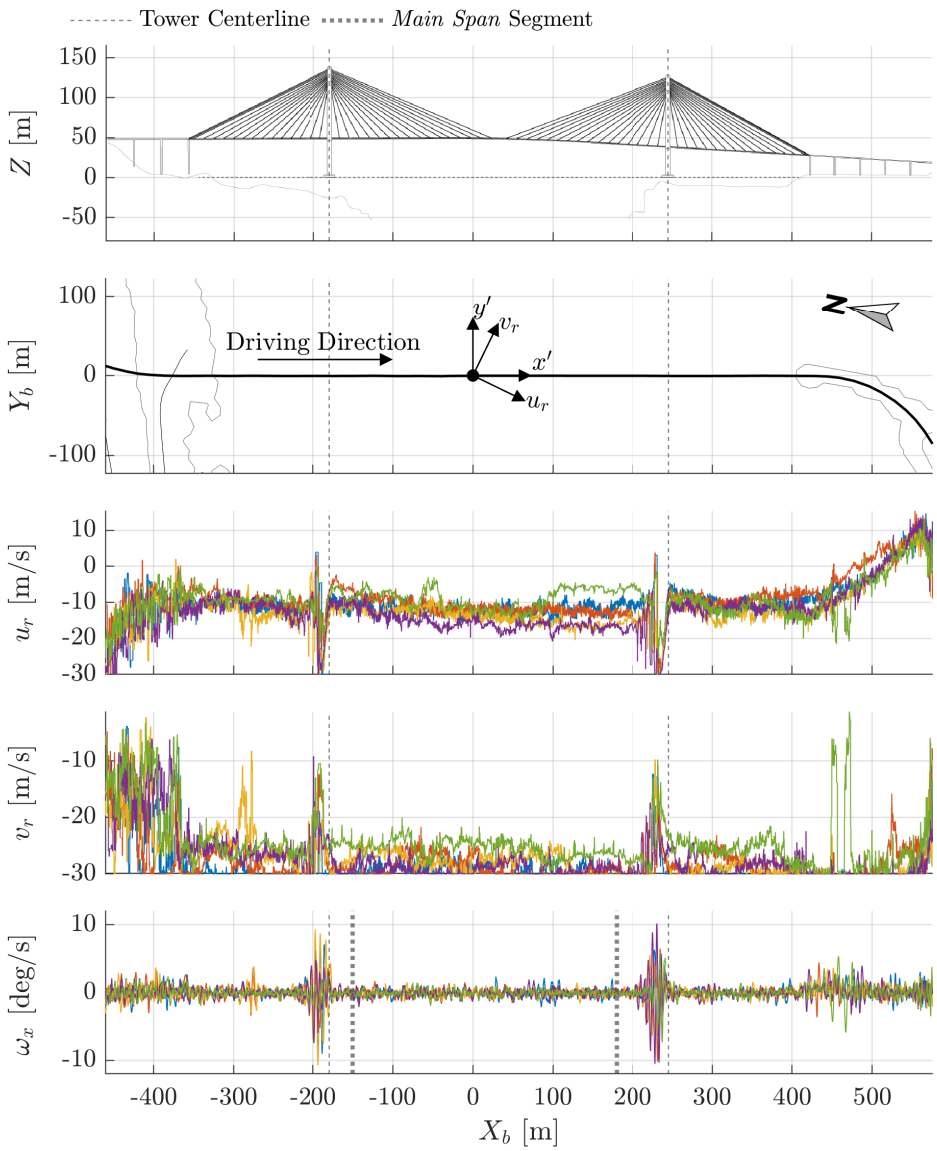

Figure 14.5: Time series of wind and roll response across the span of the bridge. ©Kartverket (terrain model & road shape)

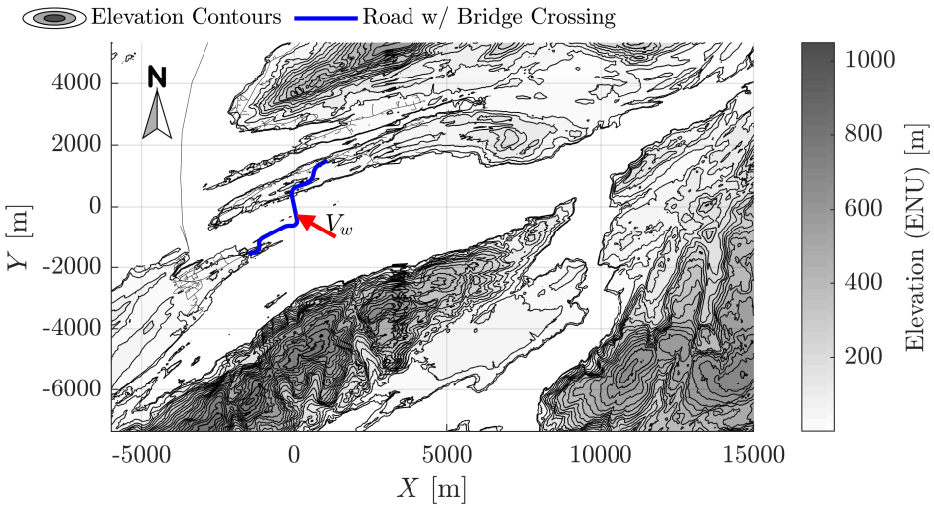

Figure 14.6: A map showing the mean wind vector at the bridge deck for the run discussed in Section 14.2. ©Kartverket (terrain model & road shape)

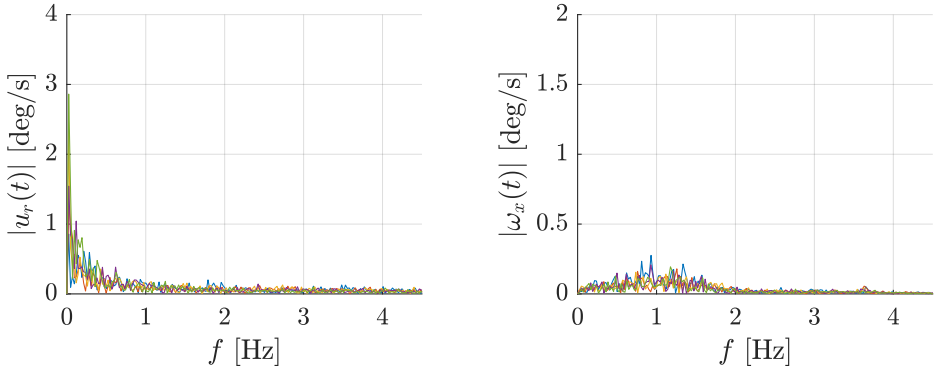

(a) Wind

(b) Roll rate

Figure 14.7: One-sided amplitude spectra of wind and roll response on the main span segment.

therefore labelled the *Main Span* segment to clarify that it has been defined slightly differently to the reference segment used previously.

Figure 14.7 shows the one-sided FFT of the wind and roll rate signals (zero meaned) from the main span segment. Neither present with outstanding peaks. The roll rate spectrum is narrower and shows that the most significant response is between 0 and 2 Hz. The spectra are significantly different to their counterparts for the near tower segments that are shown in Figures 14.10 and 14.12.

Vehicle roll frequency

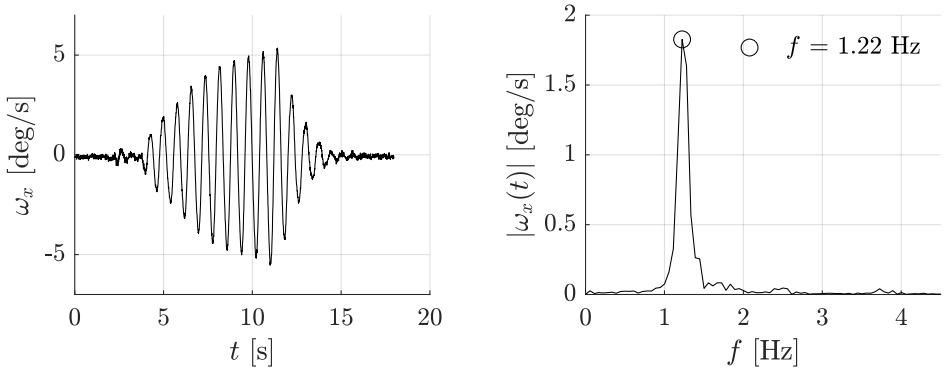

(a) Time series

(b) Spectrum

Figure 14.8: Results from a manual shake test.

The vehicle was manually shaken in order to identify the vehicle's roll mode. The side of the test vehicle was pushed periodically in a manner so as to match the natural response of the suspension to rolling motion. The procedure was repeated until the test gave a significant roll response and a smooth periodical signal.

The resulting time series can be seen in Figure 14.8a next to the one-sided FFT in Figure 14.8b. The results indicate that the vehicle's natural frequency is close to 1.22 Hz. An attempt to identify the damping coefficient from the decay of the signal from about $t = 11$ s revealed that the roll frequency changes with amplitude.

Despite this non-linearity, the vehicle's natural roll frequency at large amplitudes near 5 deg/s (as shown in Figure 14.8a) lies close to this value of 1.22 Hz. The spectral curve from this shake test (Figure 14.8b) has been included for comparison with the spectra from the near tower segments in Figures 14.10b and 14.12b.

Near tower measurements

For illustrative purposes, the signals u_r and ω_x shown in Figure 14.5 have been replotted on a new set of axes in Figures 14.9 and 14.11. They have been plotted against time rather than a spatial coordinate where $t = 0$ corresponds to a given coordinate along the bridge axis preceding the towers. The total wind magnitude V_r has also been plotted. Breaks in the time series appear where clipping was observed in one or both of the components u_r or v_r (i.e. clipped values have not been plotted).

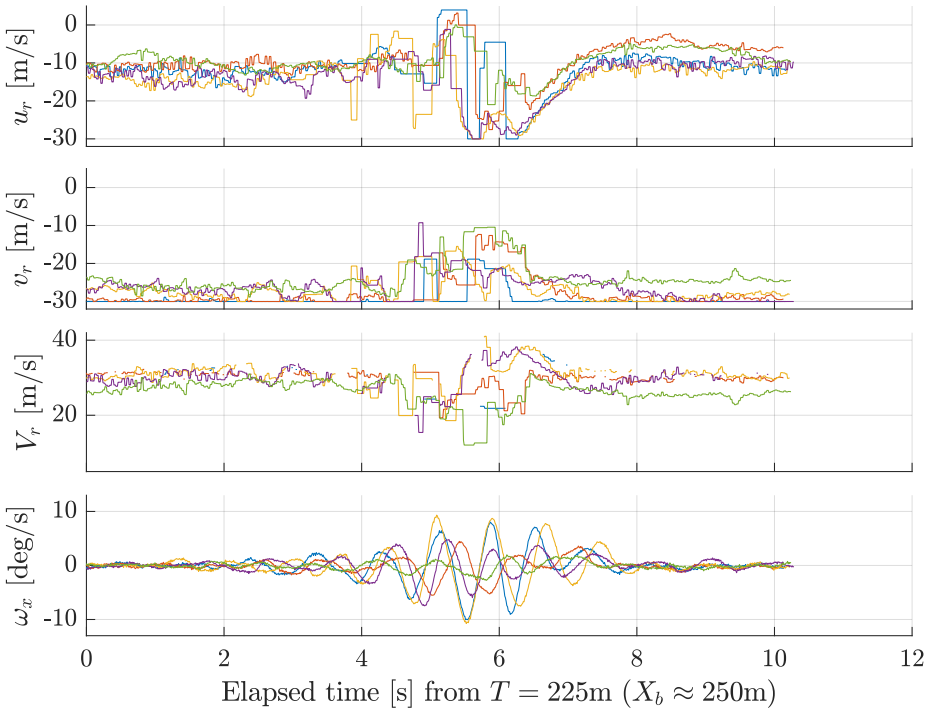

Figure 14.9: Time series of wind and roll response near the North tower (measured while driving at 30 kph).

Note: the gaps seen in some lines exist because clipped values have not been plotted.

Roll behaviour

It is clear to see the sinusoidal roll behaviour of the vehicle in its approach to both the North (Figure 14.9) and South towers (Figure 14.11). Barring perhaps one

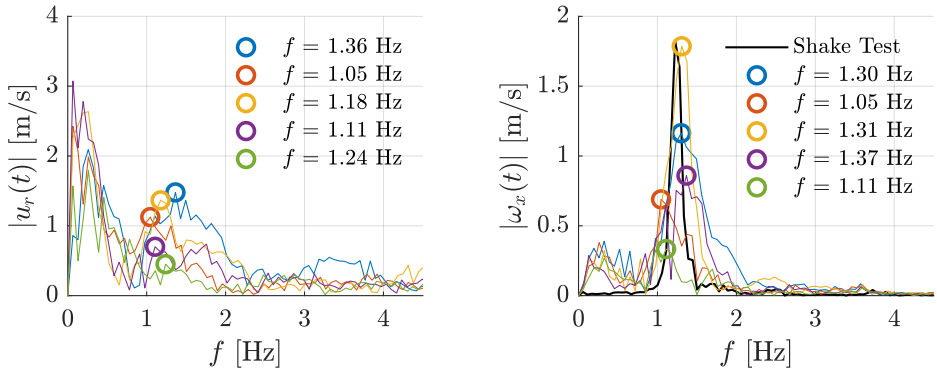

(a) Wind (b) Roll rate

Figure 14.10: One-sided amplitude spectra of wind and roll response near the North tower.

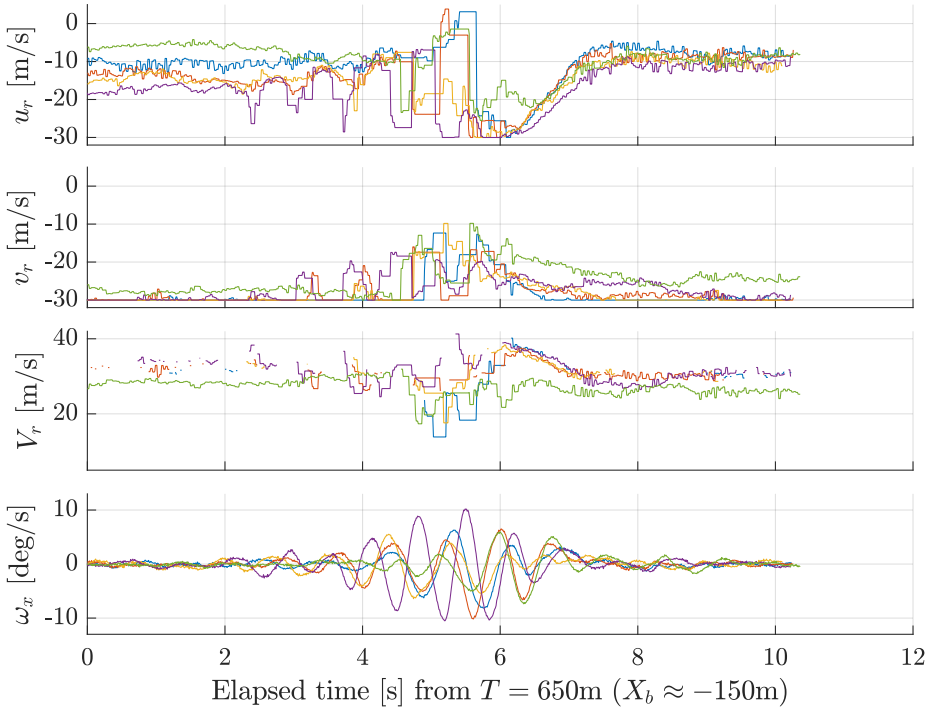

Figure 14.11: Time series of wind and roll response near the South tower (measured while driving at 30 kph).

Note: the gaps seen in some lines exist because clipped values have not been plotted.

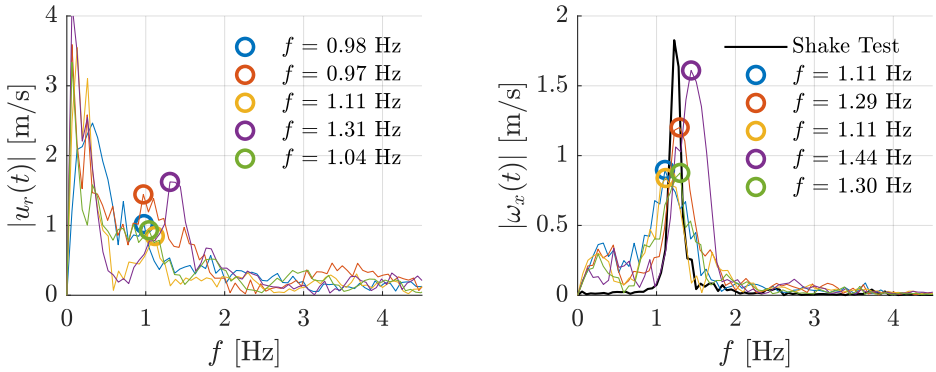

(a) Wind

(b) Roll rate

Figure 14.12: One-sided amplitude spectra of wind and roll response near the South tower.

time series from the North tower – plotted in a green colour – every passing of the tower wake at this driving speed demonstrates an unambiguous growth and decay in oscillatory roll response of a very similar frequency. This is reflected in the peaks seen in the spectra shown in Figures 14.10b and 14.12b for the North and South towers respectively.

Note that in order to improve the frequency resolution of these spectra, the time series used in the FFT include data from an extra 20 m along the bridge axis before and after that which is shown in Figures 14.9 and 14.11.

Wind features

Figures 14.10a and 14.12a show the spectra of the corresponding wind component signals u_r. These are less clear than the roll rate yet distinctly different to the spectra plotted from the main span in Figure 14.7a. Note that the axis limits for the spectra at the towers are the same as those given for the main span which makes for an easy comparison.

The wind component spectra suggest that there are two distinct features of the wind profiles near the towers. One set of peaks is of a lower magnitude and higher frequency which generally corresponds closely with the peaks identified in the corresponding roll rate spectrum. This is believed to be evidence of a vortex street in the wake of the bridge towers. These peaks have been identified by picking the maximum value for the portion of the spectrum curve above $f = 0.9$ Hz. In some cases, at the South tower, this peak is somewhat ambiguous. Nonetheless, the majority of the spectra at both the towers show evidence of increased amplitude in the range between 1 and 1.5 Hz.

Note that the anti-spike algorithm has again affected the results by introducing a flat signal at various points in time, giving the signals a step or box-like appearance. This may affect the amplitude spectra as well.

The second set of higher magnitude, lower frequency peaks are also evident in the spectra and are most likely associated with the inverse gusts caused by the shielding effect of the towers as described in Chapter 13. The vehicle will roll in tact with lateral handling response to the inverse gust. No attempt has been made to estimate this low frequency from the spectra given the short length of the signals used.

Vortex dimensions

One of the wind component signals (u_r) at the South tower – the purple line – has a much closer resemblance to the roll response than the other repetitions. It looks, in similarity with the roll response, like a sinusoid of constant frequency which increases in magnitude over a period of about 4 seconds before dying out.

This oscillation of about 1.4-1.5 Hz is superimposed with a slower process; the inverse gust caused by the shielding effect of the tower. From about $t = 6$ s, it is only the inverse gust profile that is evident as the wind speed recovers to the reference value.

These oscillations in the wind are not as clear to see in any of the other signals and the roll rate reaches a maximum of about 10 deg/s which is higher than any other repetition at the South tower. This appears to be something of a worst case for vehicle comfort/safety and so this repetition will be studied in more detail.

Influence zone

The data from this repetition has been isolated and replotted on a new set of axes in Figure 14.13 along with the roll rate. In this case the signals are plotted along the bridge axis where the offsets of the CG and anemometer from the main GNSS antenna have been taken into account. The alignment between these signals is therefore different to that shown on the time axis previously.

The *influence zone* is where the the vortex is deemed to be observable either through the roll response or the direct measurement of the wind. In Figure 14.13, the estimated boundaries have been chosen by inspection from the second set of axes. The part of the road centreline that falls between these boundaries is then highlighted with a thick black line on the diagram sketched directly above.

The diagram has been rotated such that the mean wind vector points down the page. It gives an impression of where observation of the vortex street begins and ends. The influence zone is long and starts up to 5.6D to the left of the centre of the tower. This exposes the vehicle to the regular oscillation of wind for a sufficient period of time to allow for the build up of a significant roll response.

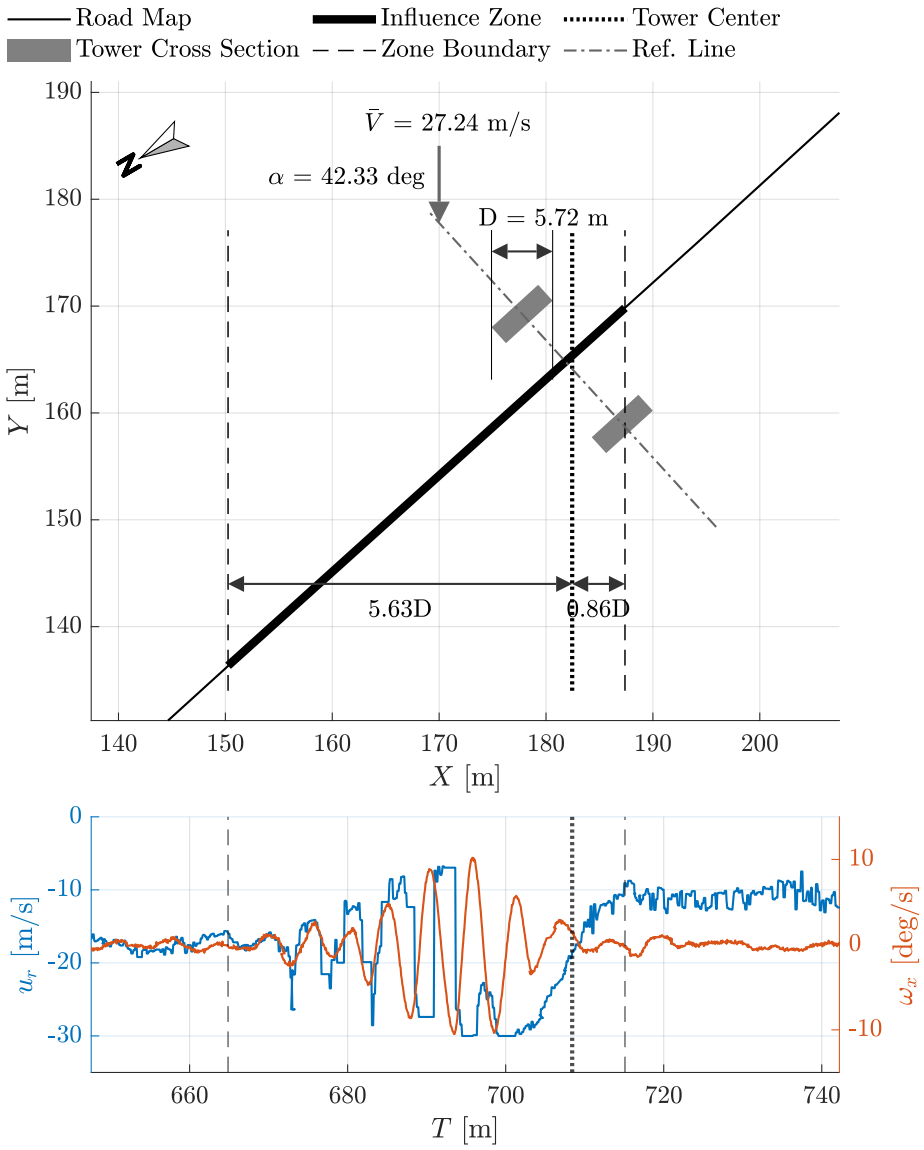

Figure 14.13: Approximate geometry of the vortex street at the South tower.

Note that due to the clipping of the wind data, there will be some uncertainty in the mean wind speed and incidence angle. The incidence angle will affect the dimensions of the influence zone and so the true dimensions may differ from the 5.6D value.

The mean wind vector presented in Figure 14.13 has been estimated using an averaging of wind signals near the South tower. It is therefore a more local estimate than the reference value presented in previous chapters.

Flow parameters

Using the details of the flow given in Figure 14.13 it is possible to estimate the Strouhal number,

$$\mathrm{St} = \frac{f D}{U}. \tag{14.1}$$

The spectral peaks in the wind component u_r shown in Figures 14.10a and 14.12a lie, as values rounded to the nearest 0.1 Hz, between 1 and 1.4 Hz. For the case shown in Figure 14.13, the peak in the wind spectrum is 1.3 Hz, which along with the following,

$$D = 5.7 \text{ m}$$
$$U = 27.2 \text{ m/s},$$

gives a Strouhal number of 0.27, where D is defined in Figure 14.1. Using the kinematic viscosity for air at sea level from the International Standard Atmosphere [1], $\nu = 1.46 \times 10^{-5}$ m^2/s, the Reynolds number is estimated,

$$\mathrm{Re} = \frac{UD}{\nu}, \tag{14.2}$$

to give $\mathrm{Re} = 1.1{\times}10^7$.

14.3 Discussion

It is clear that it was not comfortable – and perhaps not even safe – for the test vehicle to cross through the tower wake at the driving speed of 30 kph. This is significant because the test vehicle is of a type and dimension that is often seen on Norwegian roads. The Volkswagen Crafter (test vehicle), Mercedes Sprinter and similar vehicle models are often used as ambulances, taxis or goods vehicles.

The Helgeland bridge in particular connects the mainland of Norway to the island of Alsta, hosting the town of Sandnessjøen. There is a hospital in Sandnessjøen and many people living on the mainland are in fact reliant on the Helgeland bridge for having access to certain medical treatments. Maintaining safe passage for these

vehicles across the bridge is extremely important. Patients in a critical condition should not be exposed to the violent rolling motion that was observed in approach to the towers.

Consequently, there are some critical questions around the vortex street observations. The flow conditions were such that the absolute shedding frequency coincided with the vehicle's roll mode over a significant segment (distance) of road near both the North and South towers:

1. How often does this absolute shedding frequency present itself on the Helgeland bridge?
2. Might there be similar examples at other bridges?
3. How could the violent roll response observed here be mitigated?

There is reason to believe that this phenomenon was caused by a unique set of flow parameters (including tower geometry) at the Helgeland bridge that are unlikely to be seen elsewhere on the Norwegian road network. This is argued using a statistical and empirical argument next.

Parameters of the Helgeland vortex street - statistical argument

Table 14.2 summarises the key geometric and flow parameters for the towers at each of the cable-supported bridges visited during the field campaign. Assuming that the field experiments performed here are representative of the overall statistics for significant wind events at Norwegian bridges, then the Helgeland bridge is a unique case.

In reality, the $\alpha = 0$ case was actively prioritised and so there may be a bias in the sample set of incidence angles. On the other hand, there should be little bias in the geometric parameters other than that resulting from the preference given to visiting longer cable-supported bridges. Whether there is a correlation between the aspect ratio AR and the tower spacing P/D and bridge length is unknown.

Nonetheless, the aspect ratio AR at Helgeland is uniquely high and the spacing P/D uniquely low in the current sample set. The incidence angle is also the highest absolute value at 42° compared to the next highest value of 20°. Similarly, the Reynolds number is the highest at about twice the values at Nærøysund and Tjeldsund 1. At Hardanger and Hålogaland however – owing mainly to the large dimension of the towers – the Reynold's number is similar.

All the parameters in Table 14.2 are known to influence the presence of different vortex shedding regimes and the Strouhal number in the wake flow. By virtue of the fact that the Helgeland bridge case is an outlier in α, AR and P/D, then it might be concluded that the observed roll-inducing vortex shedding is also an outlier. This argument can be probed further using the conclusions given in Section 14.1 based on empirical data extracted from the literature.

Table 14.2: Tower flow and geometric parameters.

	α [°]	V_{ref} [m/s]	Re $\times 10^6$	AR	P/D
Hålogaland	-1	17	8.4	1.6	2.7
Hardanger	12	16	8.2	1.1	3.5
Helgeland	42	25	9.8	2.9	2.4
Nærøysund	-20	15	4.3	1.3	3.3
Tjeldsund 1	-3	17	3.8	-	2.8

Flow parameters are based on reference values. The values for Helgeland therefore vary slightly from the more local estimation of flow parameters near the South tower presented in Figure 14.13.

Empirical argument

The sections of the Helgeland bridge towers are rectangular with an aspect ratio of 2.9. The Strouhal number for a rectangular section with AR= 3 (see Norberg [147] in Figure 14.2a) has been shown to be roughly constant (St = 0.17) in the range $10 < \alpha < 50°$ and significantly higher than St= 0.1 near $\alpha = 0$. The relatively high incidence angle $\alpha = 42°$ at the Helgeland bridge is therefore likely to contribute to a higher Strouhal number than if the incidence angle had been closer to 0. If Norberg's result is applicable to the current case, the Strouhal number would be equally high at incidence angles in the range 10° through 50°.

The vortex shedding regime will also be influenced by the paired arrangement of the tower's two sections. As concluded in Section 14.1, the flow regime and Strouhal number in the wake of paired cylinders is highly sensitive to the incidence angle. In particular, when $P/D = 2.0$ or 2.5 (compare to 2.4 at Helgeland), then two separate Strouhal number can be observed at incidence angles above ∼40°. The higher Strouhal number, observed behind the leading tower, will exceed the envelope of values observed in the wakes of a single rectangular sections (envelope shown by grey lines in Figure 14.2b). The highest Strouhal number for singular rectangular sections reported in the literature is below 0.2.

The high St number of 0.27 may be one of two observable frequencies in the wake of the Helgeland tower. The path of the girder places the vehicle in the wake of the leading tower. This would mean that the higher value has been observed. The fact that there appears to be a jump (bifurcation) in Strouhal number before 40° for all paired circular and rectangular sections in Figure 14.2 – where the values of P/D are all similar to the Helgeland case – supports this hypothesis.

The Helgeland case is at $\alpha = 42°$, which may only be just above the incidence at the jump/bifurcation. The vortex shedding may not have been observed at all had the incidence angle been as little as 2° lower. At angles below 40° the square-

section curves (Alam) in Figure 14.2 suggest that the Strouhal number – and by extension also the frequency – would be about half the value. The roll response would ostensibly have been limited at this frequency.

Wake width

The vortex-induced response observed at 30 kph is significant in magnitude largely owing to the duration of time the vehicle spends under the influence of the vortex street. The duration is long partly because of the low driving speed but also because the vortex shedding is evident along a long segment of the road.

Figure 14.13 shows that the vortex street appears to extend quite far to the left of the tower. It was observed in Chapter 13 that the inverse gust (shielding effect) was also shifted quite far to the left compared to the expected position immediately downwind of the obstruction (tower).

It is hypothesized that the combination of a high aspect ratio rectangular section and the spacing between the two sections has a channelling effect that turns the flow through the columns and aligns it – and the vortex street – with the bridge girder. There is some evidence for this in Figure 13.4a (see the wind vectors in proximity to the centre of the tower).

If the incidence were to be smaller then the vortex shedding would be less problematic. The vortex street would cover a shorter segment of the girder and oscillatory loads on the vehicle would build up over a shorter duration of time. As argued above, the vortex shedding would likely also be at a lower Strouhal number and frequency at a lower incidence.

On the other hand, the vortex shedding frequency, and its prominence over a longer section of the girder, would possibly be maintained, or worsen, at a higher incidence. One of the upper branches plotted in Figure 14.2b remains roughly constant between $\alpha = 40°$ and 60°, while the rest drop off slowly towards 90°. It is possible that the vortex shedding observed here would be similarly problematic at incidence angles above 42° and may be less problematic at angles exceeding 60°.

Wind speed

If it is assumed that the Strouhal number is Reynold's number independent, then the shedding frequency is a linear function of the wind speed as described by Equation 14.1. A 10% change in wind speed would shift the shedding frequency 10% away from the natural roll frequency of the vehicle. The occurrence of a high amplitude roll response in the vortex street is therefore likely to be affected to the wind speed as well. In reality, the Strouhal number may be Reynold's number dependent as well, thus making it less certain how changes in wind speed would affect the observed shedding frequency.

Driving speed

The roll response was not noticed during the field sessions until the repetitions at 30 kph were performed. The vehicle response upon passing the towers at the higher speeds (60, 70 and 80 kph) was not noticeably different in nature to that experienced in passing the towers at any of the other bridges, where no such observations of vortex-induced response have been made.

Figures 14.14 and 14.15 show the time series of the roll rate measured along a 160 m segment that passes by the North and South towers respectively. Each of the signals in these two figures have been used to estimate an amplitude spectrum that can be seen in Figure 14.16.

It is clear from the time series that the excitation of the natural roll frequency is most evident at the 30 kph driving speed. There is some oscillation at this frequency near 4 seconds of elapsed time in the 60 kph signals as well. These oscillations are subsequently dominated by a lower frequency component nearer 5 seconds. This same, lower frequency response is seen at 70 kph and 80 kph without much evidence of the preceding higher frequency excitation at the natural roll frequency.

The lower frequency response follows closely the handling response (lateral acceleration A_y and ω_z) and is the response to the inverse gust created by the shielding effect of the tower discussed in Chapter 13.

The domination of the response to the vortex street at 30 kph is clear in the amplitude spectra of Figure 14.16. The peak in the 30 kph spectra near 1.3 Hz is prominent. At 60 kph however, two spectral peaks of similar prominence are evident in almost every repetition. In some cases, the highest value is the high frequency one, but in most cases the response associated with the inverse gust is the dominant peak, albeit only just.

From the 70 kph and 80 kph spectra it is clear that there is in fact some energy above 1 Hz in the roll response signals, indicating that there may be some excitation of the vehicle's natural roll frequency. At 80 kph at the South tower however, the energy associated with passing through the inverse gust is almost completely dominant.

It is hypothesized that the inverse gust response would continue to be dominant at higher driving speeds and that the spectrum seen at the 30 kph would be approached by decreasing the driving speed from 60 kph. For example, at 50kph it is likely that the high frequency content associated with the response to vortex shedding would result in higher spectral peaks than the low frequency content associated with the inverse gust.

Driving slower than 30 kph would approach the static driving case, for which the roll response may increase further, possibly even to rollover of the vehicle. The static case could be investigated in the wind tunnel.

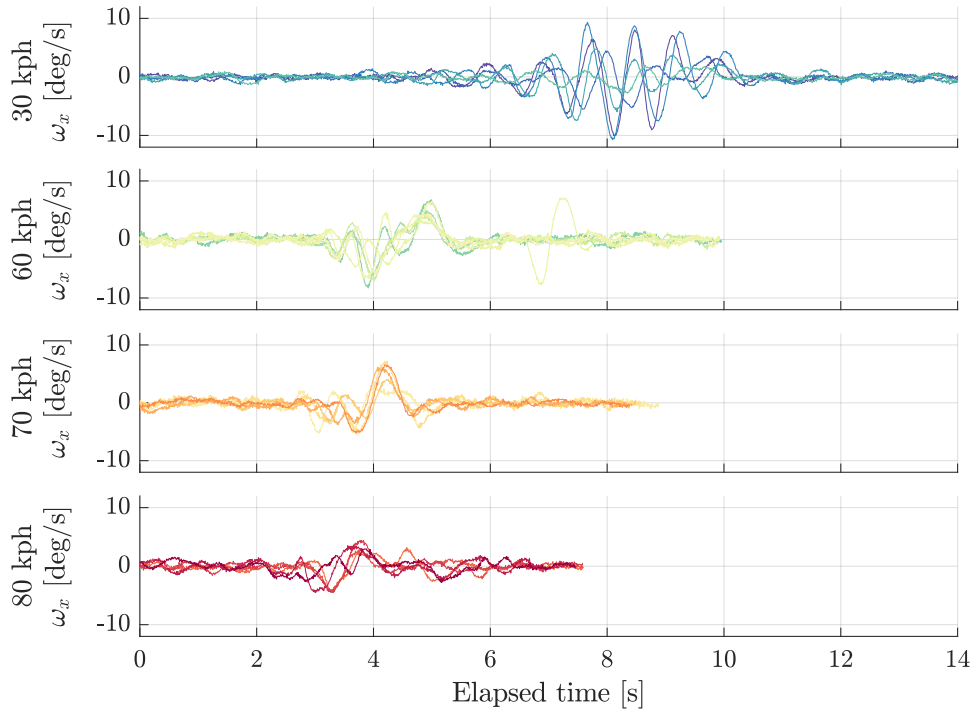

Figure 14.14: A comparison of time series at different driving speeds at the North tower.

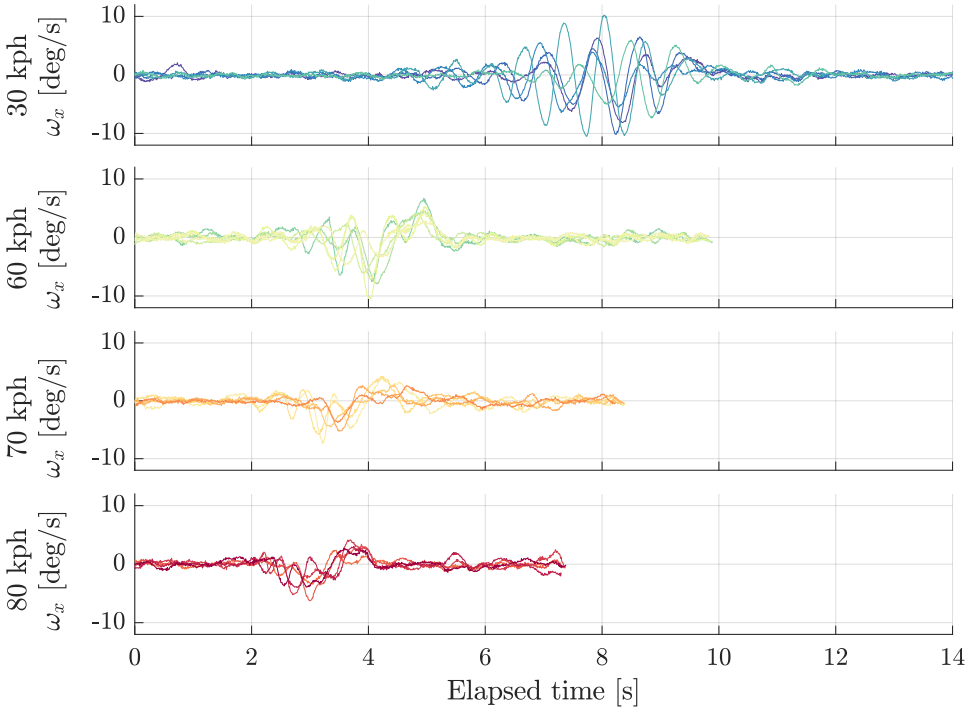

Figure 14.15: A comparison of time series at different driving speeds at the South tower.

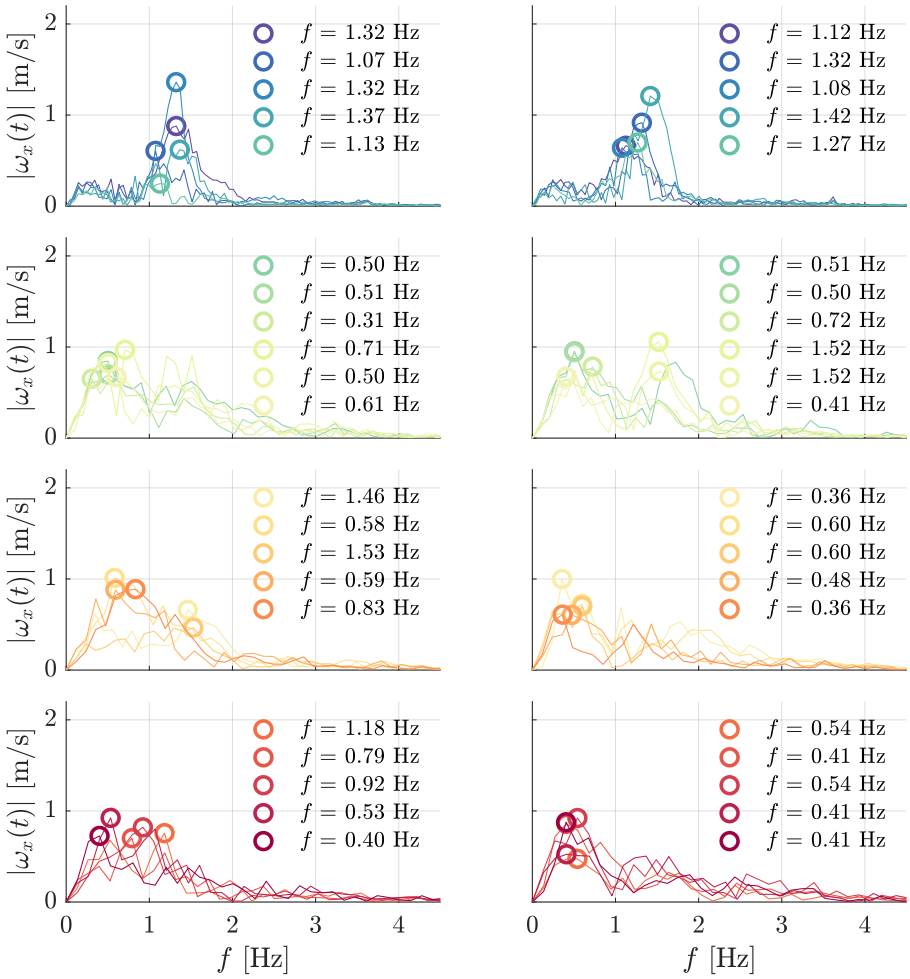

(a) North Tower (b) South Tower

Figure 14.16: Spectra for the time series at different speeds

The circled points are the peaks within the plotted domain.

Three-dimensional effects

Without any empirical evidence from wind tunnel experiments it is difficult to form an hypothesis around the effects of the three-dimensional parameters of the bridge tower geometry. The South tower at the Helgeland bridge is sketched in Figure 14.17 using a parallel projection. The in-plane wind vector points into the page (i.e. the sketch shows the bridge tower as seen in the wind direction). A number of three-dimensional effects are apparent:

- The tower columns are tapered both above and below the girder.
- The tower columns are inclined inwards towards the top and bottom, with a kink at girder height.
- The girder is inclined and the vehicle in the leeward lane (sketched) travels downwards when passing through the paired tower columns.

The impact of each of these three-dimensional features on vortex shedding is unknown. It would be interesting to study this tower geometry in the wind tunnel to see which flow parameters are necessary to create the vortex shedding phenomenon observed in the field and how robust the shedding frequency is to changes in geometry and flow conditions.

Turbulence intensity

Another flow parameter that may influence the occurrence of vortex shedding is the turbulence intensity of the incoming flow. By inspection of Figure 8.13 (the wind profile for the leeward lane at the Helgeland bridge) it is clear that the turbulence intensity was low at Helgeland compared to at some of the other bridges. This is likely explained by the upstream terrain which is 2-3 km of open water.

One hypothesis is that the vortex shedding would not have been sufficiently coherent to cause the observed build up of roll response if the incoming turbulence intensity had been higher. Again, this would be interesting to study in the wind tunnel.

14.4 Conclusions

A large-scale coherent vortex street has been observed in the wakes of both the North and South towers of the Helgeland bridge while travelling in the leeward lane with the test vehicle:

- The vortex shedding frequency observed in the clearest case (repetition) of oscillatory flow is 1.3 Hz corresponding to a Strouhal number of 0.27.

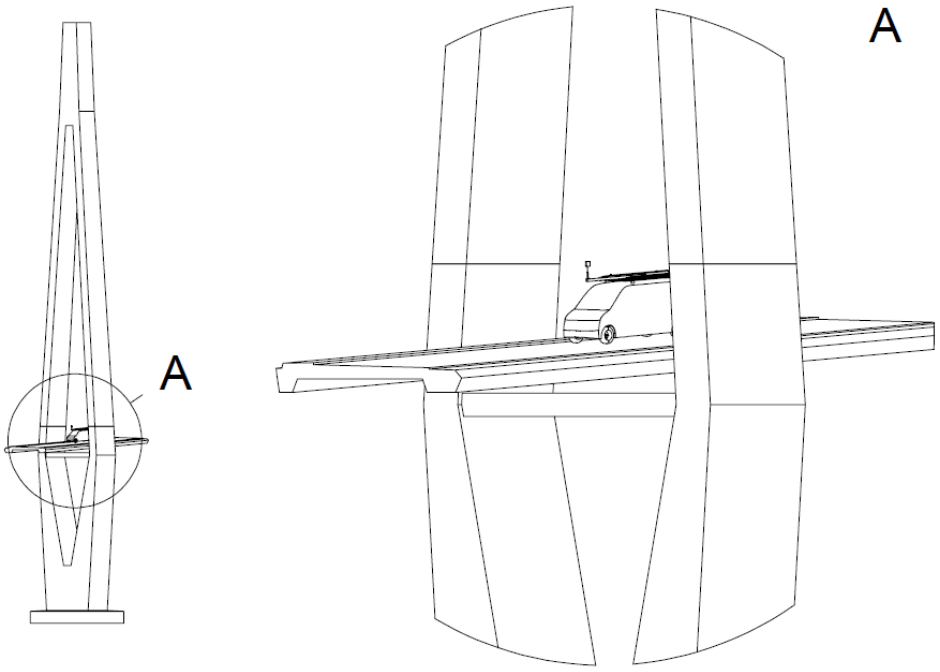

Figure 14.17: A sketch of the Helgeland bridge and the test vehicle on the deck.

- The following parameters describe the flow and geometry of the paired tower columns: Re$\sim 10^7$, $U = 27$ m/s, $\alpha = 42°$, AR= 2.9 and $P/D = 2.4$.
- The vehicle oscillated about it's roll axis in response to the oscillatory flow across a span of approximately 50 m of the bridge girder, reaching a maximum absolute roll rate of 10 deg/s.
- The oscillation of wind speed was observed to start up to 5.63D perpendicularly (to the wind vector) away from the centre-point of the tower cross-section.

The flow parameters at the Helgeland bridge towers are unique compared to those seen at other bridges in this work. The wind incidence α is the highest absolute value (42° vs. the second highest at 20°), the aspect ratio for the tower sections is the highest (2.9 vs. the second highest at 2.6) and the spacing between columns is the lowest (P/D =2.4). In addition to this the mean wind speed was high at 25 m/s (vs. a second highest value of 17 m/s).

It is hypothesized that the relatively high Strouhal number observed is a result of the high aspect ratio of the tower section combined with a low spacing P/D and an incidence angle near 45°. The high wind velocity in combination with the high Strouhal number leads to a relatively high shedding frequency that matches the natural roll frequency of the test vehicle and leads to a strong response.

How often does this absolute shedding frequency present itself on the Helgeland bridge?

The shedding frequency that was observed may be less likely to match the vehicle's roll frequency at different wind speeds (assuming the Strouhal number is Reynold's number independent). Similarly, the shedding frequency would likely be lower at lower incidence angles (though it would possibly maintain a similar value at higher incidence angles). This would suggest that small changes in wind speed and/or a reduction in the incidence could change the shedding frequency and vortex shedding mechanism significantly. Changes to the incidence angle may also move the vortex street away from the girder, thereby exposing the vehicle to the vortices for a shorter duration of time.

The specific conditions observed during the experiment may therefore be uniquely associated with the significant response of the test vehicle. If this is a wind speed and direction that is often seen at the Helgeland bridge, then the conditions necessary for this unique response may nonetheless occur regularly.

Might there be similar examples at other bridges?

The tower geometry and placement of the Helgeland bridge are fairly unique. The tower sections have a higher aspect ratio than any of the other visited bridges and the bridge protrudes out into a very wide fjord with 2-3 km of open water fetch

from which the 45° incidence is possible with South-easterly winds. Most wind-exposed bridges in Norway are straddled by land on either side. The strongest winds typically follow the topographical channel and are incident at $\alpha = 0°$ (perpendicular to the girder). A mapping of Norwegian bridge tower geometries, surrounding terrain and wind statistics is recommended, though the Helgeland case is most likely an outlier.

How could the violent roll response observed here be mitigated?

It is clear that increasing the driving speed can significantly reduce the significance of the roll response. On the other hand, increasing the driving speed also increases the response to the inverse gust (shielding) caused by the tower's obstruction of the flow.

Further work

A parametric study of the flow around paired high aspect ratio cylinders is recommended for the wind tunnel (or using CFD). The sections should remain parallel to one another in the staggered configuration in contrast to what has been presented in the literature. The effects of Reynold's number Re, incidence α, spacing P/D, and cross-sectional aspect ratio AR should each be studied. A further extension would be to consider typical three-dimensional effects like taper or lean and the effect of the girder on the Strouhal number and vortex shedding mechanism.

The response observed here was significant because the vortex shedding was coherent, large-scale and covered a long segment of the bridge girder. The ability to predict the Strouhal number and shedding mechanism for any given bridge tower could be combined with statistical wind data to quantify the likelihood of similar vortex-induced responses being observed on bridges in Norway.

Chapter 15

Conclusion

15.1 Summary of conclusions

This thesis contributes to a better understanding of vehicle handling response to wind gusts on various types of bridges. The results can be used by road authorities to better direct efforts towards providing safe passage on road bridges whilst striking an appropriate balance between serviceability and cost. The most significant contributions are:

- An instrumented test vehicle has been established that can record wind, vehicle and driver response in severe crosswinds and winter conditions on Norwegian road bridges.
  - The system can be used to quickly identify inhomogeneities in the wind field over bridges and link them to features of the local topography or the bridge's structural geometry.
  - Critical features of the wind can in turn be linked to the measured handling and vibrational response of the vehicle.
  - The mean wind speed profile near bridge towers can be measured and the quality of the results makes possible the comparison to wind tunnel results.
- A preliminary analysis of vehicle-bridge interaction suggests that it is unlikely to be a critical consideration for accident analyses on Norwegian road bridges.
- The vehicle-driver system was observed to respond the most to inverse gusts in the frequency range 0.5-2.75 Hz and the reduced frequency range 0.25-1 (spatial gust periods of 1-4 vehicle lengths). This builds on the existing knowledge of critical temporal and spatial gust periods for crosswind sensitivity of vehicle-driver systems.

- In theory – as demonstrated by the frequency response function of the single-track model – the vehicle handling system's sensitivity to crosswinds increases with driving speed. Here it was found that a severe, adverse handling response is much less likely at a driving speed of 30 kph compared to 60, 70 and 80 kph.
- There are predictable crosswind gusts that often lie in both the critical frequency and reduced frequency ranges when driving at the common Norwegian speed limit of 80 kph. These gusts are formed in:
  - the wakes of bridge towers,
  - the wakes of columns that stand windward of the girder and protrude above the road surface (like the cable support piers at Tjeldsund),
  - the pressure wave and/or separation bubble above sizeable substructure elements (like the counterweight at Tjeldsund), or
  - the transition from a fixed-base road to an elevated girder at the abutments (which includes tunnel entrances/exits, finite embankment geometries and sudden topographical drops).
- All towers encountered in the field were of a critical dimension to induce a significant handling response of the vehicle-driver system.
- A step-change in wind speed was observed at multiple abutments. The dimension – or spatial period – of the step-change was found to be critical in only a handful of the observed cases. The change in wind speed occurs over such a long distance that the gust frequency (and reduced frequency) often lies on the lower limit of the critical range. The same gusts may be more critical at higher driving speeds.
- The unique structural design of the Tjeldsund bridge means that 5 critical gusts are encountered in short succession on each crossing. The clustering of critical gusts was difficult for the driver to handle.
- The likelihood of encountering critical gusts of a significant amplitude (>7 m/s) in a stochastic wind field on a bridge is increased by:
  - the presence of complex upstream terrain that increases the general turbulence intensity in the atmospheric boundary layer (seen here at the Hardanger bridge), or
  - driving in the leeward lane on the deck of a girder with a bluff cross-section (seen here at the cantilevered Dolmsund and Måløy bridges).
- Front-axle skid events were experienced as a result of a stochastic gust on the main span of the Hardanger bridge (complex upstream terrain) and in the leeward lane of the Dolmsund bridge (separation over a bluff section).

- The flow separation over girders with a bluff cross-section significantly increases (of the order of 2 times compared to the more streamlined girders of cable-supported bridges) the likelihood of observing resultant responses that exceed a proposed sensory threshold. The driver is therefore made continually aware of significant wind perturbations. This may continually strain/tire the driver.
- The mean wind speed profile in the wake of the towers have clear similarities with wind tunnel results found in the literature despite key differences in the flow parameters. It is plausible that wind tunnel studies can be used to predict the mean wind profile in the wake of towers in the field.
- A large scale vortex shedding phenomenon was observed in the wake of the Helgeland bridge towers with a shedding frequency of 1.3 Hz and a Strouhal number of 0.27.
  - The shedding frequency matched the vehicle's roll mode and induced a response where the vehicle body reached a roll rate of up to 10 deg/s.
  - It is hypothesized that a similar response is unlikely at other bridges due to the unique tower geometry and flow conditions observed at the Helgeland bridge.
  - If the observed combination of wind direction and mean wind speed at the Helgeland bridge is typical, then similar vortex shedding is likely to be seen at this location again.
  - It may be beneficial to drive at a higher driving speed to avoid the build up of roll response to vortex shedding. The response to the vortex shedding decreased in severity with increased driving speed, though the response to the inverse gust in the wake of the tower increased. An optimal driving speed likely lies in the range 30 to 60 kph.
- Single-point measurements of wind speed and direction (on the bridge) are unlikely to be appropriate to characterise wind-related accident risks on their own. The predictable gusts behind obstacles and stochastic gusts resulting from terrain and/or separation over the bridge girder make the wind field inhomogeneous along the span. Accident prediction methods should consider this inhomogeneity.

15.2 Practical implications and further research needs

Some general recommendations to infrastructure owners regarding the design of bridges and mitigation of accidents are given below. Additional research is needed to provide more targeted recommendations and solutions.

1. Special attention should be paid to structural features that can act as obstacles to the wind over the bridge deck. From a vehicle safety perspective, these should be avoided where possible.

    - This pertains particularly to structural elements that stand taller than the bridge deck, but also to large elements that remain below the deck.
    - Single obstacles placed far away from each other along the girder axis are preferable to clusters of obstacles in close proximity to one another.
    - As a rule of thumb, it is better to use elements with a dimension parallel to the girder (width) smaller than 1 times the smallest expected vehicle length or larger than 4 times the length of the longest vehicles. This range may be narrower by consideration of the speed limits (by moving gust frequencies away from the 0.5-2.75 Hz range even if they remain within $0.25 < k_f < 1$). Further research on the transient behaviour of vehicle-driver systems in response to crosswinds is necessary to increase confidence in these ranges.
    - Vortex shedding mechanisms behind bridge towers should be studied further in order to understand whether or not such oscillatory flows pose a real and substantial threat to vehicle safety on Norwegian road bridges. This should start by studying the shedding frequency as a function of the cross-sectional aspect ratio AR, spacing ratio P/D, angle of incidence α, Reynold's number and wind speed.

2. The surrounding terrain should be carefully considered along with statistics of wind speed and direction to determine the likelihood of observing eddies of a safety-critical size on the bridge deck.

    - It may be possible to predict gusts/eddies of a critical dimension and amplitude through in-situ monitoring, possibly by evaluating the distribution of gust amplitude ΔV_w.
    - Otherwise, wind characterisation studies can be performed a-priori to identify critical wind directions (with respect to upstream terrain) and predict the likelihood of high amplitude gusts ($\Delta V_w > 7$ m/s) of a critical spatial dimension.
    - More research is needed to establish robust methodologies that provide appropriate gust predictions.

3. The likelihood of observing eddies of a safety-critical size will also be affected by the cross-sectional shape of the girder. It will be useful to have a better understanding of typical eddy sizes, how these relate to cross-section dimensions (like thickness and chord length) and how these could be mitigated through design changes and/or retrofitting.

4. The current results are based on measurements taken using a single test vehicle. It is not known if all conclusions drawn in this work are transferable to the different types of vehicles that travel across Norwegian road bridges now and in the future. Further research is needed to generalise the current conclusions.

15.3 Recommendations for future work

Given the research needs that have just been identified, the following studies are recommended as future work:

1. A better understanding of the transient behaviour of the vehicle-driver system to wind perturbations could be gained by separating the contribution of unsteady aerodynamics loads from that of the driver. Which contributes the most to adverse handling response (unsteady aerodynamics or driver steering input)? Does each respective contribution depend on gust frequency and/or reduced frequency? This could, for example, be studied by identifying the time series of aerodynamic loads acting on the vehicle in the field. One possible force identification method is an augmented Kalman filter that makes use of IMU measurements, driver steering, and a single-track model to estimate external loads acting on the vehicle. This could lead to a better definition of exactly which gusts – in terms of amplitude and period – are critical. The force identification method can be applied using a variety of drivers and vehicle types.
2. Terrain effects can be studied in the field using ground-fixed instruments. In many cases these instruments are already installed for bridge monitoring purposes or as part of initial design studies. The data can be studied to find a good prediction methodology for critical gusts. A risk assessment for vehicles may then combine a-priori knowledge of site-specific turbulence characteristics for different wind directions with in-situ monitoring to close the bridge or set appropriate speed limits.
3. The relationship between bridge girder geometry and turbulence characteristics in the space above each lane can be studied through additional field measurements with the test vehicle. Alternatively, typical sections can be modelled in the wind tunnel. It may be possible to avoid eddies of a safety-critical size by breaking the turbulence up into smaller scales using retrofitted fins, railings or other geometries that do not provide complete shielding. Complete shielding is likely to be expensive and/or apply excessive aerodynamic loads on the bridge.
4. The wakes of bridge towers – both the mean wind speed profile of the inverse

gust as well as oscillatory vortex shedding – can be studied in the wind tunnel to better predict the gust amplitude and period in the field. The pressure field and wake around structures like the cable support piers and the counterweight at Tjeldsund can also be studied. Parametric wind tunnel studies combined with a survey of wind statistics could be used to predict the dimensions of inverse gusts behind towers as well as any vortex shedding frequencies.

References

[1] ISO2533:1975 Standard Atmosphere.

[2] NS-EN 1991-1-4:2005+NA:2009, Eurokode 1: Laster påkonstruksjoner, Del 1-4: Allmenne laster, Vindlaster.

[3] ISO 2631-1:1997 Mechanical vibration and shock - Evaluation of human exposure to whole-body vibration - Part 1: General requirements, May 1997.

[4] ISO 2631-4:2001 Mechanical vibration and shock - Evaluation of human exposure to whole-body vibration - Part 4: Guidelines for the evaluation of the effectsof vibration and rotational motion on passenger and crew comfort in fixed guideway transport systems, Feb. 2001.

[5] *A policy on geometric design of highways and streets*. American Association of State Highway and Transportation Officials, 2001. ISBN 1560511567.

[6] EN 12299:2009 Railway applications - Ride comfort for passengers - Measurement and comfort. Online, Apr. 2009. European Standard.

[7] N400:2022 Bruprosjektering, Jan. 2022. Digitale vegnormer.

[8] Orwell Bridge closure protocol summary. Online, 2022. Highways England.

[9] W. S. Abbasi, S. U. Islam, L. Faiz, and H. Rahman. Numerical investigation of transitions in flow states and variation in aerodynamic forces for flow around square cylinders arranged inline. *Chinese Journal of Aeronautics*, 31 (11):2111–2123, Nov. 2018. doi: 10.1016/j.cja.2018.08.020.

[10] M. Abe. *Vehicle Handling Dynamics*. Butterworth-Heinemann, 2nd edition, 2009. ISBN 978-0-08-100390-9.

[11] H. Abedi, S. Sarkar, and H. Johansson. Numerical modelling of neutral atmospheric boundary layer flow through heterogeneous forest canopies in complex terrain (a case study of a swedish wind farm). *Renewable Energy*, 180:806–828, Dec. 2021. doi: 10.1016/j.renene.2021.08.036.

[12] J. Aboueian and A. Sohankar. Identification of flow regimes around two staggered square cylinders by a numerical study. *Theoretical and Computational Fluid Dynamics*, 31(3):295–315, Feb. 2017. doi: 10.1007/s00162-017-0424-2.

[13] E. Achenbach and E. Heinecke. On vortex shedding from smooth and rough cylinders in the range of reynolds numbers $6x10^3$ to $5x10^6$. *Journal of Fluid Mechanics*, 109:239–251, Aug. 1981. doi: 10.1017/s002211208100102x.

[14] E. Adeeb, B. A. Haider, and C. H. Sohn. Flow interference of two side-by-side square cylinders using IB-LBM – effect of corner radius. *Results in Physics*, 10:256–263, Sept. 2018. doi: 10.1016/j.rinp.2018.05.039.

[15] A. Agrawal, L. Djenidi, and R. Antonia. Investigation of flow around a pair of side-by-side square cylinders using the lattice boltzmann method. *Computers & Fluids*, 35(10):1093–1107, Dec. 2006. doi: 10.1016/j.compfluid.2005.05.008.

[16] M. M. Alam and Y. Zhou. Intrinsic features of flow around two side-by-side square cylinders. *Physics of Fluids*, 25(8):085106, Aug. 2013. doi: 10.1063/1.4817670.

[17] M. M. Alam, H. Bai, and Y. Zhou. The wake of two staggered square cylinders. *Journal of Fluid Mechanics*, 801:475–507, July 2016. doi: 10.1017/jfm.2016.303.

[18] A. Alexandridis, B. Repa, and W. Wierwille. The influence of vehicle aerodynamic and control response characteristics on driver-vehicle performance. Technical report, 1979.

[19] J. Anderson. *Fundamentals of Aerodynamics*. McGraw-Hill, 5th edition, 2011.

[20] T. Argentini, E. Ozkan, D. Rocchi, L. Rosa, and A. Zasso. Cross-wind effects on a vehicle crossing the wake of a bridge pylon. *Journal of Wind Engineering and Industrial Aerodynamics*, 99(6-7):734–740, June 2011. ISSN 0167-6105. doi: 10.1016/j.jweia.2011.01.021.

[21] T. Askeland, June 2022. Private communication.

[22] C. Baker. A simplified analysis of various types of wind-induced road vehicle accidents. *Journal of Wind Engineering and Industrial Aerodynamics*, 22(1):69–85, Apr. 1986. doi: 10.1016/0167-6105(86)90012-7.

[23] C. Baker. Measures to control vehicle movement at exposed sites during windy periods. *Journal of Wind Engineering and Industrial Aerodynamics*, 25 (2):151–161, Jan. 1987. doi: 10.1016/0167-6105(87)90013-4.

[24] C. Baker. High sided articulated road vehicles in strong cross winds. *Journal of Wind Engineering and Industrial Aerodynamics*, 31(1):67–85, Oct. 1988. doi: 10.1016/0167-6105(88)90188-2.

[25] C. Baker. Ground vehicles in high cross winds part I: Steady aerodynamic forces. *Journal of Fluids and Structures*, 5(1):69–90, Jan. 1991. doi: 10.1016/0889-9746(91)80012-3.

[26] C. Baker. Ground vehicles in high cross winds part II: Unsteady aerodynamic forces. *Journal of Fluids and Structures*, 5(1):91–111, Jan. 1991. doi: 10.1016/0889-9746(91)80013-4.

[27] C. Baker. Ground vehicles in high cross winds part III: The interaction of aerodynamic forces and the vehicle system. *Journal of Fluids and Structures*, 5(2):221–241, Mar. 1991. doi: 10.1016/0889-9746(91)90478-8.

[28] C. Baker. The quantification of accident risk for road vehicles in cross winds. *Journal of Wind Engineering and Industrial Aerodynamics*, 52:93–107, May 1994. doi: 10.1016/0167-6105(94)90041-8.

[29] C. Baker and S. Reynolds. Wind-induced accidents of road vehicles. *Accident Analysis and Prevention*, 24(6):559–575, Dec. 1992. doi: 10.1016/0001-4575(92)90009-8.

[30] R. C. Battista and M. S. Pfeil. Bridge dynamics and aerodynamics: design and practical requirements for high structural performance and safety. *Structure and Infrastructure Engineering*, 14(4):491–508, 2018. ISSN 1573-2479. doi: 10.1080/15732479.2017.1406962.

[31] P. W. Bearman. On vortex shedding from a circular cylinder in the critical reynolds number régime. *Journal of Fluid Mechanics*, 37(3):577–585, July 1969. doi: 10.1017/s0022112069000735.

[32] A. Brandt, S. Sebben, B. Jacobson, E. Preihs, and I. Johansson. Quantitative high speed stability assessment of a sports utility vehicle and classification of wind gust profiles. In *SAE Technical Paper Series*. SAE International, Apr. 2020. doi: 10.4271/2020-01-0677.

[33] I. M. Brooks, S. Söderberg, and M. Tjernström. The turbulence structure of the stable atmospheric boundary layer around a coastal headland: Aircraft observations and modelling results. *Boundary-Layer Meteorology*, 107(3): 531–559, June 2003. doi: 10.1023/a:1022822306571.

[34] C. S. Cai and S. R. Chen. Framework of vehicle-bridge-wind dynamic analysis. *Journal of Wind Engineering and Industrial Aerodynamics*, 92(7-8):579–607, 2004. ISSN 01676105. doi: 10.1016/j.jweia.2004.03.007.

[35] C. S. Cai and S. R. Chen. Wind vibration mitigation of long-span bridges in hurricanes. *Journal of Sound and Vibration*, 274(1-2):421–432, 2004. ISSN 0022-460X. doi: 10.1016/j.jsv.2003.09.013.

[36] C. S. Cai, W. Zhang, X. Liu, W. Peng, S. R. Chen, Y. Han, and J. X. Hu. Framework of wind-vehicle-bridge interaction analysis and its applications. *Journal of Earthquake and Tsunami*, 07(03):1350020, Sept. 2013. ISSN 1793-4311. doi: 10.1142/S1793431113500206.

[37] C. S. Cai, J. X. Hu, S. R. Chen, Y. Han, W. Zhang, and X. Kong. A coupled wind-vehicle-bridge system and its applications: a review. *Wind and Structures*, 20(2):117–142, Feb. 2015. doi: 10.12989/was.2015.20.2.117.

[38] A. Camara. Traffic stability in the Orwell Bridge under wind actions. Technical report, City, University of London, 2019.

[39] A. Camara, I. Kavrakov, K. Nguyen, and G. Morgenthal. Complete framework of wind-vehicle-bridge interaction with random road surfaces. *Journal of Sound and Vibration*, 458:197–217, 2019. ISSN 10958568. doi: 10.1016/j.jsv.2019.06.020.

[40] B. Y. B. Chan and M. M. S. Cheung. Performance and operational allowable speed limit for vehicles on cable stayed bridges. *Bridge Structures*, 6(1-2): 3–24, 2010. ISSN 1573-2487. doi: 10.3233/BRS-2010-005.

[41] S. Charuvisit, K. Kimura, and Y. Fujino. Effects of wind barrier on a vehicle passing in the wake of a bridge tower in cross wind and its response. *Journal of Wind Engineering and Industrial Aerodynamics*, 92(7):609–639, 2004. ISSN 0167-6105.

[42] S. Charuvisit, K. Kimura, and Y. Fujino. Experimental and semi-analytical studies on the aerodynamic forces acting on a vehicle passing through the wake of a bridge tower in cross wind. *Journal of Wind Engineering and Industrial Aerodynamics*, 92(9):749–780, 2004. ISSN 0167-6105.

[43] D. Chatterjee and G. Biswas. The effects of Reynolds and Prandtl numbers on flow and heat transfer across tandem square cylinders in the steady flow regime. *Numerical Heat Transfer, Part A: Applications*, 59(6):421–437, Mar. 2011. doi: 10.1080/10407782.2011.552374.

[44] F. Cheli, R. Corradi, E. Sabbioni, and G. Tomasini. Wind tunnel tests on heavy road vehicles: Cross wind induced loads—Part 1. *Journal of Wind Engineering and Industrial Aerodynamics*, 99(10):1000–1010, Oct. 2011. doi: 10.1016/j.jweia.2011.07.009.

[45] F. Cheli, F. Ripamonti, E. Sabbioni, and G. Tomasini. Wind tunnel tests on heavy road vehicles: Cross wind induced loads—Part 2. *Journal of Wind Engineering and Industrial Aerodynamics*, 99(10):1011–1024, Oct. 2011. doi: 10.1016/j.jweia.2011.07.007.

[46] N. Chen, Y. Li, B. Wang, Y. Su, and H. Xiang. Effects of wind barrier on the safety of vehicles driven on bridges. *Journal of Wind Engineering and Industrial Aerodynamics*, 143:113–127, 2015. ISSN 0167-6105. doi: https://doi.org/10.1016/j.jweia.2015.04.021.

[47] S. Chen and C. Cai. Accident assessment of vehicles on long-span bridges in windy environments. *Journal of Wind Engineering and Industrial Aerodynamics*, 92(12):991–1024, Oct. 2004. ISSN 01676105. doi: 10.1016/j.jweia.2004.06.002.

[48] S. Chen and F. Chen. Simulation-based assessment of vehicle safety behavior under hazardous driving conditions. *Journal of Transportation Engineering*, 136(4):304–315, 2009. ISSN 0733-947X. doi: 10.1061/(asce)te.1943-5436.0000093.

[49] S. R. Chen and J. Wu. Performance enhancement of bridge infrastructure systems: Long-span bridge, moving trucks and wind with tuned mass dampers. *Engineering Structures*, 30(11):3316–3324, 2008. ISSN 0141-0296. doi: 10.1016/j.engstruct.2008.04.035.

[50] S. R. Chen, C. S. Cai, and M. Levitan. Understand and improve dynamic performance of transportation system - a case study of Luling Bridge. *Engineering Structures*, 29(6):1043–1051, 2007. ISSN 0141-0296. doi: 10.1016/j.engstruct.2006.07.019.

[51] S. R. Chen, C. C. Chang, and C. S. Cai. Study on stability improvement of suspension bridge with high-sided vehicles under wind using tuned-liquid-damper. *JVC/Journal of Vibration and Control*, 14(5):711–730, 2008. ISSN 1077-5463. doi: 10.1177/1077546307083275.

[52] Z. Chen and B. Chen. Recent research and applications of numerical simulation for dynamic response of long-span bridges subjected to multiple loads. *Scientific World Journal*, 2014. ISSN 1537744X. doi: 10.1155/2014/763810.

[53] M. M. S. Cheung and B. Y. B. Chan. Operational requirements for long-span bridges under strong wind events. *Journal of Bridge Engineering*, 15(2):131–143, Mar. 2010. ISSN 1084-0702. doi: 10.1061/(ASCE)BE.1943-5592.0000044.

[54] Y. K. Cheung, F. T. Au, D. Y. Zheng, and Y. S. Cheng. Vibration of multi-span non-uniform bridges under moving vehicles and trains by using modified beam vibration functions. *Journal of Sound and Vibration*, 228(3):611–628, 1999. ISSN 0022460X. doi: 10.1006/jsvi.1999.2423.

[55] E. Cheynet, N. Daniotti, J. B. Jakobsen, and J. Snaebjornsson. Improved long-span bridge modeling using data-driven identification of vehicle-induced vibrations. *Structural Control and Health Monitoring*, 27(9), 2020. ISSN 1545-2255. doi: 10.1002/stc.2574.

[56] C.-B. Choi and K.-S. Yang. Three-dimensional instability in the flow past two side-by-side square cylinders. *Physics of Fluids*, 25(7):074107, July 2013. doi: 10.1063/1.4813628.

[57] C.-B. Choi and K.-S. Yang. Three-dimensional instability in flow past a rectangular cylinder ranging from a normal flat plate to a square cylinder. *Physics of Fluids*, 26(6):061702, June 2014. doi: 10.1063/1.4883176.

[58] C.-B. Choi, Y.-J. Jang, and K.-S. Yang. Secondary instability in the near-wake past two tandem square cylinders. *Physics of Fluids*, 24(2):024102, Feb. 2012. doi: 10.1063/1.3682373.

[59] S. Coleman and C. Baker. High sided road vehicles in cross winds. *Journal of Wind Engineering and Industrial Aerodynamics*, 36:1383–1392, Jan. 1990. doi: 10.1016/0167-6105(90)90134-x.

[60] S. Coleman and C. Baker. The reduction of accident risk for high sided road vehicles in cross winds. *Journal of Wind Engineering and Industrial Aerodynamics*, 44(1-3):2685–2695, Oct. 1992. doi: 10.1016/0167-6105(92)90060-n.

[61] S. Coleman and C. Baker. An experimental study of the aerodynamic behaviour of high sided lorries in cross winds. *Journal of Wind Engineering and Industrial Aerodynamics*, 53(3):401–429, Dec. 1994. doi: 10.1016/0167-6105(94)90093-0.

[62] R. Cooper. Atmospheric turbulence with respect to moving ground vehicles. *Journal of Wind Engineering and Industrial Aerodynamics*, 17(2):215–238, Aug. 1984. doi: 10.1016/0167-6105(84)90057-6.

[63] M. Craymer. Geodetic Toolbox. MATLAB Central File Exchange, Feb. 2022. Retrieved 14 February, 2022.

[64] P. de Theije. meanangle. MATLAB Central File Exchange, Sept. 2022. Retrieved 7 September, 2022.

[65] J. D'Errico. interparc. MATLAB Central File Exchange, Dec. 2021. Retrieved 3 December, 2021.

[66] J. D'Errico. arclength. MATLAB Central File Exchange, Dec. 2021. Retrieved 12 December, 2021.

[67] J. D'Errico. distance2curve. MATLAB Central File Exchange, Nov. 2021. Retrieved 30 November, 2021.

[68] J. D'Errico. inpaint_nans. MATLAB Central File Exchange, Mar. 2022. Retrieved 21 March, 2022.

[69] R. G. Dominy. A technique for the investigation of transient aerodynamic forces on road vehicles in cross winds. *Proceedings of the Institution of Mechanical Engineers, Part D: Journal of Automobile Engineering*, 205(4):245–250, oct 1991. doi: 10.1243/pime_proc_1991_205_180_02.

[70] X. Dong, Y. Jiang, Z. Zhong, and W. Zeng. Rollover threshold investigation of a heavy-duty vehicle during cornering based on multi-body dynamics. *Advances in Mechanical Engineering*, 10(7):168781401878950, July 2018. doi: 10.1177/1687814018789505.

[71] F. Dorigatti, M. Sterling, D. Rocchi, M. Belloli, A. D. Quinn, C. J. Baker, and E. Ozkan. Wind tunnel measurements of crosswind loads on high sided vehicles over long span bridges. *Journal of Wind Engineering and Industrial Aerodynamics*, 107-108:214–24, Aug. 2012. ISSN 0167-6105. doi: 10.1016/j.jweia.2012.04.017.

[72] F. Duchaine, M. Boileau, Y. Sommerer, and T. Poinsot. Large eddy simulation of flow and heat transfer around two square cylinders in a tandem arrangement. *Journal of Heat Transfer*, 136(10), July 2014. doi: 10.1115/1.4027908.

[73] A. Dumont and M. Tille. *Voies de circulation*, volume 25. EPFL Press, 1st edition, 2017.

[74] K. K. Dunham. Coastal highway route E39 – extreme crossings. *Transportation Research Procedia*, 14:494–498, 2016. doi: 10.1016/j.trpro.2016.05.102.

[75] S. Dutta, K. Muralidhar, and P. Panigrahi. Influence of the orientation of a square cylinder on the wake properties. *Experiments in Fluids*, 34(1):16–23, Jan. 2003. doi: 10.1007/s00348-002-0484-x.

[76] S. Dutta, P. K. Panigrahi, and K. Muralidhar. Experimental investigation of flow past a square cylinder at an angle of incidence. *Journal of Engineering Mechanics*, 134(9):788–803, Sept. 2008. doi: 10.1061/(asce)0733-9399(2008)134:9(788).

[77] L. Eboli, G. Mazzulla, and G. Pungillo. Combining speed and acceleration to define car users' safe or unsafe driving behaviour. *Transportation Research Part C: Emerging Technologies*, 68:113–125, July 2016. doi: 10.1016/j.trc.2016.04.002.

[78] R. Eyre and I. Smith. Wind and traffic induced dynamic behaviour of some steel box girder bridges. In *Proc. of a Symposium on Dynamic Behaviour of Bridges*, Crowthorne, Berkshire, England, 1977. Transport and Road Research Laboratory.

[79] T. Favre, J. J. Näfver, J. Jerrelind, A. S. Trigell, and G. Efraimsson. Static coupling between detached-eddy simulations and vehicle dynamic simulations of a generic road vehicle model with different rear configurations in unsteady crosswind. *International Journal of Vehicle Design*, 72(4):332, 2016. doi: 10.1504/ijvd.2016.082384.

[80] E. M. Felde. Bilist rasar over stengd måløybru, meiner ein er sett fleire tiår tilbake i tid. *NRK Nyheter*, Dec. 2013. URL `https://www.nrk.no/vestland/krev-endra-stengekrav-pa-maloybrua-1.11424197`.

[81] A. Fenerci and O. Øiseth. Measured buffeting response of a long-span suspension bridge compared with numerical predictions based on design wind spectra. *Journal of Structural Engineering (United States)*, 143(9):1–15, 2017. ISSN 07339445. doi: 10.1061/(ASCE)ST.1943-541X.0001873.

[82] A. Fenerci, O. Øiseth, and A. Rønnquist. Long-term monitoring of wind field characteristics and dynamic response of a long-span suspension bridge in complex terrain. *Engineering Structures*, 147:269–284, Sept. 2017. doi: 10.1016/j.engstruct.2017.05.070.

[83] D. C. Forbes, G. J. Page, M. A. Passmore, and A. P. Gaylard. A fully coupled, 6 degree-of-freedom, aerodynamic and vehicle handling crosswind simulation using the DrivAer model. *SAE International Journal of Passenger Cars - Mechanical Systems*, 9(2):710–722, Apr. 2016. doi: 10.4271/2016-01-1601.

[84] T. Fukagawa, S. Shimokawa, E. Itakura, H. Nakatani, and K. Kitahama. Modeling of transient aerodynamic forces based on crosswind test. *SAE International Journal of Passenger Cars - Mechanical Systems*, 9(2):572–582, Apr. 2016. doi: 10.4271/2016-01-1577.

[85] M. Gala, Sept. 2021. Private communication.

[86] A. Guissart, T. Andrianne, G. Dimitriadis, and V. E. Terrapon. Numerical and experimental study of the flow around a 4:1 rectangular cylinder at moderate reynolds number. *Journal of Wind Engineering and Industrial Aerodynamics*, 189:289–303, June 2019. doi: 10.1016/j.jweia.2019.03.026.

[87] W. H. Guo and Y. L. Xu. Safety Analysis of Moving Road Vehicles on a Long Bridge under Crosswind. *Journal of Engineering Mechanics*, 132(4):438–446, Apr. 2006. ISSN 0733-9399. doi: 10.1061/(ASCE)0733-9399(2006)132:4(438).

[88] H. Hacışevki and A. Teimourian. Comparison of flow structures in the wake region of two similar normal flat plates in tandem and a square cylinder. *Experimental Thermal and Fluid Science*, 69:169–177, Dec. 2015. doi: 10.1016/j.expthermflusci.2015.08.007.

[89] W. S. Han, L. Ma, and A. R. Chen. Dynamic analysis of random traffic flow running on super long-span cable-stayed bridge under crosswind. *Environmental Vibrations: Prediction, Monitoring, Mitigation and Evaluation, Vols I and Ii*, pages 1214–1219, 2009.

[90] Y. Han, K. Li, X. He, S. Chen, and F. Xue. Stress analysis of a long-span steel-truss suspension bridge under combined action of random traffic and wind loads. *Journal of Aerospace Engineering*, 31(3), 2018. ISSN 0893-1321. doi: 10.1061/(ASCE)AS.1943-5525.0000843.

[91] Z. Han, D. Zhou, J. Tu, C. Fang, and T. He. Flow over two side-by-side square cylinders by CBS finite element scheme of spalart–allmaras model. *Ocean Engineering*, 87:40–49, Sept. 2014. doi: 10.1016/j.oceaneng.2014.05.006.

[92] X. He, F. Xue, Y. Zou, S. Chen, Y. Han, B. Du, X. Xu, and B. Ma. Wind tunnel tests on the aerodynamic characteristics of vehicles on highway bridges. *Advances in Structural Engineering*, 23(13):2882–2897, 2020. ISSN 1369-4332. doi: 10.1177/1369433220924791.

[93] G. J. Heydinger, R. A. Bixel, W. R. Garrott, M. Pyne, J. G. Howe, and D. A. Guenther. Measured vehicle inertial parameters-NHTSA's data through November 1998. In *International Congress & Exposition*. SAE International,

Mar. 1999. doi: https://doi.org/10.4271/1999-01-1336. URL https://doi.org/10.4271/1999-01-1336.

[94] G. Hoffmann. save2pdf. MATLAB Central File Exchange, Jan. 2022. Retrieved 19 January, 2022.

[95] J. Howell, D. Forbes, M. Passmore, and G. Page. The effect of a sheared crosswind flow on car aerodynamics. *SAE International Journal of Passenger Cars - Mechanical Systems*, 10(1):278–285, mar 2017. doi: 10.4271/2017-01-1536.

[96] G. Hu, K. Tse, Z. Chen, and K. Kwok. Particle image velocimetry measurement of flow around an inclined square cylinder. *Journal of Wind Engineering and Industrial Aerodynamics*, 168:134–140, Sept. 2017. doi: 10.1016/j.jweia.2017.06.001.

[97] R. Huang, B. Lin, and S. Yen. Time-averaged topological flow patterns and their influence on vortex shedding of a square cylinder in crossflow at incidence. *Journal of Fluids and Structures*, 26(3):406–429, Apr. 2010. doi: 10.1016/j.jfluidstructs.2010.01.003.

[98] T. Huang, Z. Gu, C. Feng, and W. Zeng. Transient aerodynamics simulations of a road vehicle in the crosswind condition coupled with the vehicle's motion. *Proceedings of the Institution of Mechanical Engineers, Part D: Journal of Automobile Engineering*, 232(5):583–598, Aug. 2017. doi: 10.1177/0954407017704609.

[99] N. Humphreys and C. Baker. Forces on vehicles in cross winds from moving model tests. *Journal of Wind Engineering and Industrial Aerodynamics*, 44 (1-3):2673–2684, Oct. 1992. doi: 10.1016/0167-6105(92)90059-j.

[100] S. U. Islam, H. Rahman, and C. Zhou. Effect of gap spacings on flow past row of rectangular cylinders with aspect ratio 1.5. *Ocean Engineering*, 119: 1–15, June 2016. doi: 10.1016/j.oceaneng.2016.04.022.

[101] S. U. Islam, R. Manzoor, Z. C. Ying, and Z. U. Islam. Numerical investigation of different aspect ratios for flow past three inline rectangular cylinders. *Journal of the Brazilian Society of Mechanical Sciences and Engineering*, 40 (9), Aug. 2018. doi: 10.1007/s40430-018-1334-y.

[102] S. U. Islam, G. Nazeer, and S. H. Shigri. Numerical investigation of different flow regimes for square cylinders in staggered configuration. *KSCE Journal of Civil Engineering*, 23(5):2188–2197, Mar. 2019. doi: 10.1007/s12205-019-0726-6.

[103] ISO. ISO 16290:2013(E), 2013.

[104] J. A. C. J. L. Rosales, A. Ortega. A numerical investigation of the convective heat transfer in unsteady laminar flow past a single and tandem pair of square cylinders in a channel. *Numerical Heat Transfer, Part A: Applications*, 38(5):443–465, Oct. 2000. doi: 10.1080/104077800750020388.

[105] E. Johnson. STL File Reader. MATLAB Central File Exchange, Apr. 2022. Retrieved 29 April, 2022.

[106] I. S. Jones and L. A. Wilson. Techniques for the reconstruction of rollover accidents involving sport utility vehicles, light trucks and minivans. In *SAE Technical Paper Series*. SAE International, Mar. 2000. doi: 10.4271/2000-01-0851.

[107] M. Juhlin. Aerodynamic loads on buses due to crosswind gusts – on-road measurements. *Vehicle System Dynamics*, 46:827–835, Sept. 2008. doi: 10.1080/00423110802037081.

[108] Kartverket. Vbase 4.03, UTM EUREF89, June 2016. URL `https://register.geonorge.no/register/versjoner/produktark/kartverket/vbase`.

[109] J. D. Kee, J. H. Rho, K. H. Kim, and D. H. Lee. High speed driving stability of passenger car under crosswind effects. *International Journal of Automotive Technology*, 15(5):741–747, Aug. 2014. doi: 10.1007/s12239-014-0077-8.

[110] H. G. Kim and V. C. Patel. Test of turbulence models for wind flow over terrain with separation and recirculation. *Boundary-Layer Meteorology*, 94 (1):5–21, Jan. 2000. doi: 10.1023/a:1002450414410.

[111] K. C. Kim, H. S. Ji, and S. H. Seong. Flow structure around a 3-d rectangular prism in a turbulent boundary layer. *Journal of Wind Engineering and Industrial Aerodynamics*, 91(5):653–669, Apr. 2003. doi: 10.1016/s0167-6105(02)00459-2.

[112] M. K. Kim, D. K. Kim, S. H. Yoon, and D. H. Lee. Measurements of the flow fields around two square cylinders in a tandem arrangement. *Journal of Mechanical Science and Technology*, 22(2):397–407, Feb. 2008. doi: 10.1007/s12206-007-1041-6.

[113] S.-J. Kim, C.-H. Yoo, and H.-K. Kim. Vulnerability assessment for the hazards of crosswinds when vehicles cross a bridge deck. *Journal of Wind Engineering and Industrial Aerodynamics*, 156:62–71, Sept. 2016. ISSN 01676105. doi: 10.1016/j.jweia.2016.07.005.

[114] S.-J. Kim, J.-H. Shim, and H.-K. Kim. How wind affects vehicles crossing a double-deck suspension bridge. *Journal of Wind Engineering and Industrial Aerodynamics*, 206:104329, Nov. 2020. doi: 10.1016/j.jweia.2020.104329.

[115] B. Kitchenham and S. Charters. Guidelines for performing systematic literature reviews in software engineering. Technical report, 2007. Technical Report EBSE-2007-01.

[116] C. Knisely. Strouhal numbers of rectangular cylinders at incidence: A review and new data. *Journal of Fluids and Structures*, 4(4):371–393, July 1990. doi: 10.1016/0889-9746(90)90137-t.

[117] V. Kolar, D. A. Lyn, and W. Rodi. Ensemble-averaged measurements in the turbulent near wake of two side-by-side square cylinders. *Journal of Fluid Mechanics*, 346:201–237, Sept. 1997. doi: 10.1017/s0022112097006307.

[118] D. Kumar and S. Sen. Flow-induced vibrations of a pair of in-line square cylinders. *Physics of Fluids*, 33(4):043602, Apr. 2021. doi: 10.1063/5.0038714.

[119] N. Labonnote, A. Rønnquist, B. Manum, and P. Rüther. Additive construction: State-of-the-art, challenges and opportunities. *Automation in Construction*, 72:347–366, Dec. 2016. doi: 10.1016/j.autcon.2016.08.026.

[120] R. Lamm. *Highway design and traffic safety engineering handbook*. McGraw-Hill, 1999. ISBN 0070382956.

[121] A. Lankadasu and S. Vengadesan. Interference effect of two equal-sized square cylinders in tandem arrangement: With planar shear flow. *International Journal for Numerical Methods in Fluids*, 57(8):1005–1021, July 2008. doi: 10.1002/fld.1670.

[122] A. Laurent. Polar/cartesian into degree north reference. MATLAB Central File Exchange, Feb. 2022. Retrieved 1 February, 2022.

[123] A. A. Lawson, R. G. Dominy, D. B. Sims-Williams, and P. Mears. A comparison between on-road and wind tunnel surface pressure measurements on a mid-sized hatchback. In *SAE Technical Paper Series*. SAE International, Apr. 2007. doi: 10.4271/2007-01-0898.

[124] N. Lewington, L. Ohra-aho, O. Lange, and K. Rudnik. The application of a one-way coupled aerodynamic and multi-body dynamics simulation process to predict vehicle response during a severe crosswind event. In *SAE Technical Paper Series*. SAE International, Mar. 2017. doi: 10.4271/2017-01-1515.

[125] S. Li, Z. Gu, T. Huang, Z. Chen, and J. Liu. Coupled analysis of vehicle stability in crosswind on low adhesion road. *International Journal of Numerical Methods for Heat and Fluid Flow*, 28(8):1956–1972, Sept. 2018. doi: 10.1108/hff-01-2018-0013.

[126] C.-H. Liu and J. M. Chen. Observations of hysteresis in flow around two square cylinders in a tandem arrangement. *Journal of Wind Engineering and Industrial Aerodynamics*, 90(9):1019–1050, Sept. 2002. doi: 10.1016/s0167-6105(02)00234-9.

[127] Z. Liu, T. Guo, L. Huang, and Z. Pan. Fatigue life evaluation on short suspenders of long-span suspension bridge with central clamps. *Journal of Bridge Engineering*, 22(10), 2017. ISSN 1084-0702. doi: 10.1061/(ASCE)BE.1943-5592.0001097.

[128] X. Lou and K. Zhang. Experimental study on a yawed square cylinder in oscillatory flows. *Ocean Engineering*, 196:106859, Jan. 2020. doi: 10.1016/j.oceaneng.2019.106859.

[129] X. Lou, T. Zhou, Y. Zhou, H. Wang, and L. Cheng. Experimental investigation on wake characteristics behind a yawed square cylinder. *Journal of Fluids and Structures*, 61:274–294, Feb. 2016. doi: 10.1016/j.jfluidstructs.2015.11.017.

[130] K. Lundahl, K. Berntorp, B. Olofsson, J. Aslund, and L. Nielsen. Studying the influence of roll and pitch dynamics in optimal road-vehicle maneuvers. In *23rd International Symposium on Dynamics of Vehicles on Roads and Tracks*, pages 1–10, Qingdao, China, 2013.

[131] L. Ma, W.-s. Han, and B.-h. Ji. Probability of overturning for vehicles moving on a bridge deck in a wind environment considering stochastic process characteristics of excitations. *Journal of Performance of Constructed Facilities*, 29(1):0401403411, Feb. 2015. ISSN 0887-3828. doi: 10.1061/(ASCE)CF.1943-5509.0000479.

[132] L. Ma, D. Zhou, W. Han, J. Wu, and J. Liu. Transient aerodynamic forces of a vehicle passing through a bridge tower's wake region in crosswind environment. *Wind and Structures, An International Journal*, 22(2):211–234, 2016. ISSN 1226-6116. doi: 10.12989/was.2016.22.2.211.

[133] L. Ma, X. Chen, J. Wu, and W. Han. Aerodynamic interference mechanism of moving vehicles on a bridge deck in crosswind environment. *Journal of Bridge Engineering*, 23(4):04018011, Apr. 2018. doi: 10.1061/(asce)be.1943-5592.0001194.

[134] C. C. MacAdam. Static turning analysis of vehicles subject to externally applied forces - a moment arm ratio formulation. *Vehicle System Dynamics*, 18(6):345–357, Jan. 1989. doi: 10.1080/00423118908968926.

[135] C. C. MacAdam, M. W. Sayers, J. D. Pointer, and M. Gleason. Crosswind sensitivity of passenger cars and the influence of chassis and aerodynamic properties on driver preferences. *Vehicle System Dynamics*, 19(4):201–236, Jan. 1990. doi: 10.1080/00423119008968942.

[136] A. J. Macdonald. *Wind loading on buildings*. Wiley, 1975. ISBN 0470559764.

[137] O. Mankowski, D. Sims-Williams, R. Dominy, B. Duncan, and J. Gargoloff. The bandwidth of transient yaw effects on vehicle aerodynamics. *SAE International Journal of Passenger Cars - Mechanical Systems*, 4(1):131–142, Apr. 2011. doi: 10.4271/2011-01-0160.

[138] J. Mayer, M. Schrefl, and R. Demuth. On various aspects of the unsteady aerodynamic effects on cars under crosswind conditions. In *SAE Technical Paper Series*. SAE International, Apr. 2007. doi: 10.4271/2007-01-1548.

[139] K. Mayer. UTM2LatLong GeoTiff Converter. MATLAB Central File Exchange, Feb. 2022. Retrieved 14 February, 2022.

[140] Z. Midjiyawa, E. Cheynet, J. Reuder, H. Ágústsson, and T. Kvamsdal. Potential and challenges of wind measurements using met-masts in complex topography for bridge design: Part I – integral flow characteristics. *Journal of Wind Engineering and Industrial Aerodynamics*, 211:104584, Apr. 2021. doi: 10.1016/j.jweia.2021.104584.

[141] R. Mills, J. Sheridan, and K. Hourigan. Particle image velocimetry and visualization of natural and forced flow around rectangular cylinders. *Journal of Fluid Mechanics*, 478:299–323, Mar. 2003. doi: 10.1017/s0022112002003439.

[142] M. Mirzaei and A. Sohankar. Numerical study of convective heat transfer and fluid flow around two side by side square cylinders using turbulence model. *Heat and Mass Transfer*, 49(12):1755–1769, Aug. 2013. doi: 10.1007/s00231-013-1216-x.

[143] M. Mohebi, P. du Plessix, R. J. Martinuzzi, and D. H. Wood. Effect of thickness-to-chord ratio on the wake of two-dimensional rectangular cylinders. *Physical Review Fluids*, 2(6):064702, June 2017. doi: 10.1103/physrevfluids.2.064702.

[144] T. Nagahisa, A. Okajima, and R. Shibata. Unsteady aerodynamic forces on a vehicle model passing in a wake (experiments). *Nippon Kikai Gakkai Ronbunshu, B Hen/Transactions of the Japan Society of Mechanical Engineers, Part B*, 53(485):40–48, 1987. ISSN 0387-5016.

[145] J. Niu and Z. Zhu. Numerical study of three-dimensional flows around two identical square cylinders in staggered arrangements. *Physics of Fluids*, 18 (4):044106, Apr. 2006. doi: 10.1063/1.2194077.

[146] Y. Noguchi, M. Suzuki, C. Baker, and K. Nakade. Numerical and experimental study on the aerodynamic force coefficients of railway vehicles on an embankment in crosswind. *Journal of Wind Engineering and Industrial Aerodynamics*, 184:90–105, Jan. 2019. doi: 10.1016/j.jweia.2018.11.019.

[147] C. Norberg. Flow around rectangular cylinders: Pressure forces and wake frequencies. *Journal of Wind Engineering and Industrial Aerodynamics*, 49 (1-3):187–196, Dec. 1993. doi: 10.1016/0167-6105(93)90014-f.

[148] O. Øiseth, A. Rönnquist, and R. Sigbjörnsson. Time domain modeling of self-excited aerodynamic forces for cable-supported bridges: A comparative study. *Computers and Structures*, 89(13-14):1306–1322, 2011. ISSN 00457949. doi: 10.1016/j.compstruc.2011.03.017.

[149] A. Okajima. Numerical simulation of flow around rectangular cylinders. *Journal of Wind Engineering and Industrial Aerodynamics*, 33(1-2):171–180, Mar. 1990. doi: 10.1016/0167-6105(90)90033-9.

[150] A. Okajima, H. Ueno, and H. Sakai. Numerical simulation of laminar and turbulent flows around rectangular cylinders. *International Journal for Numerical Methods in Fluids*, 15(9):999–1012, Nov. 1992. doi: 10.1002/fld.1650150906.

[151] S. Outten and S. Sobolowski. Extreme wind projections over Europe from the Euro-CORDEX regional climate models. *Weather and Climate Extremes*, 33:100363, sep 2021. doi: 10.1016/j.wace.2021.100363.

[152] S. Ozgoren, Muammer; Dogan. Quantitative flow characteristics for side-by-side square cylinders via PIV. In *EFM11 – Experimental Fluid Mechanics 2011*, 2012.

[153] H. B. Pacejka. *Tire and Vehicle Dynamics*. Butterworth-Heinemann, 3rd edition, 2012. ISBN 9780080970165. doi: 10.1016/C2010-0-68548-8.

[154] M. A. Passmore and S. Mansor. The measurement of transient aerodynamics using an oscillating model facility. In *SAE Technical Paper Series*. SAE International, Apr. 2006. doi: 10.4271/2006-01-0338.

[155] C. G. Patel, S. Sarkar, and S. K. Saha. Mixed convective vertically upward flow past side-by-side square cylinders at incidence. *International Journal of Heat and Mass Transfer*, 127:927–947, Dec. 2018. doi: 10.1016/j.ijheatmasstransfer.2018.06.129.

[156] B. M. Paulsen and J. L. Schroeder. An examination of tropical and extratropical gust factors and the associated wind speed histograms. *Journal of Applied Meteorology and Climatology*, 44(2):270–280, Feb. 2005. doi: 10.1175/jam2199.1.

[157] R. Pawlowicz. M_Map: A mapping package for MATLAB, version 1.4m, 2020.

[158] J. Peterka, R. Meroney, and K. Kothari. Wind flow patterns about buildings. *Journal of Wind Engineering and Industrial Aerodynamics*, 21(1):21–38, Aug. 1985. doi: 10.1016/0167-6105(85)90031-5.

[159] K. Petersen, R. Feldt, S. Mujtaba, and M. Mattsson. Systematic mapping studies in software engineering. In *Proceedings of the 12th International Conference on Evaluation and Assessment in Software Engineering*, EASE'08, pages 68–77, Swindon, GBR, 2008. BCS Learning & Development Ltd.

[160] Ø. W. Petersen, O. Øiseth, and E. M. Lourens. The use of inverse methods for response estimation of long-span suspension bridges with uncertain wind loading conditions: Practical implementation and results for the Hardanger Bridge. *Journal of Civil Structural Health Monitoring*, 9(1):21–36, 2019. ISSN 21905479. doi: 10.1007/s13349-018-0319-y.

[161] A. Pullin, G. Frampton, B. Livoreil, and Petrokofsky. Guidelines and standards for evidence synthesis in environmental management, version 5.0. Online, 2018. URL `http://www.environmentalevidence.org/information-for-authors`.

[162] A. D. Quinn, M. Sterling, A. P. Robertson, and C. J. Baker. An investigation of the wind-induced rolling moment on a commercial vehicle in the atmospheric boundary layer. *Proceedings of the Institution of Mechanical Engineers, Part D: Journal of Automobile Engineering*, 221(11):1367–1379, Nov. 2007. doi: 10.1243/09544070jauto537.

[163] *VBOX 3i Dual Antenna RTK*. Racelogic, Sept. 2020. Datasheet.

[164] K. Reif, editor. *Bosch Automotive Handbook, 10th Edition*. Robert Bosch GmbH, 2018.

[165] S. Reymert. A digital mapping of the literature on vehicle-bridge-wind systems, 2020. Available on Zenodo.

[166] D. Rocchi, L. Rosa, E. Sabbioni, M. Sbrosi, and M. Belloli. A numerical-experimental methodology for simulating the aerodynamic forces acting on a moving vehicle passing through the wake of a bridge tower under cross wind. *Journal of Wind Engineering and Industrial Aerodynamics*, 104-106: 256–265, 2012. ISSN 01676105. doi: 10.1016/j.jweia.2012.03.012.

[167] E. Sabbioni, M. Sbrosi, D. Rocchi, and R. Galeotti. Dynamic response of vehicle-driver couple to the aerodynamic loads due to the crossing of a bridge tower wake. *SAE International Journal of Commercial Vehicles*, 5(1): 83–93, Apr. 2012. doi: 10.4271/2012-01-0214.

[168] L. Salati, P. Schito, D. Rocchi, and E. Sabbioni. Aerodynamic study on a heavy truck passing by a bridge pylon under crosswinds using CFD. *Journal of Bridge Engineering*, 23(9):04018065, Sept. 2018. doi: 10.1061/(asce)be.1943-5592.0001277.

[169] A. Sanyal and A. Dhiman. Wake interactions in a fluid flow past a pair of side-by-side square cylinders in presence of mixed convection. *Physics of Fluids*, 29(10):103602, Oct. 2017. doi: 10.1063/1.5005118.

[170] S. Schaible. *Fahrzeugseitenwindempfindlichkeit unter natürlichen Bedingungen*. PhD thesis, RWTH Aachen, 1998.

[171] G. Schewe. On the force fluctuations acting on a circular cylinder in crossflow from subcritical up to transcritical reynolds numbers. *Journal of Fluid Mechanics*, 133:265–285, Aug. 1983. doi: 10.1017/s0022112083001913.

[172] S. Schlesinger. Terminology for model credibility. Technical report, 1979.

[173] B. Schofield. *Model-Based Vehicle Dynamics Control for Active Safety*. PhD thesis, Lund University, 2008.

[174] J. Shang, Q. Zhou, M. M. Alam, H. Liao, and S. Cao. Numerical studies of the flow structure and aerodynamic forces on two tandem square cylinders with different chamfered-corner ratios. *Physics of Fluids*, 31(7):075102, July 2019. doi: 10.1063/1.5100266.

[175] G. J. Sheard, M. J. Fitzgerald, and K. Ryan. Cylinders with square cross-section: wake instabilities with incidence angle variation. *Journal of Fluid Mechanics*, 630:43–69, July 2009. doi: 10.1017/s0022112009006879.

[176] Q. Shui, C. Duan, D. Wang, and Z. Gu. New insights into numerical simulations of flow around two tandem square cylinders. *AIP Advances*, 11(4): 045315, Apr. 2021. doi: 10.1063/5.0042797.

[177] E. Simiu. *Wind effects on structures*. Wiley, 1986. ISBN 047186613X.

[178] D. Sims-Williams. Cross winds and transients: Reality, simulation and effects. *SAE International Journal of Passenger Cars - Mechanical Systems*, 4 (1):172–183, Apr. 2011. doi: 10.4271/2011-01-0172.

[179] J. Snæbjörnsson, C. Baker, and R. Sigbjörnsson. Probabilistic assessment of road vehicle safety in windy environments. *Journal of Wind Engineering and Industrial Aerodynamics*, 95(9-11):1445–1462, Oct. 2007. doi: 10.1016/j.jweia.2007.02.020.

[180] A. Sohankar. Large eddy simulation of flow past rectangular-section cylinders: Side ratio effects. *Journal of Wind Engineering and Industrial Aerodynamics*, 96(5):640–655, May 2008. doi: 10.1016/j.jweia.2008.02.009.

[181] A. Sohankar. A numerical investigation of the flow over a pair of identical square cylinders in a tandem arrangement. *International Journal for Numerical Methods in Fluids*, 70(10):1244–1257, Dec. 2011. doi: 10.1002/fld.2739.

[182] A. Sohankar. A LES study of the flow interference between tandem square cylinder pairs. *Theoretical and Computational Fluid Dynamics*, 28(5):531–548, Sept. 2014. doi: 10.1007/s00162-014-0329-2.

[183] A. Sohankar, S. Mohagheghian, A. A. Dehghan, and M. D. Manshadi. A smoke visualization study of the flow over a square cylinder at incidence and tandem square cylinders. *Journal of Visualization*, 18(4):687–703, Mar. 2015. doi: 10.1007/s12650-015-0275-0.

[184] A. Sohankar, M. Abbasi, M. Nili-Ahmadabadi, and M. M. Alam. Experimental study of the flow around two finite square cylinders. 2018. doi: 10.24423/AOM.2965.

[185] *Nærøysund Bru, Oversikt*. Statens Vegvesen, 1978. Arbeidstegning.

[186] *12-2950 Hardangerbrua, Oversikt*. Statens Vegvesen, 2011. Arbeidstegning.

[187] *Hålogalandsbrua, Oversikt*. Statens Vegvesen, 2014. Arbeidstegning.

[188] *16-1481 Dolmsundbrua Oversiktstegning*. Statens Vegvesen, 2017. Som Bygd.

[189] *Helgelandsbrua, Skråstagbru, Oversikt*. Statens Vegvesen Nordland, 1989. Arbeidstegning.

[190] M. Sterling, A. Quinn, D. Hargreaves, F. Cheli, E. Sabbioni, G. Tomasini, D. Delaunay, C. Baker, and H. Morvan. A comparison of different methods to evaluate the wind induced forces on a high sided lorry. *Journal of Wind Engineering and Industrial Aerodynamics*, 98(1):10–20, Jan. 2010. doi: 10.1016/j.jweia.2009.08.008.

[191] D. Sumner. Two circular cylinders in cross-flow: A review. *Journal of Fluids and Structures*, 26(6):849–899, Aug. 2010. doi: 10.1016/j.jfluidstructs.2010.07.001.

[192] D. Sumner, M. Richards, and O. Akosile. Two staggered circular cylinders of equal diameter in cross-flow. *Journal of Fluids and Structures*, 20(2):255–276, Feb. 2005. doi: 10.1016/j.jfluidstructs.2004.10.006.

[193] D. Sumner, N. Rostamy, D. Bergstrom, and J. Bugg. Influence of aspect ratio on the mean flow field of a surface-mounted finite-height square prism. *International Journal of Heat and Fluid Flow*, 65:1–20, June 2017. doi: 10.1016/j.ijheatfluidflow.2017.02.004.

[194] J. Sun, L. Li, and W. Hou. Gust response of long span bridge-vehicle system. Oxford, U.K., International Academic Publishers, 1989. ISBN 7800030652; 9787800030659.

[195] C. Tan. *An investigation of comfortable lateral acceleration on horizontal curves*. PhD thesis, The Pennsylvania State University, 2005.

[196] P. Theissen. *Unsteady Vehicle Aerodynamics in Gusty Crosswind*. PhD thesis, Technical University of Munich, Jan. 2012.

[197] X. Tian, M. C. Ong, J. Yang, and D. Myrhaug. Unsteady RANS simulations of flow around rectangular cylinders with different aspect ratios. *Ocean Engineering*, 58:208–216, Jan. 2013. doi: 10.1016/j.oceaneng.2012.10.013.

[198] X. Tong, S. Luo, and B. Khoo. Transition phenomena in the wake of an inclined square cylinder. *Journal of Fluids and Structures*, 24(7):994–1005, Oct. 2008. doi: 10.1016/j.jfluidstructs.2008.03.004.

[199] M. Tsubokura, T. Nakashima, M. Kitayama, Y. Ikawa, D. H. Doh, and T. Kobayashi. Large eddy simulation on the unsteady aerodynamic response of a road vehicle in transient crosswinds. *International Journal of Heat and Fluid Flow*, 31(6):1075–1086, Dec. 2010. doi: 10.1016/j.ijheatfluidflow.2010.05.008.

[200] T. Tunay, L. Drugge, and C. J. O'Reilly. On coupling methods used to simulate the dynamic characteristics of heavy ground vehicles subjected to crosswind. *Journal of Wind Engineering and Industrial Aerodynamics*, 201:104194, June 2020. doi: 10.1016/j.jweia.2020.104194.

[201] B. W. van Oudheusden, F. Scarano, N. P. van Hinsberg, and D. W. Watt. Phase-resolved characterization of vortex shedding in the near wake of a square-section cylinder at incidence. *Experiments in Fluids*, 39(1):86–98, May 2005. doi: 10.1007/s00348-005-0985-5.

[202] *Tjeldsundbrua*. Vegdirektoratet, 1965. Arbeidstegning.

[203] *Måløybrua, Oversikt*. Vegdirektoratet, 1988. Ferdigbrutegning.

[204] *Crafter Tekniske data*. Volkswagen Nyttekjøretøy, Jan. 2018. Datasheet.

[205] A. Wagner and J. Wiedemann. Crosswind behavior in the driver's perspective. In *SAE Technical Paper Series*. SAE International, Mar. 2002. doi: 10.4271/2002-01-0086.

[206] S. Walsh, Sept. 2021. Private communication.

[207] B. Wang and Y.-L. Xu. Safety analysis of a road vehicle passing by a bridge tower under crosswinds. *Journal of Wind Engineering and Industrial Aerodynamics*, 137:25–36, Feb. 2015. ISSN 01676105. doi: 10.1016/j.jweia.2014.11.017.

[208] B. Wang, Y. Li, H. Yu, and H. Liao. Dynamic reliability evaluation of road vehicle subjected to turbulent crosswinds based on monte carlo simulation. *Shock and Vibration*, 2017:1–12, 2017. doi: 10.1155/2017/2365812.

[209] D. Wang, H. Ai, and A. Chen. Numerical simulation of alternating wind environment above the girder near A-shaped pylon for zhengxin yellow river bridge in cross wind. pages 496–499, 2011. ISBN 9781457702907. doi: 10.1109/ICETCE.2011.5775390.

[210] F. Wang, X. Zheng, J. Hao, and H. Bai. Numerical analysis of the flow around two square cylinders in a tandem arrangement with different spacing ratios based on POD and DMD methods. *Processes*, 8(8):903, July 2020. doi: 10.3390/pr8080903.

[211] H. Wang, J. Mao, and B. Spencer. A monitoring-based approach for evaluating dynamic responses of riding vehicle on long-span bridge under strong winds. *Engineering Structures*, 189:35–47, July 2019. ISSN 18737323. doi: 10.1016/j.engstruct.2019.03.075.

[212] S. Wang, F. Yang, Z. Yang, and Q. Ma. Dynamic responses of long-span cable-stayed bridge with the action of both running vehicles and wind loads. In *Proceedings of the International Offshore and Polar Engineering Conference*, volume 2018-June, pages 428–433. International Society of Offshore and Polar Engineers, 2018. ISBN 9781880653876.

[213] S. Wang, W. Cheng, R. Du, and Y. Wang. Unsteady RANS modeling of flow around two-dimensional rectangular cylinders with different side ratios at Reynolds number 6.85×10^5. *Mathematical Problems in Engineering*, 2020: 1–13, Sept. 2020. doi: 10.1155/2020/2163928.

[214] T. Wang, W. Han, F. Yang, and W. Kong. Wind-vehicle-bridge coupled vibration analysis based on random traffic flow simulation. *Journal of Traffic and Transportation Engineering (English Edition)*, 1(4):293–308, 2014. ISSN 2095-7564.

[215] Y. Wang, H.F.; Zhou. The finite-length square cylinder near wake. *Journal of Fluid Mechanics*, 638:453–490, Oct. 2009. doi: 10.1017/s0022112009990693.

[216] E. Watanabe, T. Maruyama, H. Tanaka, and S. Takeda. Design and construction of a floating swing bridge in osaka. *Marine Structures*, 13(4-5): 437–458, 2000. ISSN 0951-8339. doi: 10.1016/S0951-8339(00)00016-2.

[217] N. Winkler, L. Drugge, A. S. Trigell, and G. Efraimsson. Coupling aerodynamics to vehicle dynamics in transient crosswinds including a driver model. *Computers and Fluids*, 138:26–34, Oct. 2016. doi: 10.1016/j.compfluid.2016.08.006.

[218] P. Wong, N. Ko, and A. Chiu. Flow characteristics around two parallel adjacent square cylinders of different sizes. *Journal of Wind Engineering and Industrial Aerodynamics*, 54-55:263–275, Feb. 1995. doi: 10.1016/0167-6105(94)00046-g.

[219] S. Wordley. *On-road Turbulence*. PhD thesis, Monash University, 2009.

[220] S. Wordley and J. W. Saunders. On-road turbulence. *SAE International Journal of Passenger Cars - Mechanical Systems*, 1(1):341–360, Apr. 2008. doi: 10.4271/2008-01-0475.

[221] S. Wordley and J. W. Saunders. On-road turbulence: Part 2. *SAE International Journal of Passenger Cars - Mechanical Systems*, 2(1):111–137, Apr. 2009. doi: 10.4271/2009-01-0002.

[222] H. Xiang, Y. Li, S. Chen, and C. Li. A wind tunnel test method on aerodynamic characteristics of moving vehicles under crosswinds. *Journal of Wind Engineering and Industrial Aerodynamics*, 163:15–23, Apr. 2017. doi: 10.1016/j.jweia.2017.01.013.

[223] H. Xiang, Y. Li, S. Chen, and G. Hou. Wind loads of moving vehicle on bridge with solid wind barrier. *Engineering Structures*, 156:188–196, 2018. ISSN 0141-0296.

[224] F. Xu, B. Li, C. Cai, and Z. Zhang. Experimental investigations on aerostatic characteristics of bridge decks under various conditions. *Journal of Bridge Engineering*, 19(7), 2014. ISSN 1084-0702. doi: 10.1061/(ASCE)BE.1943-5592.0000601.

[225] J. Xu, K. Yang, Y. Shao, and G. Lu. An experimental study on lateral acceleration of cars in different environments in Sichuan, Southwest China. *Discrete Dynamics in Nature and Society*, 2015:1–16, 2015. doi: 10.1155/2015/494130.

[226] Y.-L. Xu. *Wind Effects on Cable-Supported Bridges*. John Wiley and Sons, 2013. doi: 10.1002/9781118188293.

[227] S. C. Yen and J. H. Liu. Wake flow behind two side-by-side square cylinders. *International Journal of Heat and Fluid Flow*, 32(1):41–51, Feb. 2011. doi: 10.1016/j.ijheatfluidflow.2010.09.005.

[228] D.-H. Yoon, K.-S. Yang, and C.-B. Choi. Flow past a square cylinder with an angle of incidence. *Physics of Fluids*, 22(4):043603, Apr. 2010. doi: 10.1063/1.3388857.

[229] D.-H. Yoon, K.-S. Yang, and C.-B. Choi. Three-dimensional wake structures and aerodynamic coefficients for flow past an inclined square cylinder. *Journal of Wind Engineering and Industrial Aerodynamics*, 101:34–42, Feb. 2012. doi: 10.1016/j.jweia.2011.10.012.

[230] H. Yu, B. Wang, Y. Li, and M. Zhang. Driving risk of road vehicle shielded by bridge tower under strong crosswind. *Natural Hazards*, 96(1):497–519, 2019. ISSN 15730840. doi: 10.1007/s11069-018-3554-y.

[231] J. Zhang, J. Wang, X. Tan, G. Gao, and X. Xiong. Detached eddy simulation of flow characteristics around railway embankments and the layout of anemometers. *Journal of Wind Engineering and Industrial Aerodynamics*, 193:103968, Oct. 2019. doi: 10.1016/j.jweia.2019.103968.

[232] Q. Zhang, C. Su, Y. Zhou, C. Zhang, J. Ding, and Y. Wang. Numerical investigation on handling stability of a heavy tractor semi-trailer under crosswind. *Applied Sciences*, 10(11):3672, May 2020. doi: 10.3390/app10113672.

[233] W. Zhang, C. S. Cai, F. Pan, and Y. Zhang. Fatigue life estimation of existing bridges under vehicle and non-stationary hurricane wind. *Journal of Wind Engineering & Industrial Aerodynamics*, 133:135–45, Oct. 2014. ISSN 0167-6105. doi: 10.1016/j.jweia.2014.06.008.

[234] X. Zhang and C. Proppe. The influence of strong crosswinds on safety of different types of road vehicles. *Meccanica*, 54(9):1489–1497, Jan. 2019. doi: 10.1007/s11012-019-00952-1.

[235] X. Zhang and C. Proppe. Risk assessment of road vehicles under wind gust excitation. *Journal of Computational and Nonlinear Dynamics*, 15(10), Aug. 2020. doi: 10.1115/1.4047638.

[236] Q. Zhou and L. D. Zhu. Numerical and experimental study on wind environment at near tower region of a bridge deck. *Heliyon*, 6(5):e03902, 2020. ISSN 2405-8440.

[237] Y. Zhou and S. Chen. Fully coupled driving safety analysis of moving traffic on long-span bridges subjected to crosswind. *Journal of Wind Engineering and Industrial Aerodynamics*, 143:1–18, 2015. ISSN 01676105. doi: 10.1016/j.jweia.2015.04.015.

[238] Y. Zhou and S. Chen. Vehicle ride comfort analysis with whole-body vibration on long-span bridges subjected to crosswind. *Journal of Wind Engineering and Industrial Aerodynamics*, 155:126–140, 2016. ISSN 01676105. doi: 10.1016/j.jweia.2016.05.001.

[239] Y. Zhou and L. Sun. Effects of high winds on a long-span sea-crossing bridge based on structural health monitoring. *Journal of Wind Engineering and Industrial Aerodynamics*, 174:260–268, 2018. ISSN 0167-6105.

[240] Y. Zhou, Z. Wang, Y. Qian, H. Yang, and Y. Wei. Numerical simulation of the flow around two square cylinders using the lattice boltzmann method. *Physics of Fluids*, 33(3):037110, Mar. 2021. doi: 10.1063/5.0040020.

[241] J. Zhu and W. Zhang. Probabilistic fatigue damage assessment of coastal slender bridges under coupled dynamic loads. *Engineering Structures*, 166: 274–85, July 2018. ISSN 0141-0296. doi: 10.1016/j.engstruct.2018.03.073.

[242] J. Zhu, W. Zhang, and M. X. Wu. Evaluation of Ride Comfort and Driving Safety for Moving Vehicles on Slender Coastal Bridges. *Journal of Vibration and Acoustics*, 140(5), Oct. 2018. ISSN 1048-9002. doi: 10.1115/1.4039569.

[243] L. Zhu, L. Li, Y. Xu, and Q. Zhu. Wind tunnel investigations of aerodynamic coefficients of road vehicles on bridge deck. *Journal of Fluids and Structures*, 30:35–50, Apr. 2012. doi: 10.1016/j.jfluidstructs.2011.09.002.

Symbols

$\mathbf{A}$	state matrix
A_f	projected vehicle body area (front)
A_{gust}	gust amplitude
A_i	acceleration, $i = [x, y, z]$
α	angle of incidence of wind on bridge towers where $\alpha = 0$ corresponds to wind perpendicular to girder (see Figure 13.1 or 14.1)
α_1	side-slip angle of front tyres
α_2	side-slip angle of rear tyres (same as α_r for a non-steered rear axle)
α_f	side-slip angle of front axle
α_r	side-slip angle of rear axle
AR	aspect ratio (of tower cross-section), note different definitions used in Chapters 13 and 14
A_s	projected vehicle body area (side)
$\mathbf{B}$	input matrix
$b5$	indicates signal has been filtered with a low-pass Butterworth filter with a cut-off frequency of 5Hz
β	angle of incidence of in-plane wind vector relative to vehicle (as would be measured by a stationary anemometer), see Figure 1.2
$\mathbf{C}$	output matrix
C_f	front-axle cornering stiffness
C_i	aerodynamic force coefficient, $i = [S, L, D, Y, P, R]$, see Section 1.1.1
C_r	rear-axle cornering stiffness
D	a characteristic length dimension
δ	steering angle (of wheels, not steering wheel)
D_{gust}	spatial period of gust (typically taken from plot on X_b-axis)
$\mathbf{D}$	feed-through matrix
Δt_G	time taken to drive through a gust

Δt_{l_b}	time taken to drive length of vehicle body
E	an earth-fixed reference frame (X-Y-Z) (defined with an origin at the centre of each bridge using the ENU convention), see Figure 1.6
f	frequency (sometimes used to denote a function)
F_1	lateral tyre force (front axle), see Figure A.1
F_2	lateral tyre force (rear axle), see Figure A.1
F_i	aerodynamic force, $i = [S, L, D, Y, P, R]$, see Section 1.1.1
$F_{y,max}$	maximum achievable lateral tyre force
$F_{y,i}$	lateral tyre reaction force ($i = [r, l]$), see Figure 1.3
$F_{z,i}$	vertical tyre reaction force ($i = [r, l]$), see Figure 1.3
γ	angle of incidence of in-plane wind vector (as measured by an anemometer moving with the vehicle), see Figure 1.2
h_b	height of vehicle body (from ground)
h_{cg}	height of c.g. of vehicle (from ground), see Figure 6.3
I_{xx}	roll moment of inertia (vehicle)
I_{zz}	yaw moment of inertia (vehicle)
k_f	reduced frequency
l_b	length of vehicle body
l_{cp}	longitudinal distance forward from c.g. to centre of pressure (vehicle)
l_f	longitudinal distance from c.g. to front axle
l_{nsp}	longitudinal distance rearward from c.g. to neutral steer point (vehicle)
l_r	longitudinal distance from c.g. to rear axle
l_{wb}	wheel base
m	mass (vehicle)
m_f	proportion of vehicle mass carried by the front axle
M_i	aerodynamic moment, $i = [S, L, D, Y, P, R]$, see Section 1.1.1
m_r	proportion of vehicle mass carried by the rear axle
μ	friction coefficient
ν	kinematic viscosity (of air)
ω_0	natural frequency
ω_i	rotation rate, $i = [x, y, z]$
ω_n	damped natural frequency
P	distance between paired cylinder cross-sections (see Figure 14.1)
P_{CT}	comfort indicator developed for passengers on trains on transition curves [6]
ϕ	angle of incidence of in-plane wind vector relative to bridge (polar on X''-Y'')

Ψ	wind heading in earth-fixed reference frame
Ψ_h	yaw attitude of vehicle body in E-system (from antenna A–rear to B–front), see Figure A.3
Ψ_t	heading over ground of rear antenna A in E-system, see Figure A.3
$\mathbf{r_A}$	vector from IMU to GNSS antenna A (rear), see Figure 6.5
$\mathbf{r_B}$	vector from IMU to GNSS antenna B (front), see Figure 6.5
$\mathbf{r_{cg}}$	vector from IMU to c.g., see Figure 6.5
Re	Reynold's number
ρ	density (of air)
$\mathbf{r_{wm}}$	vector from IMU to anemometer (point of measurement), see Figure 6.5
s	normalised position along curvilinear path (values between 0 and 1), see T
S	a vehicle-fixed coordinate system (x'-y'-z', fixed to IMU), see Figure 1.6
St	Strouhal number
T	an axis that follows the road (distance travelled along its curvilinear)
t	time
θ_y	pitch attitude/angle (vehicle)
u	wind component along vehicle x' (S-frame)
U	a vehicle-fixed coordinate system (x-y-z), see Figure 1.6, sometimes refers to a characteristic wind speed
U_a	accident wind speed
u_r	wind component parallel with North pole on anemometer (see Figure 14.4)
U_{ref}	component of reference wind along bridge axis (stationary observer)
u^*	normalised wind speed (by reference value of wind speed)
v	wind component along vehicle y' (S-frame)
$v_{b,0}$	fundamental value of the basic wind velocity [2]
V_c	critical driving velocity (instability for oversteered vehicles)
V_{cr}	cruise control speed
$\mathbf{v}_f$	vector velocity of front axle, see Figure A.1
V_r	mangitude of in-plane wind vector (as measured by an anemometer moving with the vehicle), see Figure 1.2
$\mathbf{v}_r$	vector velocity of rear axle, see Figure A.1
v_r	wind component perpendicular with North pole on anemometer (see Figure 14.4)

V_{ref}	component of reference wind perpendicular to bridge axis (stationary observer)
V_w	mangitude of in-plane wind vector (as would be measured by a stationary anemometer), see Figure 1.2
V_y	lateral velocity (vehicle), see Figure A.1
w_b	track width
w_t	width of vehicle body (without side mirrors)
x^*-y^*	normalised coordinates (by D) with $-y^*$ aligned with mean wind vector
X_b-Y_b	the E-system rotated about Z such that X is aligned with the driving direction in the windward lane
X''-Y''	alternative earth-fixed coordinates with $-Y''$ aligned with the mean wind vector and the origin at the centre-point of the respective tower cross-section
y^*_Δ	perpendicular distance from wind profile measurement line (in driving lane) to centre of cross section of windward tower
ζ	damping ratio

Acronyms & Abbreviations

ABL Atmospheric Boundary Layer

CAD Computer Aided Design

CF Compact Flash

CFD Computational Fluid Dynamics

CG Center of Gravity

DGNSS Differential GNSS

DLC Double Lane Change

DTM Digital Terrain Model

ECEF Earth-centered, Earth-fixed

ENU East-north-up

ESA European Space Agency

FFT Fast Fourier Transform

GNSS Global Navigation Satellite System

GPS Global Positioning System

GUI Graphical User Interface

IMU Inertial Measurement Unit

KF Kalman filter

LPV Linear Parameter-varying

MSD Mean Standard Deviation

NPRA Norwegian Public Roads Administration (Statens Vegvesen, SVV)

NTNU Norges Teknisk-Naturvitenskaplige Universitet (Norwegian University of Science and Technology)

PC Personal Computer

PDF Probability Density Function

PIV Particle Image Velocimetry

PSD Power Spectral Density

RMS Root Mean Square

RTK Real Time Kinematic

VW Volkswagen

Appendix A

Updating a vehicle handling model

A set of controlled manoeuvres were performed to provide data sets for the calibration and validation of the model. These tests are presented along with a calibration of the model parameters and a discussion on validation.

A.1 Single track model

A single track model describes the handling dynamics of a vehicle; the in-plane translation and rotation of the vehicle body in response to steering input. The reference plane in this work will be the ground-plane of the ENU systems of one of the test sites.

As can be seen in Figure A.1 the full three-dimensional mass distribution of the vehicle body, the kinematics of its suspension and location of its wheels is reduced to a two-dimensional bicycle representation. The model consists of a single lumped mass m with yaw moment of inertia I_{zz} and a single wheel representing the lumped cornering characteristics of all the wheels on each axle. The test vehicle has two axles with two wheels each. These are represented in the model by one steered wheel at the front and one non-steered wheel at the rear.

Borrowing notation from Pacejka [153], the magnitude of the lateral tyre forces at the front and rear are denoted F_1 and F_2 respectively and are, in this simplified model, a known function of the side-slip angles α_1 and α_2. The side-slip angle is defined as the difference between the orientation of the tyre and its direction of travel (defined by velocity vectors $\mathbf{v}_r$ and $\mathbf{v}_f$). At the front, the side-slip angle of the tyre α_1 differs from the side-slip at the front axle location α_f due to the steering angle δ.

The velocities V_x and V_y are the components of the velocity vector of the vehicle

at the CG, while ω_z is the yaw rate and A_y the acceleration that would be measured by an IMU placed at the CG. In this chapter, no external loads are considered to be acting on the vehicle.

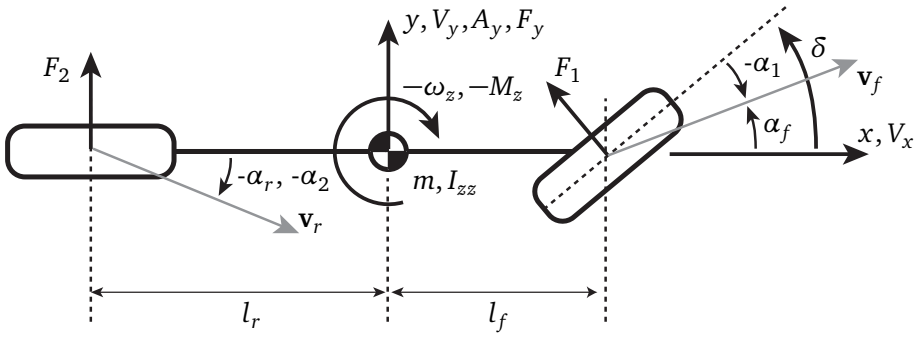

Figure A.1: A single-track model of vehicle handling dynamics.

Tyre models

A model of the lateral tyre forces F_i is needed before the equations of motion are introduced. There are numerous tyre models and the lateral force is really a function of more than just the side-slip angle. For a succinct introductory discussion to tyre modelling see §2.5 in [153]. The following chapters go on to discuss multiple tyre models in depth.

The tyre model used here will be a function of the side-slip angle only and will consider only the lateral force generated by the tyre and not any other forces or moments. For a given vertical wheel load, the lateral force F_i can be plotted against $-\alpha_i$ to give a curve with a positive slope in the upper, right quadrant of the Cartesian plane. This will be seen later. For the majority of real tyres and tyre models, the slope is constant for small values of $-\alpha_i$. The constant slope is often termed the cornering stiffness and is denoted C_i.

Note that the cornering stiffness used here will be specific to the single-track representation of the vehicle and is an equivalent stiffness for the lumped cornering characteristics of all the wheels on a given axle. This parameter will not be the same as the one that would be measured by a dedicated laboratory test on a single wheel/tyre.

Equations of motion

The equations of motion of the system can be written in state-space form with the states V_y and ω_z [10, 153],

$$\begin{bmatrix} \dot{V}_y \\ \dot{\omega_z} \end{bmatrix} = \begin{bmatrix} \frac{-(C_f+C_r)}{mV_x} & \frac{mV_x^2+C_r l_r-C_f l_f}{mV_x} \\ \frac{C_r l_r-C_f l_f}{I_{zz}V_x} & \frac{-(C_r l_r^2+C_f l_f^2)}{I_{zz}V_x} \end{bmatrix} \begin{bmatrix} V_y \\ \omega_z \end{bmatrix} + \begin{bmatrix} \frac{C_f}{m} \\ \frac{C_f l_f}{I_{zz}} \end{bmatrix} \begin{bmatrix} \delta \end{bmatrix}. \tag{A.1}$$

This is a version of the single-track model that does not model the longitudinal dynamics of the the vehicle. V_x is not a state, yet a parameter of $\mathbf{A}$. The system is therefore linear parameter-varying LPV and can be written [173],

$$\dot{\mathbf{x}} = \mathbf{A}(V_x)\,\mathbf{x} + \mathbf{B}\mathbf{u}, \tag{A.2}$$

where $\mathbf{x} = [V_y, \omega_z]^T$ and $\mathbf{u} = \delta$.

A.2 Calibration data

For the purposes of calibrating and validating the single-track model, a series of controlled manoeuvres were performed at Værnes International Airport in Stjørdal, Norway on two separate occasions; 19.06.20 and 01.07.20. The tests are summarised in Tables A.1 and A.2. Details of the manoeuvres are given in appendix A.3. All manoeuvres were performed using a human driver. Note that the ramp steer manoeuvres were repeated in the second session to improve the quality of the input signal (test 6).

A satellite image of the airport can be seen in Figure A.2 where the arenas for the tests have been highlighted. The ramp steer manoeuvres (tests 1,6) were performed on the rapid-exit taxiway, the step steer and frequency sweep (2,3) on the runway while the slalom and double lane change (4,5) tests took place at the base location.

Vector translation

An estimate of the velocity at the CG is needed from the VBOX system. This will allow comparison between the model and real-world measurements. V_y is one of the states of the single track model and the state matrix is linear parameter-varying on V_x. The side-slip angles at the front and rear (α_f and α_r) are also useful in that they can be used to estimate the cornering stiffness parameter of the linear tyre model.

The VBOX outputs two angles measured clockwise from North, Ψ_h and Ψ_t as can be seen in Figure A.3. The first value Ψ_h is the heading of the vehicle; the

Figure A.2: Test locations at Værnes aiport. (aerial images – © norgeskart.no)

Test ID	Description	Subtest ID	Specification
1	Ramp Steer	A	60 kph
		B	80 kph
2	Step Steer	A	60 kph
		B	80 kph
3	Frequency Sweep	A	60 kph
		B	80 kph
4	Slalom	A	60 kph
		B	80 kph
5	Double Lane Change	A	60 kph
		B	80 kph

Table A.1: Manoeuvres performed 19.06.20.

Test ID	Description	Subtest ID	Specification
6	Ramp Steer	A	60 kph
		B	80 kph

Table A.2: Manoeuvres performed 01.07.20.

angle from North of the vector $\mathbf{r}_{AB}^{E}$ projected onto the reference ellipsoid. The E superscript indicates that the vector references the earth-fixed coordinate system. The angle is derived using data from both antennae A and B. The second value Ψ_t is the angle from North of the vector $\mathbf{v}_{A}^{E}$ projected onto the reference ellipsoid. This is the *course over ground* or track velocity vector of the rear antenna A.

The vector $\mathbf{v}_{A}^{S}$ can be approximated using the difference $\Psi_t - \Psi_h$, the in-plane magnitude of $\mathbf{v}_{A}^{E}$ and the its vertical component (all given by the VBOX's GNSS engine). $\mathbf{v}_{A}^{S}$ is the velocity at A in the S reference frame. Note that the angle created by the vertical difference in position between A and B (pitch) has not been considered and so the vector is only an approximation.

By defining $\boldsymbol{\omega}_{\text{IMU}}^{S} = [\omega_{x'}, \omega_{y'}, \omega_{z'}]^T$, the velocity at the IMU can be related to that at antenna A,

$$\mathbf{v}_{A}^{S} = \mathbf{v}_{\text{IMU}}^{S} + \boldsymbol{\omega}_{\text{IMU}}^{S} \times \mathbf{r}_{A}^{S}. \tag{A.3}$$

Using this relation, the vehicle velocity at ground for the front and rear axles can be derived,

$$\mathbf{v}_{f}^{S} = \mathbf{v}_{\text{IMU}}^{S} + \boldsymbol{\omega}_{\text{IMU}}^{S} \times \mathbf{r}_{f}^{S}, \tag{A.4}$$

$$\mathbf{v}_{r}^{S} = \mathbf{v}_{\text{IMU}}^{S} + \boldsymbol{\omega}_{\text{IMU}}^{S} \times \mathbf{r}_{r}^{S}. \tag{A.5}$$

It is assumed that the IMU location and the CG location are the same and that the vectors $\mathbf{r}_{A}^{S}$, $\mathbf{r}_{f}^{S}$ and $\mathbf{r}_{r}^{S}$ remain constant. The body/structure of the vehicle between the IMU and the rear GNSS antenna is therefore assumed to be perfectly stiff. The centre-points on the axles are not expected to move significantly in relation to the CG in the U frame and the rotations of the body S in relation to the U frame are assumed to be small.

A.3 Test descriptions

Six manoeuvres were performed with the VW Crafter and the full data acquisition system installed. All available channels were recorded using the VBOX Test Suite software supplied with the equipment from the manufacturer. The tests are described here.

1. Ramp steer: The vehicle is brought up to a given speed. This speed is to be held constant throughout the manoeuvre. A slight steering angle is then applied by the driver and is slowly increased up to a prescribed value of steering angle or lateral acceleration is achieved. It is desirable to increase the steering angle slowly and steadily such that an assumption of stationary driving is valid. It is also desirable to increase the lateral acceleration to a level whereby the non-linear properties of the tyre become apparent.

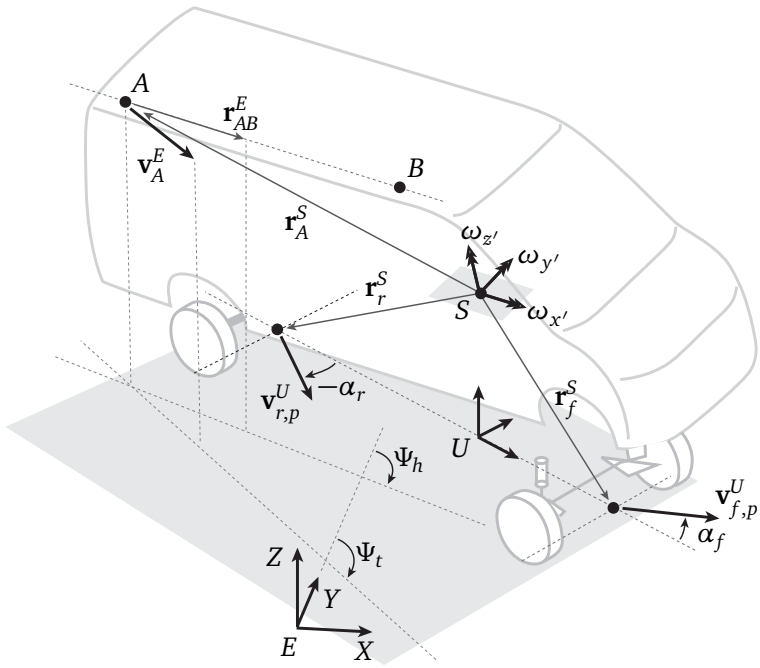

Figure A.3: Translating GNSS data to give side-slip estimates at the front and rear axles.

2. Step steer: The vehicle is brought up to a given speed. This speed it to be held constant for as long as possible after a sudden step input in steering angle is applied. The steering angle (or size of the step) is decided beforehand. The roll dynamics are of particular interest and it is desirable to create an input signal that most closely resembles a step function.

3. Frequency sweep: The vehicle is brought up to a given speed. This speed is to be held as constant as possible as the driver inputs a sinusoidal input of a fixed amplitude. The frequency of the sinusoid is varied. It is preferable to create a sinusoidal input as closely as possible.

4. Slalom: The vehicle is brought up to a given speed. The vehicle is then driven through the track as described in Figure A.4 without using the accelerator or brake pedals.

5. Double Lane Change: The vehicle is brought up to a given speed. The vehicle is then driven through the track as described in Figure A.5 without using the accelerator or brake pedals.

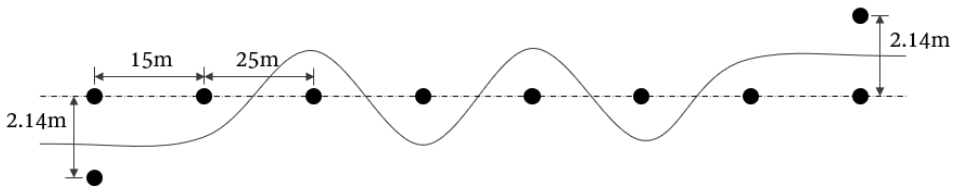

Figure A.4: Diagram of cone set-up for slalom manoeuvre.

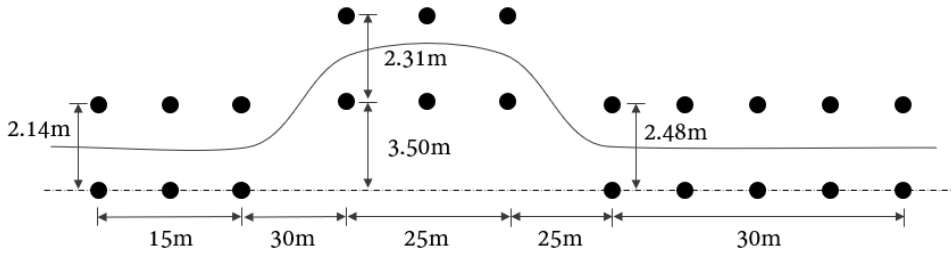

Figure A.5: Diagram of cone set-up for double lane change manoeuvre.

A.4 Cornering stiffness

The ramp steer manoeuvre can be used to plot the cornering characteristics at the front and rear axles. The steering wheel angle δ_{sw} – and consequently the lateral acceleration A_y and yaw rate ω_z – are increased at a very slow rate whilst maintaining a constant longitudinal speed V_x. Assuming that the vehicle is in steady-state motion ($\dot{V}_y \to 0$, $\dot{\omega}_z \to 0$), the force and moment balance from Figure A.1 gives F_1 and F_2,

$$\begin{aligned} F_1 &= \frac{m_f \omega_z V_x}{\cos\delta} \\ F_2 &= m_r \omega_z V_x, \end{aligned} \tag{A.6}$$

where $m_f = ml_r/l$ and $m_r = ml_f/l$ are the known vertical axle loads at the front and rear respectively. The yaw rate is measured by the IMU, the speed by GNSS and the steering angle by the string-pot/potential divider at the steering column.

A typical time series from test 6B, the ramp steer manoeuvre at 80 kph can be seen in Figure A.6. Values of $-\alpha_1$ and $-\alpha_2$ can be estimated for each data point in the time series using the method described in Section A.2 along with values of F_1 and F_2 estimated by Equation A.6. The plot of F_i vs. $-\alpha_i$ should reveal a linear relationship that can be used to estimate C_i; see Figure A.7.

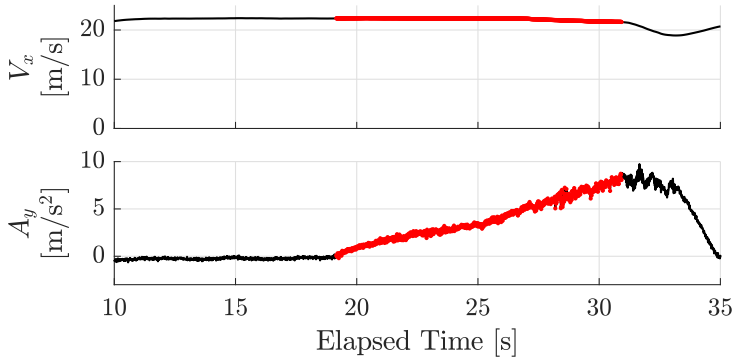

Figure A.6: Typical time series for the ramp steer manoeuvre. Data points included in the cornering characteristic curves are highlighted in red.

The force estimates Equation A.6 are only valid under the steady-state assumption and so only a subset of the data is used for the linear regression. As indicated by the highlighted data points in Figure A.6, this subset is from the time period in which there is non-zero A_y and roughly constant V_x.

Figure A.7 shows each axles cornering characteristics (side force versus slip angle). As expected, the high-velocity data extends to higher forces and side-slip angles. At the rear it even appears to extend beyond the linear operating range of

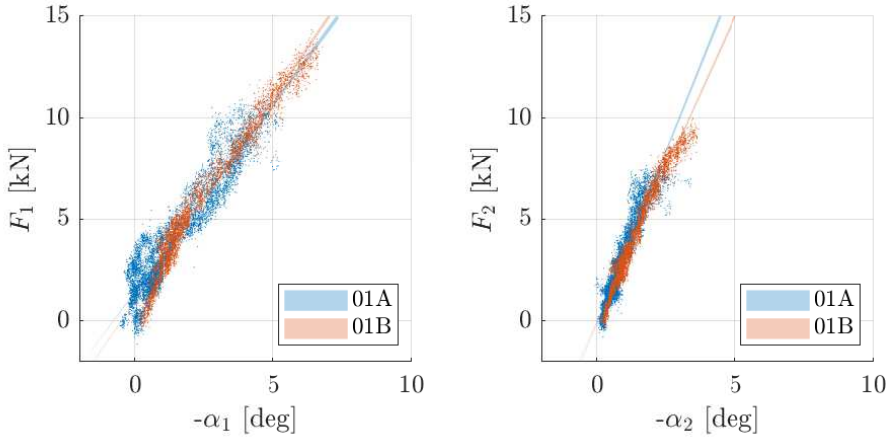

(a) Front (b) Rear

Figure A.7: Cornering characteristic curves at the front and rear axles. Data from all repetitions are plotted. Shaded patches give the 95% confidence interval for the linear regressions.

the tyres. This can be observed in Figure A.7b, where the red dots appear to start following a concave curve at the top of the linear range. The same cannot be said to occur at the front, even though the side-slip angles extend to higher values. It might be that the linear operating range of the tyres at the front is wider due to the higher vertical load.

The higher vertical load should also, according to laboratory tests (see Figure 1.3 in [153]), lead to a higher cornering stiffness. On the contrary, it is clear to see that the slope in Figure A.7a is lower than that in Figure A.7b. The lower slope could be the result of effects such as steering compliance, load transfer or other effective force and moment changes resulting from the kinematics of the suspension. See Chapter 1 of [153] for a thorough explanation of these mechanisms and their influence on the effective cornering characteristics of an axle compared to an individual tyre. Equally to the steering compliance at the front, there could be kinematics at the rear that cause non-zero effective steering angles there as well.

There could be discrepancies in the measurement signals as well. For example, the lateral acceleration signal may be affected by the roll attitude of the vehicle. At non-zero roll attitude, the gravity vector will have a component in the y direction of the IMU. Methods to compensate for the gravity vector should be investigated in future studies. Here, the cornering stiffness estimates will be used as a starting point for a model calibration/updating procedure.

A.5 Model calibration

Using the initial values of C_i estimated by the linear regression above, the system equations Equation A.2 can be solved using Simulink with an automatically selected variable time step solver and a parameter-varying state matrix on V_x. The longitudinal velocity V_x used in the simulation is derived from GNSS data using the methods presented above (Figure A.3) and the steering angle δ is the one estimated by measurements taken at the steering column.

A comparison between the measured and modelled data can be seen in Figure A.8. The two subplots present a selection of time series for one execution of the slalom manoeuvre at the two speeds of 60 and 80 kph. At a glance, there is very good agreement between model and measurement, especially in the yaw rate ω_z and lateral acceleration A_y signals. At the higher speed there is more significant disagreement in the lateral velocity V_y.

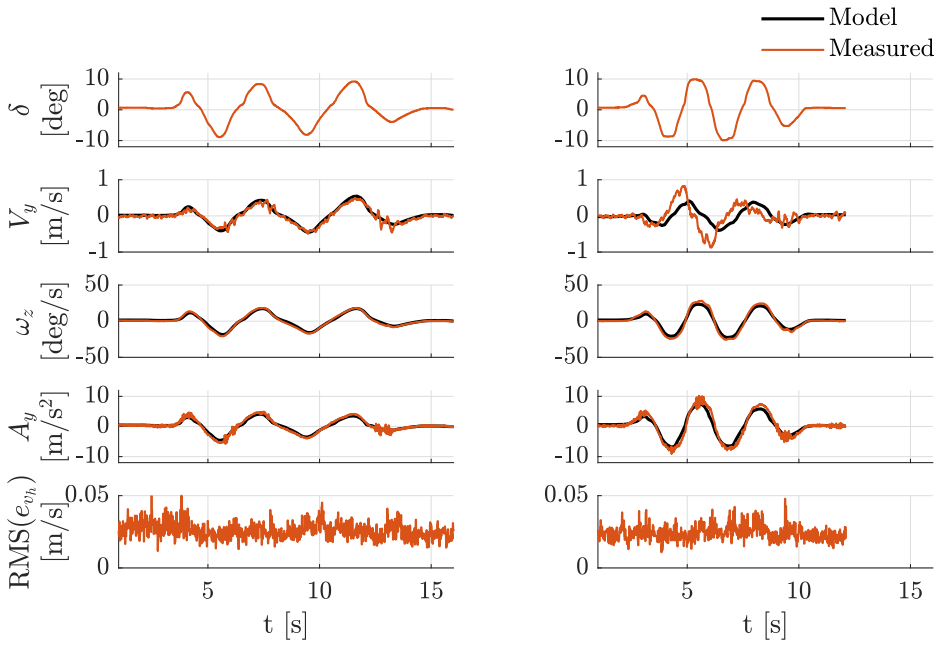

(a) 60 kph, 4A-01

(b) 80 kph, 4B-01

Figure A.8: Comparisons of model and measurements during the slalom manoeuvre.

The last set of axes in each plot shows the RMS of the error as estimated by the VBOX GNSS engine e_{V_y}. There is no apparent increase in this error estimate in the time period in which there is disagreement between modelled and measured

V_y (at 80 kph, see Figure A.8b). This indicates that the issue lies with the model and not errors in the measured signal.

Figure A.9a shows the difference Δ = (Measured) − (Model) for the signals plotted in Figure A.8. A spatial variable X (East) is used along the x axis of the plots for easier comparison between the two driving speeds. Once again, it is clear that the model is more successful at predicting the handling behaviour at the lower speed. At the higher speed, where the Δ signals reach larger values, the disparity appears to grow in tact with the steering input. This is suggestive of a systematic error in the model.

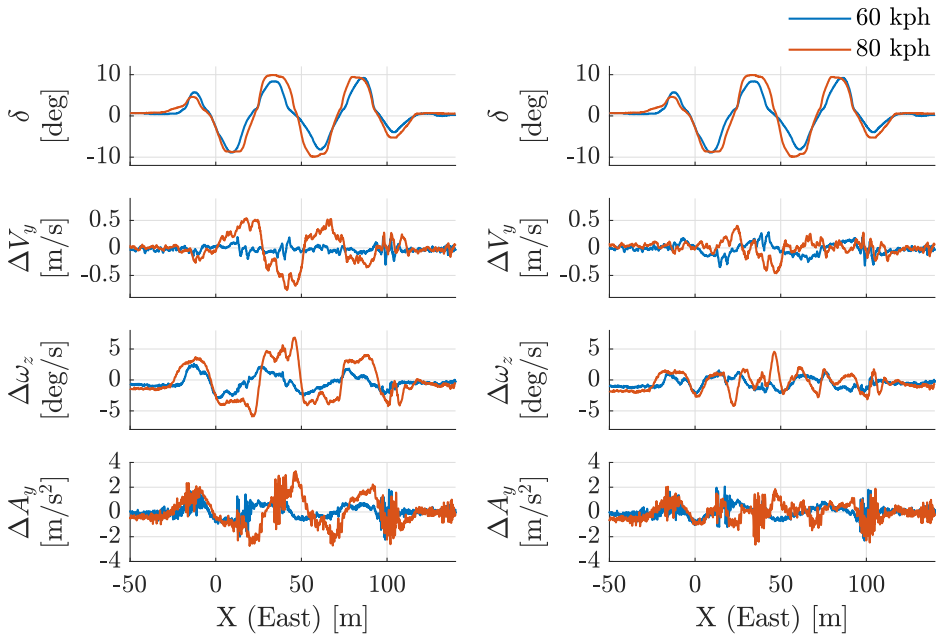

(a) Ramp Steer Estimates

(b) Brute Force Optimised Estimates

Figure A.9: Comparisons of pre- and post-optimised values of cornering stiffness for tests 4A-01 and 4B-01.

Parameter updating

The single track model is simple and is founded on multiple assumptions and simplifications. To overcome this it is possible to update some of the parameters. The updated parameters adjust for complexities that are not captured by the model. For example, at high lateral accelerations it might be that the side-slip at one of the axles extends beyond the linear operating range of the tyres. Updating the

cornering stiffness to a lower value could improve the accuracy of the simulations.

The parameters of the single track model include those related to the mass distribution of the vehicle, m, I_{zz}, l_f and l_r and the cornering characteristics of the axles C_f and C_r. As discussed above, there is uncertainty in the steering estimate (steering column vs. true wheel angle). This could be compensated for by adjusting the values of cornering stiffness. It might be necessary to adjust the inertial parameters as well to achieve an optimal result.

Optimisation problem

An optimisation problem can be defined to seek optimal values of l_f, l_r, C_f and C_r. There is only one distinct value of l_r for any value of l_f and so there are three design variables.

Looking at the differences between model and measurement shown in Figure A.9, it is logical to define a successful model as one where the three signals ΔA_y, $\Delta\omega_Z$ and ΔV_y remain as close to zero as possible. The objective function is proposed as a weighted sum of each respective variance,

$$f(x_1, x_2, x_3) = k_1 \mathrm{var}\left(\Delta A_y\right) + k_2 \mathrm{var}\left(\Delta\omega_z\right) + k_3 \mathrm{var}\left(\Delta V_y\right). \tag{A.7}$$

The weights k_1, k_2 and k_3 are chosen such that each term on the right hand side of Equation A.7 have the same absolute value for the model with the initial design variables (iteration 0). For simplicity, the weights are determined once and the same values are used in all subsequent optimisations. The data set used is the first repetition of the step steer manoeuvre performed at 80 kph (test no. 2B-01).

The design variables define the cornering stiffness parameters and position of the CG as follows,

$$C_f = x_1 C_f^0 \tag{A.8}$$

$$C_r = x_2 C_r^0 \tag{A.9}$$

$$f = x_3(l_f + l_r), \tag{A.10}$$

where the 0 superscript denotes the initial values of $C_f^0 = 95,000$ and $C_r^0 = 167,000$; rounded estimates from the linear regression of the ramp steer data.

Figure A.10 demonstrates the theory behind the optimisation algorithm. The process is iterative and starts by mapping the objective function across a coarsely discretised limitation of the design domain. The limits are chosen manually with a priori knowledge of the sensitivities of the model gained through trial-and-error. A 5×5 grid is chosen in the x_1x_2 plane along with three values of x_3.

One way to visualise this is as three surfaces, one for each value of x_3 as is shown in Figure A.10a. This plot also shows that at iteration 0, there is a clear minimum on each surface. The minimum of all three surfaces is chosen as the

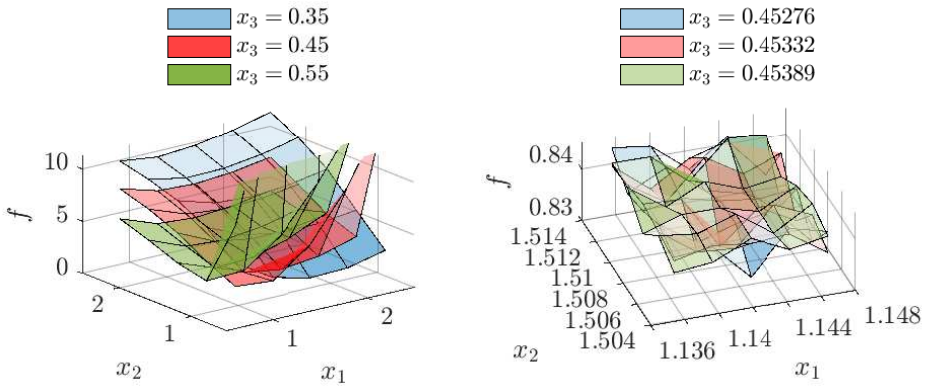

(a) Iteration 0 (b) Iteration 19

Figure A.10: The objective function surfaces at the beginning and end of an optimisation procedure using data from the step steer manoeuvre at 80 kph (2B-01).

basis for the next iteration. A new $5 \times 5 \times 3$ grid, centered at said minimum is defined. The new limits are chosen such that the range in each design variable is reduced by 25%. The method repeats until a convergence condition is met.

Figure A.10b shows the last iteration of the aforementioned optimisation procedure. The ranges in the x_1, x_2 and x_3 directions have been significantly reduced and visually, there is no longer a clear minimum. A logical convergence parameter ξ might be the distance between the current minimum $\min\left(f_{i,j,k}\right)$ and the mean value objective function for all values in the grid, $\text{mean}\left(f_{i,j,k}\right)$. This is then normalised by the mean to give,

$$\xi = \frac{\text{mean}\left(f_{i,j,k}\right) - \min\left(f_{i,j,k}\right)}{\text{mean}\left(f_{i,j,k}\right)}, \tag{A.11}$$

where $i = \{1,..,5\}$, $j = \{1,..,5\}$ and $k = \{1,2,3\}$. The iterative procedure stops when one of two conditions are met:

1. The convergence parameter has changed by less than 0.1% between all of the last 4 iterations.

2. The convergence parameter has increased between all of the last 4 iterations.

This optimisation algorithm was chosen to be as understandable and robust as possible. It presents a brute force approach to a gradient-descent method and is not particularly efficient. It is nonetheless easy to implement and insightful. Due to the simple model, it does not take more than a matter of minutes for the optimisation to

complete. Critically, it will be seen below that the optimisation method is successful in calibrating the parameters of the single track model.

In order to keep the CG from attaining unrealistic values, a constraint is placed on f to remain within 15% of the original estimate. The design space is still reduced by 25% in each iteration. There is simply an upper and lower boundary in the x_3 direction. The minimum is therefore not necessarily at the center of the proposed design domain at each iteration.

Optimisation results

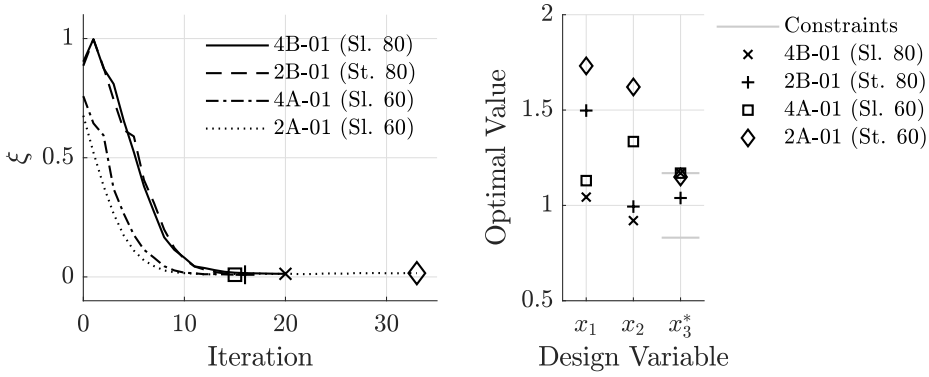

(a) Progression (b) Results

Figure A.11: An overview of 4 executions of the optimisation procedure.

Figure A.11 shows the progression and results of 4 executions of the optimisation method. The algorithm was tested with data from two different manoeuvres at two different speeds; the slalom and step steer manoeuvres at 60 and 80 kph. It is clear from Figure A.11a that the convergence parameters reached asymptotic values before the iterations were stopped.

The resulting optimal values are shown in Figure A.11b, where it is noted that x_3 has been normalised by the iteration 0 value $x_3^* = x_3/x_3^0$. Three of the executions suggest a larger value of f close to top of the 15% upper boundary. The only result that can be verified by a logical argument is 2B-01, the step steer manoeuvre at 80 kph.

There is very little change in l_f, a parameter determined with high confidence by measuring the vertical axle loads. Meanwhile, a 50% increase in C_f would make the cornering stiffness at the front and rear more similar to one another. This agrees better with expectations from theory, where the cornering stiffness is thought to be positively related to vertical tyre load.

Validation

The four sets of optimal parameters (Sl-80, St-80, Sl-60, St-60) can be tested with data sets different to those used in the optimisation. As an initial test, the remaining repetitions of the same manoeuvres (slalom and step steer) can be used for evaluation. The optimised values clearly outperformed the initial values in every case.

The optimal parameter sets were then tested using data sets from two other manoeuvres, the frequency sweep (F. Sweep) and double lane change (DLC), at the two speeds of 60 and 80 kph. Figure A.12 maps out the percentage change in the objective function for each set of optimised parameters on four different sets of axes, one for each manoeuvre. The (optimal) parameter sets used in each simulation are plotted along the horizontal axis and all repetitions of each manoeuvre have been simulated and plotted.

The data shows good agreement between repetitions. The last three parameters sets are shown to improve the models ability to replicate the real data on all new data sets. Those derived from the slalom manoeuvre at 80 kph only improve performance on the data from the frequency sweep manoeuvre at the same driving speed.

Interestingly, the parameter set that most consistently reduces the objective function across data sets and repetitions is the one derived from data set 2B-01. This is the same set of optimised parameters that was identified above as being easiest to verify using a logical argument.

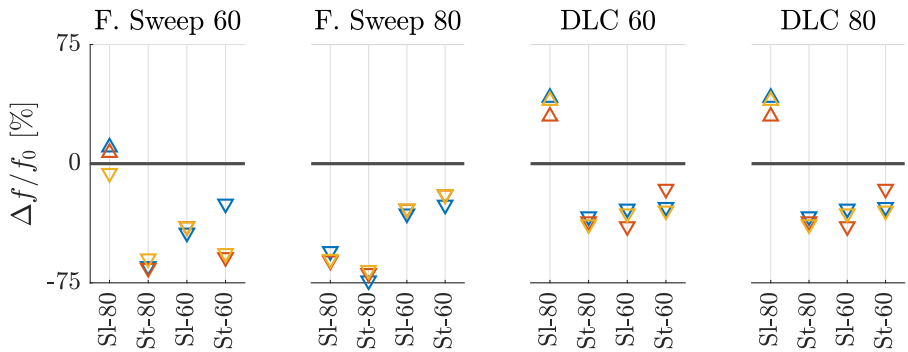

Figure A.12: A performance comparison of the optimised parameter sets.

Conclusions

The single track model is too simple to provide an equally accurate surrogate for the test vehicle in all manoeuvres and at all speeds presented here. The model

parameters can be updated on one data set and produce improved results on another. One of these optimal parameter sets has shown better consistency between manoeuvres and speeds and can be verified by a logical argument.

Making further improvements will involve additional complexities, with each additional degree of freedom or parameter requiring additional estimation, calibration and validation. In addition to this, the operating conditions the vehicle will experience on the bridge will be different to those at the test arena. The tyres will perform differently on a snow-covered road at -5° than on the runway at Værnes airport at 27-28°. This variability will not be considered in this work, but is a logical next step in future studies.

Appendix B

Variables for vehicle-bridge interaction

$$a_1 = -\frac{1}{\dot{x}_v}(K_1 + K_2), \tag{B.1}$$

$$\vec{b}_1 = \frac{1}{\dot{x}_v}\left(K_1\vec{X}^T\Big|_{x=x_1} + K_2\vec{X}^T\Big|_{x=x_2}\right), \tag{B.2}$$

$$\vec{b}_2 = \left(K_1\vec{X'}^T\Big|_{x=x_1} + K_2\vec{X'}^T\Big|_{x=x_2}\right), \tag{B.3}$$

$$a_2 = \frac{1}{\dot{x}_v}(K_2 l_2 - K_1 l_1), \tag{B.4}$$

$$a_3 = K_1 + K_2, \tag{B.5}$$

$$a_4 = K_1, \tag{B.6}$$

$$a_5 = -\frac{1}{\dot{x}_v}(K_1 l_1 - K_2 l_2), \tag{B.7}$$

$$\vec{b}_3 = \frac{1}{\dot{x}_v}\left(K_1 l_1\vec{X}^T\Big|_{x=x_1} - K_2 l_2\vec{X}^T\Big|_{x=x_2}\right), \tag{B.8}$$

$$\vec{b}_4 = \left(K_1 l_1\vec{X'}^T\Big|_{x=x_1} - K_2 l_2\vec{X'}^T\Big|_{x=x_2}\right), \tag{B.9}$$

$$a_6 = \frac{1}{\dot{x}_v}\left(K_2 l_2^2 + K_1 l_1^2\right), \tag{B.10}$$

$$a_7 = K_1 l_1 - K_2 l_2, \tag{B.11}$$

$$a_8 = K_1 l_1. \tag{B.12}$$

$$\vec{c}_1 = \frac{1}{\dot{x}_v}\left(K_f\vec{X}\Big|_{x=x_1} + K_r\vec{X}\Big|_{x=x_2}\right) \tag{B.13}$$

$$\mathbf{D}_1 = -\frac{1}{\dot{x}_v}\left(K_f\vec{X}\vec{X}^T\Big|_{x=x_1} + K_r\vec{X}\vec{X}^T\Big|_{x=x_2}\right) \tag{B.14}$$

$$\mathbf{D}_2 = -\left(K_f\vec{X}\vec{X}'^T\Big|_{x=x_1} + K_r\vec{X}\vec{X}'^T\Big|_{x=x_2}\right) \tag{B.15}$$

$$\vec{c}_2 = \frac{1}{\dot{x}_v}\left(K_f l_f\vec{X}\Big|_{x=x_1} - K_r l_r\vec{X}\Big|_{x=x_2}\right) \tag{B.16}$$

$$\vec{c}_3 = -\left(K_f\vec{X}\Big|_{x=x_1} + K_r\vec{X}\Big|_{x=x_2}\right) \tag{B.17}$$

$$\vec{c}_4 = -K_f\vec{X}\Big|_{x=x_1} \tag{B.18}$$

Appendix C

Measuring the CG height using load cells

Figure C.1: The test vehicle being backed into place on the end of an hydraulic vehicle lift. Each of the rear wheels was resting on a load cell when measurements of rear axle weight and angle were taken to estimate the height of the CG. (Photo: NTNU/Sebastian Reymert)

Appendix D

CAD model

Figure D.1: The scanning process involves the placement of many randomly placed reference markers on the surfaces that are to be scanned. (Photo: NTNU/Sebastian Reymert)

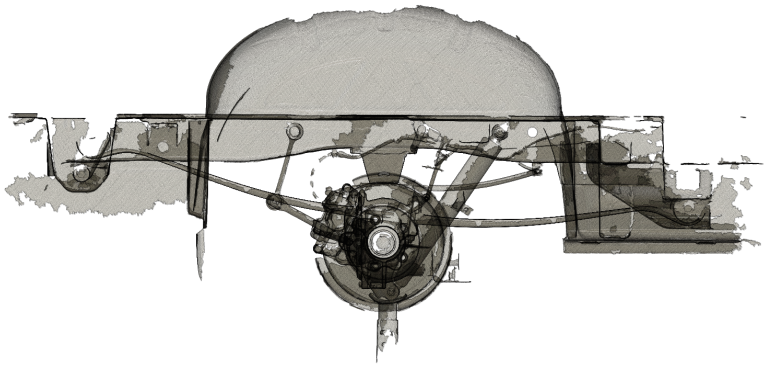

Figure D.2: The scanner and the accompanying software produces a point cloud from which a 3D mesh has been generated. Shown here is the mesh generated to represent the geometry of the rear right undercarriage. (Image: NTNU/Sebastian Reymert)

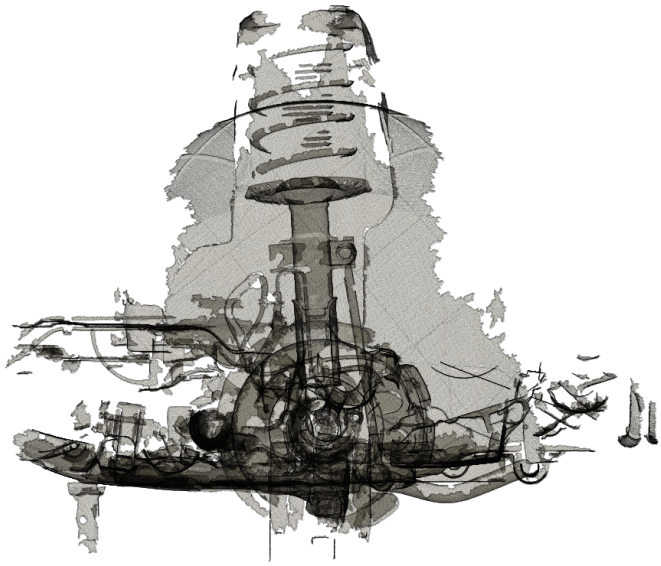

Figure D.3: The mesh of the front right suspension. (Image: NTNU/Sebastian Reymert)

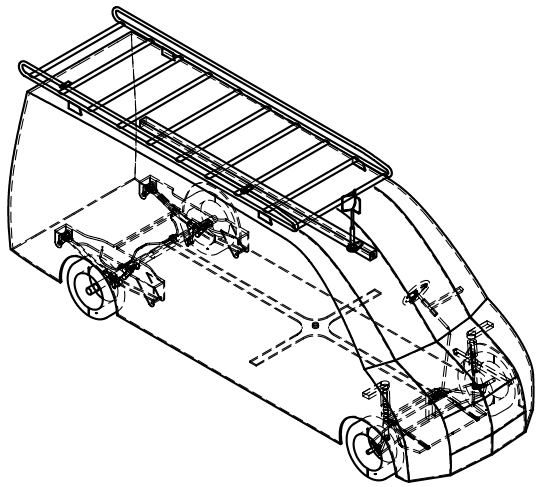

Figure D.4: A drawing of the vehicle model generated from the CAD file in Fusion 360. The geometry has been created as simply as possible with particular focus on making component geometries easy to assemble into a multi-body model with correct kinematics.

Appendix E

Handling GNSS position errors

Some examples of typical GNSS position errors will be shown first to demonstrate to motivate the use of snapping, smoothing, interpolation and extrapolation to correct errors in the GNSS data.

Typical GNSS Position Errors

Two types of error can be observed in the raw GNSS data; disturbances and dropouts. In the first type, the position signals (latitude, longitude and height) often present with spurious step-like features followed by small-scale oscillations. Figure E.1 shows an example of this in proximity to the tower of a suspension bridge.

In the second type, the GNSS system loses it's connection to all satellites. An example is shown in Figure E.2 with data from the Dovre mountain pass. The dropout is seen in the same location during each passage on one side/lane/direction of the road. A 4G cellular mast is located nearby.

Figure E.3 shows a situation where we see a combination of disturbances and a complete dropout. This is seen where the vehicle enters or exits a tunnel. The loss of signal is almost always accompanied by a period of disturbance.

The Need for Corrections

Later in this work, we will make use of the ability to plot wind and vehicle-driver response signals as a function of a spatial coordinate rather than time. It is desirable to correct disturbances and fill in dropouts to make these plots as accurate, insightful and illustrative as possible. In some cases, it is useful to refer to the vehicle's position along the centreline of the road rather than its absolute position in X-Y.

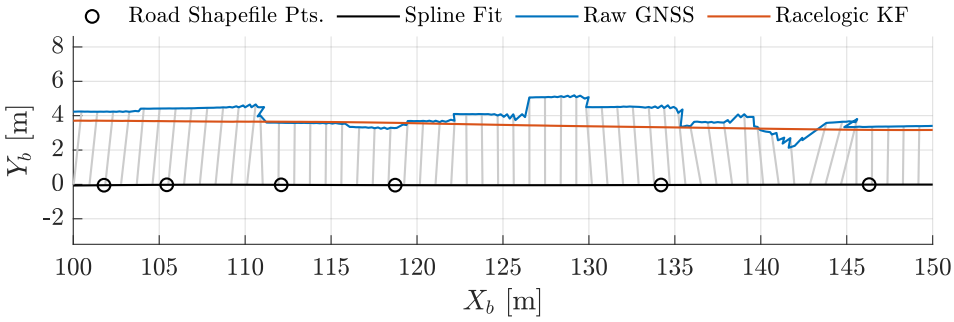

Figure E.1: Disturbances in the raw GNSS position signals.

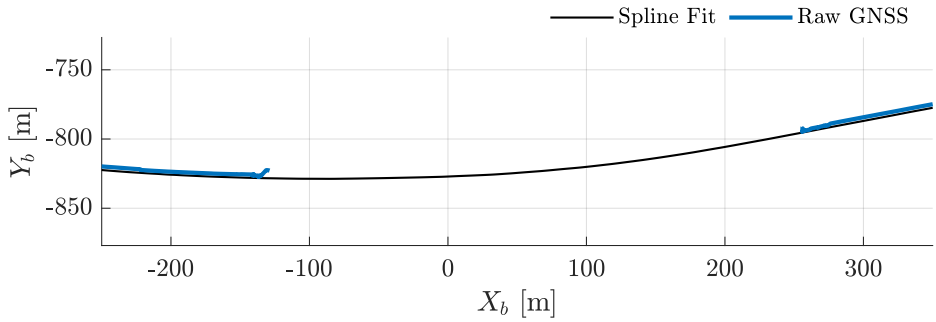

Figure E.2: An example of GNSS dropout on the Dovre mountain pass.

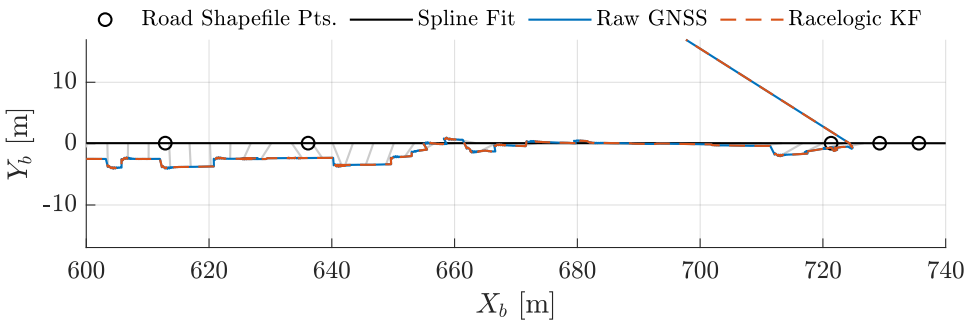

Figure E.3: An example of a GNSS position signal upon entry to a tunnel on the Hardanger bridge.

Choosing a Correction Method

One alternative for correcting disturbances and dropouts has been implemented by Racelogic (the VBOX manufacturer). The VBOX has been programmed with a Kalman filter (KF) that fuses GNSS and IMU data to smooth position signals and fill in dropouts. Figure E.1 shows how the aforementioned disturbances have been dealt with by the KF. On the other hand, Figure E.4 gives an example where the KF has failed to deliver a smooth signal. The raw signal is smooth – as we expect of the vehicle's motion – and so there is little reason to believe the cause of this step discontinuity is physical.

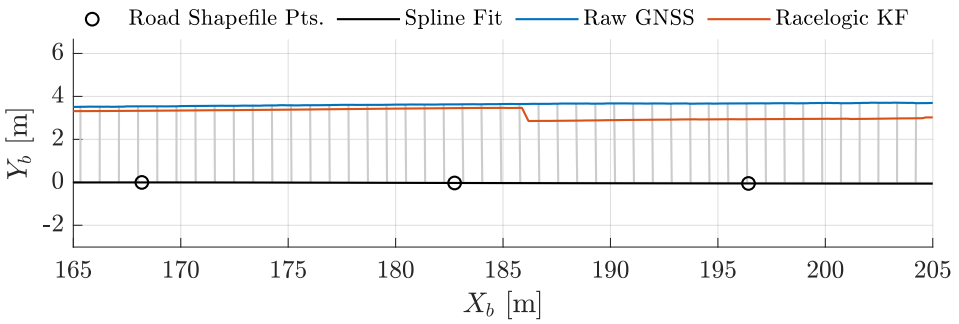

Figure E.4: Disturbances in the Racelogic Kalman-filtered GNSS position signals.

In Figure E.3, the raw and KF signals are the same because the filter failed to initialise. This data was collected at the Hardanger bridge, a bridge which runs between two tunnels that penetrate each respective side of a deep fjord. Clearly, the time spent in the open, on the bridge span, was not sufficient to allow for initialisation of the filter. The failure to initialise has been confirmed by interpreting the KF status code; a channel available on the VBOX system.

The strength of the KF is that it is a model-based method that has a clear physical interpretation. Unfortunately, the model is not available to the user, nor is Racelogic willing to share any other details of the filter [85]. The performance is generally good, though discontinuities still appear. A disadvantage in this case is that the KF does not always initialise and therefore cannot be relied upon across all data sets.

One option in the current work would be to develop an in-house, offline KF. It could be made specifically for the purpose of profiling the wind and vehicle-driver response on the bridge. This was not completed for this work, but will be considered in the future.

Instead, it was decided to use the raw GNSS data in this work. In the cases where the compact flash card was not used during the field experiments – and therefore no raw data is available – the KF data is used instead.

A Smoothing Method

If it is assumed that the vehicle travels along the path of the road in a smooth, monotonically increasing or decreasing fashion, then a simple spline-based snapping and smoothing method can be developed.

The location and geometry of any Norwegian road longer than 50 m can be downloaded from Kartverket [108] as a series of points in latitude, longitude and height. For importing to MATLAB, the shapefile format is convenient with the `m_shaperead` function from [157]. Figure E.5 shows the road network near the Hardanger bridge, where the road that crosses the bridge itself is shown using a thick black line.

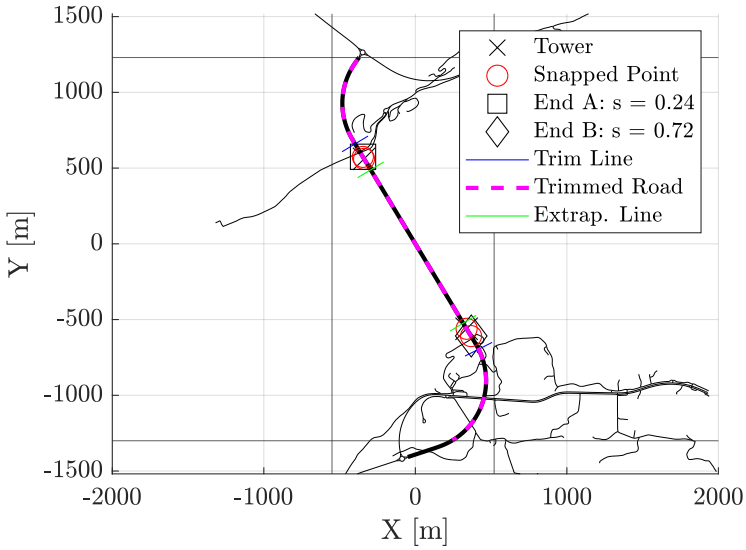

Figure E.5: Setting geometrical reference points and trimming position data. ©Kartverket (road shape)

An interval of this road (indicated by the horizontal and vertical lines) is chosen and these points are used as reference for fitting a piecewise cubic spline curve. The closest point on the curve to each point in the raw GNSS data is found by the `distance2curve` algorithm. Each *snapped* point has a position in ENU coordinates X-Y on the curve as well a normalised position along the curve s. It takes values from 0 to 1.

Figures E.4, E.2 and E.3 show the reference points (downloaded from Kartverket) and the resulting cubic spline. The grey lines then show the correspondence between raw VBOX positions and their respective positions on the spline after smoothing.

The smoothing itself is performed on the s versus t (time) curve. A new series of s values is produced by a spline interpolation on t using a sparsely sampled series of the s-t curve as the reference points for the spline. This process effectively discards all the data between the selected reference points and places it with a spline interpolation.

This is justified for use here because the vehicle is generally driven at a constant, cruise-controlled speed. Any transitions in speed are kept to a minimum and performed as smoothly as possible. We expect smooth and slow changes to the slope of the s-t curve.

A regular interval in time is chosen to define the reference points. The chosen time interval needs to be large enough to smooth out disturbances without being so large as to augment any changes in slope/speed.

A 2-second interval was chosen through trial-and-error. A future study might look to use a repeatable methodology for this choice, though the smoothing is manually checked for each signal presented in this work. The choice of a 2-second interval appears to be universally appropriate for the data presented here and has not been changed for any particular data set.

Handling Disturbances and Dropouts

This method lends itself well to dealing with dropouts. For non-edge dropouts, any of the chosen 2-second reference points within a dropout interval are simply removed from the series of reference points for the s-t spline. The result is demonstrated in Figure E.7b. The dropout intervals can be identified using the *number of satellites* signal available from the VBOX.

The tunnel entrance/exit events are handled by manually defining a point at which the spline interpolation is dropped in favour of a linear extrapolation. By plotting all of the raw GNSS data, a point can typically be identified that separates stable position data from that which has been disturbed.

This defines the line labelled *extrapolation line* in Figures E.5 and E.6. Data is sought up to the *trim* line and sometimes a number of seconds beyond. Data between the extrapolation and trim lines is extrapolated using the slope immediately preceding the extrapolation line. An example of the results of the extrapolation can be seen in Figure E.7a.

Refer once more to Figure E.1 to see how the raw data is finally mapped to the closest point on the road centreline following this smoothing process. Note that this is the position of antenna A along the centreline of the road. The vehicle is long and the CG is approximately 3 m forward of antenna A in the vehicle's x' axis and the anemometer is approximately 4.5 m ahead.

Translation to Point of Measurement

The translation from antenna A to the CG and anemometer will be approximate. The x-component of -$\mathbf{r}_A + \mathbf{r}_{cg}$ (approx. 3 m) and -$\mathbf{r}_A + \mathbf{r}_{WM}$ (approx. 4.5 m) are each respectively added to the snapped position of antenna A in a vector addition. For simplicity, the gradient of the road spline is used to estimate the direction of x'; the vehicle's forward axis in the ENU system.

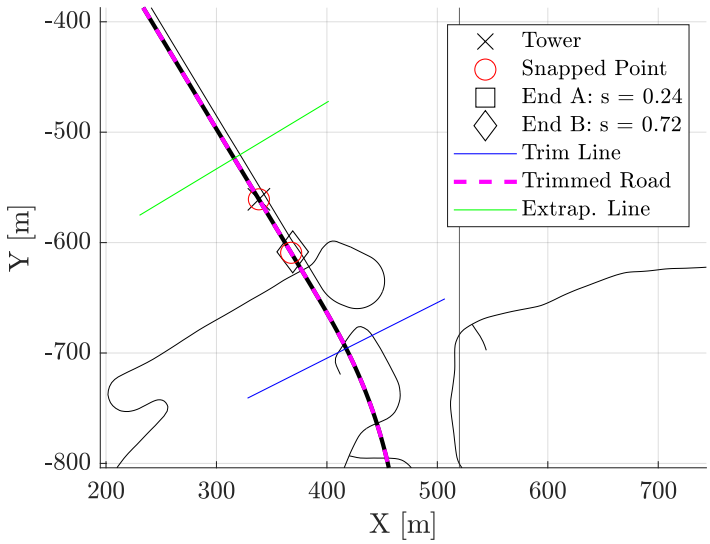

Figure E.6: An enlarged view of the tower, end, trim and extrapolation reference features. ©Kartverket(road shape)

Translating Wind Measurements

The components of the wind vector $\mathbf{v}_w^E$ in the ENU reference frame can be estimated:

$$u_w^E + iv_w^E = (u_w^U + V_A + iv_w^U)e^{i\Psi_h}, \tag{E.1}$$

where u_w^U and v_w^U are the wind components in the U reference frame, which will be assumed to be aligned with the anemometer.

With this assumption we are ignoring any static or dynamic angular offset the anemometer may have relative to x in the U system. This means any compliance in the vehicle structure, roof rack and strut between the wheels' contact point on the ground and the anemometer's point of measurement is ignored. In other words, the S and U systems are aligned. These angles are expected to be very small compared

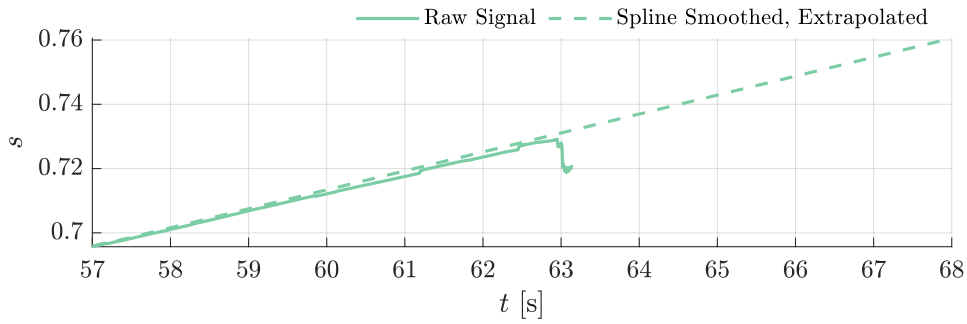

(a) Example of extrapolation

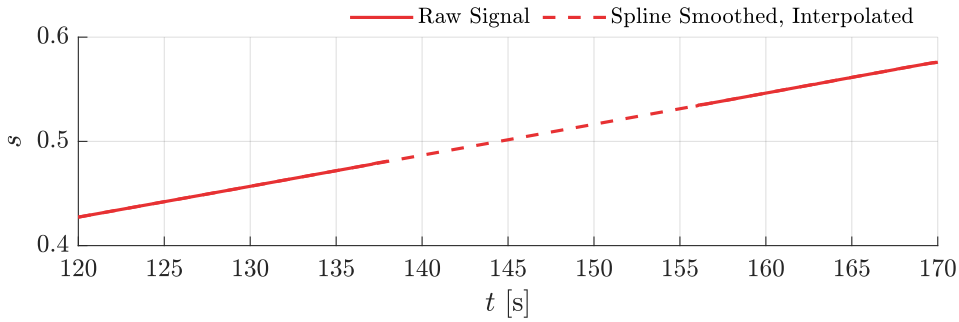

(b) Example of interpolation

Figure E.7: Spline smoothing, interpolation and extrapolation of distance travelled along the road s.

to variations in wind direction and will not have a significant effect on the results of the wind profile analysis.

V_A is the magnitude of the velocity vector at antenna A. In Equation E.1 it is assumed that the direction of this vector is aligned with positive x in the U system. Consequently, no account is made for the possibility of a sideslip velocity at A. The sideslip component is assumed to be small compared to the features of interest in the wind profile.

The term within the parentheses gives the wind velocity in the U system compensating for the vehicle's velocity. The $e^{i\Psi_h}$ term rotates this with the vehicle's heading to give the wind vector in the ENU system. Note that with the assumptions given above, Ψ_t is equal to Ψ_h.

In summary, the 2D wind vector in the ENU, earth-fixed reference frame can be estimated by compensating for the vehicle's speed and transforming the raw anemometer measurement $\mathbf{v}_w^U$ with the vehicle's velocity and direction of travel respectively. The transformation relies on the two signals V_A and Ψ_h which are estimated by the VBOX's GNSS engine.

Smoothing Velocity and Heading

For consistent and successful application of Equation E.1, the velocity and heading signals need to be as accurate as possible without adding noise to the wind measurements.

The speed and heading measurements are also smoothed by the VBOX KF. However, as explained above, raw GNSS data will be used here. The signals are subject to the same dropouts as the position data. The same step discontinuities (from disturbances) as in Figure E.1 have not been observed, though the signals are relatively noisy.

To deal with noise and discontinuities, the heading and speed signals are first filtered using a moving median with a window of 3 seconds. The median is more robust in filtering outliers than the mean. Any dropouts are subsequently filled using a spline. The spline is only used to *fill* in the missing signal and does not affect the value where information is available. Where extrapolation is needed, a constant value equal to the nearest non-NaN value is used.

The extrapolation is really only relevant in the Hardanger bridge case where there are tunnel entrances/exits at each of the abutments that block and disturb GNSS signals. Every effort was made to maintain a constant speed in and out of the tunnels. This is also consistent with the linear extrapolation in the smoothing of the position data.

Figure E.8 demonstrates the bridging of the gaps in velocity and heading signals whereas Figure E.9 demonstrates the *nearest non-NaN* extrapolation. The median filter followed by a spline filling appears to apply realistic corrections to the heading

and speed signals.

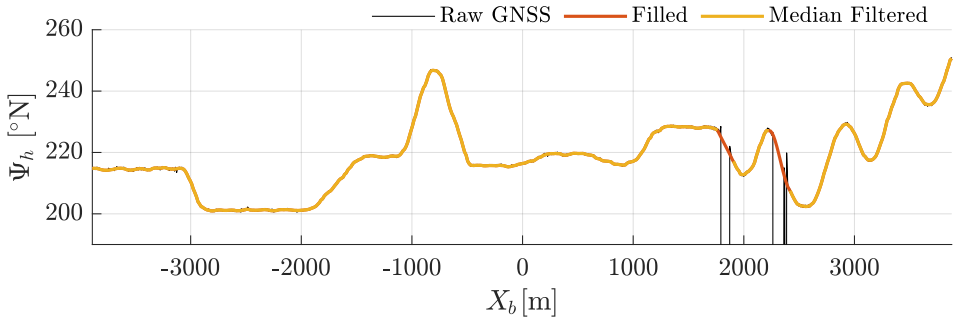

(a) Heading

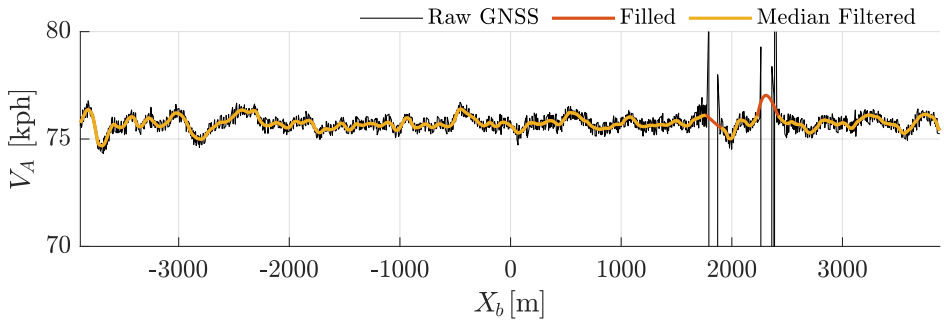

(b) Velocity

Figure E.8: Examples of interpolation.

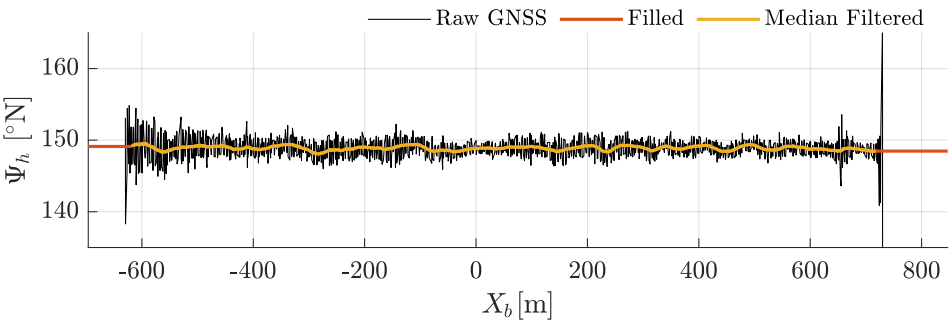

(a) Heading

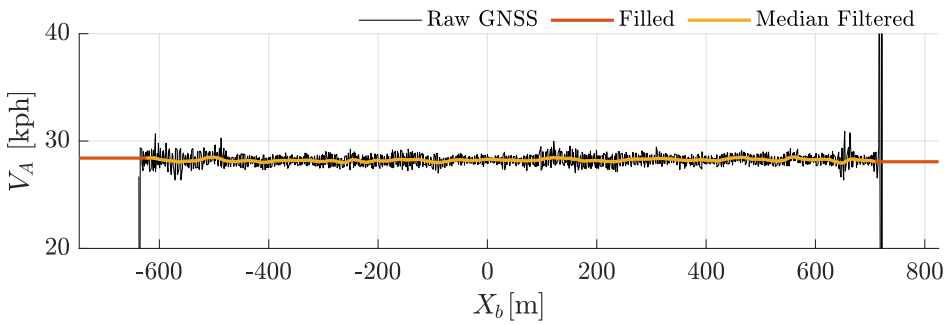

(b) Velocity

Figure E.9: Examples of extrapolation.

Appendix F

Wind/response profiles at Frøya

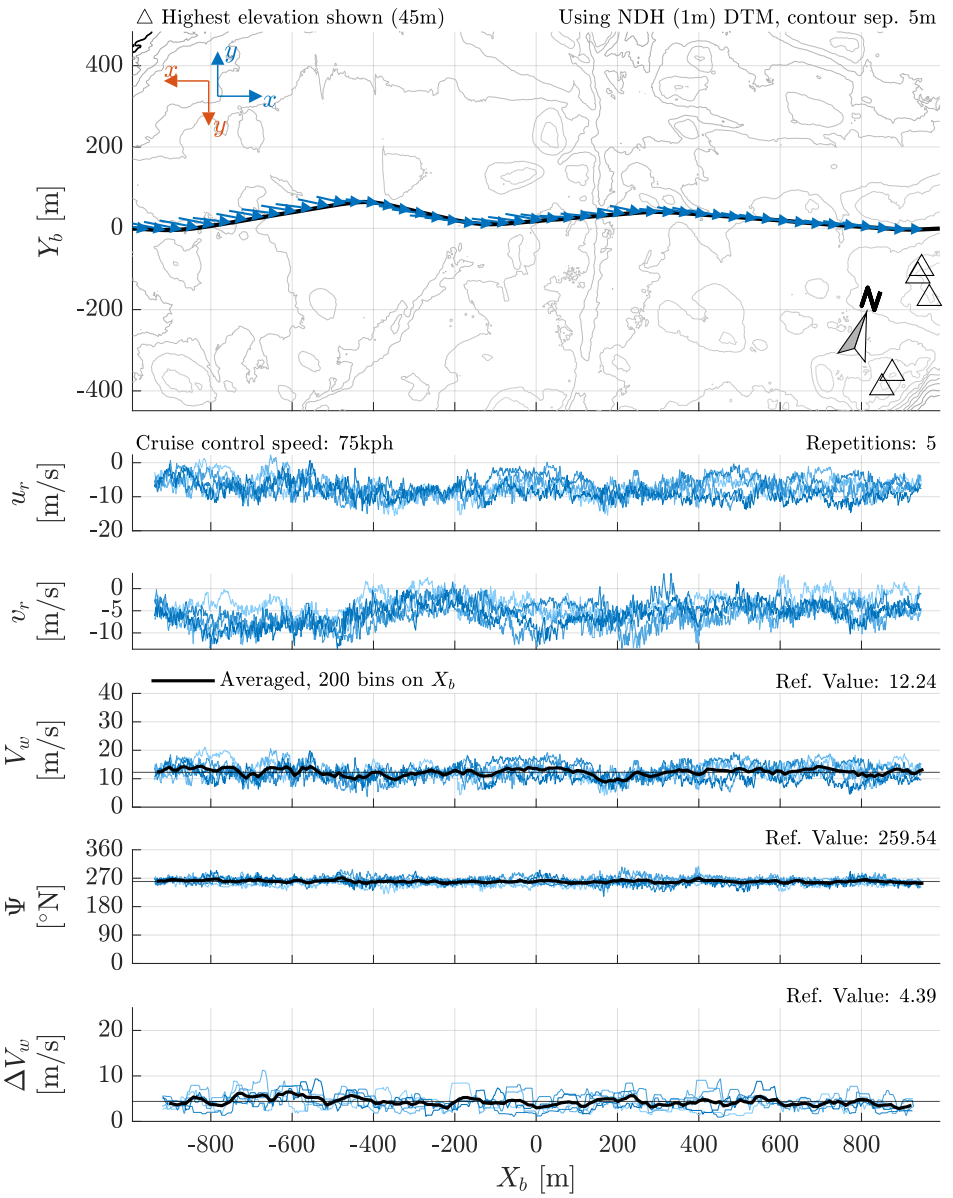

Figure F.1: Wind profile, Frøya, windward lane (vehicle travels left to right), see Section 8.3 for full explanation. ©Kartverket (terrain model & road shape)

u_r and v_r: raw wind in vehicle-fixed anemometer reference frame (see Figure 14.4 for explanation of r), V_w: in-plane wind magnitude in earth-fixed reference frame, Ψ: wind heading from North, ΔV_w: maximum change of V_w within moving 45 m window.

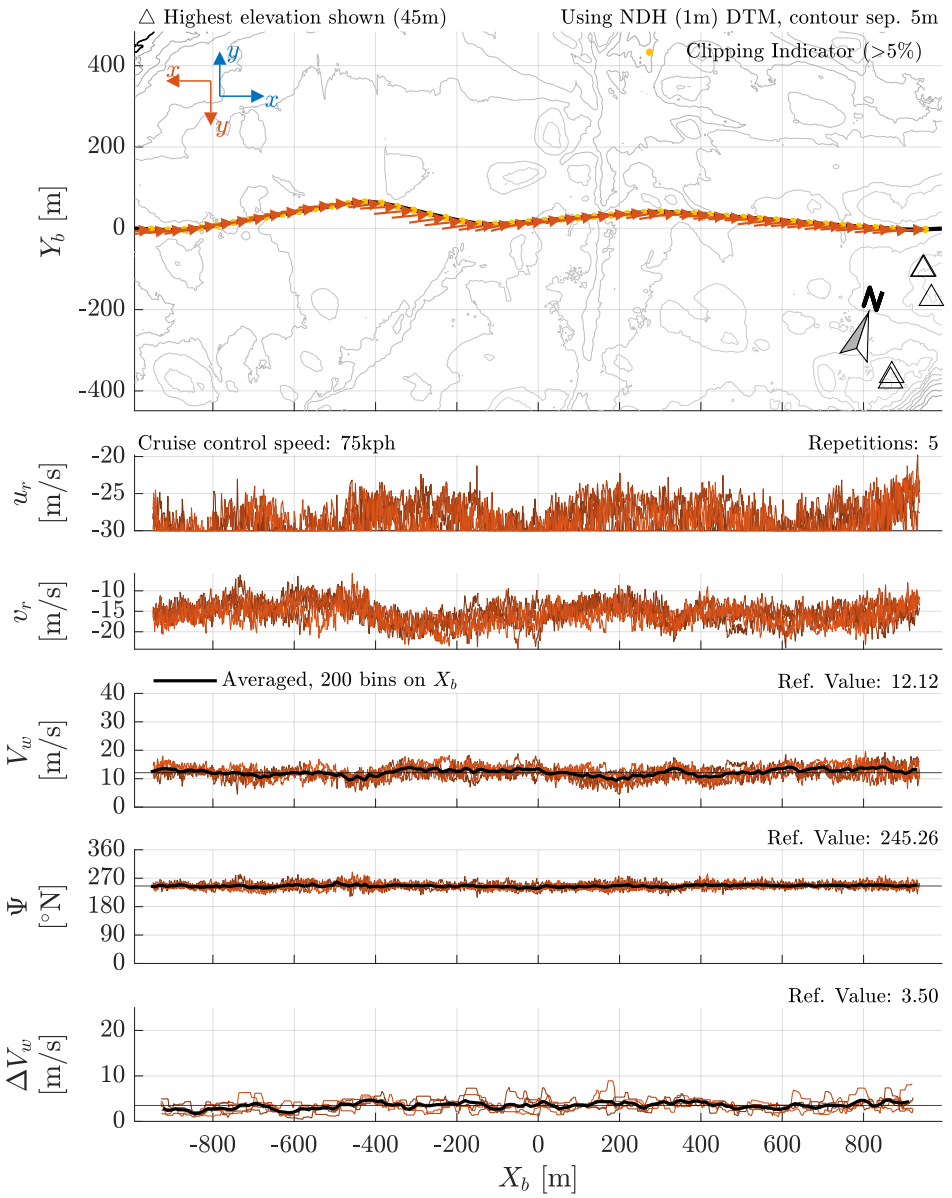

Figure F.2: Wind profile, Frøya, leeward lane (vehicle travels right to left), see Section 8.3 for full explanation. ©Kartverket (terrain model & road shape)

u_r and v_r: raw wind in vehicle-fixed anemometer reference frame (see Figure 14.4 for explanation of r), V_w: in-plane wind magnitude in earth-fixed reference frame, Ψ: wind heading from North, ΔV_w: maximum change of V_w within moving 45 m window.

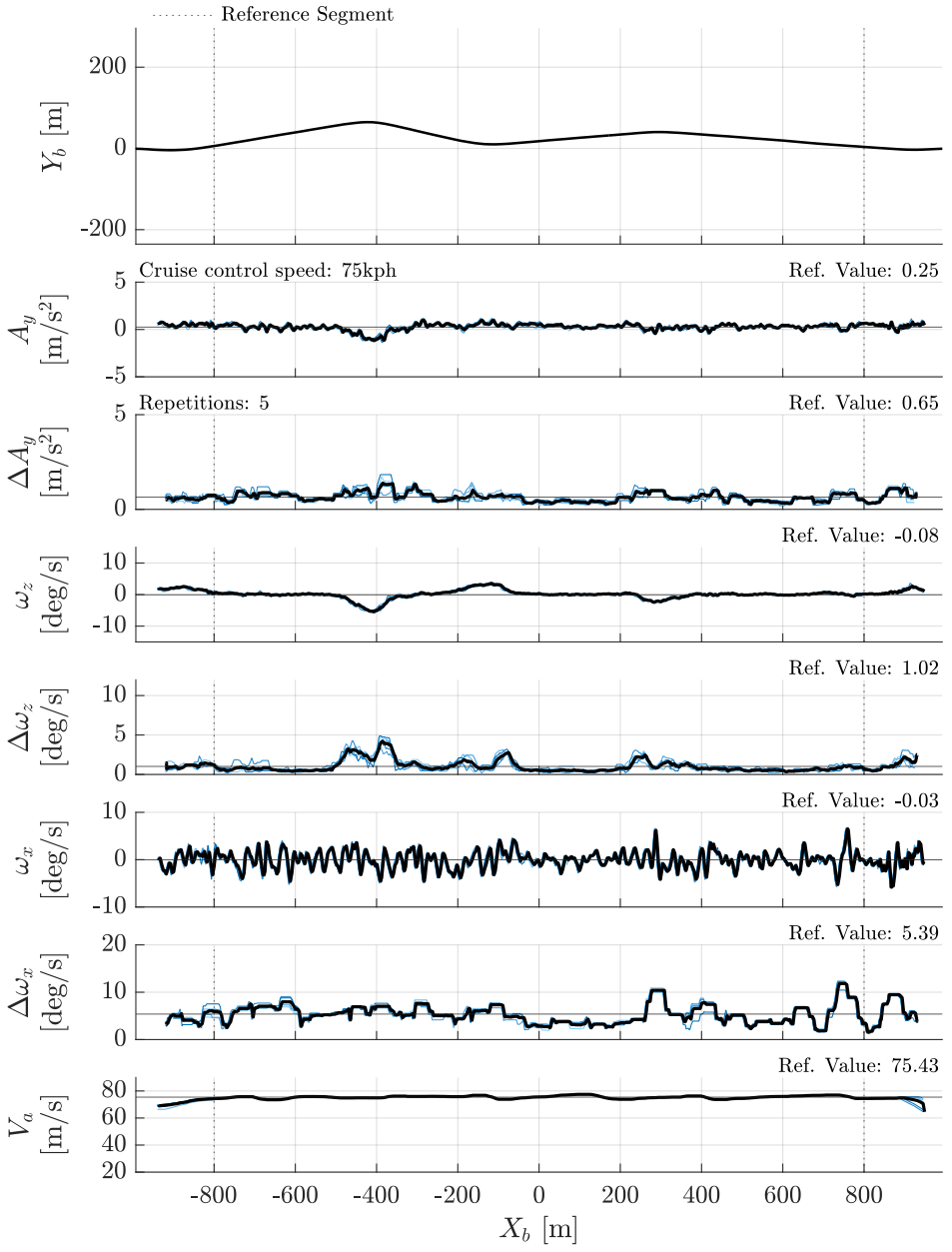

Figure F.3: Response profile, Frøya, windward lane (vehicle travels left to right), see Section 9.2 for full explanation. ©Kartverket (terrain model & road shape)

All signals measured by Inertial Measurement Unit and filtered by a low-pass Butterworth filter with a cut-off of 5 Hz, A_y: lateral acceleration, ω_z: yaw rate, ω_x: roll rate, $\Delta(i)$: maximum minus minimum of signal i within 2-second sliding window, V_a: GNSS speed measured at antenna A (see Figure A.3).

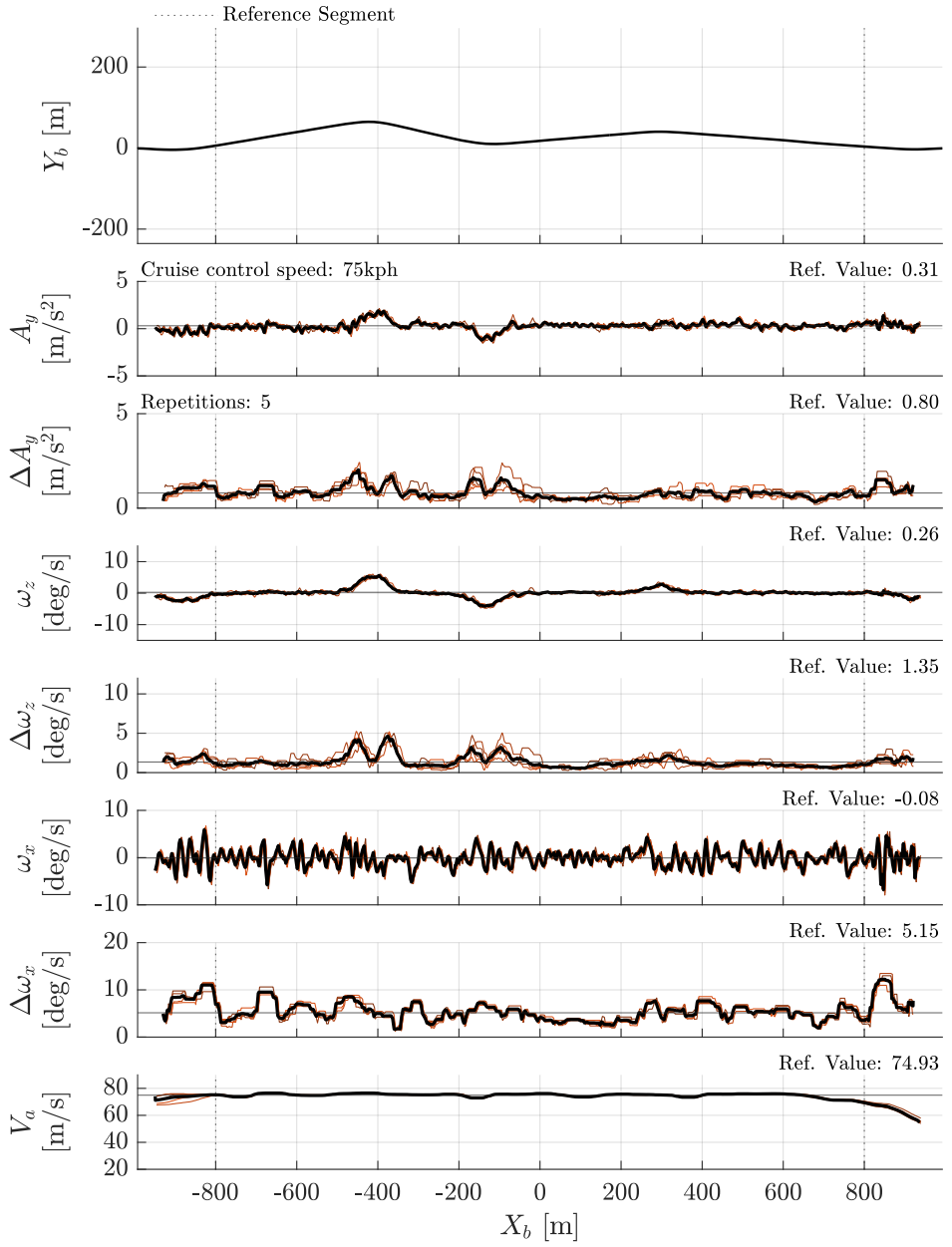

Figure F.4: Response profile, Frøya, leeward lane (vehicle travels right to left), see Section 9.2 for full explanation. ©Kartverket (terrain model & road shape)

All signals measured by Inertial Measurement Unit and filtered by a low-pass Butterworth filter with a cut-off of 5 Hz, A_y: lateral acceleration, ω_z: yaw rate, ω_x: roll rate, $\Delta(i)$: maximum minus minimum of signal i within 2-second sliding window, V_a: GNSS speed measured at antenna A (see Figure A.3).

ISBN 978-82-326-6227-2 (printed ver.)
ISBN 978-82-326-6117-6 (electronic ver.)
ISSN 1503-8181 (printed ver.)
ISSN 2703-8084 (online ver.)

NTNU

Norwegian University of
Science and Technology